



**Universidade Federal do Espírito Santo**

**Programa de Pós-Graduação em Astrofísica, Cosmologia e Gravitação**

## **Modified Gravity and Large Scale Structure Cosmology: a linear and non-linear treatment**

**Guilherme Brando de Oliveira**

Thesis submitted as part of the requirements for the degree of  
Doctor of Philosophy in Astronomy & Physics

Supervisor: Prof. Felipe Tovar Falciano  
*Cosmo, Centro Brasileiro de Pesquisas Físicas (Brazil)*

Co-supervisor: Prof. David Wands  
*ICG, University of Portsmouth (UK)*



**2022**

**Universidade Federal do Espírito Santo**

**Centro de Ciências Exatas**

Programa de Pós-Graduação em Astrofísica, Cosmologia e Gravitação

**Modified Gravity and Large Scale Structure Cosmology: a linear and non-linear treatment**

Guilherme Brando de Oliveira

A presente tese "*Modified Gravity and Large Scale Structure Cosmology: a linear and non-linear treatment*" foi submetida no ano de 2022 ao PPG-Cosmo por *Guilherme Brando de Oliveira* como parte dos requisitos para a obtenção do título de Doutor em Astronomia e Física.

Caso esta tese venha a ser aprovada, esta folha deverá ser substituída pela correspondente de aprovação.

# Abstract

This thesis consists of a comprehensive study of beyond- $\Lambda$ CDM cosmologies, in particular I investigate possible consequences of scalar-tensor theories of gravity on the Large Scale Structure of the Universe. Within the Standard Model of Cosmology, General Relativity is assumed to be the theory that describes gravity in all scales and this is supported by the highly accurate Astrophysical and Solar System tests. Notwithstanding, at cosmological scales, we still lack gravity tests with the same constraining power. Therefore, in addition to the motivation from the well-known conceptual problems of the Cosmological Constant, it is reasonable to investigate if General Relativity is the correct gravity theory at the largest scales of the Universe.

In order to increase the accuracy of our cosmological tests of gravity, I develop numerical tools based on the linear and nonlinear regimes of cosmological perturbation theories, as well as a non-perturbative approach using quasi N-body simulations. I also present different ways of testing the large freedom introduced by modified theories of gravity in the parameter space. Indeed, modified gravity models cannot avoid introducing extra parameters besides the usual six cosmological parameters of the  $\Lambda$ CDM model.

The main results of the thesis have been published in four papers cited along the text and I have tried to condensate them mainly in Chapters 3, 4 and 6. In chapter 3 I discuss the impact of modified gravity on cosmological observables such as the modifications Horndeski theories introduce in the growth and light propagation equations of motion. In particular, I perform a detailed analysis of the No Slip Gravity at the linear regime of structure formation. Then, I discuss how early modified gravity theories change the matter power spectrum at large and small scales.

In Chapter 4, I start by analyzing the matter power spectrum at linear scales, namely how it is defined within  $\Lambda$ CDM and how massive neutrinos introduce a scale dependent on the growth function. Then, I introduce the formulation of the N-Body gauge, a specific coordinate system that facilitates the interpretation of Newtonian simulations within a relativistic framework, by consistently introducing the effects coming from photons, neutrinos and dark energy. As stage-IV LSS surveys will probe the Universe at increasingly large scales; it is imperative to include these species in our analysis inasmuch at large scales their imprint can be above the 1% threshold. I also present new cosmological tests of gravity by combining this framework with relativistic N-Body simulations. At the end I show how to correctly combine modified gravity effects and Newtonian simulations.

In Chapter 5, I outline all the nonlinear mathematical tools have I have studied and developed during this project and on Chapter 6 I present the results of how we can construct computationally fast new numerical tools using all the new developments I have done in modified gravity, from linear to nonlinear scales. Chapter 7 ends the thesis with some conclusions and three future avenues I plan to pursue in the next few years.

# Resumo

Esta tese consiste num estudo amplo sobre cosmologias além- $\Lambda$ CDM, em particular as possíveis consequências de teorias de gravidade escalares-tensoriais na estrutura em grande escala do Universo foram estudadas. Dentro do Modelo Padrão da Cosmologia, a Relatividade Geral é tomada como a teoria que descreve a gravidade em todas as escalas, fato este que possui suporte em testes Astrofísicos e do Sistema Solar. Entretanto, em escalas cosmológicas, testes gravitacionais ainda não possuem o mesmo poder de vínculo. Desta maneira, o estudo em teorias alternativas de gravidade, além da usual motivação de explicar problemas conceituais da Constante Cosmológica, ainda se faz extremamente necessário.

Para aumentar o poder de precisão em testes de gravidade em escalas cosmológicas, eu desenvolvi ferramentas numéricas baseadas em teoria de perturbação cosmológica, em ordem linear e não-linear, assim como um tratamento não-perturbativo usando simulações de quasi N-corpos. Eu também exponho diferentes caminhos para testarmos a grande liberdade que temos no espaço de parâmetros introduzidos por teorias de gravidade modificada. De fato, ao trabalharmos com tais modelos, a introdução de parâmetros extra, além dos seis parâmetros cosmológicos do modelo  $\Lambda$ CDM, é inevitável.

Os principais resultados desta tese foram publicados em quatro artigos, citados ao longo do texto, e seus conteúdos foram condensados nos Capítulos 3, 4 e 6. No Capítulo 3, o impacto que teorias de gravidade alternativa possuem em observáveis cosmológicos é discutido. Em particular eu apresento uma análise, a nível linear, detalhada do modelo de gravidade No Slip, e como essa teoria impacta a formação de estruturas e a propagação da luz. Além disso, no mesmo capítulo, eu brevemente discuto como teorias de gravidade primitivas modificam o espectro de potência em largas e pequenas escalas.

No Capítulo 4, eu começo analisando o espectro de potência da matéria em escalas lineares, especificamente como ele é definido no modelo  $\Lambda$ CDM, e como neutrinos massivos introduzem uma dependência de escala na função de crescimento. Após, eu introduzo a formulação do calibre de N-corpos, um sistema de coordenadas específico que facilitam a interpretação de simulações Newtonianas num contexto relativístico. Isso é possível através da introdução, de maneira consistente com o tratamento Newtoniano, de espécies relativísticas, como fótons, neutrinos e energia escura. Como os levantamentos cosmológicos de estágio-IV vão o Universo em escalas cada vez maiores; é imperativo que possamos incluir tais espécies em nossas análises, já que seu efeito em grandes escalas pode ir além do limite de 1% quando comparadas a um Universo com somente matéria escura. Ao final do capítulo eu apresento como podemos combinar gravitação modificada com simulações Newtonianas.

No Capítulo 5, eu exponho todo o ferramental matemático a nível não-linear que eu estudei e desenvolvi ao longo desta tese. E, no Capítulo 6, eu apresento os resultados de como podemos construir ferramentas rápidas computacionalmente usando todo o ferramental que eu desenvolvi em gravidade modificada, indo de escalas lineares para não-lineares. O Capítulo 7 fecha a presente teste com algumas conclusões, e possíveis linhas de pesquisa futuras que eu almejo desenvolver.

# Acknowledgments / Agradecimentos

Primeiramente, eu gostaria de agradecer ao meu orientador Felipe Tovar, que me acompanha há quase dez anos nessa minha jornada acadêmica. Seu olhar crítico sobre a física foi um grande ensinamento para mim, assim como a liberdade e incentivo que ele sempre me deu foram sem dúvida alguma determinantes para o meu doutorado. Agradeço a ele também a sua amizade e colaboração. Espero que no futuro continuemos a trabalhar e a trocar juntos. Gostaria também de agradecer ao meu grande colaborador e amigo, Bruno Moraes, que topou de livre e espontânea vontade me ajudar a trilhar 3 dos meus 4 anos de doutorado.

Não posso também deixar de mencionar professores que muito me ensinaram em suas aulas, conversas e colaborações. Em primeiro lugar, o Professor Júlio Fabris, que, desde o momento que eu cheguei à UFES, me acolheu de maneira incrível. Além do profissional, sempre vou carregar na memória os jogos do nosso Glorioso que vimos juntos. Em segundo lugar, agradeço ao Professor Nelson Pinto Neto, que não só me acompanhou no doutorado, mas também durante o mestrado. Por último gostaria de agradecer ao Professor Davi Cabral, da UFES, que apesar de eu ter cursado apenas uma disciplina com ele, Relatividade Geral II, sempre esteve disposto a conversar abertamente sobre assuntos profundos da física, em especial, gravitação.

I'll now thank my external collaborators and mentors. First, I would like to thank Eric Linder, for giving me the opportunity of my first visit to a University outside Brazil. The opportunity to collaborate with him was a very insightful part of my PhD. I'd also want to thank Professors David Wands and Kazuya Koyama, for the warm welcome they gave me at the ICG, an inspiring place to do research at. Specifically, I would like to thank Kazuya for his patience and guidance throughout much of the work developed in this thesis.

Gostaria também de agradecer à minha família, por sempre terem me dado todo o suporte financeiro e familiar para que eu pudesse trilhar uma carreira acadêmica. Em especial, agradeço ao meu pai por ter sempre me incentivado a ler sobre ciência, à minha mãe por todo seu apoio incondicional, e por último ao meu padrasto, irmã e cunhado, que sempre estiveram ao meu lado.

Agradeço também aos meus amigos e amigas de longa data: Hans, Gustavo, Johnny, Miti, Yuri, Sanchez, João Fillype, Zig, Caio, Vamp, Mike Love, GdP, Felipe, Augusto, John, Cassar, Lfog, Fma, Ana Carolina, Julia, Ana Luiza e a tantos outros e outras que não caberiam nesse pequeno texto. Obrigado também aos amigos e companheiros de doutorado, Renan, David, Raquel e Rahima.

Again, I'm also indebted to the great friends I've made during my time abroad. Julian, Caroline and Sonia, my roommates when I was in England. MPRK-A, the captain of the Green Army and the ICG Galaticos, Laura, Mike Wang, Chris and Natalie (the bruhs), Jacob (aka the Big-J), Bart (who is also a collaborator) and Robyn. All of you made my time in the UK more special.

Por último, eu gostaria de agradecer ao Flávio Ramos e ao Emmanuel Sodré, que, no dia 12 de agosto de 1904 fundaram a minha maior paixão, o Botafogo de Futebol e Regatas, o Glorioso. Ser um alvinegro de coração e alma não é uma tarefa simples, assim como tudo na vida, no entanto, toda vez que a Estrela Solitária entra em campo, a vida faz sentido. Obrigado por tudo Botafogo, e obrigado ao meu tio, Renato, por me apresentar ao Botafogo.

Agradeço à Fundação de Amparo a Pesquisa do Estado do Espírito Santo, FAPES, pelo auxílio financeiro. Agradeço também a Coordenação de Aperfeiçoamento de Pessoal de Nível Superior, CAPES, pelo auxílio financeiro durante meu ano na Inglaterra.

# Contents

<b>1. Introduction</b>	<b>1</b>
1.1. Standard Model of Cosmology . . . . .	1
1.2. Perturbations . . . . .	7
1.2.1. Newtonian Gauge . . . . .	12
1.2.2. Comoving Gauge . . . . .	12
1.2.3. Synchronous Gauge . . . . .	13
1.3. Boltzmann Equations . . . . .	14
1.4. Cornerstone Observations . . . . .	22
1.4.1. CMB . . . . .	22
1.4.2. Supernovae Ia . . . . .	23
1.4.3. BAO . . . . .	25
1.4.4. Redshift-space distortions . . . . .	26
1.4.5. Gravitational lensing . . . . .	28
<b>2. Modified Gravity</b>	<b>30</b>
2.1. Introduction . . . . .	30
2.2. Lovelock Theorem . . . . .	30
2.3. Scalar-Tensor Theories . . . . .	31
2.4. Linear Perturbation Theory . . . . .	35
<b>3. Linear tests of modified gravity</b>	<b>43</b>
3.1. Growth and light propagation in Horndeski gravity . . . . .	43
3.2. Structure formation in No Slip gravity . . . . .	46
3.3. Early modified gravity . . . . .	51
<b>4. Linear N-Body gauge</b>	<b>55</b>
4.1. The Linear Matter Power Spectrum in MG Theories . . . . .	55
4.2. N-body gauge . . . . .	59
4.3. Modified gravity . . . . .	62
<b>5. Non-Linear Universe</b>	<b>75</b>
5.1. Large Scale Structure of the Universe . . . . .	75
5.2. Growth in LCDM . . . . .	75
5.2.1. SPT in LCDM . . . . .	76
5.2.2. Lagrangian Perturbation Theory . . . . .	81
5.3. SPT in Modified Gravity . . . . .	86
5.4. 2LPT in Modified Gravity . . . . .	88
5.5. COLA . . . . .	94

<b>6. Enabling power spectrum emulation in beyond-<math>\Lambda</math>CDM cosmologies with COLA</b>	<b>102</b>
6.1. Introduction . . . . .	102
6.2. Methodology . . . . .	104
6.2.1. COLA . . . . .	104
6.2.2. Emulators . . . . .	104
6.2.3. Boost and response function . . . . .	106
6.3. $\Lambda$ CDM Analyses . . . . .	107
6.3.1. Variation of cosmology parameters . . . . .	107
6.3.2. Inclusion of massive neutrinos . . . . .	110
6.4. Modified Gravity . . . . .	111
6.4.1. Fixed cosmology . . . . .	113
6.4.2. Varying cosmology . . . . .	114
6.5. Closing remarks . . . . .	116
<b>7. Conclusions and Future Avenues</b>	<b>120</b>
7.1. Conclusion . . . . .	120
7.2. Future . . . . .	121
7.2.1. Relativistic simulations . . . . .	121
7.2.2. Emulators in Horndeski Gravity . . . . .	121
7.2.3. Extracting Modified Gravity from LSS data . . . . .	121
<b>A. hiclass specifications N-body gauge</b>	<b>122</b>
<b>B. COLA specifications</b>	<b>125</b>
<b>C. Small variations of cosmological parameters</b>	<b>129</b>

# Introduction

## 1.1. Standard Model of Cosmology

The success of the standard model of cosmology,  $\Lambda$ CDM, is widely regarded as the greatest achievement of modern cosmology. It is a parametrization of our Universe that relies on three fundamental ingredients: a cosmological constant, described by the Greek letter  $\Lambda$ ; an exotic and unknown species called cold dark matter (CDM); and ordinary baryonic matter. The status of “standard description” of our Universe is due to the ability of this model in describing in a reasonably good account the following observations:

- The existence of the cosmic microwave background (CMB);
- The large scale structure (LSS) distribution in our Universe;
- The observed abundances of hydrogen (including deuterium), helium, and lithium, produced during the Big Bang Nucleosynthesis (BBN);
- The current accelerated expansion of the Universe, caused by dark energy.

The fundamental description of the concordance model also relies on a simple and direct assumption, the Cosmological Principle. It states that our Universe is homogeneous and isotropic at large scales. That is, we have no privileged point in spacetime in which the Universe should be preferably observed. This has been the subject of much dispute throughout history, and it has been (and continues) to be tested and put to proof in different scenarios. One last ingredient in the  $\Lambda$ CDM model is the assumption of General Relativity [1] as the fundamental description of gravity in *all scales*.

With these assumptions for our cosmological model, the dynamical system governing the evolution of the Universe is given by Einstein’s field equations:

$$G_{\mu\nu} + \Lambda g_{\mu\nu} = \frac{8\pi G}{c^4} T_{\mu\nu}, \quad (1.1)$$

where  $G_{\mu\nu}$  is the Einstein tensor,  $c$  is the speed of light,  $G_N$  is Newton’s gravitational constant and  $T_{\mu\nu}$  the energy-momentum tensor of matter species. This is a complicated and highly complex set of partial differential equations of up to second order in the metric  $g_{\mu\nu}$ . It determines the structure of space-time in a covariant and coordinate independent fashion. However, the standard model assumes the Cosmological Principle is valid, and, therefore, it will enforce spatial symmetries on our system of Equations. These symmetries are captured by the so-called Friedmann-Leamître-Robertson-Walker (FLRW) metric:

$$ds^2 = g_{\mu\nu} dx^\mu dx^\nu = -c^2 dt^2 + a^2(t) \left[ \frac{dr^2}{1 - \mathcal{K}r^2} + r^2 (d\theta^2 + \sin^2 \theta d\varphi^2) \right]. \quad (1.2)$$

Where  $\mathcal{K} = -1, +1, 0$  represents the spatial metric topology: negatively curved, positively curved and flat, respectively.  $a(t)$  is the scale factor characterizing the expansion/contraction of the Universe. The set of spatial coordinates  $(r, \theta, \varphi)$  are comoving coordinates, as they expand or contract alongside with the Universe. Going a bit deeper in the structure of this line element, we are able to define important quantities in cosmology as well. One of these quantities is the notion of redshift,  $z$ . Since photons travel in null geodesics we have that:

$$dt = \pm \frac{a(t)}{\sqrt{1 - \mathcal{K}r^2}} dr. \quad (1.3)$$

If we integrate the above equation from a time of emission  $t_e$  to a time observed  $t_o$ , we arrive at:

$$\int_{t_e}^{t_o} \frac{dt}{a(t)} = \int_0^{r_1} \frac{1}{\sqrt{1 - \mathcal{K}r^2}} dr = f(r_1), \quad (1.4)$$

where  $r_1$  is the comoving radial coordinate at the time of emission, and

$$f(r_1) = \begin{cases} \sin^{-1} r_1 & \mathcal{K} = +1; \\ r_1 & \mathcal{K} = 0; \\ \sinh^{-1} r_1 & \mathcal{K} = -1. \end{cases} \quad (1.5)$$

By performing the same computation for a subsequent photon emitted at  $t_e + \delta t_e$  and observed at  $t_o + \delta t_o$ , we arrive to an integral similar to (1.4):

$$\int_{t_e + \delta t_e}^{t_o + \delta t_o} \frac{dt}{a(t)} = \int_0^{r_1} \frac{1}{\sqrt{1 - \mathcal{K}r^2}} dr = f(r_1), \quad (1.6)$$

then we have that

$$\int_{t_e}^{t_o} \frac{dt}{a(t)} = \int_{t_e + \delta t_e}^{t_o + \delta t_o} \frac{dt}{a(t)}, \quad (1.7)$$

and in the limit where the frequency of the photon  $\nu \ll t_o - t_e$ , we take  $\delta t = \nu^{-1}$ , which leads to  $a(t_e)\nu_e = a(t_o)\nu_o$ . Since  $\lambda\nu = c$  we obtain

$$\frac{a(t_e)}{a(t_o)} = \frac{1}{1 + z}, \quad (1.8)$$

where I have defined implicitly  $z = \frac{\lambda(t_o) - \lambda(t_e)}{\lambda(t_e)}$ . This is a fundamental relation, as it relates the scale factor to an observable quantity,  $z$ .

While the choice of line element to describe the geometry of the Universe fixes the left hand side of Einstein's field Equations (1.1), we have yet to specify the description of the matter components in the Universe. This is captured in the RHS of Equations (1.1), in the  $T_{\mu\nu}$  term, which for a perfect fluid [2] is written as:

$$T_{\mu\nu} = \left( \rho(t) + \frac{p(t)}{c^2} \right) u_\mu u_\nu + p(t) g_{\mu\nu}, \quad (1.9)$$

where  $\rho(t)$  is the energy density of the fluid,  $p(t)$  the pressure and  $u^\mu$  the 4-velocity. From now on I'm going to set  $c = 1$ .

By plugging Equations (1.2) and (1.9) into (1.1), we arrive at the Friedmann Equations:

$$H(t) = \frac{\dot{a}}{a} = \frac{8\pi G}{3}\rho(t) - \frac{\mathcal{K}}{a^2} + \frac{\Lambda}{3} \quad (1.10)$$

$$\frac{\ddot{a}}{a} = -\frac{4\pi G}{3}(\rho(t) + 3p(t)) + \frac{\Lambda}{3}, \quad (1.11)$$

with  $H(t)$  being the physical Hubble factor. Equation (1.10) is called the Hamiltonian constraint, while Equation (1.11) is a dynamical equation that involves the second derivative of the scale factor, or the first derivative of the Hubble factor. I will now focus on the RHS of the Hamiltonian equation, where are the different ingredients in our Universe.

The first term on the RHS of Equation (1.10) represents the sum of all matter species in the Universe. These are: cold dark matter, photons, neutrinos (massless or massive) and baryons. If we assume that the energy-momentum tensor is conserved for each species, the quantities describing these fluids are subjected to a governing conservation equation:

$$\dot{\rho}_i = -3H(\rho_i + p_i), \quad (1.12)$$

where the subscript  $i$  refers to one of the aforementioned species,  $i = c, \gamma, \nu, b$ , CDM, photons, neutrinos and baryons respectively. Equation (1.12) tells us then that if we have a relation between the two quantities of a perfect fluid,  $\rho$  and  $p$ , we can determine its time evolution. The relation between these two quantities is given by a dimensionless parameter  $w = \frac{p}{\rho}$ , called equation of state parameter, and, depending of the fluid in question, can be time dependent. However, for simple species such as CDM and photons, this parameter is constant, being equal to 0 and 1/3 respectively. Massless neutrinos are essentially photons, as they have no rest mass they never become non-relativistic. The other two cases, baryons and massive neutrinos are a bit more complex, but at background level of the expansion of the Universe in the largest scales their equation of state parameter can be set to 0.

Therefore, with these simple statements we are able to find the evolution for non-relativistic matter and relativistic matter in our universe as a function of the scale factor:

$$\rho = \rho_{0,i} \times \begin{cases} a^{-3} & \text{for non-relativistic;} \\ a^{-4} & \text{for relativistic.} \end{cases} \quad (1.13)$$

Where  $\rho_{0,i}$  is some initial density constant.

The second term of the RHS in Equation (1.10) is known as the curvature term. It is related to the shape of our Universe, and depending on its values,  $(-1, +1, 0)$ , the topology of the cosmos is considered closed, open or flat, respectively.

Figure 1.1 shows the scale factor as a function of time for different Universes with different matter and curvature compositions. We can see that in the closed case our Universe would eventually reach a turning point where,  $H = 0$ , and then recollapse in the future. This feature is not present for the other two cases.

The third term of the RHS of (1.10) is the Cosmological Constant. This term has a lengthy history in Cosmology, and I will now do a brief recap of its timeline:

- In 1915 Einstein publishes his equations of General Relativity, without a cosmological constant  $\Lambda$ ;
- In 1917 [3] Einstein adds the parameter  $\Lambda$  to force his Universe model to remain static and eternal (Einstein static universe), which he will later call "the greatest stupidity of his life";

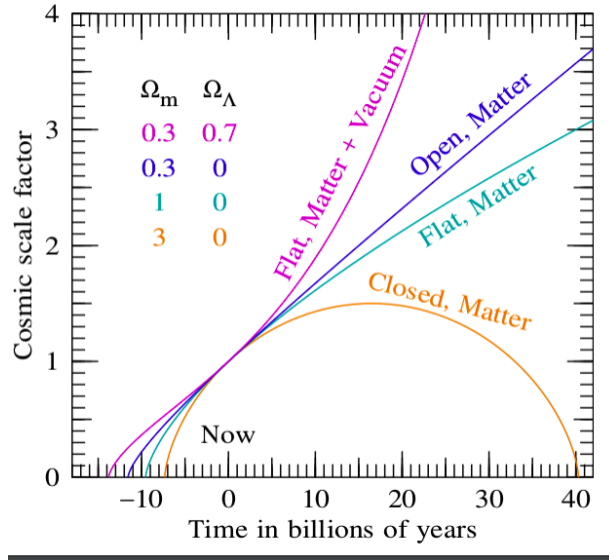


**Figure 1.1.** Evolution of the scale factor as a function of cosmic time,  $t$ . The different colors refer to different cosmic topologies.

- In 1922 [4] the Russian physicist Alexander Friedmann mathematically shows that Einstein's equations (whatever  $\Lambda$ ) remain valid in a dynamic universe.
- In 1927 [5] the Belgian astrophysicist Georges Lemaître shows that the Universe is in expansion by combining General Relativity with some astronomical observations, those of Hubble in particular.
- In 1931 Einstein finally accepts the theory of an expanding universe and proposed, in 1932 with the Dutch physicist and astronomer Willem de Sitter, a model of a continuously expanding Universe with zero cosmological constant (Einstein-de Sitter space-time).
- In 1998 two teams of astrophysicists, one led by Saul Perlmutter [6], the other led by Brian Schmidt and Adam Riess [7], carried out measurements on distant supernovae and show that the speed of galaxies recession in relation to the Milky Way increases over time. The universe is in an accelerated expansion, which requires having a strictly positive  $\Lambda$ . The universe would contain a mysterious dark energy producing a repulsive force that counterbalances the gravitational braking produced by the matter contained in the universe.

As we can see, the necessity to introduce  $\Lambda$  in Einstein's field equations stem for the need to explain the current accelerated expansion of our Universe. As we will see in this thesis, however, this is not the only solution to generate a late time accelerated expansion, but, it is the simplest known. In the same way we have an equation of state parameter for the other matter species, we can also find one for the case of the Cosmological Constant. By substituting  $p = w\rho$  in Equation (1.12), we find a general solution for the energy density of a given species as a function of the scale factor:

$$\rho(a) = \frac{\rho_0}{a^{3(1+w)}}. \quad (1.14)$$

Therefore, if we inspect Equation (1.10), we see that the Cosmological constant has no scale factor dependence, it is as the name says *constant*. From Equation (1.14) if we set  $w = -1$ ,

we have that  $\rho = \text{const.}$ , thence another feature that makes the Cosmological Constant such a mysterious and exotic component, is the fact that it is a fluid with a negative pressure  $p = -\rho$ .

Now that we have discussed the components of the Universe, I will inspect a bit closer the nuances of Equations (1.10-1.11). Present day energy densities in the Universe are measured in terms of the critical density,  $\rho_c$ . This is the value in which the Hamiltonian constraint Equation gets saturated in today's values, e.g.

$$H_0^2 = \frac{8\pi G}{3}\rho_c \quad (1.15)$$

which implies

$$\rho_c = \frac{3H_0^2}{8\pi G}. \quad (1.16)$$

Where  $H_0$  is the value of the Hubble parameter today. What this actually means is that we can then define adimensional fractional energy densities for a given species  $i$ :

$$\Omega_{i,0} = \frac{\rho_{i,0}}{\rho_c} = \frac{8\pi G\rho_{i,0}}{3H_0^2}, \quad (1.17)$$

and the sum of all species in the Universe is therefore 1:

$$\sum_i \Omega_i = 1. \quad (1.18)$$

Similarly one can define a time evolving fractional energy density via

$$\Omega_i(a) = \frac{8\pi G\rho_i(a)}{3H^2(a)}. \quad (1.19)$$

As we know, the observable Universe began with a small physical size, and from equation (1.13) we can see that since the scale factor dependence of radiation dominates for smaller values of the scale factor, the universe had different epochs. That is, in the beginning it had an era of radiation domination, then it moved to an era where non-relativistic matter dominated, and then shifted to the phase we are currently in, an epoch in which  $\Lambda$  dominates.

We can see from Figure 1.2 the adimensional evolution of the different species in our Universe as dictated by the  $\Lambda$ CDM model. The two scale factors where lines intersect correspond to the era of radiation-matter equality and the matter- $\Lambda$  equality.

One important aspect I have not yet discussed is with respect to the notion of cosmological distances. The starting point of this discussion lies in the definition of a comoving distance, which is related to the propagation of a light ray from an emitted time to an observed time:

$$\chi(t) = c \int_t^{t_0} \frac{dt'}{a(t')} = c \int_{a(t)}^1 \frac{da'}{a'^2 H(a')} = c \int_0^z \frac{dz'}{H(z')}. \quad (1.20)$$

Where we can see that since,

$$H(z) = \sqrt{\sum_i \Omega_i(z)}, \quad (1.21)$$

with  $\Omega_i(z)$  a power law function, check Equations (1.14) and (1.8), for small redshifts ( $z \ll 1$ ),  $\chi \approx cz/H_0$ . Therefore, since  $z$  is an adimensional quantity, the comoving distance has units of inverse Hubble factor. The dimensions of  $H_0$  which are commonly used are:

$$H_0 = 100h \text{ km/s/Mpc} \quad (1.22)$$

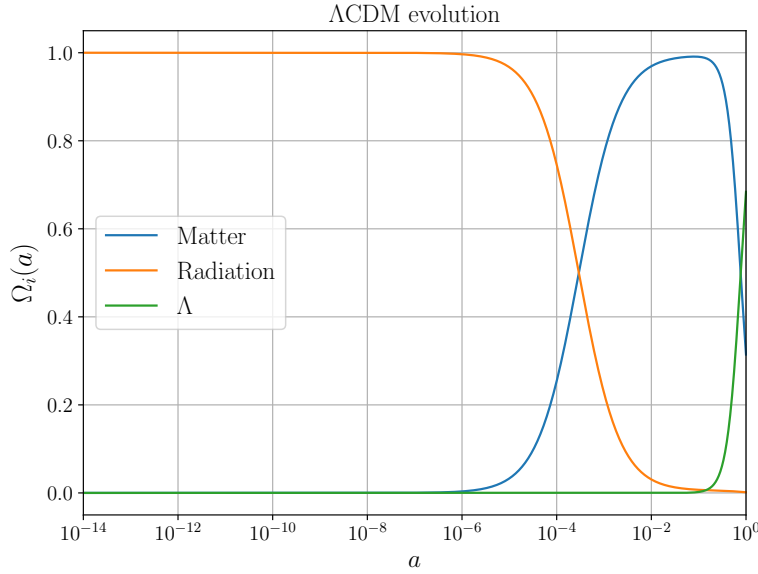


**Figure 1.2.** Evolution of the fractional energy density as a function of the scale factor within  $\Lambda$ CDM cosmology for: non-relativistic matter (solid blue), radiation (solid orange) and Cosmological Constant (solid green)

where  $h$  is the reduced Hubble constant value measured today, and its value is between  $0 < h < 1$ . The precise value of this constant is a matter of great dispute nowadays, since there is a big discrepancy on its value coming from local measurements [8, 9, 10, 11] and the inferred one from the CMB [12, 13, 14]. The former gives a number around 0.73, while the latter 0.67. As we can see the units  $H_0$  is  $\text{time}^{-1}$ , and as we have a speed of light  $c$  there,  $\chi$  is a distance. A classical way that astronomers define distance is to compute the angle  $\theta$  subtended by an object of known physical size “standard ruler”  $l$ :

$$d_A = \frac{l}{\theta}. \quad (1.23)$$

To compute the same thing in cosmology we need to remember that we are in a comoving frame, and the comoving size of the object is then  $l/a$ , and the angle subtended will be just  $\theta = l/a/\chi(a)$ . Then, substituting this in Equation (1.23) we are left with:

$$d_A = a\chi = \frac{\chi}{1+z}. \quad (1.24)$$

This relation, however, holds only for a flat Universe, and in the case of a non-vanishing  $\mathcal{K}$ , this should be corrected to:

$$d_A = \frac{a}{H_0\sqrt{\Omega_{\mathcal{K}}}} \times \begin{cases} \sinh[\sqrt{\Omega_{\mathcal{K}}H_0\chi}] & \Omega_{\mathcal{K}} > 0; \\ \sin[\sqrt{\Omega_{\mathcal{K}}H_0\chi}] & \Omega_{\mathcal{K}} < 0. \end{cases} \quad (1.25)$$

Another way of inferring distances in astronomy is via the luminosity of an object, known as “standard candle”. The observed flux in a spherical shell at a distance  $d$  is given by:

$$F = \frac{L}{4\pi d^2}, \quad (1.26)$$

where  $L$  is the known luminosity of the object. Once again, since we live in a comoving grid of coordinates, in an expanding Universe this result is generalized to:

$$F = \frac{La^2}{4\pi\chi^2(a)}. \quad (1.27)$$

Where the  $a^2$  factor in the numerator compensates to the fact that with the expansion of the Universe the comoving shell in which the luminosity is observed must account for the fact that the energy per unit of time passing through will be a factor of  $a^2$  smaller than when it was emitted by the source. The luminosity distance is then defined as:

$$d_L = \frac{\chi(a)}{a}, \quad (1.28)$$

and this relation is valid for all values of  $\mathcal{K}$ . Comparing Equations (1.25) and (1.28), we are left with the so-called Distance Duality Relation:

$$\frac{(1+z)^2 d_A}{d_L} = 1. \quad (1.29)$$

This relation has been tested in many different cosmological contexts, as it is a direct test of two basic pillars in Cosmology:

- Riemannian geometry;
- Photon number conservation.

The first item is a geometrical statement about how we define distances, angles and derivatives in our gravitation theory. The second is a statement about how electromagnetism and gravity come together, that is, in the Standard Model of fundamental interactions, gravity and electromagnetism are minimally coupled.

## 1.2. Perturbations

In the last section I focused the discussion on the general properties and dynamics in the largest scales of our Universe. The discussion revolved around describing Cosmology in a isotropic and homogeneous way. However, by just looking at the sky we can see that the Universe is not homogeneous as a whole. That is, we observe different and very complex structures, such as galaxies, clusters of galaxies, stars, etc. How can we then describe the growth of structure in our Universe? By perturbing the FLRW metric and the matter content.

This process is done by linearizing [15, 16, 17, 18] the Einstein field equations (1.1):

$$g_{\mu\nu}(\mathbf{x}, t) = \bar{g}_{\mu\nu}(t) + \delta g_{\mu\nu}(\mathbf{x}, t), \quad (1.30)$$

$$T_{\mu\nu}(\mathbf{x}, t) = \bar{T}_{\mu\nu}(t) + \delta T_{\mu\nu}(\mathbf{x}, t), \quad (1.31)$$

where the barred quantities refer to the homogeneous and isotropic background given by Equations (1.2) and (1.9), while the other quantities are small perturbations on top of these background ones. Also, much of the equations and consequences of the perturbed equations are easier to interpret using the notion of conformal time. This is a redefinition of the cosmic time coordinate  $t$ :

$$d\tau = \frac{dt}{a}. \quad (1.32)$$

This variable has the nice property that photons obey now the relation  $dr = d\tau$ , in an unperturbed flat FLRW Universe. Hence, conformal time is a measure of time based on the comoving distance travelled by a photon (this also holds for a non-flat Universe). Another important notion that needs to be introduced is the notion of the Hubble radius,  $R_H = 1/H$ , where  $H$  is the Hubble factor. This is a scale of interest when we move to presenting equations in Fourier space, as the scale in which a given Fourier mode  $k$  crosses the Hubble radius is:

$$\frac{2\pi}{k}a = \frac{1}{H} \Leftrightarrow k \sim aH = \frac{\dot{a}}{a} \quad (1.33)$$

where the dot refers to derivative with respect to conformal time. Therefore, we usually refer to the quantity  $k_H = aH$  as the cosmological horizon, and modes with  $k < k_H$  are called super-horizon, and modes with  $k > k_H$  sub-horizon.

The most general scalar linearly perturbed metric, is written as [19]:

$$g_{00} = -a^2(1 + 2A), \quad (1.34)$$

$$g_{0i} = a^2 i\hat{k}_i B, \quad (1.35)$$

$$g_{ij} = a^2 \left[ \delta_{ij}(1 + 2H_L) + 2 \left( \delta_{ij}/3 - \hat{k}_i \hat{k}_j \right) H_T \right], \quad (1.36)$$

where,  $A$  is the perturbation of the lapse function,  $B$  is a scalar perturbation in the shift, and  $H_L$  and  $H_T$  are respectively the trace and trace-free scalar perturbations of the spatial metric. For simplicity we consider a single Fourier mode with comoving wave-vector,  $\mathbf{k}$ , wave-number  $k \equiv |\mathbf{k}|$  and direction  $\hat{k}_i \equiv k_i/k$ .

The energy-momentum tensor of all particle species is given by

$$T^0_0 = -\rho - \delta\rho = -\rho(1 + \delta), \quad (1.37)$$

$$T^0_i = (\rho + p)(v_i - B_i), \quad (1.38)$$

$$T^i_0 = (\rho + p)v^i, \quad (1.39)$$

$$T^i_j = (p + \delta p)\delta^i_j + p\Pi^i_j, \quad (1.40)$$

where  $\delta\rho$  is the density perturbation,  $\delta p$  pressure perturbation,  $v_i$  velocity perturbation and  $\Pi^i_j$  the anisotropic pressure tensor,  $\rho$  and  $p$  are the background density and pressure respectively.

Einstein equations do not specify a closed system of equations, and require the addition of supplemental conditions provided by microphysics, in order to fix the dynamical degrees of freedom. The simplest example of such relations is the equation of state parameter, relating background energy density to the background pressure of a given species. In the inhomogeneous Universe the Einstein tensor  $G_{\mu\nu}$  is constructed out of nonlinear metric fluctuations combinations. These fluctuations are known to remain small even in the presence of big matter perturbations. Thence, we linearize the LHS of (1.1) to obtain a set of partial differential equations that are linear in the variables. As our focus is now on linear order perturbations, this set of equations may be linearly decoupled in order to form a set of ordinary equations of motion. This decomposition is achieved by using normal modes, that are invariant under translations and rotations, and admit a decomposition into: scalars, vectors and tensors. The eigenmodes of the Laplacian operator form a complete set:

$$\nabla^2 Q^{(0)} = -k^2 Q^{(0)} \quad (\text{scalar}), \quad (1.41)$$

$$\nabla^2 Q_i^{(\pm 1)} = -k^2 Q_i^{(\pm 1)} \quad (\text{vector}), \quad (1.42)$$

$$\nabla^2 Q_{ij}^{(\pm 2)} = -k^2 Q_{ij}^{(\pm 2)} \quad (\text{tensor}). \quad (1.43)$$

In a spatially flat Universe  $\mathcal{K} = 0$  these are plane waves:

$$Q^{(0)} = \exp(i\mathbf{k} \cdot \mathbf{x}) \quad (1.44)$$

$$Q_i^{(\pm 1)} = -\frac{i}{\sqrt{2}} (\mathbf{e}_1 \pm i\mathbf{e}_2)_i \exp(i\mathbf{k} \cdot \mathbf{x}) \quad (1.45)$$

$$Q_{ij}^{(\pm 2)} = -\sqrt{\frac{3}{8}} (\mathbf{e}_1 \pm i\mathbf{e}_2)_i (\mathbf{e}_1 \pm i\mathbf{e}_2)_j \exp(i\mathbf{k} \cdot \mathbf{x}), \quad (1.46)$$

where  $\mathbf{e}_1$  and  $\mathbf{e}_2$  are unit vectors spanning the plane transverse to  $\mathbf{k}$ . Additionally, in this decomposition, vector modes are divergence free (vorticity), while tensor modes transverse and trace free (gravitational waves):

$$\nabla^i Q_i^{(\pm 1)} = 0, \quad \nabla^i Q_{ij}^{(\pm 2)} = 0, \quad \gamma^{ij} Q_{ij}^{(\pm 2)} = 0, \quad (1.47)$$

where  $\gamma_{ij}$  is the spatial metric. This leads to the fact that curl free vectors and the longitudinal components of tensors are represented by covariant derivatives of scalar and vector modes:

$$Q_i^{(0)} = -k^{-1} \nabla_i Q^{(0)}, \quad (1.48)$$

$$Q_{ij}^{(0)} = \left( k^{-2} \nabla_i \nabla_j + \frac{1}{3} \gamma_{ij} \right) Q^{(0)}, \quad (1.49)$$

$$Q_{ij}^{(\pm 1)} = -\frac{1}{2k} \left[ \nabla_i Q_j^{(\pm 1)} + \nabla_j Q_i^{(\pm 1)} \right]. \quad (1.50)$$

The  $k$ th eigenmode of each of the scalar field fluctuations is then:

$$A(x) = A(k)Q^{(0)}, \quad \delta\rho(x) = \delta\rho(k)Q^{(0)}, \quad (1.51)$$

$$H_L(x) = H_L(k)Q^{(0)}, \quad \delta p(x) = \delta p(k)Q^{(0)}. \quad (1.52)$$

For the vector ones:

$$B_i(x) = \sum_{m=-1}^{m=+1} B(k)Q^{(m)}_i, \quad v(x) = \sum_{m=-1}^{m=+1} v_i(k)Q_i^{(m)}, \quad (1.53)$$

and for the tensor:

$$H_{\Gamma,ij} = \sum_{m=-2}^{m=+2} H_{\Gamma}^{(m)}(k)Q_{ij}^{(m)}, \quad \Pi_{ij} = \sum_{m=-2}^{m=+2} \Pi^{(m)}(k)Q_{ij}^{(m)}. \quad (1.54)$$

An arbitrary set of spatial perturbations can be formed through a superposition of the eigenmodes given their completeness. This decomposition is well known in the literature, there are different notations and conventions, but they all share the same concept and core:

- Linearize metric and energy-momentum tensor;
- Move to Fourier space, decoupled set of ordinary differential equations;
- Expand the fluctuations in eigenmodes of the Laplacian operator.

I will now present the equations of motion for the scalar sector:

$$4\pi Ga^2 [\bar{\rho}\delta + 3\mathcal{H}(\bar{\rho} + \bar{p})k^{-1}(v - B)] = k^2\Phi, \quad (1.55)$$

$$k^2 \left( A + H_L + \frac{1}{3}H_T \right) - [\partial_\tau + 2\mathcal{H}] \left( \dot{H}_T - kB \right) = -8\pi Ga^2 \bar{p}\Pi, \quad (1.56)$$

$$4\pi Ga^2 (\bar{\rho} + \bar{p}) k^{-1} (v - B) = \mathcal{H}A - \dot{H}_L - \frac{1}{3}\dot{H}_T, \quad (1.57)$$

$$(\partial_\tau + 4\mathcal{H}) (\bar{\rho} + \bar{p}) k^{-1} (v - B) = \delta p - \frac{2}{3}\bar{p}\Pi + (\bar{\rho} + \bar{p}) A, \quad (1.58)$$

where a dot now represents differentiation with respect to conformal time,  $\tau$ , and the gauge-invariant Bardeen potential are:

$$\Psi \equiv A + \mathcal{H}k^{-1} \left( B - k^{-1}\dot{H}_T \right) + k^{-1} \left( \dot{B} - k^{-1}\ddot{H}_T \right), \quad (1.59)$$

$$\Phi \equiv H_L + \frac{1}{3}H_T + \mathcal{H}k^{-1} \left( B - k^{-1}\dot{H}_T \right). \quad (1.60)$$

The conservation equations become the continuity and Euler equations:

$$\left[ \frac{d}{d\tau} + 3\frac{\dot{a}}{a} \right] \delta\rho + 3\frac{\dot{a}}{a}\delta p = -(\rho + p)(kv + 3\dot{H}_L), \quad (1.61)$$

$$\left[ \frac{d}{d\tau} + 4\frac{\dot{a}}{a} \right] (\rho + p) \frac{v - B}{k} = \delta p - \frac{2}{3}p\Pi + (\rho + p)A. \quad (1.62)$$

Equations (1.55-1.62) are not independent due to the Bianchi identities. In order to find numerical solutions for these equations it suffices to use two equations from (1.55-1.58), and the two conservation equations. The equations of motion for the vector modes are:

$$\begin{aligned} (kB^{(\pm 1)} - \dot{H}_T^{(\pm 1)}) &= 16\pi Ga^2(\rho + p)v^{(\pm 1)} - \frac{B^{(\pm 1)}}{k}, \\ \left[ \frac{d}{d\tau} + 2\frac{\dot{a}}{a} \right] (kB^{(\pm 1)} - \dot{H}_T^{(\pm 1)}) &= -8\pi Ga^2 p\Pi^{(\pm 1)}, \end{aligned} \quad (1.63)$$

and the conservation equations become

$$\left[ \frac{d}{d\tau} + 4\frac{\dot{a}}{a} \right] (\rho + p) \frac{v^{(\pm 1)} - B^{(\pm 1)}}{k} = -\frac{1}{2}p\Pi^{(\pm 1)}. \quad (1.64)$$

Since gravity does not generate any vorticity, any initial vector perturbation will simply decay with time. The equations of motion for the tensor modes are:

$$\left[ \frac{d^2}{d\tau^2} + 2\frac{\dot{a}}{a} \frac{d}{d\tau} + k^2 \right] \dot{H}_T^{(\pm 2)} = 8\pi Ga^2 p\Pi^{(\pm 2)}. \quad (1.65)$$

When no anisotropic stresses and spatial curvature is present, the tensor equation becomes a simple source-free gravitational wave propagation equation

$$\ddot{H}_T^{(\pm 2)} + 2\frac{\dot{a}}{a}\dot{H}_T^{(\pm 2)} + k^2 H_T^{(\pm 2)} = 0, \quad (1.66)$$

which has solutions

$$\begin{aligned} H_{\text{T}}^{(\pm 2)}(k\tau) &= C_1 H_1(k\tau) + C_2 H_2(k\tau), \\ H_1(x) &\propto x^{-m} j_m(x), \\ H_2(x) &\propto x^{-m} n_m(x), \end{aligned} \tag{1.67}$$

where  $H_1(x)$  and  $H_2(x)$  are the Hankel functions of the first and second kind respectively, and  $m = (1 - 3w)/(1 + 3w)$ . If:

- $w > -1/3$ : The gravitational wave amplitude is constant above the horizon ( $x \ll 1$ ) and then oscillates and damp.
- $w < -1/3$ : The gravitational wave oscillates and freeze into some value.

Even though I presented the linear order perturbed equations of motion for the 3 different types of fluctuations: scalar, vector and tensor, I will only focus on the scalar part. This is because for the formation observed in the Universe, this is the only type of perturbations that is relevant throughout all the scales and expansion history.

With that said, I will now discuss briefly the problem of gauge choice in cosmology. The covariant perturbed equations presented before are cast in a gauge invariant way, that is, they possess spurious propagating modes. However, in the same way as Maxwell's Electromagnetic Theory can be presented in a wide variety of coordinate systems, without having their physical consequences modified, we also have this same property in Cosmological Perturbation Theory. Depending on the type of observable, moment in the expansion history or even scale, a preferred coordinate system may be chosen in order to solve Equations (1.55-1.58). I will first present the coordinate freedom generator these equations have, and then will present some classes of gauges that are commonly used in the literature. First let's define a gauge transformation as:

$$\begin{aligned} \tau &= \tilde{\tau} + T, \\ x^i &= \tilde{x}^i + L^i, \end{aligned} \tag{1.68}$$

where  $T$  and  $\mathbf{L}$  are the temporal and spatial gauge generators respectively, and tilded quantities are from the original coordinate system. Under a coordinate transformation, the scalar metric fluctuations transform as:

$$\begin{aligned} A &= \tilde{A} - \dot{T} - \frac{\dot{a}}{a} T, \\ B &= \tilde{B} + \dot{L} + kT, \\ H_{\text{L}} &= \tilde{H}_{\text{L}} - \frac{k}{3} L - \frac{\dot{a}}{a} T, \\ H_{\text{T}} &= \tilde{H}_{\text{T}} + kL, \end{aligned} \tag{1.69}$$

and the matter fluctuations:

$$\begin{aligned} \delta\rho_\alpha &= \delta\tilde{\rho}_\alpha - \dot{\rho}_\alpha T, \\ \delta p_\alpha &= \delta\tilde{p}_\alpha - \dot{p}_\alpha T, \\ v_\alpha &= \tilde{v}_\alpha + \dot{L}, \end{aligned} \tag{1.70}$$

where the index  $\alpha$  represents the species in question, baryon, cold dark matter, photon or neutrino, and dots refer to time derivatives with respect to conformal time,  $\tau$ . A gauge is said to have been chosen if we have a mapping between the pair  $(T, \mathbf{L})$  and any of the functions in Equations (1.69) and/or (1.70). I will now present 3 gauges commonly used in the literature.

### 1.2.1. Newtonian Gauge

This gauge is very popular in the literature, since well within the horizon, the Poisson Equation has the same form as its Newtonian gravity counterpart. It is also called *longitudinal* gauge. The line element in this gauge is diagonal, and its fluctuations are defined as:

$$\begin{aligned} B &= H_T = 0, \\ \Psi &\equiv A \quad (\text{Newtonian potential}), \\ \Phi &\equiv H_L \quad (\text{Newtonian curvature}), \end{aligned} \tag{1.71}$$

These specifications completely fix the gauge, rendering the following form for the gauge generators:

$$\begin{aligned} L &= -\frac{\tilde{H}_T}{k}, \\ T &= -\frac{B}{k} + \frac{1}{k^2} \frac{d}{d\tau} \tilde{H}_T. \end{aligned} \tag{1.72}$$

The Einstein field equations are now given by:

$$\begin{aligned} k^2 \Phi &= 4\pi G a^2 \left[ \delta\rho + 3\frac{\dot{a}}{a}(\rho + p)\frac{v}{k} \right], \\ k^2(\Psi + \Phi) &= -8\pi G a^2 p \Pi. \end{aligned} \tag{1.73}$$

As already said, for scales well within the Hubble radius,  $k(\dot{a}/a)^{-1} \gg 1$ , the Poisson equation has the same form as its Newtonian gravity counterpart. Also, if the anisotropic stress is negligible, as it is the case of non-relativistic matter,  $\Psi = -\Phi$ . The conservation laws for the  $\alpha$ th non-interacting subsystem becomes

$$\left[ \frac{d}{d\tau} + 3\frac{\dot{a}}{a} \right] \delta\rho_\alpha + 3\frac{\dot{a}}{a} \delta p_\alpha = -(\rho_\alpha + p_\alpha)(k v_\alpha + 3\dot{\Phi}), \tag{1.74}$$

$$\left[ \frac{d}{d\tau} + 4\frac{\dot{a}}{a} \right] (\rho_\alpha + p_\alpha) \frac{v_\alpha}{k} = \delta p_\alpha - \frac{2}{3} p_\alpha \Pi_\alpha + (\rho_\alpha + p_\alpha) \Psi. \tag{1.75}$$

As we can see, the presence of the  $3\dot{\Phi}$  violates the Newtonian notion of conserving the matter perturbations. It is a relativistic correction coming from the expansion of space-time. Since  $\Phi$  is a perturbation in the scale factor  $a$ , its origin represents the perturbation to the redshifting energy density in our Universe.

### 1.2.2. Comoving Gauge

Another very popular gauge is the comoving gauge, defined by:

$$\begin{aligned} B &= v \quad (T_i^0 = 0), \\ H_T &= 0, \\ \xi &= A, \\ \zeta &= H_L \quad (\text{comoving curvature}), \end{aligned} \tag{1.76}$$

which completely fixes the gauge generators to:

$$\begin{aligned} T &= (\tilde{v} - \tilde{B})/k, \\ L &= -\tilde{H}_\Gamma/k. \end{aligned} \quad (1.77)$$

The Einstein equations become simply:

$$\dot{\zeta} - \frac{\dot{a}}{a}\xi = 0, \quad (1.78)$$

$$\dot{v} + 2\frac{\dot{a}}{a}v + k(\zeta + \xi) = -8\pi G a^2 p\Pi, \quad (1.79)$$

and the conservation laws become

$$\left[ \frac{d}{d\tau} + 3\frac{\dot{a}}{a} \right] \delta\rho_\alpha + 3\frac{\dot{a}}{a}\delta p_\alpha = -(\rho_\alpha + p_\alpha)(kv_\alpha + 3\dot{\zeta}), \quad (1.80)$$

$$\left[ \frac{d}{d\tau} + 4\frac{\dot{a}}{a} \right] (\rho_\alpha + p_\alpha) \frac{v_\alpha - v}{k} = \delta p_\alpha - \frac{2}{3}p_\alpha\Pi_\alpha + (\rho_\alpha + p_\alpha)\xi. \quad (1.81)$$

In particular the momentum conservation equation for the total matter becomes an algebraic relation between total stress fluctuations and the potential

$$(\rho + p)\xi = -\delta p + \frac{2}{3}p\Pi \quad (1.82)$$

so that these equations are a complete set. If we substitute (1.82) into (1.78) we have an equation for the comoving curvature:

$$\dot{\zeta} = \frac{\dot{a}}{a} \left[ -\frac{\delta p}{\rho + p} + \frac{2}{3} \frac{p}{\rho + p} \Pi \right]. \quad (1.83)$$

This is the fundamental equation in the comoving gauge, and it is the most appealing reason to use this gauge. It tells us that the evolution of the comoving curvature responds only to pressure gradients and anisotropic stresses. From this relation we can also check why the comoving curvature is constant during the matter domination in the Universe, since non-relativistic matter has no pressure perturbations and no anisotropic stress.

### 1.2.3. Synchronous Gauge

The synchronous gauge metric perturbations is given by the following choice:

$$\begin{aligned} A &= B = 0, \\ \eta &\equiv -\frac{1}{3}H_\Gamma - H_L, \\ h &= 6H_L, \\ T &= a^{-1} \int d\eta a \tilde{A} + c_1 a^{-1}, \\ L &= - \int d\eta (\tilde{B} + kT) + c_2. \end{aligned} \quad (1.84)$$

As is well known, this does not fully fix the gauge and we need to further supplement the values of  $(c_1, c_2)$ . Commonly, this is performed by defining  $c_1$  in a way that the initial velocity of dark matter perturbations is set to zero, and  $c_2$  is set through the initial curvature perturbation.

The variables  $\eta$  and  $h$  comprise a stable system for numerical solutions, and this is why the synchronous gauge has been widely used in a number of cosmology numerical codes.

The Einstein equations give

$$\dot{\eta} - (\dot{h} + 6\dot{\eta}) = 4\pi G a^2 (\rho + p) \frac{v}{k}, \quad (1.85)$$

$$\ddot{h} + \frac{\dot{a}}{a} \dot{h} = -8\pi G a^2 (\delta\rho + 3\delta p), \quad (1.86)$$

while the conservation equations give

$$\left[ \frac{d}{d\tau} + 3\frac{\dot{a}}{a} \right] \delta\rho_\alpha + 3\frac{\dot{a}}{a} \delta p_\alpha = -(\rho_\alpha + p_\alpha) (k v_\alpha + \frac{1}{2} \dot{h}), \quad (1.87)$$

$$\left[ \frac{d}{d\tau} + 4\frac{\dot{a}}{a} \right] (\rho_\alpha + p_\alpha) \frac{v_\alpha}{k} = \delta p_\alpha - \frac{2}{3} p_\alpha \Pi_\alpha. \quad (1.88)$$

We can see from the Euler equation in the Synchronous gauge, (1.88), that if a species has zero velocity initially it will always be zero, if it has no pressure nor anisotropic stress perturbations, such as cold dark matter.

### 1.3. Boltzmann Equations

In the last subsection I discussed how inhomogeneities are described in our Universe. In this section I will present the set of equations which combine gravity and matter in a single and unique manner [20]. This set is called the Einstein-Boltzmann equations, where the first name of it has been already discussed, while the second one will be developed now. A collection of particles is fully described by their respective position and momentum set  $\{\mathbf{x}_i, \mathbf{p}_i\}$ , which are called generalized coordinates in the phase space. This space is a  $3N$ , with  $N$  the number of particles, dimensional space. The distribution function of this collective of particles is defined in terms of the number of particles at a given time  $t$  and phase space volume:

$$N(\mathbf{x}, \mathbf{p}, t) = f(\mathbf{x}, \mathbf{p}, t) (\Delta x)^{3N} \frac{(\Delta p)^{3N}}{h_p^{3N} (2\pi)^{3N}}. \quad (1.89)$$

In the limit where the number of particles is big enough,  $f(x_i, p_i, t)$  becomes a continuous function. If the number of particles is conserved, we have that:

$$\frac{df}{dt} = 0, \quad \text{where} \quad \frac{d}{dt} = \frac{\partial}{\partial t} + \dot{x} \cdot \nabla_x + \dot{p} \cdot \nabla_p \quad (1.90)$$

However, we know that in the Universe particles move in and out of the phase space freely, which means that they have self-interacting terms, also called collision terms. This is characterized by adding a source term to the RHS of Equation (1.90):

$$\frac{df}{dt} = C[f], \quad (1.91)$$

where the interaction is usually taken to occur at the same position  $\mathbf{x}$ . I will not derive the different interaction terms that this function will have for the species in the Universe. I will rather jump ahead and discuss the components of the energy-momentum tensor in terms of the

distribution function in an expanding Universe. The zeroth-order distribution function is the Fermi-Dirac or the Bose-Einstein distributions, for fermions(+) and bosons(-) respectively:

$$f_0(x_i, p_i, t) = \frac{g_s}{h_p^3} \frac{1}{e^{\epsilon/k_B T_0} \pm 1} \quad (1.92)$$

where  $\epsilon = a\sqrt{p^2 + m^2} = \sqrt{P^2 + a^2 m^2}$ ,  $T_0 = aT$ ,  $g_s$  the degree of degeneracy of the spin particle,  $k_B$  Boltzmann and  $h_p$  Planck's constant. In an expanding Universe the conjugate momenta is defined as:

$$P_j = \begin{cases} a(\delta_{ij} + \frac{1}{2}h_{ij})p^j & \text{synchronous gauge;} \\ a(1 - \phi)p_i & \text{Newtonian gauge,} \end{cases} \quad (1.93)$$

where  $h_{ij}$  is the Synchronous gauge spatial metric, and  $p_i$  is the proper momenta. Even though in a perturbed space-time  $x_i$  and  $P_i$  remain conjugate to each other, it is common practice to replace  $P_i$  by  $q_i = ap_i$  instead, since in a unperturbed space-time, due to Hamilton's equations,  $p_i$  redshifts as  $a^{-1}$ , and in this way  $q_i$  would be constant. It is worth stressing that this is not a canonical transformation, as  $q_i$  is not the conjugate of  $x_i$ , but it is rather a transformation of variables, and I will write the 3-vector  $\mathbf{q}$  as its magnitude times its direction vector,  $q_i = qn_i$ . The energy-momentum tensor in terms of the distribution function is then:

$$T_{\mu\nu} = \int dP_1 dP_2 dP_3 \sqrt{-g} \frac{P_\mu P_\nu}{P^0} f(x^i, P_j, \tau). \quad (1.94)$$

Since we are considering small perturbation of  $T_{\mu\nu}$ , we can then expand  $f$  as:

$$f(x^i, P_j, \tau) = f_0(q) [1 + \Psi(x^i, q, n_i, \tau)]. \quad (1.95)$$

The components of Equation (1.94) are then:

$$T^0_0 = -a^{-4} \int q^2 dq d\Omega \sqrt{q^2 + m^2 a^2} f_0(q) (1 + \Psi), \quad (1.96)$$

$$T^0_i = a^{-4} \int q^2 dq d\Omega q n_i f_0(q) \Psi, \quad (1.97)$$

$$T^i_j = a^{-4} \int q^2 dq d\Omega \frac{q^2 n^i n_j}{\sqrt{q^2 + m^2 a^2}} f_0(q) (1 + \Psi). \quad (1.98)$$

These equations have no dependence on the metric fluctuations due to the redefinition of  $P_i$  by  $q$  and  $n_i$ . Therefore the determinant of the metric appearing in (1.94) disappears. Also, the above expressions have the same form in both gauges: Synchronous and Newtonian. This, however, do not mean that they are gauge invariant, as their values will differ in the gauge in which they are computed in. The fact that they share the same expressions are just due to the redefinition of the conjugate momenta.

The phase space distribution evolves following Equation (1.91), which in terms of the variables  $x_i$ ,  $q$  and  $n_i$  becomes:

$$\frac{\partial f}{\partial \tau} + \frac{dx^i}{d\tau} \frac{\partial f}{\partial x^i} + \frac{dq}{d\tau} \frac{\partial f}{\partial q} + \frac{dn^i}{d\tau} \frac{\partial f}{\partial n^i} = \left( \frac{\partial f}{\partial \tau} \right)_C, \quad (1.99)$$

where the RHS is the collision term depending on the type of the interaction between particles. The geodesic equation gives us:

$$P^0 \frac{dP^\mu}{d\tau} + \Gamma^\mu_{\alpha\beta} P^\alpha P^\beta = 0 \quad (1.100)$$

which is easy to compute  $dq/d\tau$ :

$$\frac{dq}{d\tau} = \begin{cases} -\frac{1}{2}q\dot{h}_{ij}n^in^j & \text{synchronous gauge;} \\ q\dot{\phi} - \epsilon(q, \tau)n_i\nabla_i\psi & \text{Newtonian gauge.} \end{cases} \quad (1.101)$$

The term  $df/dn_i$  is order one in perturbation theory, and so is  $dn_i/d\tau$ , which makes it second order, therefore, they can be safely neglected. Equation (1.99) then becomes:

$$\frac{\partial\Psi}{\partial\tau} + i\frac{q}{\epsilon}(\mathbf{k}\cdot\hat{\mathbf{n}})\Psi + \frac{d\ln f_0}{dq} \left[ \dot{\eta} - \frac{\dot{h} + 6\dot{\eta}}{2}(\mathbf{k}\cdot\hat{\mathbf{n}})^2 \right] = \frac{1}{f_0} \left( \frac{\partial f}{\partial\tau} \right)_C \quad (1.102)$$

in the Synchronous gauge, and

$$\frac{\partial\Psi}{\partial\tau} + i\frac{q}{\epsilon}(\mathbf{k}\cdot\hat{\mathbf{n}})\Psi + \frac{d\ln f_0}{dq} \left[ \dot{\phi} - i\frac{\epsilon}{q}(\mathbf{k}\cdot\hat{\mathbf{n}})\psi \right] = \frac{1}{f_0} \left( \frac{\partial f}{\partial\tau} \right)_C \quad (1.103)$$

in the Newtonian gauge.

I will now show the Einstein-Boltzmann equations for the fundamental species in our Universe: cold dark matter, photons, massless neutrinos and massive neutrinos.

I will begin with the simplest of the fluids we have in our Universe, cold dark matter (CDM). The lack of self and inter particles interactions, makes CDM to be fully described in terms of its density contrast and velocity dispersion, and we can derive the evolution equations straight from the energy-momentum tensor conservation,  $\nabla_\mu T^{\mu\nu} = 0$ , which implies:

$$\dot{\delta} = -(1+w) \left( \theta + \frac{\dot{h}}{2} \right) - 3\frac{\dot{a}}{a} \left( \frac{\delta P}{\delta\rho} - w \right) \delta, \quad (1.104)$$

$$\dot{\theta} = -\frac{\dot{a}}{a}(1-3w)\theta - \frac{\dot{w}}{1+w}\theta + \frac{\delta P/\delta\rho}{1+w}k^2\delta - k^2\sigma, \quad (1.105)$$

in the Synchronous gauge, and

$$\dot{\delta} = -(1+w) \left( \theta - 3\dot{\phi} \right) - \frac{\dot{a}}{a} \left( \frac{\delta P}{\delta\rho} - w \right) \delta, \quad (1.106)$$

$$\dot{\theta} = -\frac{\dot{a}}{a}(1-3w)\theta - \frac{\dot{w}}{1+w}\theta + \frac{\delta P/\delta\rho}{1+w}k^2\delta - k^2\sigma + k^2\psi, \quad (1.107)$$

in the Newtonian gauge. In the above equations I have performed a change of definition with respect to the anisotropic stress, now using the Greek letter  $\sigma$  to describe it. The former definition in Equation (1.40) is related to  $\sigma$  in the following way:

$$\sigma = \frac{2p\Pi}{3(\rho+p)}. \quad (1.108)$$

This new definition of the anisotropic stress is the one used in the public Einstein-Boltzmann solver CLASS [21], and therefore I will slowly adopt its definitions and conventions in order to connect this introductory chapter with the rest of my thesis. Another new quantity introduced in (1.104-1.107) is the fluid sound speed in its rest frame:

$$c_s^2 = \frac{\delta P}{\delta\rho}. \quad (1.109)$$

This is a perturbative quantity, and as the name suggests it is the speed in which the fluid propagates as sound waves.

For cold dark matter we have to set  $w = \delta p = \sigma = 0$  in these equations, and we arrive at:

$$\dot{\delta} = -\frac{1}{2}\dot{h}, \quad (1.110)$$

in the Synchronous gauge, which is the gauge where I will present the equations of motion from now on. Moving to massless neutrinos, we know that these have non-zero equations of state parameter, which makes its energy density and pressure perturbations related by  $\rho_{ur} = 3p_{ur} = -T^0_0 = T^i_i$ , where the subscript “ur” will be denoting these species. Therefore, its perturbations will also be related by  $\delta p = \delta\rho/3$ . From Equations (1.96-1.98) we have:

$$\bar{\rho}_{ur} = 3\bar{p}_{ur} = a^{-4} \int q^2 dq d\Omega q f_0(q), \quad (1.111)$$

for its background quantities. And its perturbed quantities are defined as:

$$\delta\rho_{ur} = 3\delta P_{ur} = a^{-4} \int q^2 dq d\Omega q f_0(q) \Psi, \quad (1.112)$$

$$\delta T^0_{i,ur} = a^{-4} \int q^2 dq d\Omega q n_i f_0(q) \Psi, \quad (1.113)$$

$$\Sigma^i_{j,ur} = T^i_{j,ur} - P_{ur} \delta^i_j = a^{-4} \int q^2 dq d\Omega q \left( n_i n_j - \frac{1}{3} \delta_{ij} \right) f_0(q) \Psi. \quad (1.114)$$

The massless neutrino distribution function is actually pretty simple, as it is just the Fermi-Dirac distribution with  $\epsilon = q$ . And then we can easily intergrate out the momenta in Equations (1.112-1.114), and expand the angular dependence appearing in  $n_i$  in terms of Legendre polynomials:

$$\begin{aligned} F_{ur}(\mathbf{k}, \mathbf{n}, \tau) &= \frac{\int q^2 dq q f_0(q) \Psi}{\int q^2 dq q f_0(q)} \\ &= \sum_{\ell=0}^{\infty} (-i)^\ell (2\ell + 1) F_{ur,\ell}(\mathbf{k}, \tau) P_\ell(\hat{\mathbf{k}} \cdot \hat{\mathbf{n}}). \end{aligned} \quad (1.115)$$

As we have seen scalar perturbations are decomposed as plane waves, therefore,  $F_\nu(\mathbf{k}, \mathbf{n}, \tau)$  are plane waves,  $e^{-i\mathbf{k}\cdot\mathbf{n}}$ , where  $\mathbf{x} = r\hat{\mathbf{n}}$ , and expansion coefficients  $F_{ur,\ell} = j_\ell(kr)$ , given by spherical Bessel functions. Plugging (1.115) into Equations (1.112-1.114) we are left with:

$$\delta_{ur} = \frac{1}{4\pi} \int d\Omega F_{ur}(\mathbf{k}, \mathbf{n}, \tau) = F_{ur,0}, \quad (1.116)$$

$$\theta_{ur} = \frac{3i}{16\pi} \int d\Omega (\mathbf{k} \cdot \mathbf{n}) F_{ur}(\mathbf{k}, \mathbf{n}, \tau) = \frac{3}{4} k F_{ur,1}, \quad (1.117)$$

$$\sigma_{ur} = -\frac{3}{16\pi} \int d\Omega \left[ (\hat{\mathbf{k}} \cdot \hat{\mathbf{n}})^2 - \frac{1}{3} \right] F_{ur}(\mathbf{k}, \mathbf{n}, \tau) = F_{ur,2}. \quad (1.118)$$

If we integrate Equation (1.102) in momenta and divide by the energy density, the Boltzmann equations for massless neutrinos becomes:

$$\frac{\partial F_{ur}}{\partial \tau} + ik\mu F_{ur} = -\frac{2}{3}\dot{h} - \frac{4}{3}(\dot{h} + 6\dot{\eta})P_2(\mu), \quad (1.119)$$

where  $\mu = \hat{\mathbf{k}} \cdot \hat{\mathbf{n}}$  and  $P_2(\mu) = \frac{1}{2}(3\mu^2 - 1)$ . Substituting (1.116-1.118) in the above equation and using the recursion relations between the Legendre polynomials we finally arrive at the equations of motion for the moments of the massless neutrinos phase-space distribution:

$$\dot{\delta}_{ur} = -\frac{4}{3}\theta_{ur} - \frac{2}{3}\dot{h}, \quad (1.120)$$

$$\dot{\theta}_{ur} = k^2 \left( \frac{1}{4}\theta_{ur} - \sigma_{ur} \right), \quad (1.121)$$

$$2\dot{\sigma}_{ur} = \frac{8}{15}\theta_{ur} - \frac{3}{5}F_{ur,3} + \frac{4}{15}(\dot{h} + 6\dot{\eta}), \quad (1.122)$$

$$\dot{F}_{ur,\ell} = \frac{k}{2\ell+1} [\ell F_{ur,(\ell-1)} - (\ell+1)F_{ur,(\ell+1)}], \quad \ell \geq 3. \quad (1.123)$$

We can see that a given moment  $\ell$  of the massless neutrinos distributions is coupled with the other moments  $\ell-1$  and  $\ell+1$ . We can also go further into the necessity of writing the Boltzmann equation (1.119), instead of just using the conservation equations (1.104-1.105) to describe the fluid, as the conservation equation and the Euler equation are just the first two moments of the Boltzmann equation. For a non-relativistic fluid at linear order and at large scales, such as the case of cold dark matter, the first two moments suffice to fully describe the evolution of the particles, however, in more general fluids we need higher moments. Another important aspect of Equations (1.120-1.123) is that this is an infinite hierarchy, that is, in principle it is a set of infinite equations of motion. However, what is commonly done in the literature is to truncate the hierarchy at a given moment  $\ell_{max}$ . Since one needs to know  $F_{ur,3}$  to close the equations of motion for the massless neutrinos in a minimal way, in the literature many approximation schemes have been proposed to tackle this problem [20, 21, 22, 23]. All of these methods rely on the asymptotic behavior of the coefficients  $F_{ur}$  that are spherical Bessel functions, which have well known asymptotic behavior for its different kinds, e.g., higher values of  $\ell$  in  $j_\ell(kr)$ . I will not be discussing the subtleties of these different schemes, and instead I refer the reader to the previous references. These approximations have all been validated between each other and as well with the full solution given by directly integrating equations (1.120-1.123) for a given big value of  $\ell_{max}$ .

We know, however, that neutrinos have masses, after observing flavour oscillations. Therefore, we must be able to define the same background and perturbed quantities for massive neutrinos as well. The evolution of the distribution function for these species is more complicated than its massless counterpart. From equations (1.96-1.98), the background density and pressure are:

$$\bar{\rho}_\nu = a^{-4} \int q^2 dq d\Omega \epsilon f_0(q), \quad \bar{p}_\nu = \frac{1}{3} a^{-4} \int q^2 dq d\Omega \frac{q^2}{\epsilon} f_0(q), \quad (1.124)$$

with  $\epsilon = \sqrt{q^2 + a^2 m_\nu^2}$ , and the perturbations:

$$\delta\rho_\nu = a^{-4} \int q^2 dq d\Omega \epsilon f_0(q) \Psi, \quad (1.125)$$

$$\delta p_\nu = \frac{1}{3} a^{-4} \int q^2 dq d\Omega \frac{q^2}{\epsilon} f_0(q) \Psi, \quad (1.126)$$

$$\delta T^0_i = a^{-4} \int q^2 dq d\Omega q n_i f_0(q) \Psi, \quad (1.127)$$

$$\Sigma^i_j = a^{-4} \int q^2 dq d\Omega \frac{q^2}{\epsilon} \left( n_i n_j - \frac{1}{3} \delta_{ij} \right) f_0(q) \Psi. \quad (1.128)$$

Expanding the perturbation  $\Psi$  in a Legendre series:

$$\Psi(\mathbf{k}, \hat{\mathbf{n}}, q, \tau) = \sum_{\ell=0}^{\infty} (-i)^{\ell} (2\ell + 1) \Psi_{\ell}(\mathbf{k}, q, \tau) P_{\ell}(\hat{\mathbf{k}} \cdot \hat{\mathbf{n}}), \quad (1.129)$$

then the perturbations take the form:

$$\delta\rho_{\nu} = 4\pi a^{-4} \int q^2 dq \epsilon f_0(q) \Psi_0, \quad (1.130)$$

$$\delta p_{\nu} = \frac{4\pi}{3} a^{-4} \int q^2 dq \frac{q^2}{\epsilon} f_0(q) \Psi_0, \quad (1.131)$$

$$(\rho_{\nu} + p_{\nu}) \Theta_{\nu} = 4\pi k a^{-4} \int q^2 dq q f_0(q) \Psi_1, \quad (1.132)$$

$$(\rho_{\nu} + p_{\nu}) \sigma_{\nu} = \frac{8\pi}{3} a^{-4} \int q^2 dq \frac{q^2}{\epsilon} f_0(q) \Psi_2. \quad (1.133)$$

The evolution of the perturbations  $\Psi_{\ell}$  is governed by the Boltzmann equations, and leads to the following set of equations:

$$\dot{\Psi}_0 = -\frac{qk}{\epsilon} \Psi_1 + \frac{\hbar}{6} \frac{d \ln f_0}{d \ln q}, \quad (1.134)$$

$$\dot{\Psi}_1 = \frac{qk}{3\epsilon} (\Psi_0 - 2\Psi_2), \quad (1.135)$$

$$\dot{\Psi}_2 = \frac{qk}{5\epsilon} (2\Psi_1 - 3\Psi_3) - \left( \frac{\hbar}{15} + \frac{2\dot{\eta}}{5} \right) \frac{d \ln f_0}{d \ln q}, \quad (1.136)$$

$$\dot{\Psi}_{\ell \geq 3} = \frac{qk}{(2\ell + 1)\epsilon} (\ell \Psi_{\ell-1} - (\ell + 1) \Psi_{\ell+1}). \quad (1.137)$$

Due to the dependence on the internal momenta  $q$ , the numerical integration takes more computational time than in the other cases so far. This integration has been fully implemented in the Einstein-Boltzmann solvers, with different numerical integration techniques, each of them validated and proved to agree below 0.1% [21]. In the same way we need to truncate the hierarchy, and [20] found that the truncation scheme:

$$\Psi_{\ell_{max}+1} \approx \frac{(2\ell + 1)\epsilon}{q\kappa\tau} \Psi_{\ell_{max}} - \Psi_{\ell_{max}-1}, \quad (1.138)$$

works pretty well. Since massive neutrinos decay rapidly once they become non-relativistic, it is possible to choose a smaller maximum multipole than in the massless neutrinos case.

Now we will discuss photons, which play an important role in the physics evolution of the early-Universe. Before recombination photons and baryons were tightly coupled in the primordial plasma. After recombination the Universe slowly becomes transparent, and photons travel more freely, while still interacting with matter and transferring energy and momentum. Even though there are many processes occurring between photons and baryons before recombination, the main interaction is Thomson scattering, the elastic scattering of electromagnetic radiation by free charged particles. Therefore, the modifications that will happen with respect to the Boltzmann equations for massless neutrinos are the collision terms in the RHS of Equation (1.99). Additionally, photons are linearly polarized, thus having two polarizations in which they can propagate, and, therefore, we will need two Legendre-expanded averaged functions to describe the two polarizations. When scattering off with the electron density perturbations with

wavenumber  $\mathbf{k}$  in the medium, photons with direction  $\hat{\mathbf{n}}$  get linearly polarized with respect to the plane perpendicular to its direction. This allow us to track both the sum and difference of the phase-space density. The former is denoted by  $F_\gamma(\mathbf{k}, \hat{\mathbf{n}}, \tau)$ , and the latter  $G_\gamma(\mathbf{k}, \hat{\mathbf{n}}, \tau)$ . The linear collisional operators for both are:

$$\left(\frac{\partial F_\gamma}{\partial \tau}\right)_C = an_e \sigma_T \left[ -F_\gamma + F_{\gamma 0} + 4\hat{\mathbf{n}} \cdot \mathbf{v}_e - \frac{1}{2}(F_{\gamma 2} + G_{\gamma 0} + G_{\gamma 2}) P_2 \right], \quad (1.139)$$

$$\left(\frac{\partial G_\gamma}{\partial \tau}\right)_C = an_e \sigma_T \left[ -G_\gamma + \frac{1}{2}(F_{\gamma 2} + G_{\gamma 0} + G_{\gamma 2})(1 - P_2) \right], \quad (1.140)$$

where  $v_e$  and  $n_e$  are the velocity and mean density of electrons.  $P_2$  is a term that appears due to the Thomson scattering dependence on polarization, its averaging gives in the end a term depending on  $1 + \cos^2 \theta$  in the cross section even for unpolarized photons. Expanding  $F_\gamma$  and  $G_\gamma$  in Legendre polynomials, and making the following identifications:

$$\hat{\mathbf{n}} \cdot \mathbf{v}_e = -\frac{i\theta_b}{k} P_1(\hat{\mathbf{k}} \cdot \mathbf{v}_e), \quad (1.141)$$

$$F_{\gamma 1} = \frac{4\theta_\gamma}{3k}, \quad (1.142)$$

$$F_{\gamma 2} = 2\sigma_\gamma, \quad (1.143)$$

we rewrite Equations (1.139-1.140) as:

$$\left(\frac{\partial F_\gamma}{\partial \tau}\right)_C = an_e \sigma_T \left[ \frac{4i}{k} (\theta_\gamma - \theta_b) P_1 + \left( 9\sigma_\gamma - \frac{1}{2}G_{\gamma 0} - \frac{1}{2}G_{\gamma 2} \right) P_2 \right] \quad (1.144)$$

$$- \sum_{\ell \geq 3}^{\infty} (-i)^\ell (2\ell + 1) F_{\gamma \ell} P_\ell \Big], \quad (1.145)$$

$$\left(\frac{\partial G_\gamma}{\partial \tau}\right)_C = an_e \sigma_T \left[ \frac{1}{2}(F_{\gamma 2} + G_{\gamma 0} + G_{\gamma 2})(1 - P_2) - \sum_{\ell \geq 3}^{\infty} (i)^{-\ell} (2\ell + 1) G_{\gamma \ell} P_\ell \right]. \quad (1.146)$$

And the Boltzmann equation for photons are:

$$\dot{\delta}_\gamma = -\frac{4}{3}\theta_\gamma - \frac{2}{3}\dot{h}, \quad (1.147)$$

$$\dot{\theta}_\gamma = k^2 \left( \frac{1}{4}\delta_\gamma - \sigma_\gamma \right) + an_e \sigma_T (\theta_b - \theta_\gamma), \quad (1.148)$$

$$2\dot{\sigma}_\gamma = \frac{8}{15}\theta_\gamma - \frac{3}{15}kF_{\gamma 3} + \frac{4}{15}\dot{h} + \frac{8}{5}\dot{\eta} - \frac{9}{5}an_e \sigma_T \sigma_\gamma + \frac{1}{10}an_e \sigma_T (G_{\gamma 0}G_{\gamma 2}), \quad (1.149)$$

$$\dot{F}_\gamma = \frac{k}{2\ell + 1} [\ell F_{\gamma(\ell-1)} - (\ell + 1)F_{\gamma(\ell+1)}] - an_e \sigma_T, \quad \ell \geq 3, \quad (1.150)$$

$$\dot{G}_\gamma = \frac{k}{2\ell + 1} [\ell G_{\gamma(\ell-1)} - (\ell + 1)G_{\gamma(\ell+1)}] \quad (1.151)$$

$$+ an_e \sigma_T \left[ -G_{\gamma \ell} + \frac{1}{2}(F_{\gamma 2} + G_{\gamma 0}G_{\gamma 2}) \left( \delta_{\ell 0} + \frac{\delta_{\ell 2}}{5} \right) \right]. \quad (1.152)$$

Finally, the previous hierarchical equations are truncated at some  $\ell = \ell_{max}$ :

$$\dot{F}_{\gamma \ell} = kF_{\gamma(\ell-1)} - \frac{\ell + 1}{\tau} F_{\gamma \ell} - an_e \sigma_T F_{\gamma \ell}, \quad (1.153)$$

the same truncation is done for  $G_{\gamma\ell}$ . This is the same scheme as the one for massless neutrinos, apart from the opacity Thomson term.

We now move to baryons, the last species we are yet to discuss in this section. For all scales of interest in cosmology, baryons are non-relativistic, therefore, they have no anisotropic stress,  $\sigma = 0$ , and their equation of state and sound speed are much less than unity. In Equations (1.104-1.107) we can safely neglect the terms that involve  $\delta p/\delta\rho$ , with the exception to the one multiplied by  $c_s^2 k^2 \delta$ , which is important at high  $k$  values. As we have seen, baryons and photons exchange momentum when they are tightly coupled, and due to momentum conservation we must add a  $an_e\sigma_T(\theta_b - \theta_\gamma)$  term in the first moment of the Boltzmann equations for baryons. We are left with:

$$\dot{\delta}_b = -\theta_b - \frac{1}{2}\dot{h}, \quad (1.154)$$

$$\dot{\theta}_b = -\frac{\dot{a}}{a}\theta_b + c_s^2 k^2 \delta_b + \frac{4\rho_\gamma}{3\rho_b} an_e\sigma_T(\theta_b - \theta_\gamma), \quad (1.155)$$

where the square of the sound speed is given by:

$$c_s^2 = \frac{\dot{p}_b}{\dot{\rho}_b} = \frac{k_B T}{M_{\text{mol.}}} \left[ 1 - \frac{1}{3} \frac{d \ln T_b}{d \ln a} \right]. \quad (1.156)$$

with  $M_{\text{mol.}}$  the mean molecular weight.

Prior recombination, we have the tight coupling era, and the main problem associated to this period, is that the dynamical equations become stiff, and usual numerical integrators end up introducing large errors when compared to the full solution. Peebles and Yu [24] introduced an approximation to solve these equations to avoid these stability issues. It is based on an expansion in the interaction rate  $\tau_c = (an_e\sigma_T)^{-1}$  (Thomson Opacity), which is large prior recombination. This approximation is called the Tight-Coupling Approximation (TCA), and it is used during early times to help solve the Boltzmann equations. There are different schemes for the TCA approximation, each varying on the order of the expansion in  $\tau_c$ , as well as the time dependence on this term. I will not go into details on this approximation, since it falls outside the scope of this thesis, and I refer the reader to the works [25, 20].

Recombination physics is a lengthy and detailed derivation, which I will not cover here as well. The basic idea behind it is that there is a time in the early Universe in which is thermodynamically favourable for ions (protons and  $\text{He}^{2+}$ ) and electrons to combine and form neutral atoms. With the rapid decrease of free electrons, the photons scattering rate falls below the expansion rate,  $H$ . This puts a halt on the interaction between photons and baryons in the primordial plasma, allowing the photons to free-stream, making the Universe transparent to radiation. This is known as photon decoupling, and it is the farthest we can go back in time, and actually observe the Universe. Since baryons and photons are now decoupled they will evolve differently, and are not bound to have the same temperature. The detailed calculation of this process can be found in many textbooks [26, 27].

In this Section I presented an overview on the mathematical aspects of cosmological linear perturbation theory. This framework, combined with the discussion of the homogeneous and isotropic discussion presented in the last section, form the fundamental pillars that the  $\Lambda$ CDM model is built on. I will now move to discuss the observational data that has allowed us to jointly probe the Universe using a rather simple machinery.

## 1.4. Cornerstone Observations

### 1.4.1. CMB

The Cosmic Microwave Background is one of the most precise and powerful probes we have in cosmology. Its origin is connected to the primordial plasma when the Universe was much younger, before the formation of stars and planets, when it was filled with an opaque cloud of hydrogen plasma. As the expansion occurred, the temperature of this plasma decreased, and the radiation in the Universe expanded to longer wavelengths, until photons and electrons combined to form neutral hydrogen atoms. Unlike the primordial plasma, these new atoms could not scatter the thermal radiation by Thomson scattering, and the Universe became transparent. This epoch in the Universe history is referred to as recombination, and, the subsequent period is referred to as photon decoupling, as the photons that once formed the plasma and were tightly coupled to baryons, began to travel freely in the Universe. The CMB was discovered by Penzias and Wilson in 1964, who observed the CMB as an almost uniform temperature across the whole sky. This observation was followed three decades later by first the Russian experiment RELIKT-1 [28] in 1983, and then the COBE satellite [29] in 1989, which discovered small temperature anisotropies in the CMB. More precise measurements of which have been made by BOOMERanG [30], MAXIMA [31], WMAP [32] and most recently, Planck [13]. Defining the temperature perturbations as:

$$\Theta(\mathbf{x}, \tau) = \frac{\delta T}{T}, \quad (1.157)$$

where  $\tau$  is conformal time,  $x$  the position and  $T$  is the average CMB temperature, which is measured at  $T = 2.725\text{K}$ . As we observe the CMB in the whole sphere of the sky, it is useful to expand the temperature perturbations in terms of spherical harmonics:

$$\Theta(\mathbf{x}, \tau) = \sum_{\ell=1}^{\infty} \sum_{m=-\ell}^{\ell} a_{\ell m}(\mathbf{x}, \tau) Y_{\ell m}, \quad (1.158)$$

where  $\ell$  and  $m$  are conjugate to a real space unit vector  $\hat{\mathbf{n}}$  representing the direction of incoming photons, and the spherical harmonics  $Y_{\ell m}$  satisfy the normalization condition:

$$\int d\Omega Y_{\ell m}(\hat{\mathbf{n}}) Y_{\ell' m'}(\hat{\mathbf{n}})^* = \delta_{\ell\ell'} \delta_{mm'}. \quad (1.159)$$

The coefficients  $a_{\ell m}$  of Equation (1.158) have mean zero, while its variance is defined by:

$$C_{\ell} = \langle |a_{\ell m}|^2 \rangle, \quad (1.160)$$

and it can also be expressed in terms of the power spectrum of the temperature perturbations in Fourier space:

$$C_{\ell} = \frac{2}{\pi} \int_0^{\infty} dk k^2 |\Theta(k, \tau)|^2. \quad (1.161)$$

So far I have discussed only the CMB temperature angular power spectrum. However, from the CMB we have a total of six angular power spectra that give us information about the photons that travelled from the last scattering surface to us. They are: the temperature  $C_{\ell}^{\text{TT}}$ , the E-mode polarization  $C_{\ell}^{\text{EE}}$  and the B-mode polarization  $C_{\ell}^{\text{BB}}$  auto correlations power spectra, and three cross-correlations ones: TE  $C_{\ell}^{\text{TE}}$ , TB  $C_{\ell}^{\text{TB}}$  and EB  $C_{\ell}^{\text{EB}}$ . The E and B modes from the CMB appear due to the fact that the cosmic microwave background is weakly polarized. Polarization is generated by Thomson scattering, and thus it is generated at the last scattering surface ( $z = 1090$ )

and during the epoch of reionization ( $z < 15$ ). This E and B polarization decomposition follows the reasoning of decomposing a polarization pattern in the sky into “electric” (E) and “magnetic” (B) components, as shown in Figure 1.3. Polarization describes the orientation of the light

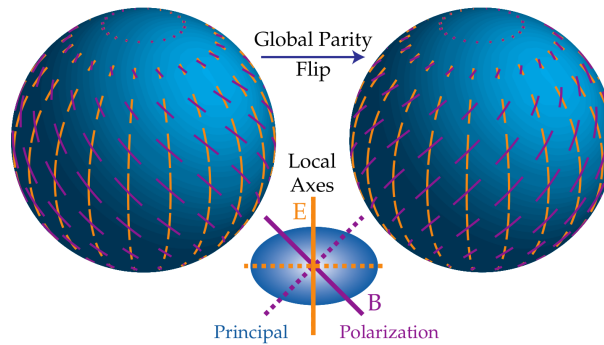


**Figure 1.3.** Decomposition of the polarization pattern into “electric” and “magnetic” components. As seen in the orange lines, the  $E$  modes are invariant under parity transformations, whilst  $B$  modes are not.

perpendicular to the direction of propagation. The dominant contribution to CMB polarization anisotropies is from density (or scalar) perturbations in the early universe. However, since scalar perturbations are parity-even, they can only generate polarizations of a specific mode, the  $E$  modes.  $B$  mode polarizations appear if there is a production of primordial gravitational waves during inflation, and they are always present in the lensed spectra of the CMB. The former depends on the inflationary model of the Early Universe, and it constitutes one of the most important topics of research in early Universe physics. The latter, arises from the fact that photon trajectory from the last scattering surface to us is distorted due to the inhomogeneities present in our Universe. This ultimately modifies the original polarization vector, which is detected by us and corresponds to a production of  $B$  modes, even if no primordial gravitational waves were generated. One of the greatest efforts of future CMB experiments is to further explore the polarization information coming from the CMB, and in order to do so we need to come up with very sophisticated methods to separate  $B$  modes produced by the lensing of the photons, to the ones that can be possibly generated by different early Universe model. In Figure 1.4 I show the temperature angular power spectrum from the last Planck collaboration data release, where we can see the excellent agreement the  $\Lambda$ CDM model has with the data points.

### 1.4.2. Supernovae Ia

Supernovae are the byproduct of the violent end of the life of a star, and are one of the brightest objects in our Universe, often outshining their host galaxies at the peak of their brightness curve. There are four types of supernovae based on their emission spectra:

- SN II: these supernovae show Hydrogen (H) lines in their spectra;
- SN Ib: these do not have Hydrogen lines, but they do have Helium (He);
- SN Ia: no H/He lines, but with  $\text{Si}^+$  6150Å feature;
- SN Ic: no H/He lines (or very weak He), no  $\text{Si}^+$ .

The Type Ia supernovae (SN Ia) are the most popular standard candle in cosmology today, and their biggest advantages are:

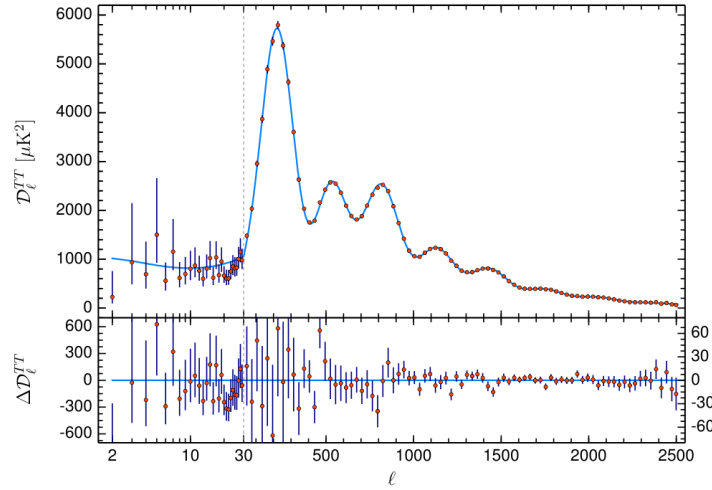


**Figure 1.4.** The CMB temperature power spectrum from [Planck2018]. The theoretical prediction is given by the blue line and the binned observational data is shown by the red points. The quantity in the y-axis is defined as  $D_\ell = \ell(\ell + 1)C_\ell/2\pi$ .

- They can be seen at cosmologically significant distances,  $z \sim 1.8$ ;
- They have small dispersion in intrinsic luminosity;
- They are frequent, transient events – can always observe more.

One of the biggest breakthroughs in cosmology happened in 1993, when Philips [33] showed that type IA Supernova, are standardizable candles, from which we can use the peak of their brightness to measure their luminosity, and from which we can get the distance of these objects from the luminosity relation:

$$m(z) - M_B = 5 \log_{10} d_L(z) - 5, \quad (1.162)$$

where  $m(z)$  is the apparent luminosity of the Supernova,  $M_B$  is their absolute luminosity and  $d_L$  is the luminosity distance to the supernova in parsecs. The redshift of the supernova can be found by observing the wavelength of its light and the shift of various absorption lines in its spectra, and with a sufficient number of supernova observations the dependence of the observed luminosity on redshift can be found. For large supernova surveys, such as the Pantheon, this is then compared to the flat  $\Lambda$ CDM theoretical prediction, and the values of cosmological parameters, such as  $\Omega_m$  and  $\Omega_\Lambda$  are inferred from it. This was the procedure taken by the two independent teams that in 1998 found that the Universe was in an accelerated expansion phase:

- High- $z$  Supernova Search: Riess et al. 1998 (AJ 116, 1009) [7].
- Supernova Cosmology Project: Perlmutter et al. 1999 (ApJ 517, 565) [6].

In Figure 1.5 I show the plot taken from Reference [6] showing the effective apparent magnitudes,  $m_B$ , measured by two independent teams, as a function of redshift.

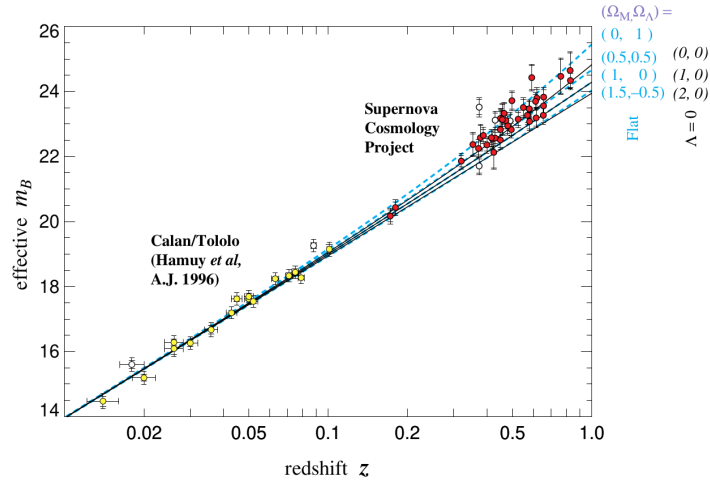


**Figure 1.5.** The effective apparent luminosity  $m_B$  versus the redshift  $z$  for 42 high-redshift SN Ia from the SCP [6] and 18 low-redshift SN Ia from the Calan/Tololo Supernova Survey [34]

### 1.4.3. BAO

Before recombination, photons and baryons were tightly coupled, and, in this way, the plasma which they formed had a non-zero sound speed. This effectively implies the baryonic perturbations in our Universe also have an oscillatory feature imprinted by this period of tight coupling with photons. This can be seen in the temperature fluctuations of the CMB. Also, since after the photon decoupling, baryons started falling inside the gravitational wells formed by the cold dark matter component of the Universe, we are also able to see these oscillations in the Large Scale Structure of our Universe, seen in Figure 1.6. This baryonic acoustic oscillation, or BAO for

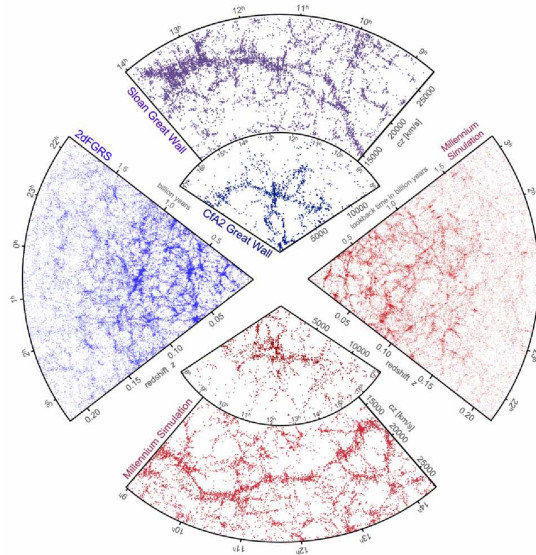


**Figure 1.6.** Figure taken from [35], representing the large scale structure of Universe with data coming from different galaxy surveys.

short, was first detected in 2005 [36] at  $\sim 100$  Mpc/ $h$ . From the location of this BAO peak, we are also able to add another evidence for a dark energy component responsible to the accelerated

expansion of our Universe. The time at which photons were freed from the Compton scattering with baryons is known as the drag epoch, and the sound horizon at that time,  $\tau_{\text{drag}}$ , can be computed as:

$$r_s(z_{\text{drag}}) = \int_0^{\tau_{\text{drag}}} d\tau c_s(\tau), \quad (1.163)$$

where  $c_s(\tau)$  is the sound speed of the photon-baryons plasma given by:

$$c_s^2 = \frac{\delta p_\gamma}{\delta \rho_\gamma + \delta \rho_b}, \quad (1.164)$$

where  $\gamma$  refers to photons and  $b$  to baryons. When performing observations of galaxies in the sky, what we actually measure is the angular and redshift distributions of galaxies as a power spectrum  $P(k_\perp, k_\parallel)$  in redshift space, where  $k_\perp$  and  $k_\parallel$  are the wave-numbers perpendicular and parallel to the line of sight respectively. From the power spectrum in redshift space it is possible to measure two quantities [37]:

$$\theta_s = \frac{r_s(z_{\text{drag}})}{(1+z)d_A(z)}, \quad (1.165)$$

$$\delta z_s = \frac{r_s(z_{\text{drag}})H(z)}{c}, \quad (1.166)$$

where  $\theta_s$  corresponds to observations orthogonal to the line of sight, while  $\delta z_s$  is instead measured by identifying in the fluctuation spectrum the oscillations along the line of sight. The current BAO data is insufficient to measure these two distances separately, but a combined distance scale can be obtained from the spherically averaged power spectrum

$$[\theta_{\text{BAO}}^2 \delta z_{\text{BAO}}]^{1/3} = \frac{r_s(z_{\text{drag}})}{\left[ (1+z)^2 d_A^2(z) c/H(z) \right]^{1/3}}, \quad (1.167)$$

or as a related effective distance:

$$d_V(z) = \left[ (1+z)^2 d_A^2(z) \frac{cz}{H(z)} \right]^{1/3}. \quad (1.168)$$

We can thus compare predictions for the distance scale  $d_V(z)$  to observational data, finding once again that a dark energy dominated Universe is favoured over a matter dominated one, see [38, 39].

#### 1.4.4. Redshift-space distortions

Galaxies are biased tracers of the underlying matter density field, that is, they are discrete probes of the large scale structure of the Universe. Their radial position can be estimated through their redshift, which is measured, for example, from the shift in their emission spectra. However, due to the presence of density perturbations, galaxies have non-zero radial peculiar velocities, which alter their measured redshift through an additional Doppler effect. This distortion is correlated with the real density perturbation, and therefore changes the statistics of the observed matter distribution. This effect was first modelled by N. Kaiser in the famous paper [40] and has come to be widely known as the Kaiser effect.

When we map out objects like galaxies in 3-dimensional space, the radial (comoving) distance to the object is determined by its measured redshift,  $z_{\text{obs}}$ . However, we should remember that

there are always two contributions to this quantity: Hubble flow  $r(z_{\text{cos}}) = \int_0^{z_{\text{cos}}} cdz/H(z)$  and the peculiar velocity of the object:

$$1 + z_{\text{obs}} = (1 + z_{\text{cos}}) \left( 1 - \frac{v_{\parallel}(\mathbf{r})}{c} \right)^{-1}, \quad (1.169)$$

$$\mathbf{s} = \mathbf{r} + \frac{(1 + z_{\text{cos}}) v_{\parallel}(\mathbf{r})}{H(z_{\text{cos}})} \hat{r}, \quad (1.170)$$

where  $z_{\text{cos}}$  is the cosmological redshift due to the expansion of the Universe and  $v_{\parallel}$  denotes the line-of-sight (LOS) component of the peculiar velocity. As an example, for a flat- $\Lambda$ CDM Universe with  $\Omega_m = 0.3$ ,  $r(z_{\text{cos}}) \approx 1.32 \text{ Gpc}/h$ , while the second term is:

$$\left. \frac{(1 + z_{\text{cos}}) v_{\parallel}(\mathbf{r})}{H(z_{\text{cos}})} \right|_{z_{\text{cos}}=0.5} \sim 1.18 \frac{v_{\parallel}}{100 \text{ km/s}} [\text{Mpc}/h], \quad (1.171)$$

which typically is of the order of  $\mathcal{O}(1 \text{ Mpc}/h)$ . For clustering statistics the second term has a

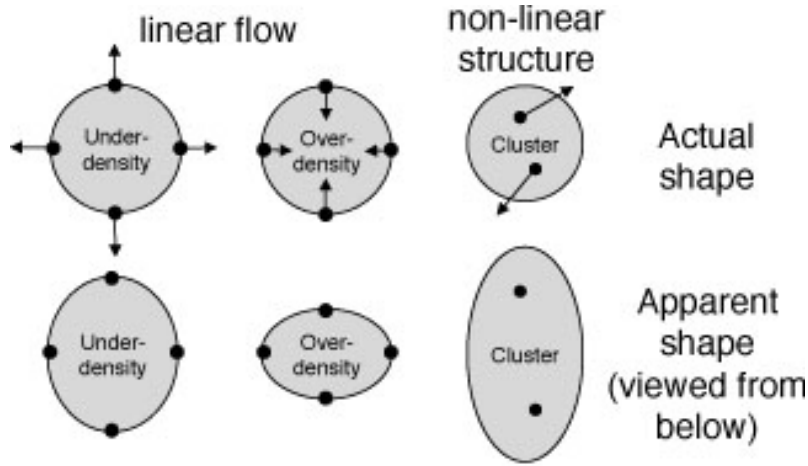


**Figure 1.7.** Diagram showing how real space structures (top row) get distorted in redshift space (bottom row). Figure taken from [41].

non-negligible contribution for the matter density field:

$$\delta_m(\mathbf{x}) = \frac{\rho_m(\mathbf{x})}{\bar{\rho}} - 1. \quad (1.172)$$

The Fourier transform of the 2-pt correlation function of this field is simply:

$$\langle \delta_m(\mathbf{x}) \delta_m(\mathbf{x}') \rangle = (2\pi)^3 \delta_D(\mathbf{k} + \mathbf{k}') P_m(\mathbf{k}), \quad (1.173)$$

which reduces to just a function of the wave-number modulus  $k$ ,  $P_m(k)$  due to the Universe being homogeneous and isotropic at large scales. However, in redshift space, the observed matter power spectrum will not be isotropic anymore, with the peculiar velocity term breaking the rotational invariance and introducing an anisotropic term. This term is the precisely the one that Kaiser computed in his original paper, and the linear matter power spectrum in redshfit space is written as:

$$P_s = (1 + \beta \mu_{\mathbf{k}}^2) P_{r,\mathbf{k}}, \quad (1.174)$$

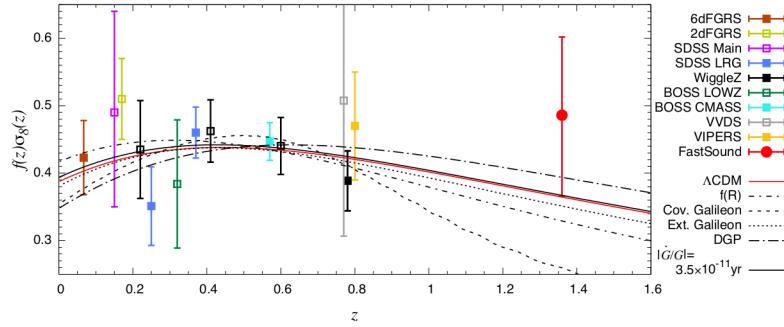


**Figure 1.8.**  $f\sigma_8$  data points from different galaxy surveys. The plot also shows the curves for different cosmological models. Figure taken from [42].

with  $\beta = f/b$  and  $\mu_{\mathbf{k}} = \mathbf{k} \cdot \hat{\mathbf{n}}_z / k$  is the cosine angle between the wave-number vector  $\mathbf{k}$  and the line of sight direction  $\hat{\mathbf{n}}_z$ . In the expression of  $\beta$ ,  $f$  is the logarithmic derivative of the matter density field with respect to the logarithm of the scale factor, and  $b$  is the linear bias term, that connects the observed galaxy density field with the underlying distribution of the matter density field. Physically, the Kaiser effect is translated as: At large scales, objects tend to coherently infall into high density region and the density field becomes squashed, hence the clustering amplitude becomes stronger along LOS, Figure 1.7 shows this effect schematically. If we only consider the linear scales and the galaxy number density, we can further rewrite Equation (1.174) as:

$$P_{\mathbf{g}}^{s,L}(\mathbf{k}) = P_{\mathbf{g}}^{s,L}(k, \mu) = b^2 (1 + \beta\mu^2)^2 P_{\mathbf{m}}^L(k), \quad \beta = \frac{f}{b} \quad (1.175)$$

and since the linear matter power spectrum can be parametrized in terms of the amplitude of the matter fluctuations at a given scale  $R = 8 \text{ Mpc}/h$ , redshift space distortions are usually parametrized by the combination  $f\sigma_8$ . In Figure 1.8, I show some measurements of this quantities for different surveys and gravity theories.

### 1.4.5. Gravitational lensing

The inhomogeneities in the Universe formed by the clustering of matter affect the path photons emitted in a given redshift take until they reach us. This is known as gravitational lensing, and it was the first observational test of General Relativity, in 1919, Eddington led a voyage to the Southern Hemisphere to observe the deflection of starlight during a solar eclipse. The magnitude of this effect [43] was in good agreement with Einstein's new theory. The power of lensing resides on the fact that it responds to all the mass distribution in the Universe, contrary to the galaxy power spectrum observed in spectroscopic surveys, which is a biased version of the cold dark matter plus baryons power spectrum.

Lensing can be divided into two categories: strong and weak. Observations of the former rely on constraining the quantity  $\Delta t H_0$ , where  $\Delta t$  is the time delay, and it depends only on the mass profile of the lens and the relative redshift between the source and lens. The latter, however, as the name suggests, is a much more subtle effect, as it involves the lensing of very distant background galaxies by foreground galaxy clusters. Individually speaking this effect is insignificant, but when we average over the whole distribution of galaxies in a given redshift the apparent distortions of the lensed image becomes a very powerful probe. This weak lensing signal can be combined with cluster abundances to constrain structure growth, as done by the Dark Energy Survey, which recently reported [44] a measure of  $S_8 = 0.776 \pm 0.017$ . This  $S_8$  parameter

---

allows us to constraint the amplitude of matter perturbations in a sphere of radius  $R = 8 \text{ Mpc}/h$ ,  $\sigma_8$ , in combination with the total matter energy density,  $\Omega_m$ .

# Modified Gravity

## 2.1. Introduction

Einstein's theory of gravity stands in the corner of the Standard Model of Cosmology. General Relativity is assumed to describe gravitational interactions from the smallest scales of our Universe to the largest distances known. It has passed many tests, from millimetre scales laboratory experiments, passing through Solar System tests and culminating in the now well known and well established gravitational waves cosmology. The many successes GR has, however, does not mean that the effort of looking for alternative theories of gravity should be halted.

When in 1998 astronomers showed for the first time that our Universe on a period of accelerated expansion, the addition of the cosmological constant,  $\Lambda$ , to explain this feature became our standard paradigm for the nature of dark energy. However, due to the poor constraints we have on modified gravity theories when using cosmological data, and due to theoretical problems the cosmological constant faces, modified gravity theories that naturally explain the expansion of our Universe remain one of the most active fields in modern cosmology. However, not only General Relativity has successfully passed many different tests, it is also the simplest theory that is able to describe a massless spin-2 field propagating in a curved space-time. Therefore, to propose new theories of gravity we need to be consistent throughout our approach.

## 2.2. Lovelock Theorem

A first step to introduce modifications of gravity is to look at the action. Assuming that the only field that mediates gravity is the metric tensor  $g_{\mu\nu}$ , the action reads:

$$S = \int d^4x \mathcal{L}(g_{\mu\nu}). \quad (2.1)$$

By extremizing this action we are able to find the equations of motion:

$$E^{\mu\nu}[\mathcal{L}] = \frac{d}{dx^\rho} \left[ \frac{\partial \mathcal{L}}{\partial g_{\mu\nu,\rho}} - \frac{d}{dx^\lambda} \left( \frac{\partial \mathcal{L}}{\partial g_{\mu\nu,\rho\lambda}} \right) \right] - \frac{\partial \mathcal{L}}{\partial g_{\mu\nu}}, \quad (2.2)$$

with  $E^{\mu\nu}[\mathcal{L}] = 0$ . Lovelock's theorem [45, 46] can then be stated as:

- *The only possible second order Euler-Lagrangian operator,  $E^{\mu\nu}$ , built from the metric in a four dimensional manifold and scalar density Lagrangian  $\mathcal{L}$  is the following:*

$$E^{\mu\nu} = \alpha \sqrt{-g} \left[ R^{\mu\nu} - \frac{1}{2} g_{\mu\nu} R \right] + \lambda \sqrt{-g} g_{\mu\nu}, \quad (2.3)$$

*with  $\alpha$  and  $\lambda$  constants,  $R_{\mu\nu}$  is the Ricci tensor, and  $R$  is the Ricci scalar.*

This means that if one tries to build another gravitational theory using *only* the metric tensor in a four dimensional space-time with only *second* order equations of motion for the field, then the result will be Einstein's Equations with a possible cosmological constant. Therefore, this theorem gives us the routes in which we can look for modifications to GR:

- Add extra fields besides the metric tensor;
- Ease the condition of *only* second order equations of motion;
- Go to higher dimensions in the manifold;
- Give up on the requirement of deriving the equations of motion from the variation of an action principle;
- Assume non-local terms.

The first, second and third conditions are the most pursued paths in the literature. The fourth can be seen as the most unconventional but has seen some research recently as well [47, 48, 49], and the last has also seen some propositions [50]. In this thesis I will focus only on the first condition.

## 2.3. Scalar-Tensor Theories

The most well established and tested alternative theories to General Relativity are Scalar-Tensor (ST) theories. These theories add, on top of the metric tensor, an extra scalar field that mediates gravity. The main reason these models are so simple when compared to others, is due to the fact that scalar fields easily respect all the symmetries we have in our manifold. Even before Einstein proposed GR, Nordstrom developed in 1912 a conformally flat theory of gravity that was based purely of a scalar field. Today, however, the majority of ST theories introduce a time-dependent coupling between gravity and matter. The idea of constants of nature being not constant, but time-dependent, dates back to the works of Dirac in 1937 on large numbers hypothesis. Jordan, then, further complemented this idea with a complete theory that pushed  $G$  to be time-dependent as it assumed the role of a scalar field. Finally, Brans and Dicke reached full maturity with this idea by proposing the now famous Jordan-Brans-Dicke (JBD) theory, one of the most well studied gravity theory alternative to GR [51, 52]. The action of JBD can be written as:

$$S = \frac{1}{16\pi} \int d^4x \sqrt{-g} [f(\phi)R + g(\phi)\nabla_\mu\phi\nabla^\mu\phi - 2\Lambda(\phi)] + \mathcal{L}_m(\Psi_m, h(\phi)g_{\mu\nu}), \quad (2.4)$$

where  $\Psi_m$  are the matter fields. We can absorb the function  $h(\phi)$  into the metric tensor:

$$h(\phi)g_{\mu\nu} \rightarrow g_{\mu\nu}. \quad (2.5)$$

This choice picks out a conformal frame in which gravity and matter are minimally coupled, therefore matter follows geodesics, but the scalar field and the metric tensor can be non-minimally coupled. This reference frame is the so-called Jordan frame and the equivalence principle in its *weak* form is satisfied. After this conformal choice of reference frame, other field redefinitions can be made in (2.4), in order to write the action in a way that it resembles the original form of JBD theory:

$$S = \frac{1}{16\pi G_N} \int d^4x \sqrt{-g} \left[ \phi R - \frac{\omega(\phi)}{\phi} \nabla_\mu\phi\nabla^\mu\phi - 2\Lambda(\phi) \right] + \mathcal{L}(\Psi_m, g_{\mu\nu}), \quad (2.6)$$

where  $\omega(\phi)$  is called the coupling function and  $\Lambda(\phi)$  is the field generalization of the Cosmological Constant. The action written in this way also leads to an easy identification of the GR limit inside the JBD theory [52, 53] e.g.:

$$\omega \rightarrow \infty, \quad (2.7)$$

$$\omega'/\omega^2 \rightarrow 0 \quad (2.8)$$

$$\Lambda(\phi) \rightarrow \text{constant}. \quad (2.9)$$

The equations of motion in the Jordan frame are found by varying (2.6) w.r.t  $g_{\mu\nu}$  and  $\phi$ :

- $\delta g_{\mu\nu}$ :

$$\phi G_{\mu\nu} + \left[ \square\phi + \frac{1}{2} \frac{\omega}{\phi} (\nabla\phi)^2 + \Lambda \right] g_{\mu\nu} - \nabla_\mu \nabla_\nu \phi - \frac{\omega}{\phi} \nabla_\mu \phi \nabla_\nu \phi = 8\pi T_{\mu\nu}. \quad (2.10)$$

- $\delta\phi$ :

$$(2\omega + 3) \square\phi + \omega' (\nabla\phi)^2 + 4\Lambda - 2\phi\Lambda' = 8\pi T, \quad (2.11)$$

where a prime represents differentiation with respect to the scalar field. We can see from Equation (2.10) that  $G_{\text{eff}} \propto \frac{1}{\phi}$ .

These theories are conformally equivalent to General Relativity, in the sense that if we perform a Weyl transformation (a class of a larger group of conformal transformations [54]) in the metric tensor, we can “conformally land” in General Relativity. A Weyl transformation is defined as:

$$g_{\mu\nu} \rightarrow e^{\Gamma(x)} \bar{g}_{\mu\nu}, \quad (2.12)$$

where  $\Gamma(x)$  is a scalar function, and the line element of the two metrics are related as  $ds^2 = e^{2\Gamma(x)} d\bar{s}^2$ . This transformation *does not* alter angles, as it merely rescales the line element, thus, preserving the conformal structure of the space-time. The Ricci tensor in the new conformal metric becomes:

$$R_{\mu\nu} = \bar{R}_{\mu\nu} - 2\bar{\nabla}_\mu \bar{\nabla}_\nu \Gamma + 2\bar{\nabla}_\mu \Gamma \bar{\nabla}_\nu \Gamma - (2\bar{\nabla}_\alpha \Gamma \bar{\nabla}^\alpha \Gamma + \square\Gamma) \bar{g}_{\mu\nu} \quad (2.13)$$

$$e^{2\Gamma} R = \bar{R} - 6\bar{\nabla}_\mu \Gamma \bar{\nabla}^\mu \Gamma - 6\square\Gamma, \quad (2.14)$$

$$e^{2\Gamma} \square\phi = \square\phi + 2\bar{\nabla}_\alpha \Gamma \nabla^\alpha \phi. \quad (2.15)$$

After some algebraic manipulations using Equations (2.13) and (2.6), we arrive at:

$$S = \frac{1}{16\pi G_N} \int d^4x \sqrt{-\bar{g}} \left[ \bar{R} - \frac{1}{2} \nabla_\mu \chi \nabla^\mu \chi + V(\chi) \right] + \mathcal{L}_m(\Psi_m, e^{2\Gamma} \bar{g}_{\mu\nu}), \quad (2.16)$$

where  $\chi$  is the new scalar field that is related to the original one. Therefore, we can see that this new multiplying factor in the matter Lagrangian introduces a non-minimal coupling between matter and gravity. The action (2.16) is the JBD action in the conformal frame, which is commonly referred as the Einstein frame, since the same action in the new metric describes Einstein’s gravity plus a minimally coupled scalar field that is now non-minimally coupled to matter. This new interaction between gravity and matter introduces the effects of a new force in the movement of massive test-particles, i.e., there is an emergence of a fifth force. This is directly seen in the non-conservation of the energy momentum tensor in the Einstein frame,

$\bar{\nabla}_\mu \bar{T}^{\mu\nu} = \sqrt{4\pi}(2\omega + 3)\bar{T}\nabla^\nu \chi$ . The geodesic motion for massive particles can be derived from the conservation of the energy-momentum tensor, and can be written as:

$$\frac{d^2 x^\mu}{d\lambda^2} + \bar{\Gamma}_{\alpha\beta}^\mu \frac{dx^\alpha}{d\lambda} \frac{dx^\beta}{d\lambda} = \sqrt{\frac{4\pi}{2\omega + 3}} \bar{\nabla}^\mu \chi \quad (2.17)$$

where  $\bar{\Gamma}_{\alpha\beta}^\mu$  is the Christoffel symbol of the conformal metric and  $\lambda$  is an affine-parameter. The universality of free-fall (Weak Equivalence Principle) is violated by the RHS of this equation.

Until now, we have considered only the so-called JBD theory, which was historically considered the most general scalar-tensor theory of gravity. However, the most general scalar tensor theory, with second order equations of motion, is not derived from Equation (2.6), but from the so-called Horndeski action:

$$S[g_{\mu\nu}, \phi] = \int d^4x \sqrt{-g} \left[ \sum_{i=2}^5 \frac{1}{8\pi G_N} \mathcal{L}_i[g_{\mu\nu}, \phi] + \mathcal{L}_m[g_{\mu\nu}, \psi_M] \right], \quad (2.18)$$

where the  $\mathcal{L}_i$  terms in the Lagrangian are:

$$\mathcal{L}_2 = G_2(\phi, X), \quad (2.19a)$$

$$\mathcal{L}_3 = -G_3(\phi, X)\square\phi, \quad (2.19b)$$

$$\mathcal{L}_4 = G_4(\phi, X)R + G_{4X}(\phi, X) \left[ (\square\phi)^2 - \phi_{;\mu\nu}\phi^{;\mu\nu} \right], \quad (2.19c)$$

$$\begin{aligned} \mathcal{L}_5 = G_5(\phi, X)G_{\mu\nu}\phi^{;\mu\nu} - \frac{1}{6}G_{5X}(\phi, X) \left[ (\square\phi)^3 \right. \\ \left. + 2\phi_{;\mu}{}^\nu \phi_{;\nu}{}^\alpha \phi_{;\alpha}{}^\mu - 3\phi_{;\mu\nu}\phi^{;\mu\nu}\square\phi \right]. \end{aligned} \quad (2.19d)$$

$X = -\frac{1}{2}\partial_\mu\phi\partial^\mu\phi$  is the kinetic term of the scalar field, and  $\psi_M$  represents matter fields minimally coupled to gravity. This theory carries the name of its original proposer, Gregory Horndeski, who introduced it in 1974 in his PhD thesis. However, the theory only gained attraction in the community in 2011, when theorists [55, 56] were looking for generalizations of Galileon theories (theories invariant under galilean transformations, constant coordinate shift). Galileons are the most general scalar-tensor theories in a flat space-time, and Horndeski's theory is its covariant equivalent for a general space-time. To derive the cosmological background equations of motion of (2.18) we vary the action with respect to the line element  $ds^2 = -N(t)dt^2 + a^2(t)d\mathbf{x}^2$ :

- $\delta N(t)$  Constraint Equation:

$$\sum_{i=2}^5 \mathcal{E}_i = 0 \quad (2.20)$$

with

$$\mathcal{E}_2 = 2XK_X - K, \quad (2.21)$$

$$\mathcal{E}_3 = 6X\dot{\phi}HG_{3X} - 2XG_{3\phi}, \quad (2.22)$$

$$\mathcal{E}_4 = -6H^2G_4 + 24H^2X(G_{4X} + XG_{4XX}) - 12HX\dot{\phi}G_{4\phi X} - 6H\dot{\phi}G_{4\phi}, \quad (2.23)$$

$$\mathcal{E}_5 = 2H^3X\dot{\phi}(5G_{5X} + 2XG_{5XX}) - 6H^2X(3G_{5\phi} + 2XG_{5\phi X}). \quad (2.24)$$

- $\delta a(t)$  Evolution Equation:

$$\sum_{i=2}^5 \mathcal{P}_i = 0 \quad (2.25)$$

where

$$\mathcal{P}_2 = K, \quad (2.26)$$

$$\mathcal{P}_3 = -2X \left( G_{3\phi} + \ddot{\phi} G_{3X} \right), \quad (2.27)$$

$$\mathcal{P}_4 = 2 \left( 3H^2 + 2\dot{H} \right) G_4 - 12H^{12} X G_{4X} - 4H\dot{X} G_{4X} - 8\dot{H} X G_{4X} - 8HX\dot{X} G_{4XX} \quad (2.28)$$

$$+ 2 \left( \ddot{\phi} + 2H\dot{\phi} \right) G_{4\phi} + 4X G_{4\phi\phi} + 4X \left( \ddot{\phi} - 2H\dot{\phi} \right) G_{4\phi X}, \quad (2.29)$$

$$\mathcal{P}_5 = -2X \left( 2H^3\dot{\phi} + 2H\dot{H}\dot{\phi} + 2H\dot{H}\dot{\phi} + 3H^2\ddot{\phi} \right) G_{5X} - 4H^2 X^2 \ddot{\phi} G_{5XX} \quad (2.30)$$

$$+ 4HX \left( \dot{X} - HX \right) G_{5\phi X} + 2 \left[ 2 \frac{d}{dt} (XH) + 3H^2 X \right] G_{5\phi} + 4HX\dot{\phi} G_{5\phi\phi}. \quad (2.31)$$

$\mathcal{E}_i$  and  $\mathcal{P}_i$  are presented in a way that they resemble the background energy density and isotropic pressure. The background value of the scalar field is given by an equation of motion of its own:

$$\frac{d}{dt} (a^3 J) = P_\phi, \quad (2.32)$$

with

$$J = \dot{\phi} K_X + 6HX G_{3X} - 2\dot{\phi} G_{3\phi} + 6H^2 \dot{\phi} (G_{4X} + 2X G_{4XX}) - 12HX G_{4\phi X} \quad (2.33)$$

$$+ 2H^3 X (3G_{5X} + 2X G_{5XX}) - 6H^2 \dot{\phi} (G_{5\phi} + X G_{5\phi X}), \quad (2.34)$$

$$\mathcal{P}_\phi = K_\phi - 2X \left( G_{3\phi\phi} + \ddot{\phi} G_{3\phi X} \right) + 6 \left( 2H^2 + \dot{H} \right) G_{4\phi} + 6H \left( \dot{X} + 2HX \right) G_{4\phi X} \quad (2.35)$$

$$- 6H^2 X G_{5\phi\phi} + 2H^3 X \dot{\phi} G_{5\phi X}. \quad (2.36)$$

$J$  is a shift charge density which is covariantly conserved whenever the action is invariant under constant shifts, e.g.,  $\phi \rightarrow \phi + \text{const.}$ . This transformation is called *shift symmetry* and it means that in the theory at hand the Horndeski  $G_i$  functions only depend on  $X$ , the kinetic term. In summary,  $J$  is a Noether current, and in shift symmetric theories  $\nabla^\mu J = 0$ .  $\mathcal{P}_\phi$  is the partial derivative w.r.t. to  $\phi$  of the pressure (2.26).

So far I have shown the equations of motion that govern the background dynamics in scalar-tensor theories of gravity. We still need, however, to discuss the dynamical evolution of the scalar field, which can lead to an accelerated expansion at late times. There are two types of solutions for the scalar field that will lead to a de-Sitter (or almost de-Sitter) phase at late-times:

- Scaling solutions [57]: trajectories in which the scalar field energy density tracks the one of the barotropic fluid (radiation or dust) that is dominant at the given era. In other terms:

$$\frac{\Omega_\phi}{\Omega_m} = \text{const.} \quad (2.37)$$

- Tracker solutions: trajectories that are insensitive to initial conditions that will eventually lead to a phase of late-time acceleration [58]. The name tracker refers to the feature that

the parameter of equation of state of the scalar field is almost constant during each phase of expansion, and it is always less or equal to the background equation of state, e.g., during radiation domination  $w_\phi \leq 1/3$  and during matter domination  $w_\phi < 0$ . Why these solutions are so attractive in the context of scalar-tensor theories? The answer is clear: they naturally solve the coincidence problem. That is, the coincidence problem poses the question of “why the Universe is expanding in an accelerated fashion *now*?”. Since many different initial conditions for the scalar field eventually evolve to the tracker solution, we are able to see that irrespective to these, we will eventually have the late-time accelerating phase without any effort.

Prior the development of quick and accurate Einstein-Boltzmann solvers in modified gravity, research in modified gravity heavily depended in performing a phase-space analysis of these theories to investigate under which values and conditions of the extra parameters of the models could describe the different stages of the evolution of the Universe, such as [59, 60]. With this, we were able to begin the discussion of parameter constraints in alternative theories of gravity, that eventually lead us to the point at we are now, where we perform Bayesian analysis inferences of the data extracted from different cosmological probes, and compare them with the models we have.

## 2.4. Linear Perturbation Theory

In the previous section we saw how the background cosmology is described and characterized in modified gravity theories. We are now in position to move our discussion to understand the inhomogeneities of our Universe using cosmological perturbation theory. Firstly we will consider only linear expansion, and, therefore, the analysis is restricted to regimes in which gravitational quantities are considerably smaller than unity.

As presented in Section 1.2, cosmological perturbation theory consists of perturbing the LHS and the RHS of Einstein’s Equation, i.e., perturbing gravity and matter. In modified gravity theories, the RHS of EE remain the same as in GR, that is, we can use all the formalism devised in Section 1.2 for these models as well. The LHS, however, contains extra terms, as seen by Horndeski’s action (2.18), and we will in the end have considerably more terms to perturb. I will first present the linear order equations of motion in the conformal Newtonian gauge metric:

$$ds^2 = a^2(t) [-(1 + 2\Psi)d\tau^2 + (1 - 2\Phi)d\mathbf{x}^2]. \quad (2.38)$$

They read:

- Einstein (0,0)

$$\begin{aligned} & k^2\Phi - \frac{1}{2}a^2H^2(-6 + 6\alpha_B + \alpha_K)\Psi - \frac{3}{2}aH(-2 + \alpha_B)\Phi' \\ & \left[ -\frac{k^2H}{a}\alpha_B - aH^3(3\alpha_B + \alpha_K) - 9aH\frac{\rho_m + p_m}{M_*^2} + 3HH'(-2 + \alpha_B) \right] \frac{1}{2}a^2V_X \\ & - \frac{1}{2}a^2H^2(3\alpha_B + \alpha_K)V_X' = -\frac{3a^2\delta\rho_m}{2M_*^2} \end{aligned} \quad (2.39)$$

- Einstein (0,i)

$$\begin{aligned}
& -\frac{1}{2}aH(-2+\alpha_B)\Psi + \Phi' - \left[ \frac{1}{2}a^2H^2\alpha_B + aH' + \frac{3a^2(\rho_m + p_m)}{2M_*^2} \right] V_X \\
& -\frac{1}{2}aH\alpha_B V_X' = -\frac{3a^2}{2M_*^2 k^2} (\rho_m + p_m) \theta_m
\end{aligned} \tag{2.40}$$

- Einstein (i,j) trace

$$(\alpha_T - \alpha_M) aH V_X - (1 + \alpha_T) \Phi + \Psi = \frac{9a^2}{2k^2 M_*^2} (\rho_m + p_m) \sigma_m \tag{2.41}$$

- Einstein (i,j) traceless

$$\begin{aligned}
& \Psi \left[ -\frac{1}{2}a^2(\alpha_B - 2)(\alpha_M + 3)H^2 - \frac{3a^2(\rho_m + p_m)}{2} - \frac{1}{2}a((\alpha_B - 2)H' + H\alpha_B') \right] \\
& -\frac{1}{2}a^2\alpha_B H V_X'' + V_X' \left[ -\frac{1}{2}a^3\alpha_B H^2 - \frac{1}{2}a^2\alpha_B(\alpha_M + 3)H^2 - \frac{(\rho_m + p_m)}{2M_*^2} - \frac{1}{2}a\alpha_B H' \right. \\
& \left. - aH' - \frac{aH\alpha_B'}{2} \right] + V_X \left[ -\frac{1}{2}a^4\alpha_B H^3 - \frac{1}{2}a^3\alpha_B(\alpha_M + 3)H^3 - \frac{1}{2}a^2H^2\alpha_B' \right. \\
& \left. - \frac{a^3H(\alpha_B M_*^2 H' + 3\alpha_M p_m + 3(\rho_m + p_m))}{2M_*^2} - a^2H'' - \frac{1}{2}a^2H(\alpha_B + 2\alpha_M + 8)H' \right. \\
& \left. + \frac{3a^2\alpha_M H p_m}{2M_*^2} - \frac{9a^2 p_m'}{2M_*^2} + a^3 H H' \right] + aH\Psi' \left( 1 - \frac{\alpha_B}{2} \right) \\
& + aH\Phi'(\alpha_M + 2) + \Phi'' = \frac{3a^2\delta p_m}{M_*^2}
\end{aligned} \tag{2.42}$$

Since Einstein-Boltzmann codes are implemented using the Synchronous gauge, whose line element reads:

$$ds^2 = a^2 \left[ -d\tau^2 + \left( \delta_{ij} + \tilde{h}_{ij} \right) dx^i dx^j \right], \tag{2.43}$$

with

$$\tilde{h}_{ij}(\tau, \mathbf{k}) = \hat{k}_i \hat{k}_j h + 6 \left( \hat{k}_i \hat{k}_j - \frac{1}{3} \delta_{ij} \right) \eta + h_{ij}, \tag{2.44}$$

let's write the same equations in this gauge as well:

- Einstein (0,0)

$$\begin{aligned}
h' &= \frac{4k^2\eta}{aH(2-\alpha_B)} + \frac{6a\delta\rho_m}{HM_*^2(2-\alpha_B)} - 2aH \left( \frac{\alpha_K + 3\alpha_B}{2-\alpha_B} \right) V_X' \\
& - 2 \left[ 3aH' + \left( \frac{\alpha_K + 3\alpha_B}{2-\alpha_B} \right) a^2H^2 + \frac{9a^2}{M_*^2} \left( \frac{\rho_m + p_m}{2-\alpha_B} \right) + \frac{\alpha_B k^2}{2-\alpha_B} \right] V_X.
\end{aligned} \tag{2.45}$$

- Einstein (0,i)

$$\eta' = \frac{3a^2\theta_m}{2k^2M_*^2} + \frac{aH}{2}\alpha_B V_X' + \left[ aH' + \frac{a^2H^2}{2}\alpha_B + \frac{3a^2}{2M_*^2}(\rho_m + p_m) \right] V_X. \tag{2.46}$$

- Einstein (i,j) trace

$$Dh'' = 2\lambda_1 k^2 \eta + 2aH\lambda_3 h' - \frac{9a^2 \alpha_K \delta p_m}{M_*^2} + 3a^2 H^2 \lambda_4 V_X' + 2a^3 H^3 \left[ 3\lambda_6 + \frac{\lambda_5 k^2}{a^2 H^2} \right] V_X. \quad (2.47)$$

- Einstein (i,j) traceless

$$\xi' = (1 + \alpha_T) \eta - aH(2 + \alpha_M) \xi + aH(\alpha_M - \alpha_T) V_X - \frac{9a^2 \sigma_m}{2M_*^2 k^2}, \quad (2.48)$$

- Scalar field

$$D(2 - \alpha_B) V_X'' + 8aH\lambda_7 V_X' + 2a^2 H^2 \left[ \frac{c_{\text{sN}}^2 k^2}{a^2 H^2} - 4\lambda_8 \right] V_X = \frac{2c_{\text{sN}}^2}{aH} k^2 \eta + \frac{3a}{2HM_*^2} [2\lambda_2 \delta \rho_m - 3\alpha_B (2 - \alpha_B) \delta p_m], \quad (2.49)$$

where  $H$  is the physical-time Hubble factor, related to the conformal one by  $\mathcal{H} = aH$ ,  $V_X$  is the scalar field perturbation in conformal time:

$$V_X = a \frac{\delta \phi}{\phi'}, \quad (2.50)$$

and  $\xi = (h' + 6\eta')/2k^2$ . The time-dependent functions  $\alpha_M$ ,  $\alpha_B$ ,  $\alpha_T$  and  $\alpha_K$  were first introduced in [61], and they capture *all* the freedom we have in Horndeski theories at the linear level. They are independent from each other, and have different physical meanings:

- $\alpha_M$ : This function is the time variation of the Planck mass  $M_*^2$ , which in certain Horndeski theories can be time-dependent. It can be seen as the rate in which the cosmological strength of gravity is evolving.
- $\alpha_B$ : *Braiding*, it describes the different couplings between the scalar field and the metric tensor. Whenever this term is non-zero dark energy can *cluster*, therefore, if this term is found to be different than zero, we have a clear evidence that dark energy is evolving in time, and its perturbations are allowed to cluster.
- $\alpha_K$ : *Kineticity*, this function captures the evolution of the kinetic energy of the scalar field fluctuations. It is only relevant at scales near the cosmological horizon, and therefore, are hard to be constrained by available LSS surveys.
- $\alpha_T$ : *Tensor excess*, in certain Horndeski theories the speed in which gravitational waves propagate,  $C_T$  in these theories may be different than that of light,  $c$ . This function captures precisely the amount in which the two differ:  $c_T^2 = c^2(1 + \alpha_T)$ . After the detection of gravitational waves followed by a gamma-ray burst from the coalescence of two neutron stars, this function has been severely constrained to  $|\alpha_T| < 10^{-15}$ . However, the frequency in which LIGO/VIRGO detectors operate is considerably close to the frequency in which scalar-tensor theories “break”. That is, modified gravity theories in which the scalar field is supposed to describe dark energy can be seen only as effective theories, where in a given frequency cut the theory would lose predictive power, and would need to be further supplemented by an appropriate UV completion [62].

The definition of these functions in terms of the Horndeski  $G_i$ 's is as follows:

$$M_*^2 \equiv 2 \left( G_4 - 2XG_{4X} - \frac{H\phi'XG_{5X}}{a} + XG_{5\phi} \right) \quad (2.51)$$

$$\alpha_M \equiv \frac{d \ln M_*^2}{d \ln a} \quad (2.52)$$

$$\begin{aligned} H^2 M_*^2 \alpha_K &\equiv 2X (G_{2X} + 2XG_{2XX} - 2G_{3\phi} - 2XG_{3\phi X}) \\ &\quad + \frac{12H\phi'X}{a} (G_{3X} + XG_{3XX} - 3G_{4\phi X} - 2XG_{4\phi XX}) \\ &\quad + 12H^2 X [G_{4X} - G_{5\phi} + X(8G_{4XX} - 5G_{5\phi X}) + 2X^2(2G_{4XXX} - G_{5\phi XX})] \\ &\quad + \frac{4H^3\phi'X}{a} (3G_{5X} + 7XG_{5XX} + 2X^2G_{5XXX}) \end{aligned} \quad (2.53)$$

$$\begin{aligned} HM_*^2 \alpha_B &\equiv \frac{2\phi'}{a} (XG_{3X} - G_{4\phi} - 2XG_{4\phi X}) + 8HX (G_{4X} + 2XG_{4XX} - G_{5\phi} - XG_{5\phi X}) \\ &\quad + \frac{2H^2\phi'X}{a} (3G_{5X} + 2XG_{5XX}) \end{aligned} \quad (2.54)$$

$$M_*^2 \alpha_T \equiv 4X (G_{4X} - G_{5\phi}) - \frac{2}{a^2} (\phi'' - 2aH\phi') XG_{5X}. \quad (2.55)$$

And the  $\lambda_i$  functions that also appear in the perturbed equations of motion are:

$$D = \alpha_K + \frac{3}{2}\alpha_B^2 \quad (2.56)$$

$$\lambda_1 = \alpha_K (1 + \alpha_T) - 3\alpha_B (\alpha_M - \alpha_T) \quad (2.57)$$

$$\lambda_2 = -\frac{3(\rho_m + p_m)}{H^2 M_*^2} - (2 - \alpha_B) \frac{H'}{aH^2} + \frac{\alpha'_B}{aH} \quad (2.58)$$

$$\lambda_3 = -\frac{1}{2} (2 + \alpha_M) D - \frac{3}{4}\alpha_B \lambda_2 \quad (2.59)$$

$$\lambda_4 = \alpha_K \lambda_2 - \frac{2\alpha_K \alpha'_B - \alpha_B \alpha'_K}{aH} \quad (2.60)$$

$$\lambda_5 = \frac{3}{2}\alpha_B^2 (1 + \alpha_T) + (D + 3\alpha_B) (\alpha_M - \alpha_T) + \frac{3}{2}\alpha_B \lambda_2 \quad (2.61)$$

$$\lambda_6 = \left( 1 - \frac{3\alpha_B H'}{\alpha_K a H^2} \right) \frac{\alpha_K \lambda_2}{2} - \frac{DH'}{aH^2} \left[ 2 + \alpha_M + \frac{H''}{aHH'} \right] - \frac{2\alpha_K \alpha'_B - \alpha_B \alpha'_K}{2aH} - \frac{3\alpha_K p'_m}{2aH^3 M_*^2} \quad (2.62)$$

$$\lambda_7 = \frac{D}{8} (2 - \alpha_B) \left[ 4 + \alpha_M + \frac{2H'}{aH^2} + \frac{D'}{aHD} \right] + \frac{D}{8} \lambda_2 \quad (2.63)$$

$$\begin{aligned} \lambda_8 &= -\frac{\lambda_2}{8} \left( D - 3\lambda_2 + \frac{3\alpha'_B}{aH} \right) + \frac{1}{8} (2 - \alpha_B) \left[ (3\lambda_2 - D) \frac{H'}{aH^2} - \frac{9\alpha_B p'_m}{2aH^3 M_*^2} \right] \\ &\quad - \frac{D}{8} (2 - \alpha_B) \left[ 4 + \alpha_M + \frac{2H'}{aH^2} + \frac{D'}{aHD} \right] \end{aligned} \quad (2.64)$$

$$c_{sN}^2 = \lambda_2 + \frac{1}{2} (2 - \alpha_B) [\alpha_B (1 + \alpha_T) + 2(\alpha_M - \alpha_T)], \quad (2.65)$$

where  $c_{sN}^2$  is the numerator of the sound speed squared of the scalar field

$$c_s^2 = \frac{c_{sN}^2}{D} \quad (2.66)$$

$$= \frac{1}{\alpha_K + \frac{3}{2}\alpha_B^2} \left[ (2 - \alpha_B) \left( -\frac{H'}{aH^2} + \frac{1}{2}\alpha_B (1 + \alpha_T) + \alpha_M - \alpha_T \right) - \frac{3(\rho_m + p_m)}{H^2 M_*^2} + \frac{\alpha'_B}{aH} \right]. \quad (2.67)$$

Horndeski theories are also plagued by different kinds of instabilities. These instabilities are such that the wrong choice of parameters for the  $\alpha_i$  functions will lead to exponentially unstable perturbations. The most important instabilities are:

- i) *Ghost instabilities*: wrong choice for the kinetic energy term, resulting in negative energy modes and a non-unitary evolution, rendering the whole theory incomplete.
- ii) *Gradient instabilities*: occurs when  $c_s^2 < 0$ . This will lead to an exponential instability that grows with a rate that is related to the shortest scale mode. These instabilities can remain unseen until this mode is effectively considered in the theory, thus, a seemingly stable linear perturbation theory in a given range may seem healthy, while the whole theory is unhealthy when looked at all scales (or via the inclusion of higher-order interactions).
- iii) *Tachyonic instabilities*: happens when the square of the mass of the perturbations is negative. This leads to a power law instability at large scales (modes outside the horizon), that once are inside the horizon they become under control. Since modes outside the horizon are hard to probe, this instability has long been not thoroughly studied, until recent [63].

In summary, to make it simple for the reader to remember/understand where these instabilities is affecting is worth pointing out that: (i) is a instability linked directly to the action of the theory, (ii) resembles an UV instability as it becomes apparent only when we consider large wave-numbers, and (iii) is an IR instability, where only small wave-numbers. Therefore, before running the complete analysis using cosmological data from different surveys, one needs to check which are the stable regions of which a given parameterization or model.

In the Effective Field Theory approach to Dark Energy [64, 65] one needs to further supplement these four time-dependent equations with an expansion history,  $H(z)$ .

I have chosen to exhibit the linear equations in the Newtonian and Synchronous gauges adopting CLASS internal units and conventions, e.g.:

$$\rho_{\text{CLASS}} = \frac{8\pi G_{\text{N}}}{3} \rho_{\text{std.}}, \quad (2.68)$$

$$c = 1, \quad (2.69)$$

where  $\rho_{\text{std.}}$  is the standard physical energy density of a given quantity, and  $c$  is the speed of light. This choice ensures that the internal dimensionful quantities have units of  $\text{Mpc}^{-1}$ , therefore, the Hubble factor  $H$  has units of  $\text{Mpc}^{-1}$ , and distances  $\text{Mpc}$ . This is just a redefinition that will make it easier to present the results found in this thesis when linear perturbation theory is used. Unless otherwise stated, this choice of conventions will be the default one. We can do the same to the background equations of motion, and set them to CLASS internal units:

$$H^2 = \frac{8\pi G}{3} \left( \sum_i \rho_i + \rho_{\text{DE}} \right) \quad (2.70)$$

$$H' = -4\pi G a \left[ \sum_i (\rho_i + p_i) + \rho_{\text{DE}} + p_{\text{DE}} \right] \quad (2.71)$$

where

$$\frac{8\pi G}{3}\rho_{\text{DE}} \equiv -\frac{1}{3}G_2 + \frac{2}{3}X(G_{2X} - G_{3\phi}) - \frac{2H^3\phi'X}{3a}(7G_{5X} + 4XG_{5XX}) + H^2\left[1 - (1 - \alpha_B)M_*^2 - 4X(G_{4X} - G_{5\phi}) - 4X^2(2G_{4XX} - G_{5\phi X})\right] \quad (2.72)$$

$$\begin{aligned} \frac{8\pi G}{3}p_{\text{DE}} \equiv & \frac{1}{3}G_2 - \frac{2}{3}X(G_{3\phi} - 2G_{4\phi\phi}) + \frac{4H\phi'}{3a}(G_{4\phi} - 2XG_{4\phi X} + XG_{5\phi\phi}) \\ & - \frac{(\phi'' - aH\phi')}{3\phi'a}HM_*^2\alpha_B - \frac{4}{3}H^2X^2G_{5\phi X} - \left(H^2 + \frac{2H'}{3a}\right)(1 - M_*^2) \\ & + \frac{2H^3\phi'XG_{5X}}{3a}, \end{aligned} \quad (2.73)$$

with the dark energy background fluid quantities given by:

$$\rho'_{\text{DE}} = -3\mathcal{H}(\rho_{\text{DE}} + p_{\text{DE}}), \quad (2.74)$$

$$w_{\text{DE}} = \frac{p_{\text{DE}}}{\rho_{\text{DE}}}. \quad (2.75)$$

Solving these equations is a necessary task in the current stage of precision cosmology. Therefore, standard Einstein-Boltzmann solvers have been devised in order to solve the modified gravity and matter equations of motion. One of these codes is the Horndeski in CLASS, `hi_class` [66, 67], code. I will now give a brief description of the code.

The code builds upon the success of the CLASS code, whose source code is written in C and numerical routines are implemented using C++ libraries. The background equations of motion are solved using standard fourth order Runge-Kutta (RK4) methods, while the perturbation module may be solved using RK4 or a stiff equation solver called `ndf5`. The initial conditions for the perturbations are given deep inside radiation domination era, and may be chosen from the usual initial conditions set by inflation at super-horizon scales: adiabatic, isocurvature, etc. The majority of modified gravity models that attempt to explain the late-time acceleration of the Universe, are late dark energy models, i.e., they are built in a way that modified gravity will only be relevant and non-negligible after matter domination era. Due to this, cosmological observables are insensitive to the initial condition of the scalar field perturbation,  $V_X$ . However, we know that by choosing them properly we may avoid exploring the extra parameter space introduced by the scalar field in MCMC analysis, thus, reducing the computational time performing this task. Nevertheless, there are also Early Modified Gravity models in the literature [68, 69, 70, 71, 72], that modify the energy budget of the Universe in an era pre-recombination, therefore, during radiation domination, and are also able to explain the late-time acceleration of our Universe. These models have been severely constrained after Planck 2015 data release, but in light of the Hubble Tension, we have seen a surge of works on them. In these models the scalar field energy density would exhibit a spike right before recombination, thus decreasing the value of the sound horizon at decoupling  $r_*$ . When dealing with models such as these, the initial conditions for the scalar field perturbations will therefore heavily impact the CMB observables. The proper initial condition for the Horndeski scalar field is described in [67], and I refer the reader to it.

Alternatively to the field description, we can instead use the approach called Effective Fluid for the dark energy field. Since in Horndeski's theories the Bianchi Identities hold, and the Energy Momentum tensor of matter species is conserved, we may move the extra Horndeski terms in Equations (2.45-2.49) to the RHS subtracting the contributions of the Einstein Tensor. The equations then assume the following form:

- Einstein (0,0)

$$k^2\eta - \frac{1}{2}\mathcal{H}h' = 4\pi G_{\text{N}}a^2 \sum_{\alpha} \delta\rho_{\alpha}^{\text{S}} \quad (2.76)$$

- Einstein (0,i)

$$k^2\eta = 4\pi G_{\text{N}}a^2 \sum_{\alpha} (\rho_{\alpha} + p_{\alpha}) \theta_{\alpha}^{\text{S}} \quad (2.77)$$

- Einstein (i,j) trace

$$h'' + 2\mathcal{H}h' - 2k^2\eta = 8\pi G_{\text{N}}a^2 \sum_{\alpha} \delta p_{\alpha}^{\text{S}} \quad (2.78)$$

- Einstein (i,j) traceless

$$h'' + 6\eta'' + 2\mathcal{H}(h' + 6\eta') - 2k^2\eta = -24\pi G_{\text{N}}a^2 \sum_{\alpha} (\rho_{\alpha} + p_{\alpha}) \sigma_{\alpha}^{\text{S}}. \quad (2.79)$$

The dummy index  $\alpha$  runs over all species, dark energy included. We define each dark energy effective fluid quantity as follows:

- Density perturbation:

$$\begin{aligned} \delta\rho_{\text{DE}}^{\text{S}} &= \delta\rho_{\text{m}} \left( -1 - \frac{2}{(\alpha_{\text{B}} - 2)M_*^2} \right) - \frac{2\alpha_{\text{B}}}{3a^2(\alpha_{\text{B}} - 2)} k^2\eta \\ &+ \frac{2HV_X}{3aM_*^2(\alpha_{\text{B}} - 2)} \left[ a^2 \left( H^2 M_*^2 (3\alpha_{\text{B}} + \alpha_{\text{K}}) + 9(p_{\text{m}} + \rho_{\text{m}}) \right) \right. \\ &\left. - 3a(\alpha_{\text{B}} - 2)M_*^2 H' + \alpha_{\text{B}} k^2 M_*^2 \right] + \frac{3\alpha_{\text{B}} + \alpha_{\text{K}}}{\alpha_{\text{B}} - 2} \frac{2H^2 V_X'}{3}. \end{aligned} \quad (2.80)$$

- Velocity divergence:

$$\begin{aligned} (\rho_{\text{DE}} + p_{\text{DE}}) \theta_{\text{DE}}^{\text{S}} &= \left[ \frac{2k^2 H'}{3a} + \frac{1}{3} \alpha_{\text{B}} H^2 k^2 + \frac{k^2(p_{\text{m}} + \rho_{\text{m}})}{M_*^2} \right] V_X \\ &+ \frac{\alpha_{\text{B}} H k^2}{3a} V_X' + \theta_{\text{m}} \left( \frac{1}{M_*^2} - 1 \right). \end{aligned} \quad (2.81)$$

- Pressure perturbation:

$$\begin{aligned} \delta p_{\text{DE}}^{\text{S}} &= \delta p_{\text{m}} \left( \frac{\alpha_{\text{K}}}{DM_*^2} - 1 \right) - \frac{2\eta k^2 (\lambda_1 - D)}{9a^2 D} \\ &- \frac{2V_X (3a^2 H^3 \lambda_6 + H k^2 \lambda_5)}{9aD} - \frac{2H(D + \lambda_3)h'}{9aD} - \frac{H^2 \lambda_4 V_X'}{3D}. \end{aligned} \quad (2.82)$$

- Anisotropic stress:

$$\begin{aligned} (\rho_{\text{DE}} + p_{\text{DE}}) \sigma_{\text{DE}} &= \frac{\alpha_{\text{M}} H}{9a} (6\eta' + h') - \frac{2k^2 \alpha_{\text{T}}}{9a^2} \eta + \frac{2Hk^2(\alpha_{\text{T}} - \alpha_{\text{M}})}{9a} V_X \\ &- \sigma_{\text{m}} \left( 1 - \frac{1}{M_*^2} \right). \end{aligned} \quad (2.83)$$

The equations (2.45-2.49) describe the linear evolution of modified gravity in a cosmological scenario. From the evolution of the matter density contrast,  $\delta_m$ , the linear metric potentials and the scalar field fluctuations  $V_X$ , we can test the impact of modified gravity has on the different cosmological observables. The Large Scale Structure of our Universe is probed by different types of cosmology surveys, such as, spectroscopic galaxy surveys, photometric galaxy surveys, 21cm intensity mapping, and others. I will focus on the first two surveys of this list.

## Linear tests of modified gravity

*In this chapter I discuss the impact modified gravity has on cosmological observables, the results of this chapter have been published in [73]. I start by discussing the modifications Horndeski theories introduce in the growth and light propagation equations of motion. I then move to discuss how a particular theory, called No Slip Gravity, impacts the structure formation of our Universe at linear order. I finish this chapter by discussing how early modified gravity theories impact the matter power spectrum at large and small scales.*

### 3.1. Growth and light propagation in Horndeski gravity

The scales in which LSS surveys up until now have probed lie deep within the cosmological horizon, i.e., on scales even bigger than the scale of radiation and matter equality,  $k_{\text{eq}} \sim 10^{-2} \text{ Mpc}^{-1}$ . Inside this regime, the timescale of the scalar field evolution is much smaller than the Hubble rate, i.e., wave-numbers where  $k \gg aH$ . This statement is called the Quasi-Static Approximation, and even though the name suggests that is only an approximation, we have results in the literature [74, 75, 76], that show that the agreement between the full solution of the scalar field fluctuation, and the QSA one inside the horizon agree to below at the level of 0.01%. The QSA limit can be taken in a specific gauge, by disregarding certain time derivatives of the metric potentials and the first and second time derivatives of the scalar field fluctuation. In the Newtonian gauge, Equations (2.39-2.41), we can then maintain only the terms proportional to  $k^2$  and sourced by the matter density perturbations  $\delta\rho_{\text{m}}$ . However, in the Synchronous gauge the procedure is as follows:

- We neglect the following terms in the Einstein and scalar field equations:  $\eta'$ ,  $\eta''$ ,  $V'_X$ ,  $V''_X$ ,  $\delta p_{\text{m}}$ ,  $\sigma_{\text{m}}$ .
- We then have algebraic relations between the perturbations in the matter density,  $\delta\rho_{\text{m}}$ , and the remaining metric potentials and scalar field fluctuation.
- We next substitute these relations into Equations (2.80-2.83).

By doing so one can separate  $\delta\rho_{\text{DE}}$  into two parts:

$$\delta\rho_{\text{DE}} = \delta\rho_{\text{DE}}^{\text{QSA}} + \delta\rho_{\text{DE, rel.}}, \quad (3.1)$$

where  $\delta\rho_{\text{DE}}^{\text{QSA}}$  is the QSA contribution to the dark energy density perturbation, and  $\delta\rho_{\text{DE, rel.}}$  encapsulates all the other terms that are not proportional to matter density perturbations. The

same procedure must also be performed for  $\sigma_{DE}$ , as this quantity captures the amount in which the Poisson gauge potentials differ from each other (in GR they are the same). Thus, we separate the anisotropic stress as:

$$\sigma_{DE} = \sigma_{DE}^{\text{QSA}} + \sigma_{DE, \text{rel.}}, \quad (3.2)$$

where the quantities with the superscript QSA refer to the QSA contribution. Following the scheme outlined above, we find:

$$\delta\rho_{DE}^{\text{QSA}} = \left( \frac{\alpha_B \lambda_2 - c_{sN}^2 [2 + M_*^2 (\alpha_B - 2)]}{c_{sN}^2 M_*^2 (\alpha_B - 2)} \right) \delta\rho_m, \quad (3.3)$$

$$(\rho_{DE} + p_{DE}) \sigma_{DE}^{\text{QSA}} = \left( \frac{\alpha_M [\alpha_B + 2\alpha_M + \alpha_T (\alpha_B - 2)] + \alpha_T \lambda_2}{3c_{sN}^2 M_*^2} \right) \delta\rho_m. \quad (3.4)$$

Figure 3.1 shows the behavior of the full dark energy density perturbations and anisotropic stress at  $z = 0$ , and their QSA counterparts. We can see that the full perturbations and the QSA contribution overlap when we move to larger  $k$  values, as expected.

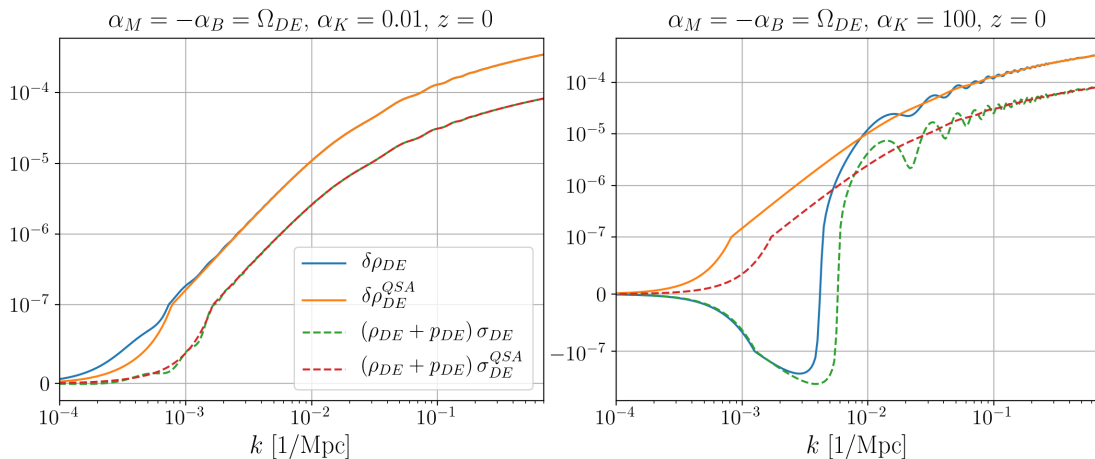


**Figure 3.1.** Comparison of the full dark energy density perturbation (solid lines) and anisotropic stress (dashed lines), and their QSA counterparts, as a function of scale at a fixed redshift,  $z = 0$ . On the left plot we show the evolution for a small kineticity value,  $c_K = 0.01$ , and on the right a larger value,  $c_K = 100$ . For  $c_K = 0.01$ , the full and QSA contributions overlap at smaller values of  $k$ , while for  $c_K = 100$  this happens only at large values of  $k$ . This is due to the sound speed of the scalar field, which is larger for  $c_K = 0.01$  than it is for  $c_K = 100$ , which pushes the QSA regime of validity to smaller scales.

This Quasi-Static Approximation is very important in the context of phenomenological tests of modified gravity usually performed by collaborations in surveys. Early proposals to investigate the effect modified gravity has on the growth of structure and propagation of light consisted in investigating the equations which relates the two Newtonian gauge metric potentials, Equation (2.38), and the matter and anisotropic stress perturbations:

$$k^2 \Phi = -\frac{3}{2} a^2 G_\Phi(k, a) \delta\rho_m, \quad (3.5)$$

$$\frac{\Phi}{\Psi} = \gamma(k, a). \quad (3.6)$$

In GR  $\Phi = \Psi$  at late times since neutrinos and radiation contribute very weakly during matter and dark energy domination. However, in ST theories the two can be different, and this is

modelled by the so-called gravitational slip function  $\gamma(k, a)$ .  $G_\Phi$  is the gravitational coupling between  $\Phi$  and matter, however,  $\Phi$  is the spatial curvature metric potential, which is then not directly observable. Due to this, what is commonly done, is to model the growth of structure via  $\Psi$ , the time-time component of the linearly perturbed Newtonian metric:

$$k^2\Psi = -\frac{3a^2G_\Psi(k, a)\delta\rho_m}{2}. \quad (3.7)$$

Historically  $G_\Psi$  is defined by the Greek letter  $\mu$ , but I chose to use  $G_\Psi$  and  $G_\Phi$  instead. It is also known that gravitational lensing is sensible to the sum of both potentials,  $\Psi + \Phi$ , also called Weyl or Lensing Potential, and therefore we can also write:

$$k^2(\Phi + \Psi) = -\frac{3a^2G_{\Phi+\Psi}(k, a)\delta\rho_m}{2}, \quad (3.8)$$

where  $G_{\Phi+\Psi}$  is historically given by the Greek letter  $\Sigma$ . There are many different notations in the literature for these parametric functions, but they all stem from the same physical consideration of parametrizing the modified gravity freedom at the level of the equations of motion, and within the QSA limit. The scale-dependence of these functions is also modelled phenomenologically, and they follow the same explicit dependence and reasoning of the case of  $f(R)$  gravity described by [77, 78]:

$$G_\Psi = \frac{1 + \beta_1\lambda_1^2k^2a^s}{1 + \lambda_1^2k^2a^s}, \quad (3.9)$$

$$\gamma = \frac{1 + \beta_2\lambda_2^2k^2a^s}{1 + \lambda_2^2k^2a^s}, \quad (3.10)$$

where  $\lambda_{1,2}$  have dimensions of length squared,  $\beta_{1,2}$  are dimensionless parameters and  $s$  is a constant. These parameters were first introduced by [79], and they capture the transitions in time and scale of  $f(R)$  gravity and some scalar-tensor theories. At early times modified gravity theories restore to general relativity, then they're equal to one. These theories transition to different values at small scales like a Yukawa potential, in a way that we recover GR values at small scales. The connection between Equations (3.9) and (3.10) and (2.52-2.55) is given in [80]. This description, however, lacks a more fundamental view, as it is merely promoting the gravitational couplings between metric potentials and matter quantities to time and scale dependent functions. Nevertheless, they still act as an agnostic and model-independent (but parametrization-dependent) test of gravity. For this reason, the approach given by the EFT of DE has also gained significant attention in the literature in the past years, since it has the ability of connecting Lagrangian terms to cosmological observables. For this reason I will show the time-independent (taking the  $k \rightarrow \infty$  limit) expressions for the different gravitational couplings and gravitational slip in Horndeski theories:

$$G_\Phi = 1 + \frac{\alpha_B^2(1 + \alpha_T) + 2\alpha_B(\alpha_M - \alpha_T)}{2c_{sN}^2}, \quad (3.11)$$

$$\bar{\eta} = \frac{\Psi}{\Psi + \Phi} = 1 + \frac{2(\beta - c_s^2)(\alpha_M - \alpha_T) + \beta\alpha_B\alpha_T}{2(\beta - c_s^2)(\alpha_M - \alpha_T) + \beta(2\alpha_B + \alpha_B\alpha_T)} \quad (3.12)$$

where  $\bar{\eta}$  is a non-standard definition of the slip to reflect the fact that projected measurement errors from Euclid are minimised for this combination, it is related to the usual slip via:

$$\gamma = \frac{\bar{\eta}}{2 - \bar{\eta}}, \quad (3.13)$$

and

$$\beta = c_s^2 - w_m + \frac{\alpha_B^2(1 + \alpha_T + 3w_m) + 2(\alpha_M - \alpha_T)\alpha_B}{2D}. \quad (3.14)$$

As the QSA is typically performed during matter domination in the above expressions we can take  $w_m \rightarrow 0$ . As has been suggested many times in the literature [81, 82], the gravitational slip can be seen as a smoking gun test for the presence of modified gravity, as any detection of  $\gamma \neq 1$  can only be due to the presence of modified gravity – or an imperfect dark energy model ( $\sigma_{DE} \neq 0$ ) [83, 84].

### 3.2. Structure formation in No Slip gravity

There is a class of Horndeski theories in which we restore the GR value for the gravitational slip,  $\gamma = 1$ , while it still modifies the growth of structure and light propagation. These theories are called No Slip Gravity, first presented in [85] with a more careful study of the stability conditions, structure formation and light propagation was carried out in [73]. In Figure 3.2 I show the ratio  $\Phi/\Psi$  for two different models, No Slip (left) and JBD-like (right), as a function of scale at 3 different redshifts. For No Slip it's clear that at scales inside the dark energy sound horizon the ratio goes to 1, while for the JBD-like case it does not.

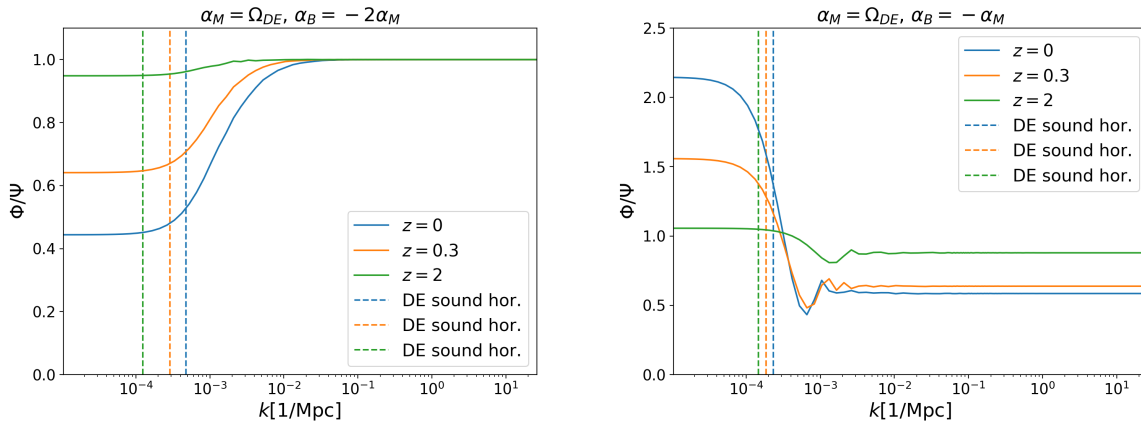


**Figure 3.2.** Ratio between the two Newtonian potentials,  $\Phi$  and  $\Psi$  as a function of scale, for two different models of gravity: No Slip gravity (left) and JBD-like parametrization (right). The different colors of the solid lines represent three different redshifts,  $z = 0$  (solid blue),  $z = 0.3$  (solid orange) and  $z = 2$  (solid green). The vertical dashed lines represent the dark energy sound horizon scale. We can see that for No Slip gravity, when the perturbations are inside the horizon they the ratio between the potentials is the same as in GR, 1, while for a different gravity model this is not the case.

We can see that if we set  $\alpha_T = 0$ , and  $\alpha_B = -2\alpha_M$ , Equation (3.12) becomes 1, while  $G_\Phi$ , as well as  $G_\Psi$ , is different than unity:

$$G_{\text{eff}} = G_\Psi = G_{\Psi+\Phi} = \frac{1}{M_*^2}, \quad (3.15)$$

that is, they become inversely proportional to the time-dependent Planck mass.

In order to construct observables and analyze the theory within the framework on the EFT of DE, we need to first choose a parameterization for the  $\alpha$  functions (2.52-2.55). The two most

used parametrizations in the literature simply set these functions as being proportional to the scale factor or the fractional energy density of dark energy:

$$\alpha_i = c_i a, \quad (3.16)$$

$$\alpha_i = c_i \Omega_{\text{DE}}, \quad (3.17)$$

respectively. Although simple and easy to get analytical expressions for the many different time-dependent functions built from the  $\alpha_i$ 's, these two parametrization are known to not describe correctly modifications of gravity. For example, the latter parametrization, has two different regimes in time that differ by a lot from what one would expect from a modified theory of gravity. At early times, the parametric functions are negligible, as they are proportional to the dark energy density, which in turn depends on the evolution of the background cosmology, and for the majority of modified theories of gravity describing dark energy,  $\Omega_{\text{DE}}$  is small at early times, and is only relevant at late-times. Therefore, we run in different problems when using these parametrizations to fit the CMB data. An even bigger problem is with respect to the kineticity function,  $\alpha_K$ , which capture the kinetic energy density of the scalar field. If this function is too small, it would lead to unphysical behaviors, such as a strong-coupling problem, which in turn leads the whole physical theory to fail theoretically. With respect to the  $\alpha_i$ 's being proportional to the scale factor, another problem emerges, as we know that the scale factor assume values between the range  $[0, 1]$ , at late times these functions can assume order unity values, and therefore over-predict the modification of gravity introduced at the linear level. These problems are thoroughly analyzed and discussed in reference [86].

To bypass this problem, and carefully investigate this theory, in the original paper of the No Slip Gravity the author introduces a parametrization which respects the behavior one would expect at early-times, that is, recovering GR, while not keeping the functions too small, and then transitioning to a more physical behavior at late times:

$$\alpha_M = \mu \left( 1 - \tanh^2 \left[ \left( \frac{\tau}{2} \right) \ln \left( \frac{a}{a_t} \right) \right] \right) = \frac{4A (a/a_t)^\tau}{[(a/a_t)^\tau + 1]}, \quad (3.18)$$

where  $a_t$  and  $\mu$  are parameters. For No Slip Gravity the condition  $c_s^2 > 0$ , Equation (2.66), takes the simple form:

$$\frac{1}{H} \frac{d(\alpha_M H)}{d \ln a} \leq \frac{3}{2} \Omega_{\text{DE}}(a) [1 + w(a)] + \frac{3}{2} \left( \Omega_m(a) - \tilde{\Omega}_m(a), \right) \quad (3.19)$$

where  $\tilde{\Omega}_m = \rho_m / 3H^2 M_*^2$ . Figure 3.3 shows the behavior of this parametrization for different values of the parameters. When we allow the background to have an expansion history different than  $\Lambda$ CDM. For the case of a dynamical dark energy assuming the form of  $w_0 - w_a$ ,  $\alpha_M$  may assume negative values in its evolution, and the parametrization given by (3.18) will not be able to correctly capture the allowed freedom present in No Slip gravity. For this case, one can still have a similar form for the running of the Planck mass, but that can now go to negative values. This form is given by:

$$\alpha_M(a) = c_M \frac{\tanh [(\tau/2) \ln(a/a_t)]}{\cosh^2 [(\tau/2) \ln(a/a_t)]} \quad (3.20)$$

$$= \frac{4c_M (a/a_t)^\tau [-1 + (a/a_t)^\tau]}{[1 + (a/a_t)^\tau]^3}. \quad (3.21)$$

Figure 3.4 shows the behavior of this parametrization for different values of the parameters. Changing  $a_t$  affects the moment where  $\alpha_M$  crosses zero, i.e. the transition time between the hill

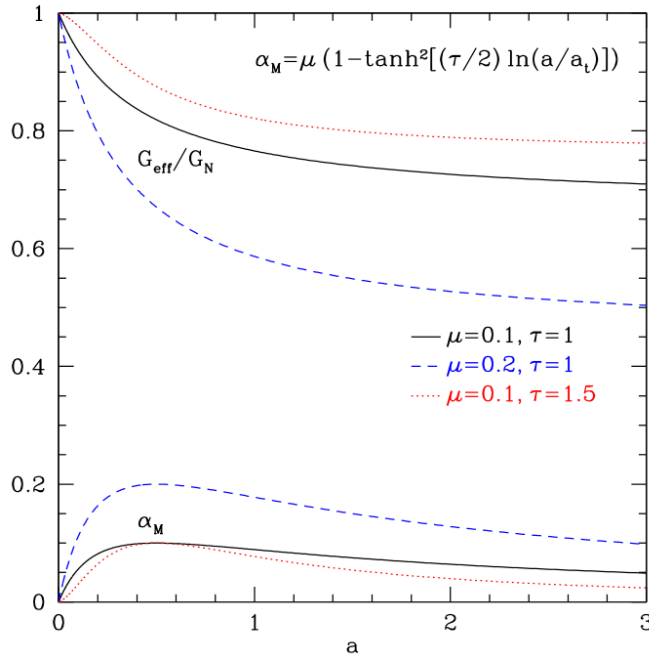


**Figure 3.3.** Evolution of the  $G_{\text{eff}} = G_{\Phi} = G_{\Psi+\Phi}$  as a function of the scale factor in No Slip gravity, Equation (3.15), and the running of the Planck Mass,  $\alpha_{\text{M}}$ , for No Slip gravity with a parametrization given by Equation (3.18). Plot taken from [85].

and valley. Increasing  $\tau$  steepens the transition, moving the minimum and maximum values of  $\alpha_{\text{M}}$  closer to the zero crossing. The amplitude of  $\alpha_{\text{M}}$  is governed by  $c_{\text{M}}$ , scaling linearly with it. Inverting the sign of  $c_{\text{M}}$  would change hills to valleys and vice versa. For  $G_{\text{eff}}$ , we see that indeed for  $c_{\text{M}} < 0$  gravity is weakened, where unity corresponds to the gravitational strength being Newton’s constant. The maximum weakening occurs at  $a_t$ . Since  $G_{\text{eff}}$  returns to unity for scale factors  $a \gg a_t$ , then smaller  $a_t$  means  $G_{\text{eff}}$  deviates from general relativity for a shorter time. Increasing  $\tau$  again squeezes the transition, but also affects the maximum amplitude.

For illustrative purposes, the plots shown below will fix  $a_t = 0.5$  and  $\tau = 1$  – values near the edge of the eventual 68% confidence limit, from reference [73], joint posterior – to more clearly show the effects of the modified gravity on observables.

Another interesting feature of this theory is that contrary to the majority of scalar-tensor theories, in which the growth of structures is enhanced, No Slip gravity suppresses the growth and light propagation, which can be seen in Figure 3.5, where the data points come from the galaxy redshift surveys of 6dFGRS [87], GAMA [88], BOSS [38], WiggleZ [89], and VIPERS [90]. The left plot in this panel shows the observable  $f\sigma_8$  for General Relativity and No Slip Gravity, while the right hand side plot the Weyl (Lensing) potential. In both cases the expansion history is fixed to the mirage model [91], a dynamical model using  $w_0 - w_a$  but  $w_a = -3.6(1 + w_0)$  that nearly preserves the  $\Lambda$ CDM distance to CMB last scattering [91] and so indicates a level of observational viability.

The sum of potentials generally decays in a universe with dark energy as matter domination wanes. However, if gravity is strengthened then it could overcome this tendency and grow the potentials. This not only gives a large integrated Sachs-Wolfe (ISW) effect (proportional to  $\dot{\Phi} + \dot{\Psi}$ ) in the CMB but can cause an anticorrelation between the ISW and the density perturbations.

Such issues are discussed in detail in [92, 93, 94], and some cubic Horndeski gravity theories

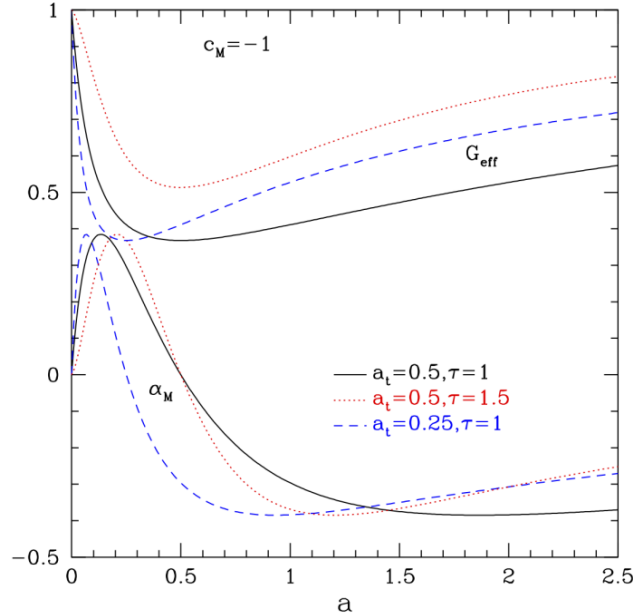


**Figure 3.4.** Evolution of the  $G_{\text{eff}} = G_{\Phi} = G_{\Psi+\Phi}$  as a function of the scale factor in No Slip gravity, Equation (3.15), and the running of the Planck Mass,  $\alpha_{\text{M}}$ , for No Slip gravity with a parametrization given by Equation (3.21). Plot taken from [73]

indeed have a negative crosscorrelation between CMB temperature perturbations and galaxy density perturbations,  $C_l^{Tg}$ . This conflicts with the prediction of  $\Lambda$ CDM, and data, and is a strong indicator against such theories. Given the preservation of the characteristic of a decaying lensing potential as in  $\Lambda$ CDM, we might expect a positive temperature-density crosscorrelation at large angles (low multipoles  $l$ ) where the ISW effect dominates. Following closely the procedure outlined in [93], one can compute the cross correlation between the CMB temperature and a galaxy survey. First we must calculate

$$C_l^{Tg} = 4\pi \int \frac{dk}{k} \Delta_l^{\text{ISW}}(k) \Delta_l^g(k) \mathcal{P}_{\mathcal{R}}(k), \quad (3.22)$$

where  $\mathcal{P}_{\mathcal{R}}$  is the power spectrum of the primordial curvature perturbations ( $\mathcal{R}(\mathbf{k})$ ), and  $\Delta_l^{\text{ISW}}$  and  $\Delta_l^g$  are the transfer functions for the ISW effect and for the galaxies. The first is given by

$$\Delta_l^{\text{ISW}} = \int_{\eta_*}^{\eta_0} d\eta (\Phi' + \Psi') j_l, \quad (3.23)$$

where  $\eta_*$  and  $\eta_0$  are the conformal time at recombination and today, respectively, and a prime here denotes a derivative with respect to  $\eta$ . The transfer functions depend on the modified gravity theory being considered and are calculated through the perturbation equations, which are solved numerically by `hi_class`.

For computations in which source number counts are present, the relevant transfer function is given as

$$\Delta_l^g \approx \Delta_l^{\text{Den}_i} + \dots, \quad (3.24)$$

where the dots represent other contributions such as redshift-space distortions, lensing, polarization, and contributions suppressed by  $H/k$  in subhorizon scales [93]. The explicit form of  $\Delta_l^{\text{Den}_i}$

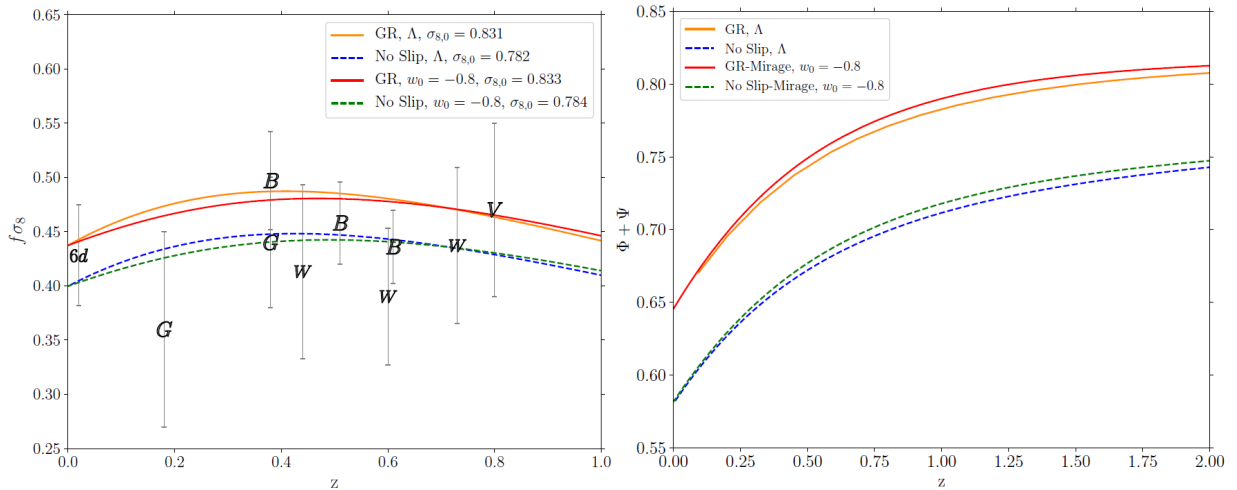


**Figure 3.5. Left:** The redshift space distortion observable  $f\sigma_8$ , basically the growth rate history, is plotted for  $\Lambda$ CDM and for mirage dark energy with present equation of state parameter  $w_0$ , in general relativity (GR) and in No Slip Gravity with  $c_M = -0.05$ ,  $a_t = 0.5$ ,  $\tau = 1$ . All curves have fixed  $\Omega_{m,0} = 0.314$  and the same initial conditions, and the derived values of  $\sigma_{8,0}$  are indicated in the legend. Galaxy redshift survey data points are shown with their error bars. Note that No Slip Gravity suppresses growth, unlike many modified gravity theories, bringing the theory into better agreement with this growth data. **Right:** The Weyl lensing potential, in CLASS code units, is plotted for  $\Lambda$ CDM and for mirage dark energy with present equation of state parameter  $w_0$ , in general relativity (GR) and in No Slip Gravity with  $c_M = -0.05$ ,  $a_t = 0.5$ ,  $\tau = 1$ . The weakened gravity in No Slip Gravity enhances the decay of the potential, in contrast to, e.g., Galileon gravity.

is

$$\Delta_l^{\text{Den}_i} = \int_0^{\eta_0} d\eta W_i b_g(\eta) \delta(\eta, k) j_l , \quad (3.25)$$

where  $\delta(\eta, k)$  is the density perturbation at the Fourier mode  $k$ ,  $j_l = j_l(k(\eta_0 - \eta))$  is a Bessel function, and  $W_i$  is a window function, discussed below. To be consistent with `hi_class` all transfer functions are normalized to the value of the curvature perturbation at some time  $k\eta_{\text{ini}} \ll 1$ , e.g.  $\delta(\eta, k) = \delta(\eta, \mathbf{k})/\mathcal{R}(\eta_{\text{ini}}, \mathbf{k})$ .

For a galaxy sample we can use the NVSS survey [96], which covers the sky north of 40 deg declination in one band. This is a large area, fairly deep survey with good overlap with the CMB ISW kernel. The selection function  $W_i$  is given by the observed number of sources per redshift,  $dN/dz$ , and we use a constant bias factor for each redshift bin. The survey selection function is given by [95] as

$$\left[ b_g(z) \frac{dN}{dz} \right]_{\text{NVSS}} = b_{\text{eff}} \frac{\alpha^{\alpha+1}}{z_0^{\alpha+1} \Gamma(\alpha)} z^\alpha e^{-\alpha z/z_0} , \quad (3.26)$$

with  $b_{\text{eff}} = 1.98$ ,  $z_0 = 0.79$ ,  $\alpha = 1.18$ , and  $\Gamma$  the gamma function. Figure 3.6 shows the results. We see that indeed No Slip Gravity gives a positive ISW cross-correlation, in agreement with the  $\Lambda$ CDM case, and observational data. Still in the context of No Slip Gravity, there is another work that studied the impact this model has on the CMB [97].

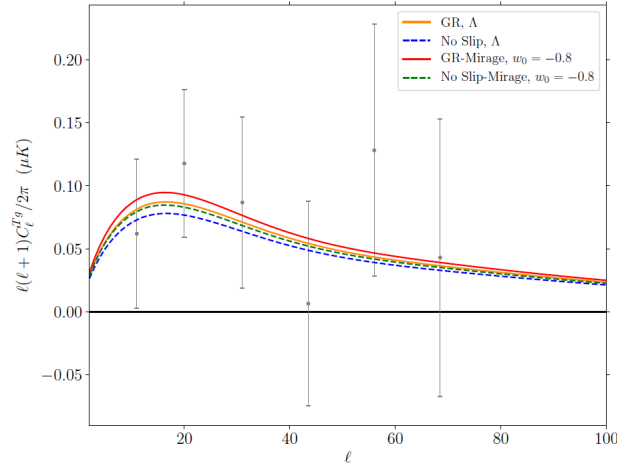


**Figure 3.6.** The ISW-galaxy cross-correlation  $C_\ell^{Tg}$  is plotted for  $\Lambda$ CDM and for mirage dark energy with present equation of state parameter  $w_0$ , in general relativity (GR) and in No Slip Gravity with  $c_M = -0.05$ ,  $a_t = 0.5$ ,  $\tau = 1$ . The data points come from the NVSS survey, as extracted from [95]. We see that, indeed, No Slip Gravity gives a positive cross-correlation.

### 3.3. Early modified gravity

As far as the CMB is concerned, however, there is not a lot information we can get to help constrain modified theories of gravity. As the majority of the dark energy models describe the modifications to GR that are only relevant at late times, the Universe around the recombination era for the majority of these theories will be very similar to  $\Lambda$ CDM. Figure 3.7 shows the angular temperature power spectrum (left) and the relative difference in percent between the modified gravity models considered and  $\Lambda$ CDM (right).

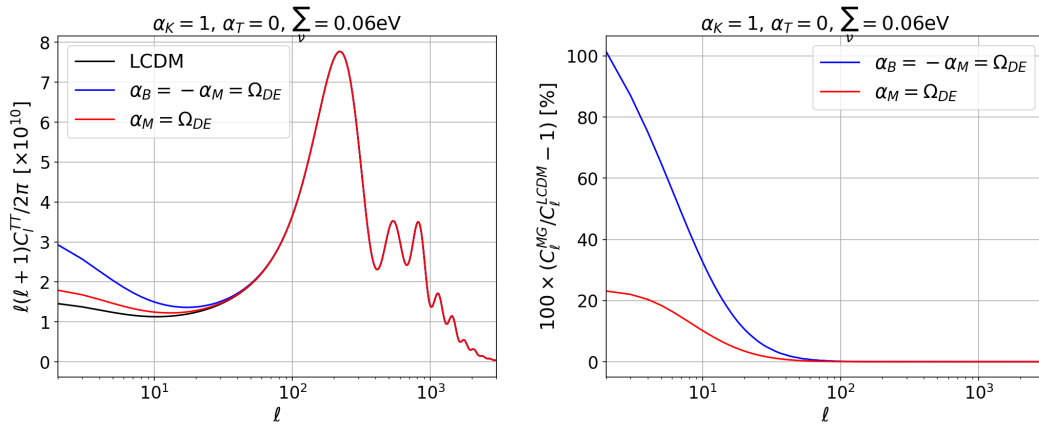


**Figure 3.7. Left:**  $C_\ell^{TT}$  for  $\Lambda$ CDM, JBD and a modified gravity theories with only running,  $\alpha_M \neq 0$ . **Right:** Relative difference between the modified gravity models and  $\Lambda$ CDM. For these particular models gravity only affects the temperature map at large scales,  $\ell < 100$ .

From the residual plots we can clearly see that the only difference between modified gravity and GR in the temperature map of the CMB is at large scales,  $\ell < 100$ . The reason for this is as mentioned above, in these models, dark energy is only relevant at late times, evidenced by the proportionality between the  $\alpha$  functions in these cases and the expansion history, which

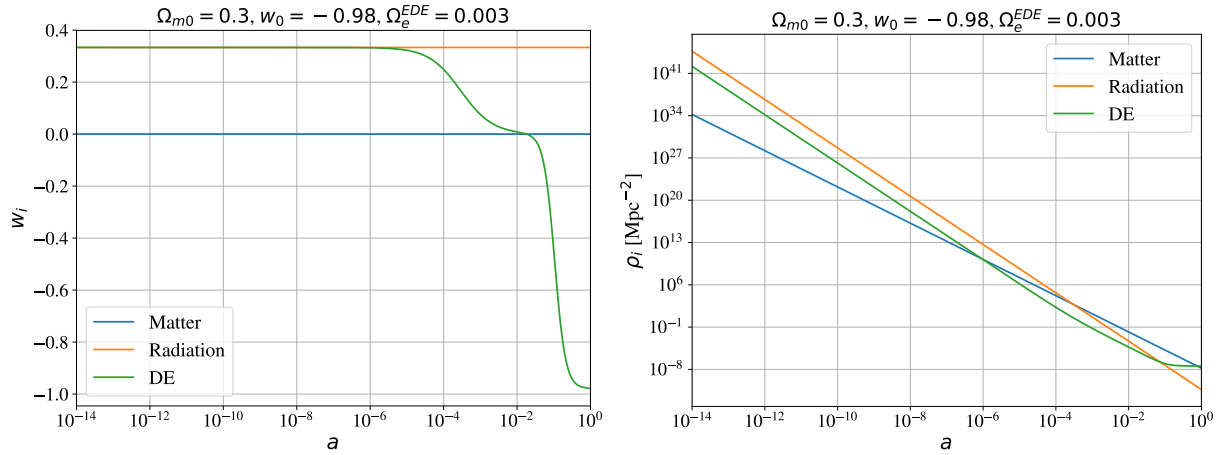


**Figure 3.8.** **Left:** Evolution of the equation of state parameter as a function of the scale factor for: non-relativistic matter (solid blue line), radiation (solid orange line) and early dark energy (solid green line). **Right:** Evolution of the background energy density as a function of the scale factor for the same species.

follows  $\Lambda$ CDM. Therefore, the only expected signal of dark energy in the CMB is through the Sachs-Wolff effect, which is caused by the evolution of the Newtonian gauge metric potentials from the time of recombination until today. As we already know, light propagation is affected by the sum of the gravitational potentials,  $\Phi + \Psi$ , and both terms of the Sachs-Wolff effect, the temperature (proportional to the pure Lensing Potential) and the integrated (proportional to the time derivative of the Lensing Potential), are clearly affected by the propagation of photons falling in and then climbing out of the gravitational potential wells [98]. The situation, however, is different when we consider theories in which the dark energy component can be non-negligible at early times, known as early dark energy (EDE) models or early modified gravity theories, which I will also refer as EDE in this section. In this case, the equation of state parameter of dark energy at early times follows the same value as radiation, which then affects the not only the location of the acoustic peaks of the CMB, but also its amplitude. One of the first early dark energy models is the Doran-Robbers model [68], which has already been well explored and constrained in the literature. In this model the dark energy fractional energy density and equation of state parameter are given by:

$$\Omega_{\text{ede}}(a) = \frac{\Omega_{\text{ede},0} - \Omega_e^{\text{EDE}} (1 - 3a^{-3w_0})}{\Omega_{\text{ede},0} + \Omega_{\text{m},0} a^{3w_0}} + \Omega_e^{\text{EDE}} (1 - a^{-3w_0}), \quad (3.27)$$

$$w_{\text{DE}}(a) = -\frac{1}{3[1 - \Omega_{\text{ede}}(a)]} \frac{d \ln \Omega_{\text{ede}}(a)}{d \ln a} + \frac{a_{\text{eq}}}{3(a + a_{\text{eq}})}. \quad (3.28)$$

Figure 3.8 shows the evolution of the equation of state of the different species in the Universe in the case of this EDE model and the evolution of the background density of the same species.

With respect to the CMB, the situation now is different than when we have a late-time dark energy model. In order to see the features in the temperature map, I plot the temperature angular power spectrum and the relative difference in percentage for two cases of  $\alpha$  functions in Figure 3.9, as well as for General Relativity with the background fixed by Equations (3.27).

We can clearly come to the realization that not only the integrated Sachs-Wolff effect imprints dark energy in the CMB, but also at higher multipoles we have a clear difference with respect to the standard model prediction. This big difference at smaller scales is what helped heavily

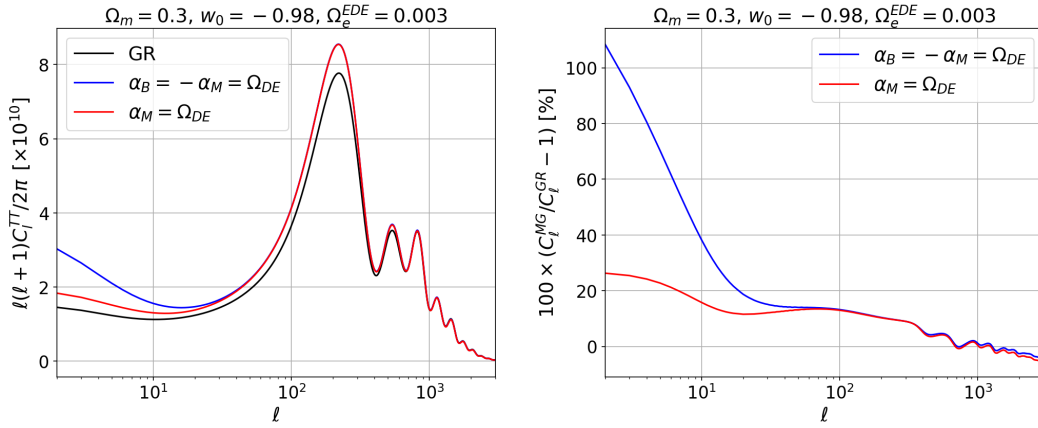


**Figure 3.9.** **Left:**  $C_\ell^{TT}$  for GR, JBD and a modified gravity theories with only running,  $\alpha_M \neq 0$ . The background is fixed to the Doran-Robbers (3.27) with parameters:  $\Omega_m = 0.3$ ,  $w_0 = -0.98$  and  $\Omega_e^{EDE} = 0.003$ . **Right:** Relative difference between the modified gravity models and  $\Lambda$ CDM. For these particular models gravity only affects the temperature map at large scales,  $\ell < 100$ .

constrain models of EDE such as the one presented now. As they affect increasingly higher multipoles, these features are severely constrained by measurements of the gravitational lensing of the CMB. Therefore, the combination of polarization maps and lensing of the CMB is generally used in combination to verify how these models can actually be realizable [99]. To wrap the discussion on how EDE models affect the cosmological observables, I will finish by discussing the impact these models have on the linear matter power spectrum.

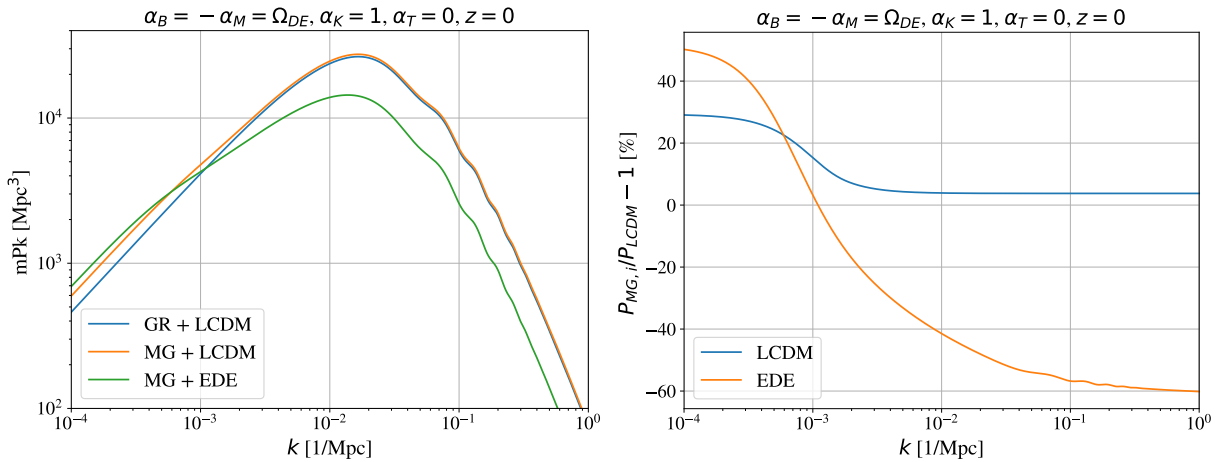


**Figure 3.10.** **Left:** Matter power spectrum at  $z = 0$  for three different cases: General Relativity with a  $\Lambda$ CDM background (solid blue), modified gravity with a  $\Lambda$ CDM background (orange blue) and modified gravity plus early dark energy theory, Equation (3.27), with parameters:  $\Omega_m = 0.3$ ,  $w_0 = -0.98$  and  $\Omega_e^{EDE} = 0.003$ . **Right:** Relative difference in percentage between the ratio of matter power spectra of modified gravity and GR, for two different background evolutions:  $\Lambda$ CDM (solid blue) and early dark energy (solid orange).

Since at early times we have one extra species contributing to the radiation energy budget, dark energy, the behavior at large values of  $k$  will be significantly affected by modified gravity, as shown in Figure 3.10. In the relative difference plot (right plot) we can compare the effect

late-time models of dark energy have on the matter power spectrum with respect to  $\Lambda$ CDM (blue line), and the features added by early-time modified gravity with respect to  $\Lambda$ CDM (orange line). With respect to the blue line, we can see an obvious effect at large scales where the matter power spectrum differs than the one from GR +  $\Lambda$ CDM. This is not an unique feature for the MG +  $\Lambda$ CDM, but rather a feature introduced by the scalar field that affects the power spectrum at large scales, since at late-times in both expansion histories, EDE and  $\Lambda$ CDM, the scalar field will behave as a cosmological constant in the background. At small scales, however, we see that the only modification MG +  $\Lambda$ CDM will have on the matter power spectrum is a constant vertical shift with respect to the 0% line, this effect will be discussed in the next section. However, the MG + EDE case at small scales will also have a slight tilt with respect to the 0% line, on top of the vertical offset. This happens since at early-times the scalar field will act like radiation, and therefore the modes that are deep inside the horizon, which have crossed the horizon at earlier times, will suffer from contributions coming from pressure perturbations of radiation and neutrinos. This then makes the matter power spectrum for this case to have a slightly different  $k$ -dependence than the MG +  $\Lambda$ CDM case. In summary, whenever we have a theory which introduces extra species acting like radiation at early times, or that introduces couplings between the dark energy and dark matter, the linear matter power spectrum at small scales will differ considerably than GR +  $\Lambda$ CDM and MG +  $\Lambda$ CDM cases.

## Linear N-Body gauge

*In this chapter I discuss the matter power spectrum at linear scales. I start by discussing how it is defined within  $\Lambda$ CDM, and how massive neutrinos introduce a scale dependent growth. I then move the discussion to the formulation of the N-Body gauge, a specific coordinate system that facilitates the interpretation of Newtonian simulations within a relativistic framework, by consistently introducing the effects coming from photons, neutrinos and dark energy. As stage-IV LSS surveys will probe the Universe at increasingly large scales the introduction of such species is imperative, as at large scales the imprint left from them can be above the 1% threshold. I finish the discussion by showing how to correctly combine modified gravity effects and Newtonian simulations. The results of this paper have been published in References [100, 101]*

### 4.1. The Linear Matter Power Spectrum in MG Theories

As we have seen in the end of the last subsection, the linear matter power spectrum will change in modified theories of gravity. To begin the study on the linear matter power spectrum, it's worth spending a little time understanding the evolution of the density contrast for the different species in our Universe, in a modified gravity theory describing dark energy.

In Figure 4.1 I plot in the top left the evolution of density contrasts as a function of conformal time for a fixed wave-number,  $k = 0.1$  1/Mpc. At early times, before decoupling (solid black vertical line), radiation and baryons are coupled together via many different processes, such as: Coulomb scattering, Thomson scattering, etc. In this era they constitute the primordial plasma, in which the baryons want to “fall” down the gravitational potentials created by cold dark matter, but get scattered by the photons, creating therefore the well-known sound waves in this plasma that are the baryon-acoustic oscillations, present in the matter power spectrum in  $k$ -space as wiggles. After decoupling baryons and photons decouple, and the baryons eventually fall down the gravitational wells, while radiation keeps oscillating until damped. Since CDM is always non-relativistic, it has the same behavior throughout the expansion history, always clustering and non-interacting with the other species besides gravitationally. Massive neutrinos have two very distinct behaviors in its evolution: at early times they are relativistic and behave like radiation, however, as time goes by, the massive neutrinos become non-relativistic. As we know, massive neutrinos act to suppress the matter power spectrum, the reason for this is that since they once were relativistic, they have a scale in which they are allowed to “free-stream”,  $k_{\text{fs}}$ . For modes smaller than this scale massive neutrinos cluster, but for scales bigger they travel freely, thence, make the clustering of matter harder. We are now left with the last species in the top left plot, dark energy, the solid magenta lines. As I'm plotting here a model in which

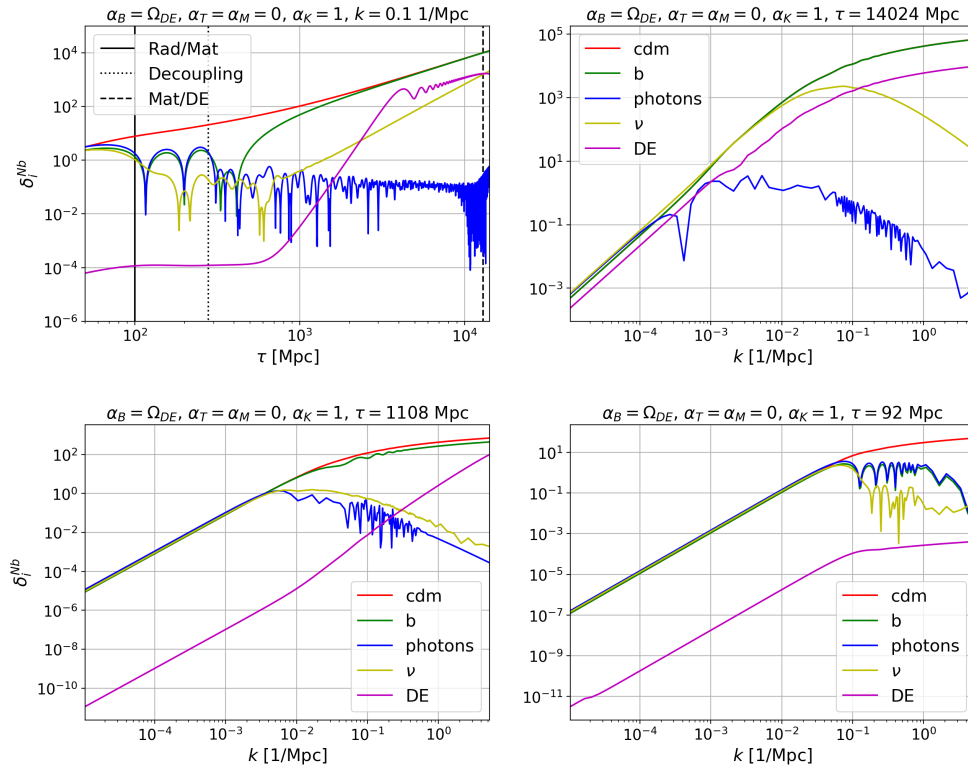


**Figure 4.1.** Evolution of the N-Body gauge density contrast of different species: cdm (red), baryons (green), photons (blue), massive neutrinos (yellow) and dark energy (purple). The top left plot shows the evolution as a function of conformal time for one specific wave-number,  $k = 0.1$  1/Mpc. The top right plot shows the dependence of the density contrast as a function of scale at conformal time ( $\tau = 14024$  Mpc, bottom left at  $\tau = 1108$  Mpc and bottom right  $\tau = 92$  Mpc). The black vertical lines in the top left plot represent the conformal time for the three eras: Radiation/Matter (solid), decoupling (dotted) and Matter/Dark Energy (dashed). Dark energy in these plots is given by the modified gravity specified in the title of each plot.

dark energy is only relevant at late-times, e.g.,  $\alpha_B = \Omega_{DE}$ , the only moment it will become non-negligible is around and after dark energy/matter equality (dashed black vertical line), and the oscillatory behavior at very late times will be soon addressed.

The other three plots in the Figure show the behavior of the perturbations in Fourier space at three different slices of conformal time, one around matter/dark energy equality (top right), one around decoupling (bottom left), and one at radiation/matter equality (bottom right). We can see that smaller modes of radiation grow, until they cross the horizon when they oscillate and then get damped. The same behavior happens for massive neutrinos at early times when they are mostly relativistic, but as time goes by we see that after horizon-crossing they get exponentially damped. Baryons, before and around decoupling have the same behavior as photons, but after decoupling will cluster with CDM, and in a specific range of wave-numbers will exhibit the well-known BAO wiggles. Cold dark matter will always cluster. The last species is DE, where we can see that they start well below all the other species, but at late times have contributions of the same order as the others. A more detailed discussion concerning dark energy will soon follow.

One of the most important quantities in cosmology is the matter power spectrum. The vast majority of LSS surveys observe biased tracers of the underlying CDM density field. That is, what they actually observe is the galaxy power spectrum, which at linear order can be written

as:

$$P_g(k, z_i) = b_i(z_i)P_m(k, z_i), \quad (4.1)$$

where  $b_i$  is called linear bias, and is a quantity that is computed by the survey collaboration or using cosmological simulations, it's generally related to the luminosity function of the galaxy (or other tracer) being observed. During matter domination, we can write the matter density perturbation as proportional to the Newtonian metric potential  $\Phi$ :

$$\delta_m(k, z) = \frac{2}{3} \frac{k^2}{a^2 H^2} \Phi(k, z) \quad (4.2)$$

then, the two point function in Fourier space gives the matter power spectrum:

$$\langle \delta_m(\mathbf{k}, z) \delta_m^*(\mathbf{k}', z) \rangle = (2\pi)^3 \delta(\mathbf{k} - \mathbf{k}') P_m(k, z). \quad (4.3)$$

During matter domination,  $\Phi$  is constant on super and sub horizon scales, and we can write it in terms of the primordial curvature perturbations,  $\zeta$ :

$$\Phi = \frac{3}{5} \zeta \quad (4.4)$$

and the expression for  $P_m$  follows:

$$P_m(k, z) = \frac{8\pi^2 k}{25 (aH)^4} A_S \left( \frac{k}{k_*} \right)^{n_s-1} T^2(k) D^2(z), \quad (4.5)$$

where  $A_S$  is the amplitude of the Primordial Power Spectrum,  $n_s$  is the scalar tilt,  $D(z)$  is the growth function solution of the matter density contrast equation during matter domination:

$$D'' + \mathcal{H}D' - 4\pi G_N \rho_m D = 0, \quad (4.6)$$

$D(z) = \frac{\delta_m(z)}{\delta_m(z_{ini})}$ . Still in (4.5) there is one last scale-dependent function,  $T(k)$ , which is the BBKS transfer function [102]. This function relates the  $\Phi$  potential on sub-horizon scales during radiation era to its constant value during the whole matter era:

$$T(k) = \frac{\Phi(k, z)}{\Phi_{\text{primordial}}}. \quad (4.7)$$

At large scales the transfer function is normalized to unity, while at larger  $k$  it describes the logarithmic-dependence of the transition to sub-horizon scales. Therefore, we separate in three different parts the shape of the linear matter power spectrum:

- i) Large scales, small  $k$ , it is proportional to  $k^{n_s}$ ;
- ii) Intermediate scales, it reaches its maximum at  $k_{\text{eq}} = a_{\text{eq}} H_{\text{eq}}$ , the scale of radiation/matter equality,  $\sim 0.01$  1/Mpc;
- iii) Small scales, large  $k$ , decays as  $\propto \frac{(\ln k)^2}{k^3}$ .

Figure 4.2 shows the  $\Lambda$ CDM linear matter power spectrum, as well as the same quantity for a model with massive neutrinos, at two different redshifts,  $z = 0$  and  $z = 2$ . We can translate from one matter power spectrum at a given redshift to the other by just using the growth function  $D(z)$ . Figure 4.3 shows the Planck 2018 paper plot of the linear matter power spectrum at

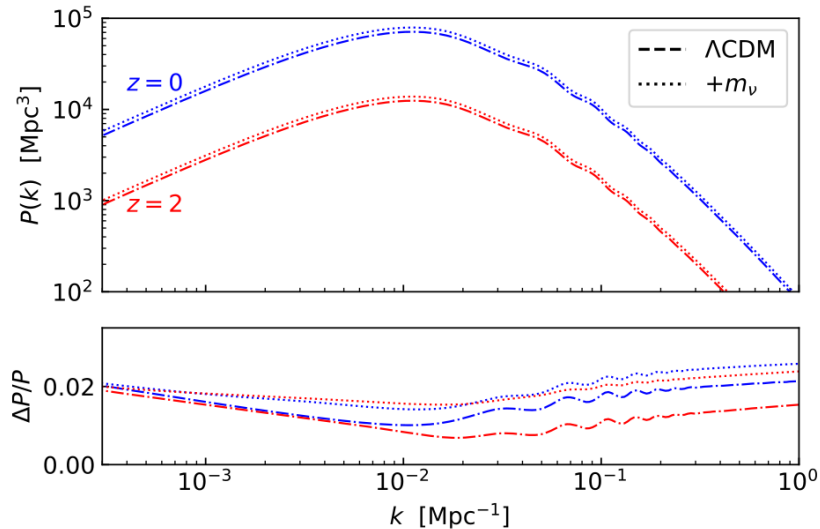


**Figure 4.2.** Matter power spectrum (including non-linear corrections using Halofit) at redshifts 0 and 2, predicted by the  $\Lambda$ CDM model with a single massive neutrino of 0.06 eV. Figure taken from [103]

redshift  $z = 0$  with the data points analyzed using  $\Lambda$ CDM assumptions. As it is known, the matter power spectrum is a gauge-dependent quantity, that is, it depends if we are solving the Einstein-Boltzmann equations in a given gauge. However, for scales inside the cosmological horizon, all the gauges must coincide, as the behavior of gravity when we move to smaller scales is well described by Newtonian gravity. This can be seen from the component 0-0 of Einstein Equations in the Newtonian gauge:

$$k^2\Phi = 4\pi G_N a^2 \left[ \delta\rho_m + 3\mathcal{H}(\rho + p) \frac{v_m}{k} \right]. \quad (4.8)$$

The last term is only relevant when  $k \ll 1$ , or in terms of the cosmological horizon  $k \sim aH$  (at  $z = 0$ ,  $aH \sim 10^{-3}$  1/Mpc). Therefore, inside the horizon, we have:

$$k^2\Phi = 4\pi G_N a^2 \delta\rho_m, \quad (4.9)$$

which matches the well-known Poisson equation in the Newtonian theory. To see that matter will have the same Newtonian behavior in the Synchronous gauge, we can check that the matter density in the Newtonian gauge and the Synchronous gauge are related via the transformation:

$$\delta\rho^S = \delta\rho^N - \alpha\dot{\rho}, \quad (4.10)$$

where

$$\alpha = \frac{\dot{h} + 6\dot{\eta}}{2k^2}, \quad (4.11)$$

which is only relevant at large scales by the same arguments of the last term in Equation 4.8. Therefore, as we can see from this discussion, the only difference we have between matter power spectra computed in different gauges is at large scales [104, 105, 106].

Since most of the LSS surveys have focused only on scales that are deep inside the horizon, these collaborations have relied on using tools such as higher order perturbation theory and Newtonian N-Body simulations to compute matter power spectrum, at linear and non-linear order. However, our Universe is inherently relativistic, and even though in a certain  $k$ -range

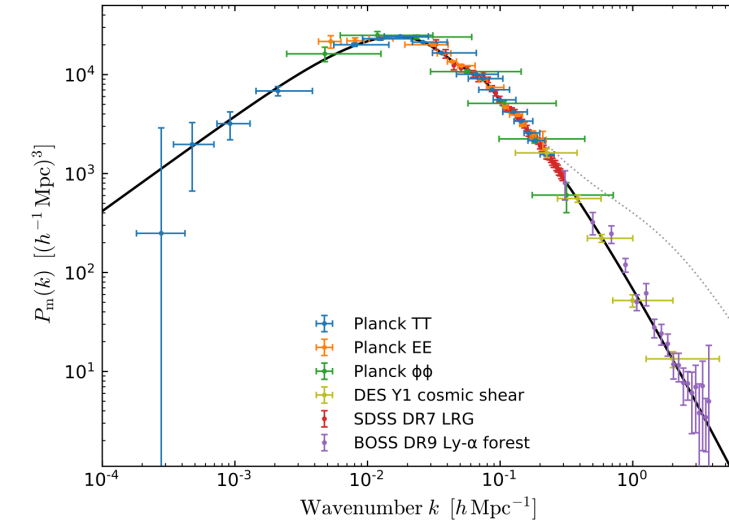


**Figure 4.3.** Linear-theory matter power spectrum (at  $z = 0$ ) inferred from different cosmological probes (the dotted line shows the impact of non-linear clustering at  $z = 0$ ). Figure taken from [103]

we can safely approximate it using Newtonian gravity, we still need to correctly account for the relativistic corrections at large scales. This problem is more intricate in the context of  $N$ -Body simulations, as the output of these codes only exists in Newtonian gravity which gives the wrong result at large scales. One way to bypass this problem is then to look for a “natural” coordinate system in which these simulations live in. In other words, we can look for a gauge which gives the correct relativistic behavior at small  $k$  values, and transitions to Newtonian gravity at large  $k$ . This specific gauge was developed by [107], and it is called the  $N$ -Body gauge.

## 4.2. $N$ -body gauge

I start by describing the following scalar metric perturbations over a homogeneous and isotropic Friedmann–Lemaître–Robertson–Walker background cosmology

$$g_{00} = -a^2 (1 + 2A) , \quad (4.12)$$

$$g_{0i} = a^2 i \hat{k}_i B , \quad (4.13)$$

$$g_{ij} = a^2 \left[ \delta_{ij} (1 + 2H_L) + 2 \left( \delta_{ij}/3 - \hat{k}_i \hat{k}_j \right) H_T \right] . \quad (4.14)$$

Which is the same metric presented in Equation (1.34);  $A$  is the perturbation of the lapse function,  $B$  is a scalar perturbation in the shift, and  $H_L$  and  $H_T$  are respectively the trace and trace-free scalar perturbations of the spatial metric. For simplicity I consider a single Fourier mode with comoving wave-vector,  $\mathbf{k}$ , wave-number  $k \equiv |\mathbf{k}|$  and direction  $\hat{k}_i \equiv k_i/k$ .

The energy-momentum tensor of all particle species is given by

$$T^0_0 = - \sum_{\alpha} (\rho_{\alpha} + \delta\rho_{\alpha}) = - \sum_{\alpha} \rho_{\alpha} (1 + \delta_{\alpha}) \equiv -\rho (1 + \delta) , \quad (4.15)$$

$$T^i_0 = \sum_{\alpha} (\rho_{\alpha} + p_{\alpha}) \hat{k}^i v_{\alpha} \equiv (\rho + p) \hat{k}^i v , \quad (4.16)$$

$$\begin{aligned} T^i_j &= \sum_{\alpha} (p_{\alpha} + \delta p_{\alpha}) \delta_j^i + \frac{3}{2} (\rho_{\alpha} + p_{\alpha}) \left( \delta_j^i / 3 - \hat{k}^i \hat{k}_j \right) \sigma_{\alpha} \\ &\equiv (p + \delta p) \delta_j^i + \frac{3}{2} (\rho + p) \left( \delta_j^i / 3 - \hat{k}^i \hat{k}_j \right) \sigma , \end{aligned} \quad (4.17)$$

where the dummy index  $\alpha$  runs over all species,  $\delta$  is the density contrast,  $\sigma$  is the anisotropic stress following the convention of [20],  $\rho$  and  $p$  are the background density and pressure respectively.

Thus far the perturbation variables are in an arbitrary gauge. The definition of the N-body gauge is such that:

- (i) the temporal slicing is fixed by setting  $B^{\text{Nb}} = v^{\text{Nb}}$ , making the constant-time hypersurfaces orthogonal to the 4-velocity of the total matter and radiation content;
- (ii) the spatial threading is fixed by setting  $H_{\text{L}}^{\text{Nb}} = 0$ , so that the physical volume element of a spatial 3-hypersurface coincides with the coordinate volume element,  $d^3x$ , i.e., the physical volume is not perturbed by metric deformations.

As pointed out in references [107, 108, 19, 109], the spatial gauge choice is equivalent to requiring that the remaining spatial metric potential,  $H_{\text{T}}^{\text{Nb}}$ , is related to the comoving curvature perturbation,  $\zeta$ , as

$$H_{\text{T}}^{\text{Nb}} = 3\zeta. \quad (4.18)$$

More generally this condition (4.18) can be used to select the spatial threading, independently of the temporal gauge choice. In particular the N-boisson gauge [110], combines the spatial gauge condition (4.18) with an alternative time slicing, which coincides with that used in the Poisson gauge<sup>1</sup>,  $kB = \dot{H}_T$ . At linear scales, the N-body and N-boisson gauge are connected by a temporal gauge transformation and either of the gauges can be used.

The simplicity of the N-body gauge is that in the absence of relativistic species (photons and neutrinos, or dark energy perturbations) both the matter density and the particle trajectories in the N-body gauge coincide at linear order with those in Newtonian N-body simulations (it is a Newtonian motion gauge [109]). Thus to track relativistic corrections to the matter density we only need to solve for the relativistic components which we expect to be well described by linear perturbation theory on sufficiently large scales.

As in Newtonian simulations, we treat baryons as pressureless matter at late times. For gravitation, I use the Einstein equations,  $G_{\mu\nu} = 8\pi G T_{\mu\nu}$  where  $T_{\mu\nu}$  includes the contribution from Cold Dark Matter (CDM), baryons, photons, neutrinos and dark energy. I emphasise that this does not mean GR is assumed, and we can include modified gravity effects as an effective dark energy fluid, using Equations (2.80-2.83).

For pressureless matter, i.e. CDM plus baryons, the evolution equations are given by

$$\delta_m^{\text{Nb}} + k v_m^{\text{Nb}} = 0, \quad (4.19)$$

$$(\partial_{\tau} + \mathcal{H}) v_m^{\text{Nb}} = -k \left( \Phi + \gamma^{\text{Nb}} \right), \quad (4.20)$$

<sup>1</sup>The Poisson gauge is such that its scalar perturbations part is the same as the well-known Newtonian gauge.

where  $'$  is the derivative with respect to the conformal time  $\tau$ , and  $\gamma^{\text{Nb}}$  introduces relativistic corrections to the Euler equation (4.20), which vanishes in the absence of relativistic species. As shown in [111],  $\gamma^{\text{Nb}}$  is given by:

$$k^2 \gamma^{\text{Nb}} = -(\partial_\tau + \mathcal{H}) H_{\text{T}}^{\text{Nb}} + 12\pi G a^2 (\rho + p) \sigma. \quad (4.21)$$

In the N-body gauge, the Bardeen potential  $\Phi$  satisfies the relativistic Poisson equation, but with contributions coming from all species including relativistic species

$$k^2 \Phi = 4\pi G a^2 \sum_{\alpha} \delta \rho_{\alpha}^{\text{Nb}}, \quad (4.22)$$

$\alpha = \{\text{cdm}, \text{b}, \gamma, \nu, \text{DE}\}$ . Quantities with a superscript Nb are computed in the N-body gauge. The  $(0i)$  component of the Einstein equations gives

$$H_{\text{T}}^{\text{Nb}} = 3\mathcal{H} A^{\text{Nb}}. \quad (4.23)$$

From the momentum conservation equation, the lapse function of the N-body gauge metric reads:

$$A^{\text{Nb}} = \frac{1}{\rho + p} \left[ (\rho + p) \sigma - \delta p^{\text{Nb}} \right], \quad (4.24)$$

with  $\delta p^{\text{Nb}}$  the total pressure perturbation in the N-body gauge.

When the relativistic species fluid quantities are negligible,  $\delta p^{\text{Nb}} = \sigma = 0$  (for example, for sufficiently late times), one has  $A^{\text{Nb}} = H_{\text{T}}^{\text{Nb}} = 0$ , which implies  $\gamma^{\text{Nb}} = 0$ . In this limit, equations (4.19), (4.20) and (4.22) coincide with the Newtonian ones:

$$\delta_m^{\text{N}} + k v_m^{\text{N}} = 0, \quad (4.25)$$

$$(\partial_\tau + \mathcal{H}) v_m^{\text{N}} = -k \Phi^{\text{N}}, \quad (4.26)$$

$$k^2 \Phi^{\text{N}} = 4\pi G a^2 \rho_m \delta_m^{\text{N}}, \quad (4.27)$$

where the superscript N denotes the perturbations in Newtonian theory. Combining equations (4.25)–(4.27) then yields the familiar second-order differential equation for the Newtonian density perturbation

$$\delta_m^{\text{N}} + \mathcal{H} \delta_m^{\text{N}} - 4\pi G a^2 \rho_m \delta_m^{\text{N}} = 0, \quad (4.28)$$

More generally, in the presence of relativistic species, combining equations (4.19)–(4.22), we obtain the second-order differential equation for the density perturbation in the N-body gauge:

$$\delta_m^{\text{Nb}} + \mathcal{H} \delta_m^{\text{Nb}} - 4\pi G a^2 \rho_m \delta_m^{\text{Nb}} = 4\pi G a^2 \delta \rho_{\text{GR}}, \quad (4.29)$$

where

$$\delta \rho_{\text{GR}} = \delta \rho_{\gamma}^{\text{Nb}} + \delta \rho_{\nu}^{\text{Nb}} + \delta \rho_{\text{DE}}^{\text{Nb}} + \delta \rho_{\text{metric}}^{\text{Nb}}, \quad (4.30)$$

and we define

$$k^2 \gamma = 4\pi G a^2 \delta \rho_{\text{metric}}. \quad (4.31)$$

The homogeneous solution to (4.29) coincides with that of the Newtonian equation (4.28) and can be obtained from Newtonian simulations. However the full solution to (4.29) includes relativistic corrections sourced by the quantities  $\delta \rho_{\gamma}^{\text{Nb}}$ ,  $\delta \rho_{\nu}^{\text{Nb}}$ ,  $\delta \rho_{\text{DE}}^{\text{Nb}}$  and  $\delta \rho_{\text{metric}}^{\text{Nb}}$  which must be evaluated using a relativistic approach, such as linear Einstein-Boltzmann codes.

To make contact with the quantities commonly evaluated in Einstein-Boltzmann codes, we can write the N-body gauge density perturbations in terms of those in the Synchronous or Poisson gauges using the linear gauge transformation

$$\delta\rho_\alpha^{\text{Nb}} = \delta\rho_\alpha^{\text{S/P}} + 3\mathcal{H}(1+w_\alpha)\rho_\alpha\frac{\theta_{\text{tot}}^{\text{S/P}}}{k^2}, \quad (4.32)$$

with  $\mathcal{H}$  being the conformal Hubble factor,  $\mathcal{H} = a'/a$ , and  $\theta_{\text{tot}}$  the total peculiar velocity divergence of all species ( $\theta = ik^j v_j$ ).  $\delta\rho_\gamma^{\text{Nb}}$ ,  $\delta\rho_\nu^{\text{Nb}}$  and  $\delta\rho_{\text{DE}}^{\text{Nb}}$  can thus all be evaluated using Equation (4.32).

The computation of  $\gamma^{\text{Nb}}$ , given by (4.21), requires  $H_{\text{T}}^{\text{Nb}}$  and  $H_{\text{T}}^{\prime\text{Nb}}$ . Using equations (4.24) and (4.23), we obtain the equation for  $H_{\text{T}}^{\text{Nb}}$ :

$$H_{\text{T}}^{\text{Nb}} = 3\frac{\mathcal{H}}{\rho+p}\left[(\rho+p)\sigma - \delta p^{\text{S/P}} + p'\frac{\theta_{\text{tot}}^{\text{S/P}}}{k^2}\right], \quad (4.33)$$

and its derivative

$$\begin{aligned} H_{\text{T}}^{\prime\text{Nb}} &= \left[\frac{\mathcal{H}'}{\mathcal{H}} - \frac{1}{(\rho+p)}(\rho'+p')\right]H_{\text{T}}^{\text{Nb}} \\ &+ 3\frac{\mathcal{H}}{\rho+p}\left[(\rho'+p')\sigma + (\rho+p)\sigma' - \delta p' + p''\frac{\theta_{\text{tot}}^{\text{S/P}}}{k^2} + p'\frac{\theta_{\text{tot}}^{\prime\text{S/P}}}{k^2}\right], \end{aligned} \quad (4.34)$$

where we used a linear gauge transformation to obtain the total pressure perturbation in the N-body gauge

$$\delta p^{\text{Nb}} = \delta p^{\text{S/P}} - p'\frac{\theta_{\text{tot}}^{\text{S/P}}}{k^2}. \quad (4.35)$$

In this way, we can compute Equation (4.21) solely in terms of fluid quantities and their time derivatives in the Synchronous or Poisson gauge.

### 4.3. Modified gravity

As we saw in the previous section, with an Einstein-Boltzmann solver we can introduce relativistic effects into Newtonian simulations. Within the framework of Modified Gravity, we need to keep in mind the following three regimes that describe our Universe:

- (a) Large-scales: gravity is relativistic and we can use the linear cosmological perturbation theory to describe the evolution of perturbations.
- (b) Intermediate-scales: gravity is ‘‘Newtonian’’ in the sense that we can take the QSA limit in the equations of motion, and all modifications of gravity are encoded by the presence of a fifth force that will modify the gravitational coupling between matter and the Newtonian potential. In this regime we may also have the presence of a screening mechanism which will make the transition to GR.
- (c) Small-scales: the screening mechanism has already kicked in and modifications to GR due to the fifth force are suppressed.

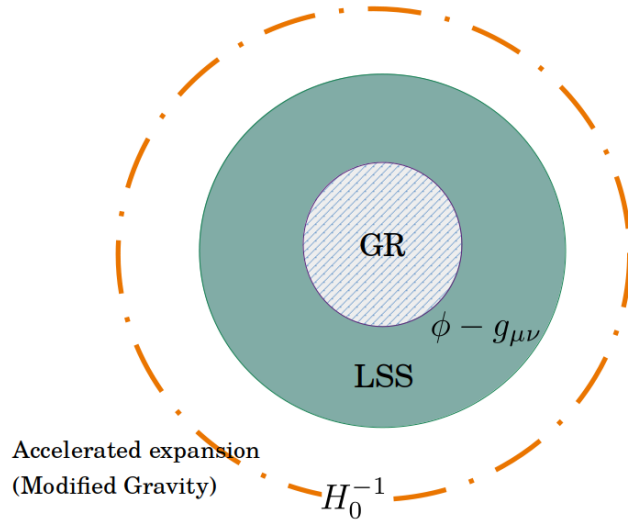


**Figure 4.4.** Schematical description of the cosmological regimes modified gravity theories transition.

Figure 4.4 depicts in a schematic way the three regimes. Regime (a) is the one described by the N-Body gauge. The other two, are more intricate, as they are connected through something called *screening mechanism*. The idea behind these mechanisms is that they are able to shield the fifth force introduced by Modified Gravity in small scales, thus recovering GR in dense regimes. In the next chapter I will give a more in-depth understanding of such mechanisms, while in the present chapter I will treat only of linear perturbations, even in the regime where they may not be valid anymore.

As shown in the previous subsection, the Newtonian equation of motion for cold dark matter and baryons (as far as we are concerned these two are indistinguishable from each other) are given by the set of Equations (4.25-4.27), which combined give Equation (4.28). This set of equations is also known as the Vlasov-Poisson equations, and they are equivalent to the Boltzmann equations for a pressureless fluid. Newtonian N-Body codes solve the discrete phase-space equivalent of these equations. To introduce modified gravity into these codes, what is usually done is to promote the Newtonian gravitational constant to a space and time dependent function, called  $G_{\text{eff}}$ . This new function, in turn, is introduced by the presence of the extra degree of freedom, which gives rise to a force term on the RHS of the geodesic equation for pressureless matter, (2.17). However, our Universe is composed not only by CDM and baryons, we also have photons, massless and massive neutrinos, and, possibly, a dark energy component different than the Cosmological Constant. From Equations (2.80-2.83) we saw that we can treat modified gravity also as a fluid, with effective fluid quantities given by these equations. Therefore, in this section I will show how we can introduce the scalar field into Newtonian N-Body simulations using the N-Body gauge, in both regimes, the small scale regime (remember that I will only focus on linear perturbations, with this I can for now forget about screening mechanisms which will later on be discussed) where modified gravity can be described by the effective gravitational constant, and large scales, where we have the interplay of the scalar field and the metric tensor that combined describe gravity.

The Poisson equation modified gravity N-Body codes are solving is the following:

$$\nabla^2 \Phi^N = 4\pi a^2 G_{\text{eff}} \rho_m \delta_m^N, \quad (4.36)$$

and the evolution equation is then

$$\delta_m^{\prime\prime\text{Nb}} + \mathcal{H}\delta_m^{\prime\text{Nb}} - 4\pi G_{\text{eff}} a^2 \rho_m \delta_m^{\text{Nb}} = 0. \quad (4.37)$$

The above equation is always valid in scales inside the horizon, which I have already stated that we can use the QSA limit in the evolution equations for modified gravity. From Equation (4.29) we see that dark energy enters in two ways on the RHS of that equation: via  $\delta\rho_{\text{DE}}^{\text{Nb}}$  and  $\sigma_{\text{DE}}$  in the computation of the term  $\delta\rho_{\text{metric}}^{\text{Nb}}$ . Therefore, using the separations (3.1) and (3.2) we can take the QSA limit, and separate what captures and models dark energy at small scales, the QSA part, from what is only relevant at large scales, the relativistic terms. Thence, moving the QSA

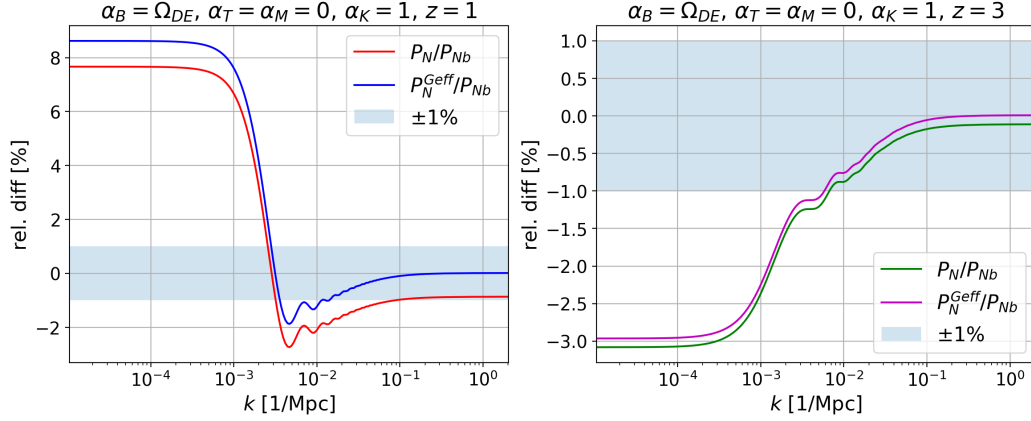


**Figure 4.5.** Relative difference in percent of the ratio between the Newtonian matter power spectrum ( $P_N$ ) with  $G_N$  as the coupling between matter and the Poisson potential, and the Newtonian matter power spectrum ( $P_N^{\text{Geff}}$ ) with coupling given by the  $G_{\text{eff}}$  function, with respect to the linear N-Body gauge matter power spectrum.

terms (which are proportional to  $\delta\rho_m$ ) from the RHS to the LHS, and coupling these terms with the term proportion to  $G_N$ , we arrive at:

$$\delta_m^{\prime\prime\text{Nb}} + \mathcal{H}\delta_m^{\prime\text{Nb}} - 4\pi G_{\text{eff}} a^2 \rho_m \delta_m^{\text{Nb}} = 4\pi G_N a^2 \delta\rho_{\text{GR, rel.}}^{\text{Nb}}, \quad (4.38)$$

with

$$\delta\rho_{\text{GR, rel.}}^{\text{Nb}} = \delta\rho_\gamma^{\text{Nb}} + \delta\rho_\nu^{\text{Nb}} + \delta\rho_{\text{DE, rel.}}^{\text{Nb}} + \delta\rho_{\text{metric, rel.}}^{\text{Nb}}, \quad (4.39)$$

$$\delta\rho_{\text{DE, rel.}}^{\text{Nb}} = \delta\rho_{\text{DE}}^{\text{Nb}} - \delta\rho_{\text{DE}}^{\text{QSA}}, \quad (4.40)$$

$$k^2 \gamma_{\text{rel.}}^{\text{Nb}} = 4\pi G \delta\rho_{\text{metric, rel.}}^{\text{Nb}}, \quad (4.41)$$

and the effective gravitational constant given by

$$G_{\text{eff}} = 1 + \frac{c_{\text{sN}}^2 (2 - 2M_*^2 + 2\alpha_T) + (\alpha_B + 2\alpha_M - 2\alpha_T + \alpha_B \alpha_T)^2}{2c_{\text{sN}}^2 M_*^2}. \quad (4.42)$$

We are now left with a relativistic equation for the motion of cold dark matter and baryons that correctly takes into account all the relativistic species. With this in hand we can then understand what is the effect of general Horndeski theories in the matter power spectrum at small, intermediate and large scales. The best way to understand these features is to compare the Newtonian prediction for the matter power spectrum which I will call  $P_N$ , built using the

solution of Equation (4.28), the prediction of the modified gravity Newtonian limit  $P_N^{\text{Geff}}$ , built using solution of (4.37) and the matter power spectrum in the N-Body gauge, built using the solution of (4.29),  $P_{\text{Nb}}$ . The first would correspond to a Newtonian simulation with only linear perturbations, the second the same situation but with modified gravity, and the last one is the fully relativistic analog.

Figure 4.5 shows the relative difference in percentage between these matter power spectra. The left plot shows the difference at  $z = 1$  between the Newtonian matter power spectra with and without small scales effects of modified gravity,  $P_N$  and  $P_N^{\text{Geff}}$  respectively, with respect to the N-Body gauge matter power spectrum. We can see that in the red curve we have not only the deviation a small  $k$  values, introduced by relativistic species, but also the deviation at large  $k$ , introduced by  $G_{\text{eff}}$ , which corresponds to a vertical shift with respect to the 0% line. This vertical

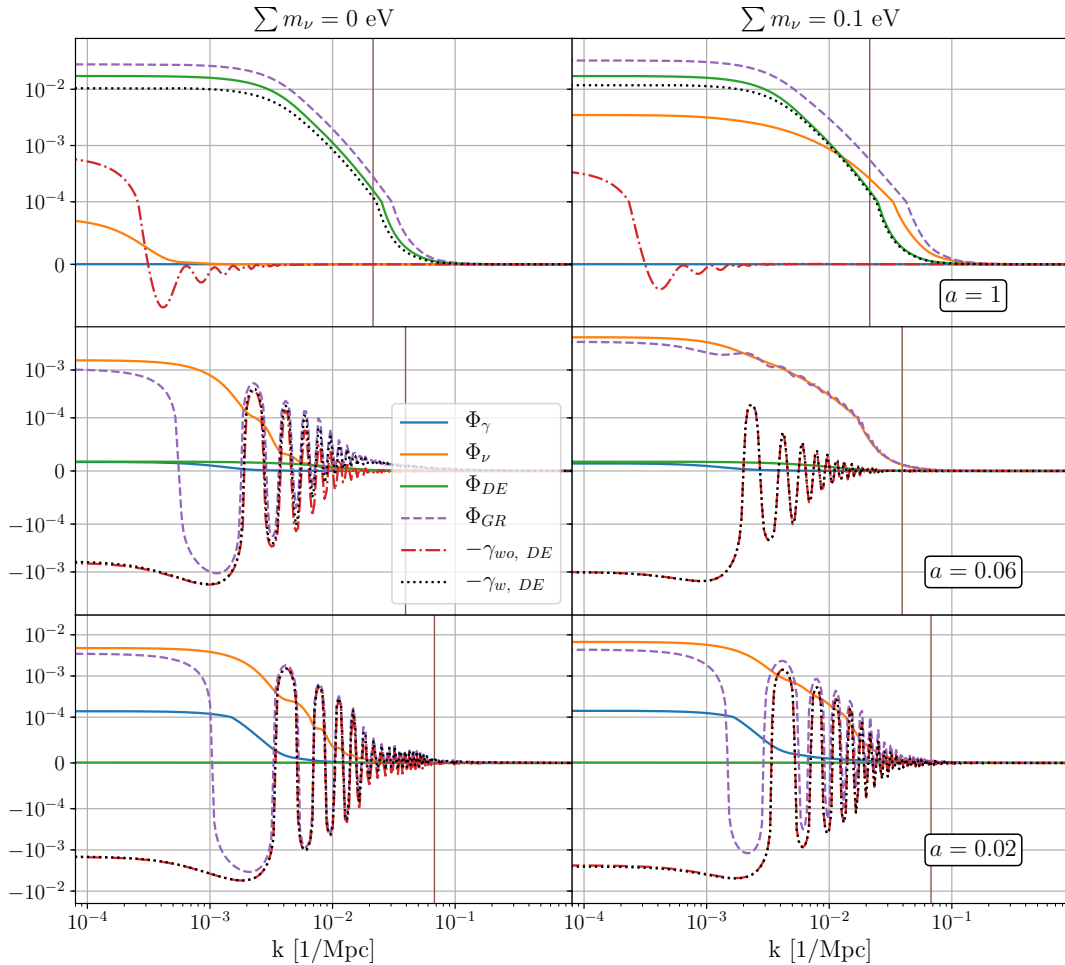


**Figure 4.6.** Individual contributions from the “force” potentials of each relativistic species, the sum  $\Phi_{\text{GR}}$  and the relativistic correction potentials with and without dark energy perturbations,  $\gamma_{\text{w}, \text{DE}}^{\text{Nb}}$  and  $\gamma_{\text{wo}, \text{DE}}^{\text{Nb}}$  respectively. The left plots are for massless neutrinos and the right massive neutrinos, each row is at a given scale factor,  $a = 1$  (top),  $a = 0.06$  (middle) and  $a = 0.02$  (bottom). The perturbations are normalised so that  $\zeta = -1$  on super-horizon scales.

shift, however, is absent in the blue curve, since both spectra,  $P_{\text{Nb}}$  and  $P_N^{\text{Geff}}$ , share the same homogeneous solution. Therefore, in these plots we can check the consistency and validity of the

N-Body gauge implementation, as we are able to recover the expected and already known effect introduced by  $G_{\text{eff}}$ . This also lets us separate and understand what are the relativistic deviations the scalar field introduces in the matter power spectrum in all scales, as well as it lets us quantify how big these deviations are. The plot on the right shows exactly the same quantity but at redshift  $z = 3$ . Since we are dealing with late time modifications of gravity we know that the effects of dark energy are bigger only towards the end of matter domination, and the biggest effects (prior to this moment in the evolution of the Universe) come from other relativistic species, such as photons and massless and massive neutrinos. As an example, to understand the impact DE has

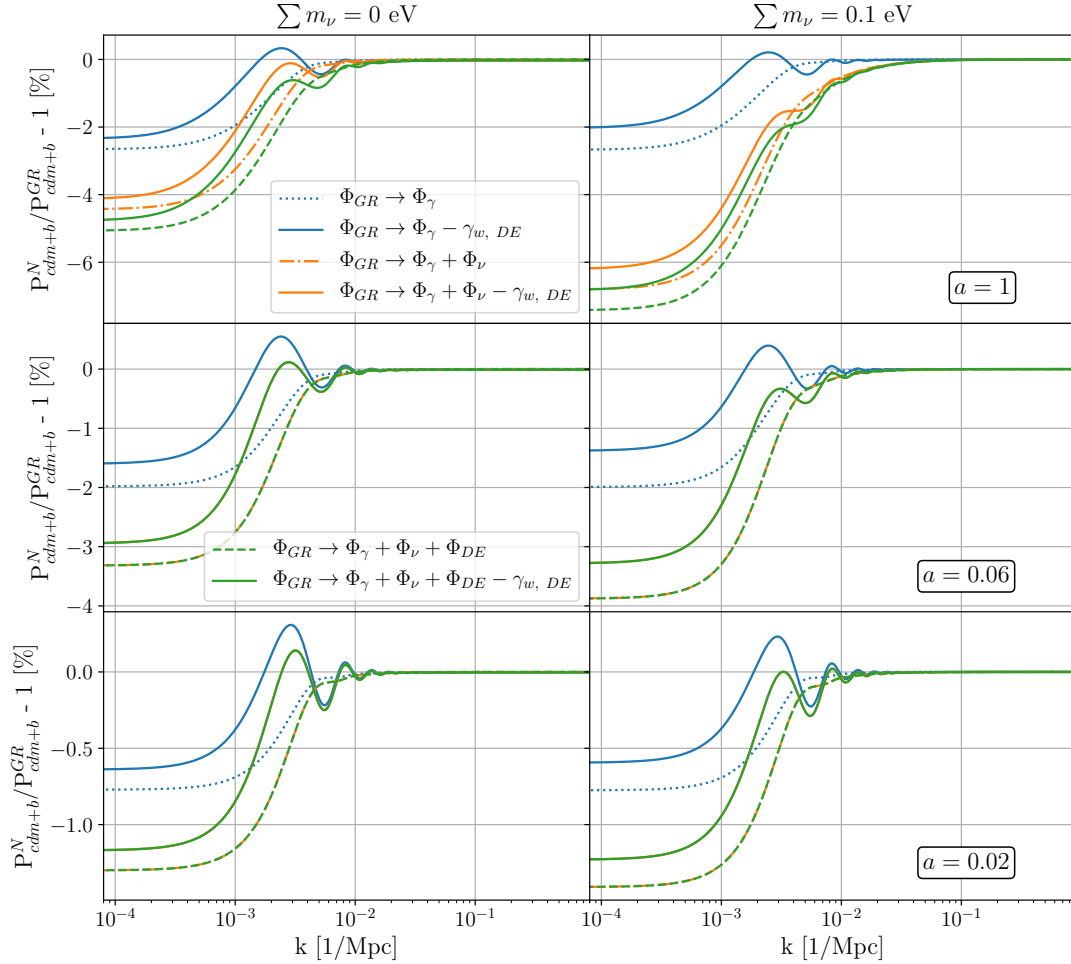


**Figure 4.7.** Relative difference in percent between the Newtonian matter power spectrum,  $P_{\text{cdm}+\text{b}}^{\text{N}}$ , and the full general relativistic N-Body gauge one,  $P_{\text{cdm}+\text{b}}^{\text{GR}}$ . The different colors show the impact when we add one relativistic specie at a time, i.e., photons (blue), neutrinos (orange) and dark energy (green). The dashed lines correspond to relativistic corrections without the term coming from the metric perturbations, Equation (4.31), while the solid ones correspond to corrections with  $\gamma^{\text{Nb}}$ . In the left column I show the contributions with only massless neutrinos, and in the right column with massive neutrinos. Dark energy perturbations are computed within k-essence theory.

on large scales we can study the case of a k-essence model, which has  $G_{\text{eff}} = 1$ . Figure 4.6 presents the “force” potentials of the relativistic species,  $k^2\Phi_\alpha = 4\pi G a^2 \delta\rho_\alpha^{\text{Nb}}$  ( $\alpha = \{\gamma, \nu, \text{DE}\}$ ), and the  $\gamma^{\text{Nb}}$  contributions. The contribution  $\gamma_{\text{wo, DE}}^{\text{Nb}}$  refers to equation (4.21) computed without the dark energy perturbations in it, that is, k-essence is present only in the background quantities. We can

see that the density perturbations of dark energy are only relevant at late times, in the  $a = 1$  (top row) plots, in which the total general relativistic “force” potential,  $\Phi_{\text{GR}} = \Phi_{\gamma} + \Phi_{\nu} + \Phi_{\text{DE}} + \gamma^{\text{Nb}}$ , gets most of its contribution from  $\gamma_{\text{w, DE}}^{\text{Nb}}$ . The lack of oscillations for intermediate  $k$  values of  $\Phi_{\text{DE}}$  and  $\gamma_{\text{w, DE}}^{\text{Nb}}$  at redshift  $z = 0$ , stems from the nature of the clustering dark energy density perturbations: the dark energy density grows and the potential  $\Phi_{\text{DE}}$  remains constant above the sound horizon  $c_s/\mathcal{H}$  while it decays below the sound horizon. Thus  $\Phi_{\text{DE}}$  is non-zero only for  $k < \mathcal{H}/c_{s, \text{DE}}$ . In contrast, at higher redshifts, since the dominant term in  $\Phi_{\text{GR}}$  comes from  $\gamma_{\text{wo, DE}}^{\text{Nb}}$ , the oscillatory and damped behavior of relativistic species appear. For the massive neutrinos case (right column plots),  $\Phi_{\nu}$  does not exhibit any oscillation as the neutrinos have already become non-relativistic. Massive neutrinos become non-relativistic for  $\sum m_{\nu} = 0.1$  eV at

$$z_{nr} = \frac{\sum m_{\nu}}{3.15 T_{0, \nu}} - 1 \sim 188,$$

with  $T_{0, \nu} \sim 1.9\text{K}$  being the temperature of the neutrinos today. The massive neutrino density perturbations under the horizon scale grow like dark matter after this epoch. The corresponding relative difference in the matter power spectra,  $P_{\text{Nb}}$  and  $P_{\text{N}}^2$ , is also shown in Figure 4.7, where the k-essence scalar field will roughly account for a 1% increase in the suppression of the N-Body matter power spectrum when compared to the Newtonian one at large scales.

As we can see from Figures 4.5 and 4.7, the effects modified gravity imprints in the matter power spectrum depends on the theory, i.e. parametrization, we choose. Since we are working with Horndeski theories it is instructive to consider different combinations of the  $\alpha_i$  functions, Equations (2.54-2.55):

- i) Only running:  $\alpha_{\text{M}} = \Omega_{\text{DE}}, \alpha_{\text{B}} = \alpha_{\text{T}} = 0;$
- ii) Only braiding:  $\alpha_{\text{B}} = \Omega_{\text{DE}}, \alpha_{\text{M}} = \alpha_{\text{T}} = 0;$
- iii) JBD-like:  $\alpha_{\text{B}} = -\alpha_{\text{M}} = \Omega_{\text{DE}}, \alpha_{\text{T}} = 0;$
- iv) Only tensor:  $\alpha_{\text{T}} = -\Omega_{\text{DE}}, \alpha_{\text{M}} = \alpha_{\text{B}} = 0.$

I will also vary the kineticity function,  $\alpha_{\text{K}}$ , in three constant values: 0.01, 1 and 100, in each of these models.

The results are presented in Figures 4.8 and 4.9. Each of the (i-iv) models above are presented in a given row, the left column plots refer to the full range of Fourier modes, while the right ones present a zoomed in version of the same interval. All curves are computed at  $z = 1$ . The plots show that the signal is greater at small wavenumbers, reaching up to above 80% for the case with just the braiding being non-zero (bottom row of Figure 4.8). The reason for this large amplitude at these scales can be understood by analyzing the scalar field fluctuation equation, (2.49). The dominant term at large scales in this equation is proportional to the synchronous gauge metric potential  $\eta$  times the sound speed. Since  $\eta$  does not depend on the kineticity – Equation (2.46) is independent of  $\alpha_{\text{K}}$  – it is the same for different values of  $c_{\text{K}}$  (remember our background is fixed for a  $\Lambda$ CDM background). As we have seen,  $c_{\text{s}}^2$  is inversely proportional to  $\alpha_{\text{K}}$ , Equation (2.66), which increases considerably the amplitude of the scalar field fluctuations, as seen in Figure 4.10, and consequentially affects the value at large scales of the relativistic correction.

The behavior at large scales seem to follow the same pattern in all models (i-iv), which indicates that these is a common behavior in all of them. At intermediate scales, however, the situation does vary for each theory. When there is only braiding (bottom row of Figure 4.8), at smaller

<sup>2</sup>Since  $G_{\text{eff}} = G_{\text{N}}$  in k-essence, we have that  $P_{\text{N}}^{\text{Geff}} = P_{\text{N}}$ .

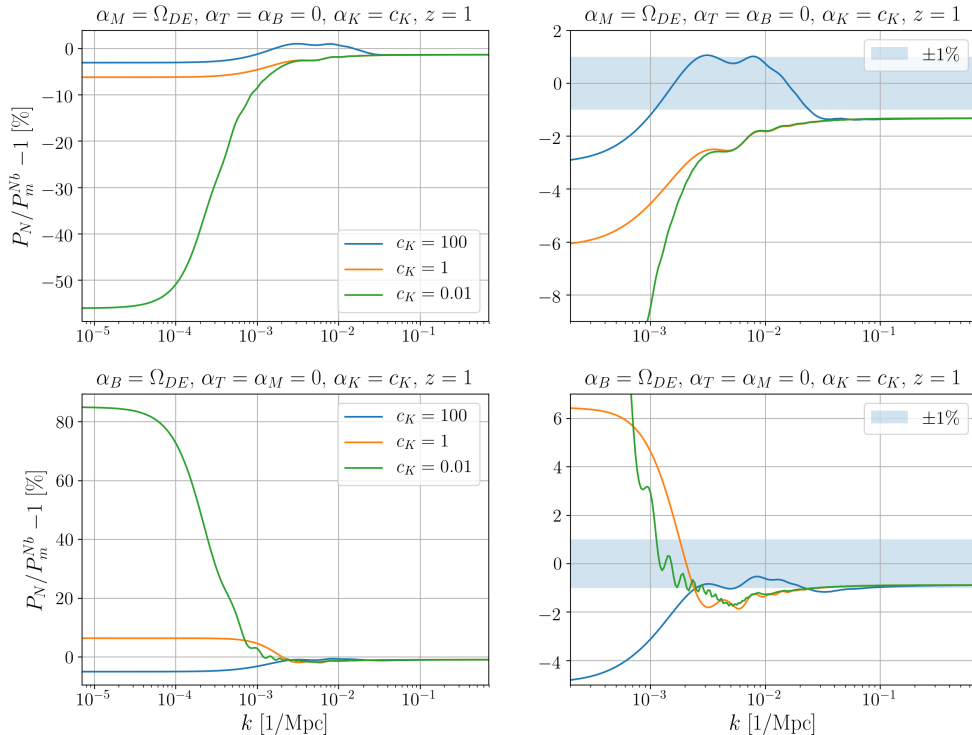


**Figure 4.8.** Relative difference between the linear Newtonian matter power spectrum  $P_N$ , Equation (4.28), and the matter power spectrum in  $N$ -body gauge in Horndeski gravity  $P_m^{\text{Nb}}$ , Equation (4.29). The top row corresponds to a modified gravity model in which we only have the running of the Planck mass,  $\alpha_M$ , and the bottom row corresponds to just braiding,  $\alpha_B$ . On the left hand side plots, we show the full interval in  $k$  while on the right we show only the scales probed by future LSS stage IV surveys. In all cases, we show three different kineticity functions,  $c_K = 100, 1, 0.01$ . We also plot the 1% deviation region (shaded blue). Our initial conditions for  $\delta_m^{\text{Nb}}$  are set at  $a = 0.01$  ( $z = 99$ ).

$k$  there is also a dependence on the value of the sound speed, as for  $c_K = 100$ , we have an enhancement of the relativistic power spectrum  $P_m^{\text{Nb}}$  with respect to the linear Newtonian one. For smaller values of the kineticity, however, after starting enhancing the power spectrum we see that there is a shift to the opposite direction, towards suppressing the power spectrum at intermediate to large scales.

This behavior is absent in the running-only case (top row of Figure 4.8), where the sign of the relative difference at large scales is independent of the sound speed. For the mixed case, Jordan-Brans-Dicke parametrization  $\alpha_M = -\alpha_B$ , the same independent of  $\alpha_K$  behavior is present. Unlike the former cases, however, the model in which there are only modifications of gravity in the tensor sector,  $\alpha_T \neq 0$ , the bulk of the modified gravity signal is not at small  $k$ , but at intermediate scales, where all the curves show a bump in the signal, and then show no enhancement or suppression at large scales. Although not shown in this work, if the opposite sign of the  $c_M, c_B$  and  $c_T$  constants is chosen, the effect on the power spectrum becomes opposite.

The final range of wave-numbers is at small scales, e.g.,  $k > 10^{-1} \text{ Mpc}^{-1}$ . In this range, in all but the  $\alpha_T \neq 0$  case, there is a vertical shift with respect to the 0% line. This displacement is caused by the gravitational constant,  $G_{\text{eff}}$ . As we can see from (4.42), at linear order, this function is scale-independent, and one can simply interpret it as a mere re-scaling of Newton's gravitational constant, and that's why we only see this effect as a vertical shift. As mentioned

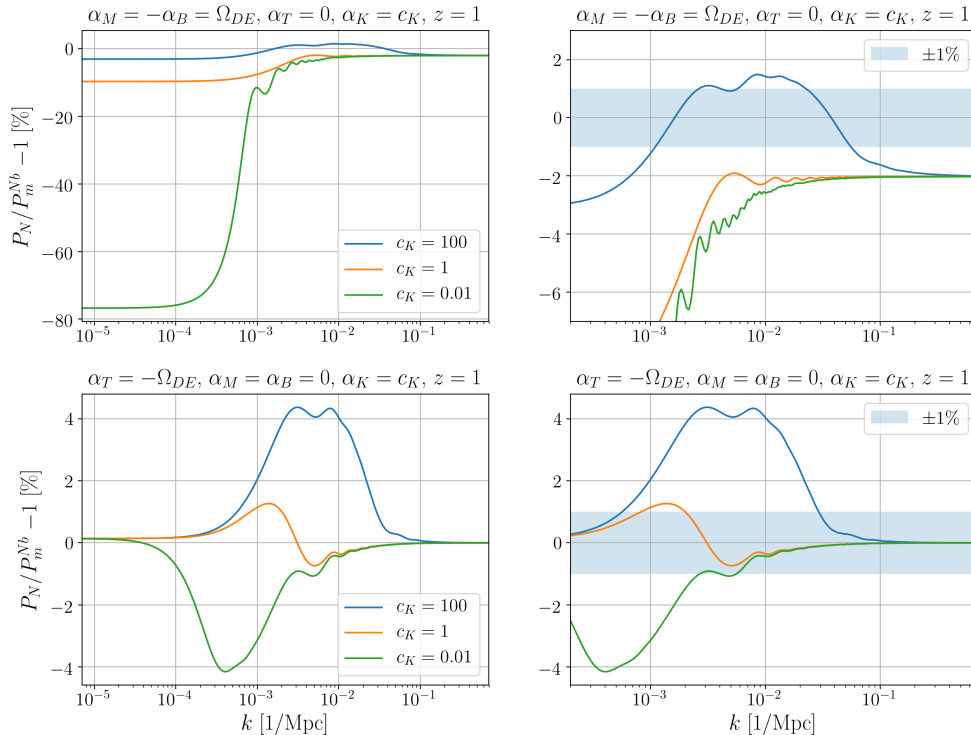


**Figure 4.9.** Relative difference between the linear Newtonian matter power spectrum  $P_N$ , Equation (4.28), and the matter power spectrum in  $N$ -body gauge in Horndeski gravity  $P_m^{\text{Nb}}$ , Equation (4.29). The top row corresponds to a modified gravity model with a Jordan-Brans-Dicke (JBD) parametrization,  $\alpha_M = -\alpha_B$ , and the bottom row shows the case only with the tensor modification,  $\alpha_T$ . On the left hand side plots, we show the full interval in  $k$ , and on the right we show the interval of scales probed by future LSS stage IV surveys. In all cases we show three different kineticity functions,  $c_K = 100, 1, 0.01$ . We also plot the 1% deviation region (shaded blue). Our initial conditions for  $\delta_m^{\text{Nb}}$  are set at  $a = 0.01$  ( $z = 99$ ).

before, in this chapter I'm focusing on linear effects, to be more precise, I'm describing how linear densities affect the matter power spectrum. Of course, in the case of photons and massless neutrinos, in the scales we are concerned they are always linear, and therefore the discussion here presented is the final word about it. For massive neutrinos with masses of around 0.15 eV neutrinos can be treated linearly, as their non-linear clustering should not affect much the dark matter power spectrum. CDM and baryons are coupled, and we know that their density increases as we move to smaller scales due to the clustering of matter, therefore they must have non-linear corrections included. For dark energy, however, the situation is a bit trickier. Since we don't know much about it so far, we don't know when (or even if) it becomes non-linear. For this non-linearities will always depend on the specific theory of gravity, for instance, for quintessence,  $c_s^2$  is always one, and therefore the scalar field never clusters. However, in general Horndeski theories the sound speed is a function of time, and therefore it is allowed to cluster freely. The scale until which dark energy clusters is given by the dark energy sound horizon:

$$k_H = \frac{aH\sqrt{2 - \alpha_B}}{c_s\sqrt{2}}, \quad (4.43)$$

if a given mode is below  $k_H$  then the amplitude of the dark energy density contrast will grow, however, once it crosses the horizon, the mode will eventually decay. There is one part of the dark energy perturbations that will always have non-linear corrections added, and we already saw

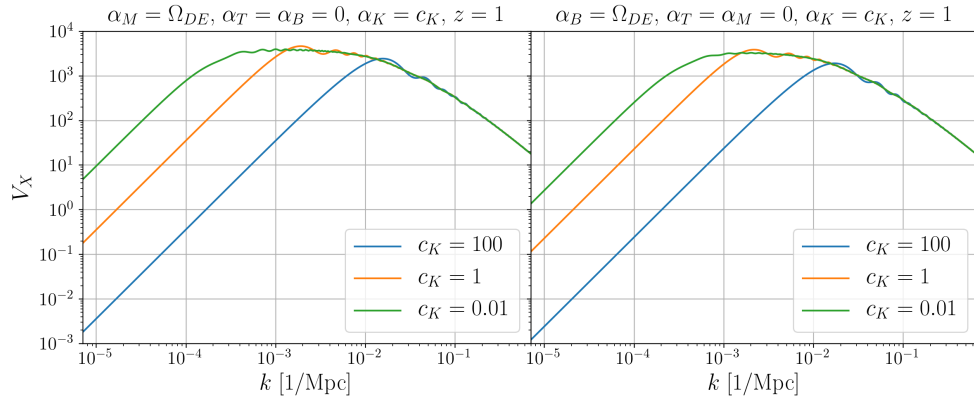


**Figure 4.10.** Scalar field fluctuation,  $V_X$ , as a function of scale for two different gravity models:  $\alpha_K = c_K$  and  $\alpha_M = \Omega_{DE}$ ,  $\alpha_K = c_K$  and  $\alpha_B = \Omega_{DE}$ , at fixed redshift,  $z = 1$ . We vary the kineticity in three different constant values,  $c_K = 100, 1$  and  $0.01$ . We can see that at large scales, smaller values of  $c_K$  have larger amplitudes. This behavior causes the enhancing of the signal at small  $k$  seen in Figures 4.8 and 4.9.

which one. When we take the QSA limit, we see that there is a part of  $\delta\rho_{DE}$  that is proportional to the matter density perturbations, which become non-linear, and therefore must be correctly modelled. The other part of the DE perturbations,  $\delta\rho_{DE,rel.}$  can become non-linear, and then we would need to solve the scalar field fluctuation equation of motion, 2.49, at second order to correctly account for non-linearities. However, we will not focus on this topic now, as we are interested only on linear densities.

As the N-Body gauge provides a way to introduce the linear relativistic effects from photons, neutrinos and dark energy (described by a scalar field or not), we want a way to safely introduce the corrections into Newtonian simulations, without spoiling the regime of validity of the N-Body gauge formalism. In other words, we want to smoothly transition from the regime where linear perturbation theory is valid, to the regime where Newtonian simulations accurately describe the density fields, and therefore non-linearities can safely be included in the terms proportional to the matter density perturbations. One way to that is to compare the ratio between the full dark energy density perturbation with its QSA counterpart. As we have seen the QSA counterpart is the one in which non-linear corrections of the matter density perturbations will be introduced at small scales. The relativistic part, however, will only have to be treated non-linear if at small scales it is non-negligible when compared to the QSA quantity.

Figure 4.11 shows the separation of these two effects and the impact of relativistic corrections in two models at  $z = 1$ . The top panels show the relative difference in percentage between the linear Newtonian matter power spectrum with and without  $G_{eff}$  effects,  $P_N^{G_{eff}}$  (solution of 4.37) and  $P_N$  (solution of 4.28) respectively, and the N-body gauge matter power spectrum, in Horndeski gravity,  $P_m^{Nb}$  (solution of 4.38). The bottom panels show the square of the sound speed of the scalar field and the relative difference between the energy density perturbations of dark energy and its QSA counterpart. As modified gravity Newtonian simulations use the QSA limit, a good check to see if our formalism will have a smooth transition from linear perturbation theory to Newtonian gravity is to quantify the agreement between the full and the QSA contribution to dark energy density perturbations. We chose to present models that have a below 0.1% agreement between  $\delta\rho_{DE}^{Nb}$  and  $\delta\rho_{DE}^{QSA}$ , at scales  $k \gtrsim 0.1 \text{ Mpc}^{-1}$ . This is roughly the scale at which linear theory breaks, and where the Newtonian approximation is correctly describing gravity. The top right plots of Figures 4.11 show the effects coming purely from relativistic effects of modified gravity. The deviations between both spectra may be above the 1% level, the usual required accuracy in

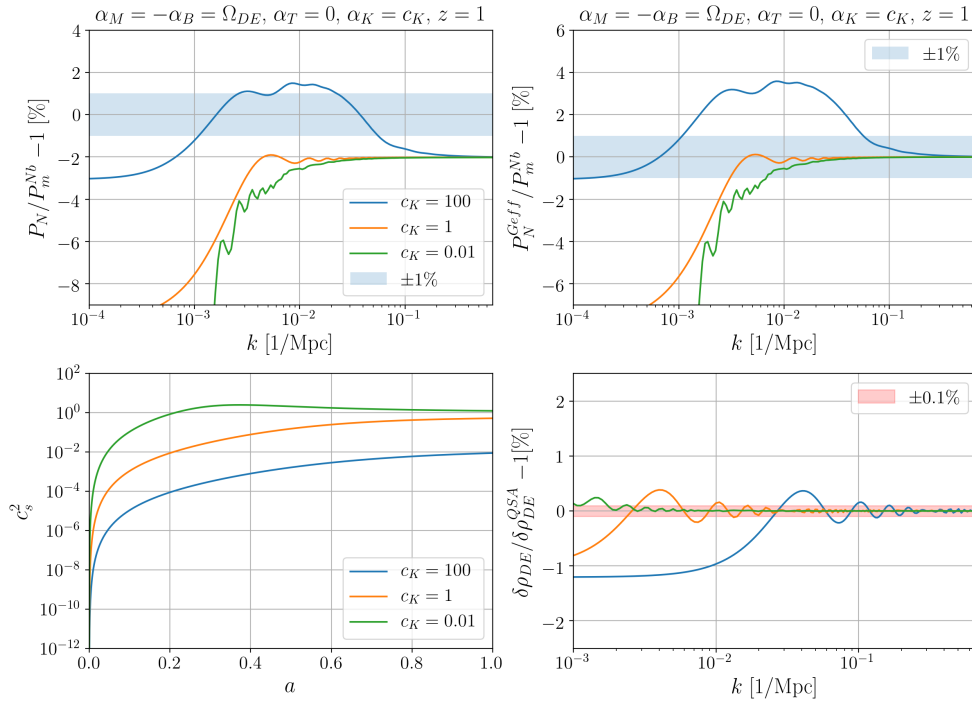


**Figure 4.11.** Impact of separating modified gravity effects on small scales in the matter power spectrum. **Top left:** Relative difference between the linear Newtonian matter power spectrum described by Equation (4.28), and the N-body gauge matter power spectrum in Horndeski gravity at redshift  $z = 1$ . **Top right:** Relative difference between the linear Newtonian matter power spectrum with  $G_{\text{eff}}$ ,  $P_N^{G_{\text{eff}}}$ , described by Equation (4.37), and the N-body gauge matter spectrum in Horndeski gravity at redshift  $z = 1$ . **Bottom left:** Squared sound speed of the scalar field as a function of the scale factor. **Bottom right:** Relative difference between the full dark energy density perturbation, Equation (2.80), and its QSA counterpart, Equation (3.3). All plots are for the same gravity model, Jordan-Brans-Dicke parametrization, and we only vary the values of the kineticity,  $c_K = 100, 1, 0.01$ . The top right plot shows the 1% deviation region (shaded blue) in which we can see that purely relativistic effects are not captured by  $G_{\text{eff}}$ , and exceed the percent-level deviation threshold at scales probed by future LSS stage IV surveys. In the bottom right plot, we show the 0.1% deviation interval (shaded red), where the relativistic contribution decay when we move to larger values of  $k$ , thus, ensuring a smooth transition to the regime of Newtonian gravity. This exhibits the validity of our formalism to implement relativistic effects in Newtonian N-body simulations. Our initial conditions for  $\delta_m^{\text{Nb}}$  are set at  $a = 0.01$  ( $z = 99$ ).

these simulations. This shows that in order to make consistent simulations in modified gravity we must include the relativistic source term,  $\delta\rho_{\text{GR}}$ , in simulations.

For completeness Figures 4.12 and 4.13 show the same plots as Figure 4.11, but for a smaller proportionality constant and different parametrization, respectively. These plots are relevant to show that as we move to stage IV LSS surveys, that will probe the Universe at higher redshifts and larger scales, we clearly see that the relativistic deviations can account for more than 1% difference when compared to the usual Newtonian spectra. The framework developed in this thesis can be used to construct these number counts, from the relativistic output of N-body simulations, using ray-tracing techniques. In Appendix A I discuss the consistency checks I have performed in order to validate the implementation of the N-Body gauge in the `hiclass` code.

A last remark on the results presented in this subsection concerns the oscillatory feature present in the relative difference between  $P_{\text{Nb}}$  and  $P_N$  (and  $P_N^{G_{\text{eff}}}$ ). We can see that in large and interme-

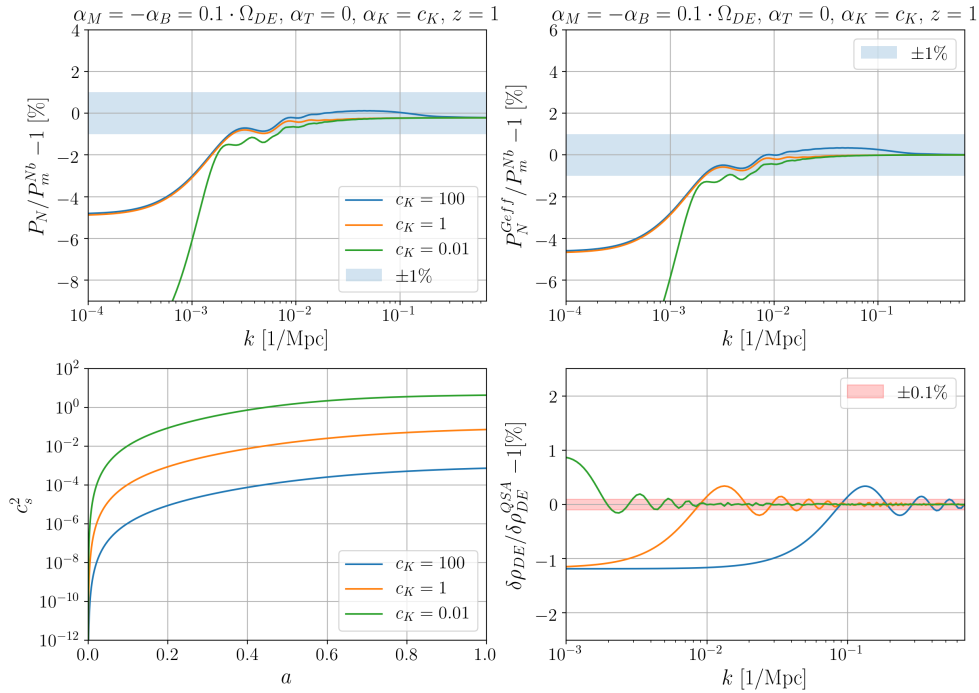


**Figure 4.12.** Same as Figure 4.11 but with a different value for the proportionality constant,  $c_B = -c_M = 0.1$ .

diate scales, there is an emergence of wiggles at these scales. This feature is a purely relativistic effect caused by the scalar field.

From the scales in which these oscillations appear, and allied with the fact that QSA contributions do not oscillate since dynamical equations become constraint equations in the QSA, we can identify these features as purely relativistic effects of modified gravity, and they reveal directly the dynamical nature of the additional degree of freedom. Figure 4.14 shows the matter power spectrum in the N-body gauge on the left, and the lensing potential on the right. We can see that oscillations are present in both of these observables, and therefore can be probed by future LSS and 21cm intensity mapping surveys.

To understand the origin of these oscillations, we also plot the evolution of the ratios  $V_X/V_X^{\text{QSA}}$  and  $\delta_m^{\text{Nb}}/\delta_m^{\text{S}}$  as a function of wavenumber,  $k$ , and conformal time,  $\tau$ , in Figure 4.15.  $V_X/V_X^{\text{QSA}}$  minimises the non-oscillatory contributions from the QSA, while  $\delta_m^{\text{Nb}}/\delta_m^{\text{S}}$  also allows us to highlight these features in the matter density contrast in the N-body gauge, since at late times and inside the horizon, the N-body gauge and the synchronous gauge are approximately the same. This highlights that any difference in behavior between the two is a purely relativistic effect.

From the scalar field fluctuation equation, (2.49), the only way acoustic waves may appear is when  $V_X$  crosses the dark energy (DE) sound horizon, defined in Equation (4.43). When a given  $k$  mode enters the sound horizon, pressure gradients from the scalar field act to counter balance the gravitational attraction. Therefore, as we can see in Figure 4.15, when the scalar field fluctuation of a specific Fourier mode crosses the sound horizon, gravity acoustic oscillations (GAOs) emerge. These GAOs, however, are damped by two effects: the damping term multiplying  $V_X'$  in Equation (2.49), and when matter density perturbations start to dominate  $V_X$ . The former is represented by the blue lines in Figure 4.15, and we can see that modes must also be inside this scale to oscillate.

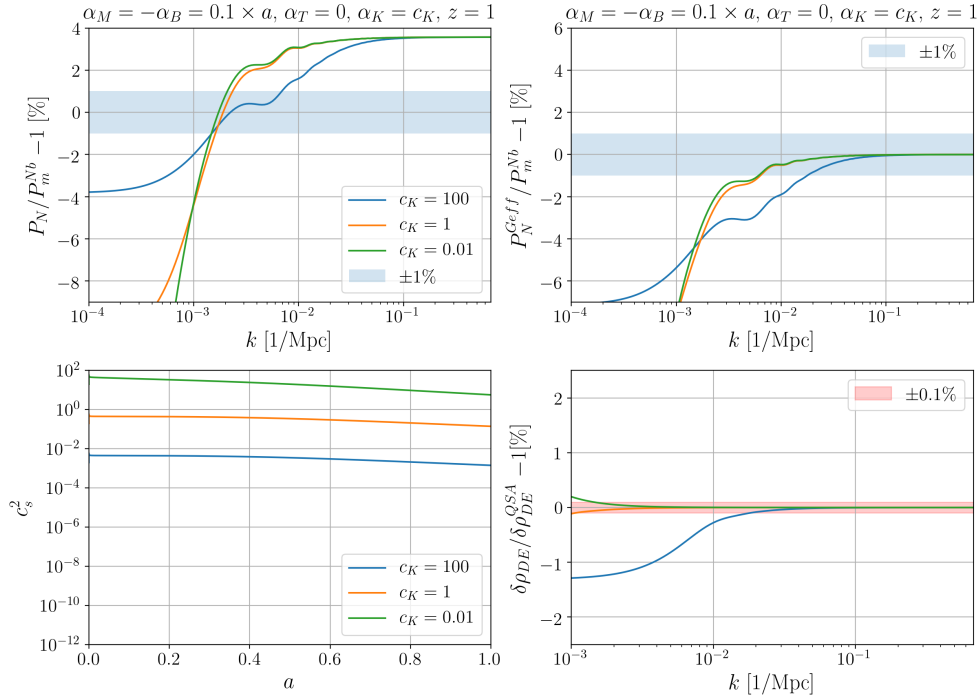


**Figure 4.13.** Same as Figure 4.11 but with a different parametrization,  $\alpha_B = -\alpha_M = 0.1 \cdot a$ .

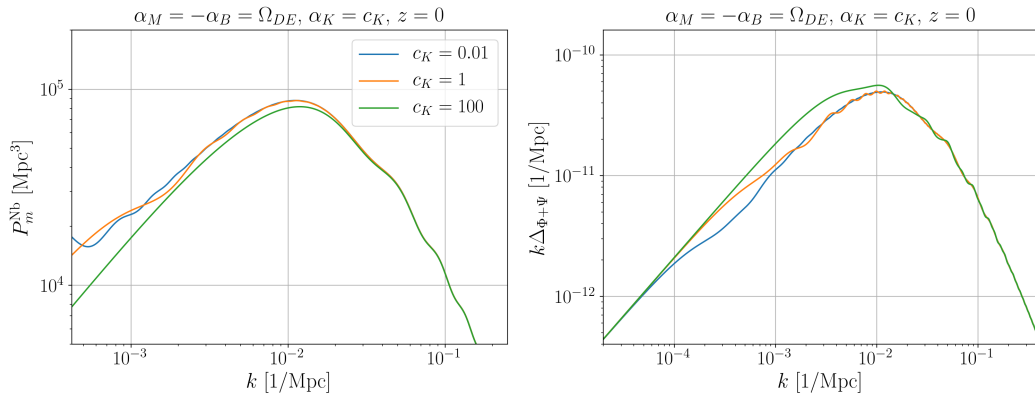


**Figure 4.14.** Oscillatory features in observable quantities. **Left:**  $N$ -body gauge matter power spectrum at redshift  $z = 0$ . **Right:** Lensing potential transfer function for the same model. Gravity acoustic oscillations appear in the matter power spectrum only in the model with low values of  $c_K$  at scales below the scale of matter-radiation equality,  $k_{\text{eq.}} \sim 10^{-2} \text{ Mpc}^{-1}$ . Since the parametrization is chosen to be proportional to the fractional dark energy density,  $\Omega_{\text{DE}}$ , modified gravity effects will only affect the matter power spectrum during the late stages of matter domination. Therefore these features do not affect the BAO oscillations, where the QSA contribution is already dominating the dark energy density perturbations, thus damping the GAOs. The same smooth behavior at small  $k$  values for lower values of the kinicity is also present in the lensing potential transfer function. However, due to the presence of anisotropic stress (gravitational slip in the Newtonian gauge potentials), for  $c_K = 100$ , the oscillations are also present at values of  $k$  bigger than  $k_{\text{eq.}}$  in the lensing potential.

Gravity acoustic oscillations are an intermediate-time effect, originating during matter domination. They are caused by the rapid evolution of the dark energy sound horizon, which at early

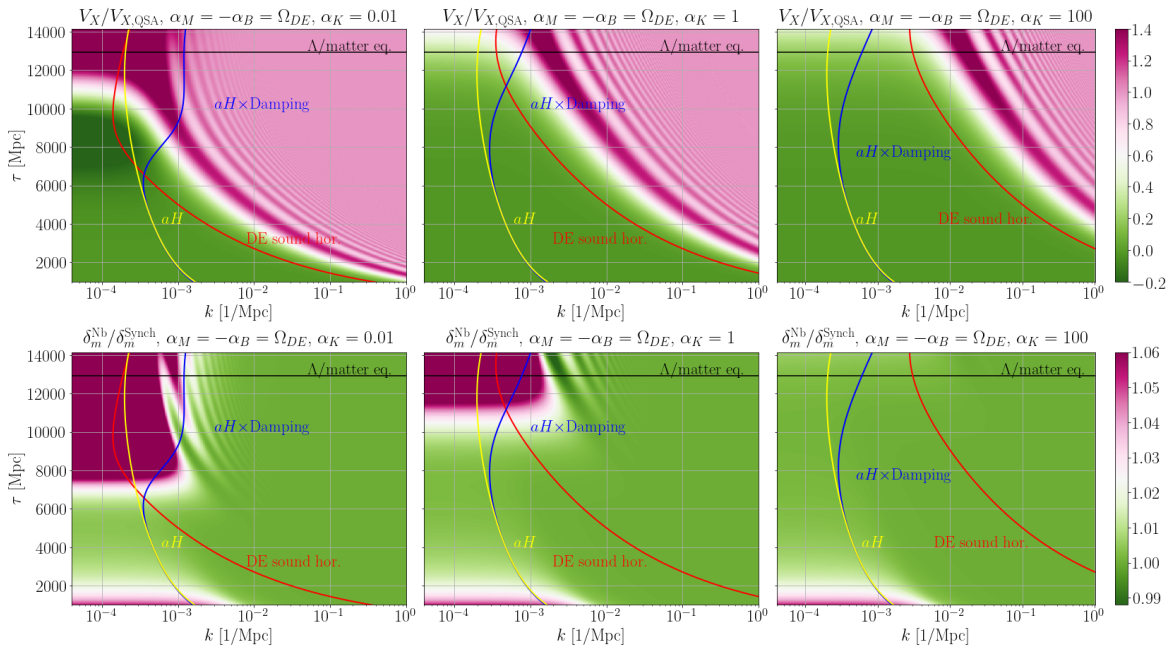


**Figure 4.15.** Scale and time dependence of GAOs. **Top row:** Two-dimensional  $(k, \tau)$  plot of the ratio  $V_X/V_X^{\text{QSA}}$  in Jordan-Brans-Dicke gravity, for three different values of kineticity,  $c_K = 0.01, 1, 100$ . **Bottom row:** Two-dimensional plot of the ratio  $\delta_m^{\text{Nb}}/\delta_m^{\text{Synch}}$  in the same theory, for three different values of kineticity,  $\alpha_K = 0.001, 1, 100$ . The dark energy sound horizon (red curve) Equation (4.43), the damping term (blue curve) in Equation (2.49) and the cosmological horizon (yellow curve)  $aH$  are also plotted. The oscillations in the top row plots occur once a given  $k$  mode crosses the dark energy sound horizon and damping scale, and, once inside this region, get slowly damped by the QSA contribution. These oscillations are seen in the matter density contrast for cases in which the crossing happens at scales much larger than the QSA regime at large  $k$ , as seen in the bottom left and center plots.

times may be orders of magnitude smaller than the Hubble horizon,  $(aH)^{-1}$ . As we have seen in Figure 4.11, the sound speed of the scalar field can start very small at early times, and then goes to order one values at late times, driving the evolution of  $k_H$ . This makes modes that were outside the dark energy sound horizon cross inside the horizon, introducing pressure gradients and hence oscillations in the gravity sector.

From the previous discussion,  $c_s^2$  depends on the choice of parametrization of the kineticity function. In the present work we fixed this to be constant throughout the expansion of the Universe. However, we know from other works in the literature that gravity acoustic waves were not present if a different parametrization for  $\alpha_K$  was chosen. Specifically, if  $\alpha_K$  was proportional to the fractional dark energy density,  $\Omega_{\text{DE}}$ , a common choice in the literature, we know that the sound speed of the scalar field is always of the same order in time, apart from a very brief interval at early times. Therefore, the dark energy sound horizon will exhibit a similar behavior to the cosmological Hubble horizon for most of the expansion history. While this discussion revolves around the use of parametrizations of Horndeski theories, in principle, we can find a covariant theory in which the sound speed evolves by orders of magnitude, specifically during matter domination, via an appropriate choice of the Horndeski functions  $G_i$ 's.

It is important to stress that GAOs do not affect the BAO peak in the matter power spectrum. This is due to the fact that the BAO scale lies inside the regime where the QSA already holds.

# Non-Linear Universe

*In this chapter I will lay down some of the mathematical tools to describe the non-linear Universe. I will start by describing higher order perturbation theories in two different, but corresponding, representations: Eulerian and Lagrangian. I will then move the discussion to introduce the idea behind a fast approximate method to generate the non-linear matter density field, the COmoving Lagrangian Approach (COLA) approach.*

## 5.1. Large Scale Structure of the Universe

In the previous chapter we have seen the remarkable power cosmological perturbation theory gives us to study modified gravity in our Universe. Linear theory has been a cornerstone of modern cosmology, and has solidified its role as the fundamental framework to test gravity in the past LSS surveys. However, as we move to the next stage LSS surveys, such as DESI and Euclid, which will become online fairly soon, we are now in a critical point in the modified gravity community. With the unprecedented precision new data will deliver to us, the theoretical side is now pushed by community to act and move to non-linear scales, in order to fully explore the potential stage IV LSS surveys will give. In the beginning of this century, gravitational instability has finally assumed a fundamental role in giving rise to the intricate structure we see in our Universe. What began in the 70s and 80s with Peebles and Yu [24] as well as Zel'dovich [112], was fully understood by others in the next decades [113, 114, 115]. Higher order perturbation theory in the Eulerian frame, also known as Standard Perturbation Theory (SPT), as well in Lagrangian [116], was finally seen as a mature and solid framework to work with to better understand structure formation in the quasi-linear scales of our Universe. Theoretical models were tested with synthetic data generated by cosmological Newtonian simulations. This has ultimately lead us to sophisticated methods of extracting information from the two-point correlation function of our Universe, which then lead to powerful tools to do data analysis in the linear and quasi-linear regime, opening the doors to the now well-established BAO data, and the first constraints using RSD.

In this chapter I will give a brief description on the fundamentals of perturbation theory in LCDM and modified gravity, as well as discuss some concepts and methods of N-Body codes.

## 5.2. Growth in LCDM

Galaxies, quasars and other structures act as biased tracers of the underlying invisible distribution of CDM in the Universe. LSS surveys aim to map the position of galaxies in a portion of the sky

by computing statistical measures of clustering in the sky using N-point functions. The simplest clustering statistics is the 2 point correlation function (2PCF), given by:

$$\xi(\mathbf{x}, \mathbf{y}) = \langle \delta(\mathbf{x})\delta(\mathbf{y}) \rangle, \quad (5.1)$$

in real space. As we know, we have up until now no proof that the Copernican Principle has been refuted, and thus we are left with homogeneity and isotropy. The former states that the density field  $\delta(\mathbf{a})$  is invariant under translations by a constant displacement  $\mathbf{l}$ ,  $\delta(\mathbf{x}) = \delta(\mathbf{x} - \mathbf{l})$ . The latter forces our density field to be the same by rotations,  $\delta(R^{-1}\mathbf{x}) = \delta(\mathbf{x})$ . Both of these symmetries then imply that  $\xi(\mathbf{x}, \mathbf{y})$  is actually a mere function of the modulus of the distance,  $r$ , between the two points in space  $(\mathbf{x}, \mathbf{y})$ :

$$\xi(\mathbf{x}, \mathbf{y}) = \xi(r). \quad (5.2)$$

To better understand the 2PCF we can think as the following: suppose we have two small regions of space  $\delta V_1$  and  $\delta V_2$  separated by a distance  $r$ . Then, the expected number of pairs of galaxy to be found with one galaxy in  $\delta V_1$  and another in  $\delta V_2$  is:

$$\langle n_{\text{pair}} \rangle = \bar{n}^2 [1 + \xi(r)] \delta V_1 \delta V_2, \quad (5.3)$$

where  $\bar{n}$  is the mean number of galaxies per unit of volume. It is now easily seen that  $\xi$  measures the excess of clustering given by a distance a  $r$ . If  $\xi = 0$ , the galaxies are not clustered, thus are equally spaced. If we have  $\xi > 0$  we have galaxies closer together, while  $\xi < 0$  farther apart. The same power spectrum we have seen in the last chapter built using the primordial curvature perturbations, the growth function and the transfer function is just the Fourier transform of this 2PCF, and since we have homogeneity and isotropy:

$$P(k) = \int \xi(r) e^{i\mathbf{k}\cdot\mathbf{r}} d^3r, \quad (5.4)$$

$$\xi(r) = \int P(k) e^{-i\mathbf{k}\cdot\mathbf{r}} \frac{d^3k}{(2\pi)^3}. \quad (5.5)$$

### 5.2.1. SPT in LCDM

This section is developed following references [26, 117, 113]. Since CDM particles are non-relativistic, at scales much smaller than the Hubble radius the equations of motion reduce essentially to those of Newtonian gravity. From a set of CDM particles in an expanding Universe at position  $\mathbf{r}$ , its density is given by  $\rho(\mathbf{r})$ , and the acceleration generated by this ensemble of particles is then

$$\frac{d\mathbf{v}}{dt} = -\frac{d\phi}{d\mathbf{r}}, \quad (5.6)$$

where  $\mathbf{v}$  is the velocity field. Now, position  $\mathbf{r}$  is just the position vector in spherical coordinates, however, it would be a lot easier if we instead changed our spatial coordinates to a system where it is comoving with our expanding Universe, therefore, we will instead use from now on the notion of comoving coordinates, which follow the evolution of the Hubble flow:

$$\mathbf{r} = a\mathbf{x}. \quad (5.7)$$

The derivative of this Equation gives us:

$$\mathbf{u}(\mathbf{x}, t) = \mathbf{v} - aH\mathbf{x}, \quad (5.8)$$

and the second derivative:

$$\dot{\mathbf{u}}(\mathbf{x}, t) = \frac{1}{a} \left[ \frac{d}{d\tau} (aH) \mathbf{x} + aH\dot{\mathbf{x}} + \ddot{\mathbf{x}} \right] = -\frac{1}{a} \nabla \phi, \quad (5.9)$$

where in the last line I used Equation (5.6). The term proportional to the position is a peculiar term, introduced by the Hubble flow, we can move it to the RHS of this equation and write:

$$\phi = \frac{1}{2} \frac{d}{d\tau} (aH) x^2 + \Phi, \quad (5.10)$$

which then rewrites the geodesic equation for position  $\mathbf{x}$  as:

$$\ddot{\mathbf{x}} + aH\dot{\mathbf{x}} = \nabla \Phi. \quad (5.11)$$

We can also find the Poisson equation for the peculiar potential  $\Phi$  if we take the Laplacian of both sides of Equation (5.10):

$$\nabla^2 \Phi(\mathbf{x}, t) = a^2 \nabla_{\mathbf{r}}^2 \phi(\mathbf{r}, t) + \frac{a^2}{2} \left[ -\frac{H^2 \Omega_m}{2} + \frac{\Lambda}{3} \right] \quad (5.12)$$

$$= \frac{3}{2} \Omega_m H^2 a^2 \delta(\mathbf{x}, t). \quad (5.13)$$

Since we are considering a large number of CDM particles, it is better to study the evolution of this ensemble by considering their phase space distribution evolution,  $f(\mathbf{x}, \mathbf{p}, t)$ , where  $\mathbf{p}$  is the peculiar momentum. As seen before, its evolution is governed by the Boltzmann equation (1.91), however, as CDM particles are collisionless the RHS of that equation is identically zero:

$$\frac{df}{dt} = \frac{\partial f}{\partial t} + \frac{\mathbf{p}}{ma^2} \cdot \nabla f - m \nabla \Phi \cdot \frac{\partial f}{\partial \mathbf{p}} = 0. \quad (5.14)$$

From Equation (1.94) we find the momentum moments of the phase space distribution:

$$\int d^3 \mathbf{p} f(\mathbf{x}, \mathbf{p}, t) = n(\mathbf{x}, t), \quad (5.15)$$

$$\int d^3 \mathbf{p} \frac{\mathbf{p}}{am} f(\mathbf{x}, \mathbf{p}, t) = \rho(\mathbf{x}, t) \mathbf{u}(\mathbf{x}, t), \quad (5.16)$$

$$\int d^3 \mathbf{p} \frac{p_i p_j}{a^2 m^2} f(\mathbf{x}, \mathbf{p}, t) = \rho(\mathbf{x}, t) u_i(\mathbf{x}, t) u_j(\mathbf{x}, t) + \sigma_{ij}(\mathbf{x}, t) \quad (5.17)$$

where  $n(\mathbf{x}, t)$  is the number density and  $\sigma_{ij}(\mathbf{x}, t)$  is the anisotropic stress of the distribution. This last quantity tells us how much the CDM particles are deviating from its single stream trajectory. During the early stages of the gravitational collapse this quantity is negligible, and, therefore, we will discard it in the following. Taking the zeroth and first moments of Equation (5.14) and the Poisson equation, we have the so called Vlasov-Poisson equations:

$$\frac{\partial \delta(\mathbf{x}, t)}{\partial t} + \frac{1}{a(t)} \nabla \cdot [(1 + \delta(\mathbf{x}, t)) \mathbf{u}(\mathbf{x}, t)] = 0, \quad (5.18)$$

$$\frac{\partial \mathbf{u}(\mathbf{x}, t)}{\partial t} + H(t) \mathbf{u}(\mathbf{x}, t) + \frac{1}{a(t)} \mathbf{u}(\mathbf{x}, t) \cdot \nabla \mathbf{u}(\mathbf{x}, t) = -\frac{1}{a(t)} \nabla \Phi(\mathbf{x}, t), \quad (5.19)$$

$$\nabla^2 \Phi = \frac{3}{2} \Omega_m H^2 a^2 \delta(\mathbf{x}, t) \quad (5.20)$$

where  $\nabla \mathbf{u}(\mathbf{x}, t)$  is the directional derivative of  $\mathbf{u}(\mathbf{x}, t)$  along the  $\mathbf{x}$  direction. We can see that in Equations (5.18-5.19) we have terms that go beyond linear order, and, if we stick to only first order terms the Equations become:

$$\frac{\partial \delta(\mathbf{x}, t)}{\partial t} + \frac{1}{a(t)} \nabla \cdot \mathbf{u}(\mathbf{x}, t) = 0, \quad (5.21)$$

$$\frac{\partial \mathbf{u}(\mathbf{x}, t)}{\partial t} + H(t) \mathbf{u}(\mathbf{x}, t) = -\frac{1}{a(t)} \nabla \Phi(\mathbf{x}, t). \quad (5.22)$$

So far we have not made any assumptions on the nature of the peculiar velocity field, and, therefore, we will decompose it using Helmholtz theorem so we can further understand it:

$$\mathbf{u}(\mathbf{x}, t) = -\nabla \Theta(\mathbf{x}, t) + \mathbf{w}(\mathbf{x}, t), \quad (5.23)$$

with  $\nabla \Theta(\mathbf{x}, t)$  and  $w = \nabla \times \mathbf{u}(\mathbf{x}, t)$  being respectively the curl and divergent free components of  $\mathbf{u}(\mathbf{x}, t)$ . I'll go further and also define  $\theta(\mathbf{x}, t) = \nabla \cdot \nabla \Theta(\mathbf{x}, t)$ . Taking respectively the divergent and the curl of the linear Euler equation of (5.21), we find:

$$\frac{\partial \theta(\mathbf{x}, t)}{\partial t} + H(t) \theta(\mathbf{x}, t) + \frac{3}{2} \Omega_m H^2(t) a(t) \delta(\mathbf{x}, t) = 0, \quad (5.24)$$

$$\frac{\partial \mathbf{w}(\mathbf{x}, t)}{\partial t} + H(t) \mathbf{w}(\mathbf{x}, t) = 0, \quad (5.25)$$

where I used Equation (5.12) in the first line to remove the Poisson potential from the equation. The solution of the Equation (5.25) gives us that the vorticity of the field decays as  $\mathbf{w}(\mathbf{x}, t) \propto 1/a(t)$ , therefore, the initial velocity will always decays in an expanding Universe. The full non-linear equation for  $\mathbf{w}(\mathbf{x}, t)$  is:

$$\frac{\partial \mathbf{w}(\mathbf{x}, t)}{\partial t} + H(t) \mathbf{w}(\mathbf{x}, t) - \nabla \times [\mathbf{u}(\mathbf{x}, t) \times \mathbf{w}(\mathbf{x}, t)] = 0, \quad (5.26)$$

where we can see that if we have zero initial vorticity, then this will remain so throughout the evolution of the Universe. If  $\mathbf{w}(\mathbf{x}, t_i) \neq 0$ , then the last term of Equation (5.26) shows that the vorticity can be amplified. The investigation of the impact of the vorticity in the growth of structure has been studied with the code GRAMSES [118]. However, throughout this thesis, I will remain considering zero initial vorticity, and with this the peculiar velocity is completely defined by its curl-free component,  $\theta(\mathbf{x}, t)$ . Note, however, that if we had not set  $\sigma_{ij} \approx 0$  for our ensemble of CDM particles, this term would be present as a source term in Equation (5.26), and then we could have a growing solution of vorticity.

I define the following Fourier transform conventions:

$$f(\mathbf{x}) = \int \frac{d^3 k}{(2\pi)^3} \tilde{f}(\mathbf{k}) e^{i\mathbf{k} \cdot \mathbf{x}}, \quad (5.27)$$

$$\tilde{f}(\mathbf{k}) = \int d^3 x f(\mathbf{x}) e^{-i\mathbf{k} \cdot \mathbf{x}}, \quad (5.28)$$

I'll also rewrite Equations (5.18-5.19) using conformal time, and taking the divergence of Equation (5.19):

$$\frac{\partial \delta(\mathbf{x}, \tau)}{\partial \tau} + \theta(\mathbf{x}, \tau) = -\delta(\mathbf{x}, \tau) \theta(\mathbf{x}, \tau) - u^j(\mathbf{x}, \tau) \partial_j \delta(\mathbf{x}, \tau), \quad (5.29)$$

$$\frac{\partial \theta(\mathbf{x}, \tau)}{\partial \tau} + aH\theta(\mathbf{x}, \tau) + \nabla^2 \Phi = -u^j(\mathbf{x}, \tau) \partial_j \theta(\mathbf{x}, \tau) - \partial_k u^j(\mathbf{x}, \tau) \partial_j u^k(\mathbf{x}, \tau) \quad (5.30)$$

where I decided to explicitly show the component of the quantities. Let's recall the linear solution, which at sufficiently large scales linear theory is an accurate description of the Universe, and Equations (5.29-5.30) become:

$$\frac{\partial \delta(\mathbf{x}, \tau)}{\partial \tau} + \theta(\mathbf{x}, \tau) = 0, \quad (5.31)$$

$$\frac{\partial \theta(\mathbf{x}, \tau)}{\partial \tau} + aH\theta(\mathbf{x}, \tau) + \nabla^2 \Phi = 0. \quad (5.32)$$

Taking the time derivative of the first equation and using the second, we get the usual second order differential growth equation for the linear density field:

$$\ddot{\delta}_m + aH\dot{\delta}_m - 4\pi G\rho_m\delta_m = 0. \quad (5.33)$$

If we divide this whole equation by the linear density today, we get:

$$\ddot{D} + aH\dot{D} - 4\pi G\rho_m D = 0, \quad (5.34)$$

where  $D$  is called the linear growth factor. This ODE has two solutions:

$$D(\tau) = D_+(\tau) + D_-(\tau), \quad (5.35)$$

a growing and a decaying solution, respectively. The linear density field can then be written as:

$$\delta(\mathbf{k}, \tau) = D_+(\tau)\delta_0(\mathbf{k}) + D_-\delta_0(\mathbf{k}), \quad (5.36)$$

where  $\delta_0(\mathbf{x}, \tau_{\text{ini}})$  is the initial density field at a given reference epoch. As we are interested in the growth of structure, we will from now on refer to as the linear growth factor the solution  $D_+(\tau)$ . At linear level, we have a one-to-one correspondence between the matter density field and its velocity divergence (Euler's equation):

$$\theta^{(1)}(\mathbf{x}, \tau_{\text{ini}}) = -aHf\delta^{(1)}(\mathbf{x}, \tau), \quad (5.37)$$

with  $f = d \ln D_+ / d \ln a$  being the growth rate.

Now, considering beyond leading order terms, we can write Equations (5.29-5.30) in Fourier space as:

$$\delta'(\mathbf{k}, \tau) + \theta(\mathbf{k}, \tau) = \int \frac{d^3 k_1}{(2\pi)^3} \int \frac{d^3 k_2}{(2\pi)^3} (2\pi)^3 \delta_D^{(3)}(\mathbf{k} - \mathbf{k}_1 - \mathbf{k}_2) \times \alpha(\mathbf{k}_1, \mathbf{k}_2) \delta(\mathbf{k}_1, \tau) \theta(\mathbf{k}_2, \tau), \quad (5.38)$$

$$\theta'(\mathbf{k}, \tau) + aH\theta(\mathbf{k}, \tau) - k^2 \Phi(\mathbf{k}, \tau) = - \int \frac{d^3 k_1}{(2\pi)^3} \int \frac{d^3 k_2}{(2\pi)^3} (2\pi)^3 \delta_D^{(3)}(\mathbf{k} - \mathbf{k}_1 - \mathbf{k}_2) \times \beta(\mathbf{k}_1, \mathbf{k}_2) \theta(\mathbf{k}_1, \tau) \theta(\mathbf{k}_2, \tau). \quad (5.39)$$

where a prime refers to differentiation with respect to conformal time, and the functions  $\alpha(\mathbf{k}_1, \mathbf{k}_2)$  and  $\beta(\mathbf{k}_1, \mathbf{k}_2)$  are the mode coupling functions, which encode the non-linear nature of the iterative solutions, and read:

$$\alpha(\mathbf{k}_1, \mathbf{k}_2) = 1 + \frac{\mathbf{k}_1 \cdot \mathbf{k}_2}{k_1^2}, \quad (5.40)$$

$$\beta(\mathbf{k}_1, \mathbf{k}_2) = \frac{\mathbf{k}_1 + \mathbf{k}_2}{k_1^2} + \frac{(\mathbf{k}_1 + \mathbf{k}_2)^2}{k_1^2 k_2^2}. \quad (5.41)$$

And the Poisson equation

$$\Phi(\mathbf{k}, \tau) = -\frac{3}{2}\Omega_m \frac{a^2 H^2}{k^2} \delta(\mathbf{k}, \tau), \quad (5.42)$$

close the Vlasov-Poisson system in Fourier space.

By inspecting Equations (5.38) and (5.39) we can see that we can find solutions for these equations iteratively. That is, since we know that at sufficiently large scales linear theory accurately describes our Universe, we can expand the density contrast and the total divergence as:

$$\delta(\mathbf{k}, \tau) = \delta^{(1)}(\mathbf{k}, \tau) + \delta^{(2)}(\mathbf{k}, \tau) + \dots + \delta^{(n)}(\mathbf{k}, \tau), \quad (5.43)$$

$$\theta(\mathbf{k}, \tau) = \theta^{(1)}(\mathbf{k}, \tau) + \theta^{(2)}(\mathbf{k}, \tau) + \dots + \theta^{(n)}(\mathbf{k}, \tau). \quad (5.44)$$

Plugging these in (5.38) and (5.39), we can find closed recursive solutions as:

$$\delta^n(\mathbf{k}, \tau) = \int d^3 k_1 \dots d^3 k_n \delta^{(n)}(\mathbf{k} - \mathbf{k}_{1\dots n}) F_n(\mathbf{k}_1, \dots, \mathbf{k}_n, \tau) \delta_0(\mathbf{k}_1) \dots \delta_0(\mathbf{k}_n) \quad (5.45)$$

$$\theta^n(\mathbf{k}, \tau) = \int d^3 k_1 \dots d^3 k_n \delta^{(n)}(\mathbf{k} - \mathbf{k}_{1\dots n}) G_n(\mathbf{k}_1, \dots, \mathbf{k}_n, \tau) \delta_0(\mathbf{k}_1) \dots \delta_0(\mathbf{k}_n), \quad (5.46)$$

where,  $\mathbf{k}_{1\dots n} = \mathbf{k}_1 + \dots + \mathbf{k}_n$ ,  $F_n$  and  $G_n$  are called  $n$ -th order kernels and  $\delta_0(\mathbf{k})$  is the initial density field. Inserting (5.45) and (5.46) in (5.43) we find the system:

$$\hat{T} \begin{bmatrix} F_n(\mathbf{k}_1, \dots, \mathbf{k}_n, \tau) \\ G_n(\mathbf{k}_1, \dots, \mathbf{k}_n, \tau) \end{bmatrix} = \sum_{j=1}^{n-1} \begin{bmatrix} -\alpha(\mathbf{k}_{1\dots j}, \mathbf{k}_{j+1\dots n}) G_j(\mathbf{k}_1, \dots, \mathbf{k}_j) F_{n-j}(k_{j+1}, \dots, k_n) \\ -\frac{1}{2}\beta(\mathbf{k}_{1\dots j}, \mathbf{k}_{j+1\dots n}) G_j(\mathbf{k}_1, \dots, \mathbf{k}_j) G_{n-j}(k_{j+1}, \dots, k_n) \end{bmatrix} \quad (5.47)$$

where

$$\hat{T} = \begin{bmatrix} \frac{d}{d\tau} & 1 \\ \frac{3}{2}\Omega_m a^2 H^2 & \frac{d}{d\tau} + aH \end{bmatrix}. \quad (5.48)$$

When solved consistently this system will give us the explicit time-dependence of the standard perturbation theory kernels,  $F_n$  and  $G_n$ . One can easily see that at linear order the RHS of Equation (5.47) is zero, and one will find  $F_1(k, \tau) = D_+(\tau)$ , and  $G_1$  can be found from Euler's equation.

Using this SPT formalism we can write the power spectrum as:

$$P_{\delta\delta} \langle \delta(\mathbf{k}, \tau) \delta(\mathbf{k}', \tau) \rangle = \sum_{n,l=1,2,\dots}^{n+l \text{ even}} \langle \delta^{(n)}(\mathbf{k}, \tau) \delta^{(l)}(\mathbf{k}', \tau) \rangle, \quad (5.49)$$

where the only non-zero contributions to the power spectrum are those with  $n+l$  even. This is a property inherited from the original quantum fluctuations in the early Universe, that grew into the structures that we now see due to the gravitational instability. Following Wick's theorem, the expected value of any  $n$ -point correlation function, where  $n$  is odd, of a given Gaussian random field vanishes. As we are writing any order of the density field in terms of its initial density,  $\delta_0$ , then, the power spectrum receives only contributions where the sum of the orders of each field is even. Therefore, at leading order we have the usual linear matter power spectrum  $P_L$ , and the next-to-leading order solution is the one-loop corrected power spectrum  $P^{1\text{-loop}}(k)$ :

$$P_{\delta\delta}^{1\text{-loop}}(k) = P_L(k) + P_{\delta\delta}^{13}(k) + P_{\delta\delta}^{22}(k) \quad (5.50)$$

with

$$\langle \delta^{(2)}(\mathbf{k}, \tau) \delta^{(2)}(\mathbf{k}', \tau) \rangle = (2\pi)^3 \delta_D^{(3)} P_{\delta\delta}^{22}(k) \quad (5.51)$$

$$\langle \delta^{(1)}(\mathbf{k}, \tau) \delta^{(3)}(\mathbf{k}', \tau) + \delta^{(3)}(\mathbf{k}, \tau) \delta^{(1)}(\mathbf{k}', \tau) \rangle = (2\pi)^3 \delta_D^{(3)} P_{\delta\delta}^{13}(k). \quad (5.52)$$

Working out the details with previous equations, one can explicitly calculate the form of  $P_{\delta\delta}^{13}$  and  $P_{\delta\delta}^{22}$ :

$$P_{\delta\delta}^{22}(k, \tau) = \int \frac{d^3p}{(2\pi)^3} [F_2(\mathbf{p}, \mathbf{k} - \mathbf{p})]^2 P_{\delta\delta}^L(\mathbf{p}, \tau) P_{\delta\delta}^L(|\mathbf{k} - \mathbf{p}|, \tau) \quad (5.53)$$

$$P_{\delta\delta}^{13}(k, \tau) = 3P_L(k, \tau) \int \frac{d^3p}{(2\pi)^3} F_3(\mathbf{p}, -\mathbf{p}, \mathbf{k}) P_L(\mathbf{p}, \tau). \quad (5.54)$$

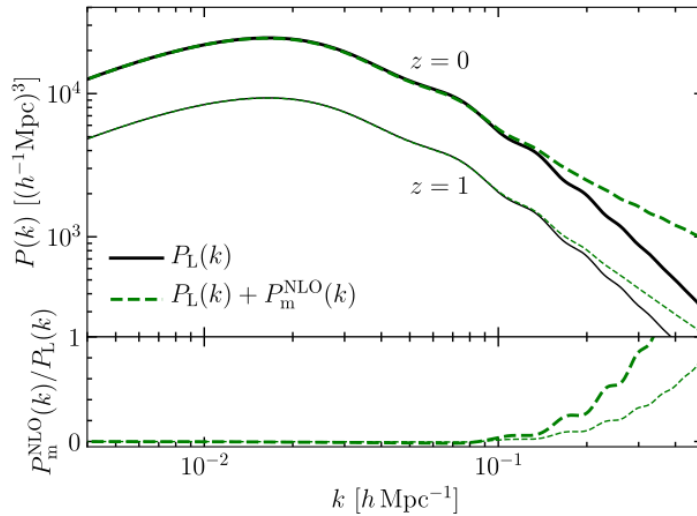


**Figure 5.1.** The top plot shows the linear matter power spectrum,  $P_L(k)$  (black solid, and the linear plus next-to-leading order correction of the power spectrum,  $P_L(k) + P_m^{\text{NLO}}(k)$  (dashed green), at two different redshifts,  $z = 0$  and  $z = 1$ . The bottom plot shows the ratio between the two, where we can see that from  $k = 0.1 h/\text{Mpc}$  non-linear corrections need to be included. Plot taken from [26].

Figure 5.1 shows us the absolute power spectrum of leading and next-to-leading order corrections, linear and 1-loop power spectrum respectively. This concludes our discussion about SPT in LCDM.

### 5.2.2. Lagrangian Perturbation Theory

In 1970 Zel'dovich introduced an alternative to the Eulerian description of perturbation theory, where the primary quantity of the analysis is the trajectory of the particle, and not its density contrast. The given CDM particle is indexed in the Lagrangian picture by its initial displacement  $\mathbf{q}$ , and the Eulerian coordinate position at conformal time  $\tau$  is then given by:

$$\mathbf{x}(\tau) = \mathbf{q} + \Psi(\mathbf{q}, \tau). \quad (5.55)$$

Zel'dovich's original idea was to relate the displacement vector field  $\Psi$  at a later time directly from its initial displacement:

$$\Psi(\mathbf{q}, \tau) = g(\tau)\Psi(\mathbf{q}). \quad (5.56)$$

In fact, this relation is exact at linear order, as  $g(\tau) \propto D_+$ , however, it has obvious shortcomings as it does not incorporate gravitational acceleration. At linear order, any particle will move in a straight line (in comoving coordinates) in the direction given by their initial velocity, the movement is simply inertial. The connection between the Eulerian density contrast description to the one where the displacement of particles is evolved rises from a simple argument of mass conservation:

$$[1 + \delta(\mathbf{x}, \tau)] d^3x = d^3q, \quad (5.57)$$

where the volume distortion is captured by the Jacobian:

$$\mathcal{J} = \left| \frac{d^3x}{d^3q} \right| = \det \left[ \delta_{ij}^{(K)} + \frac{\partial \Psi}{\partial \mathbf{q}} \right] = \det \left[ \delta_{ij}^{(K)} + \Psi_{i,j} \right] \quad (5.58)$$

where a comma refers to derivative with respect to the initial Lagrangian position. We then have:

$$\delta = \frac{1}{\mathcal{J}} - 1 \quad (5.59)$$

which at linear order is simply:

$$\delta^1(\mathbf{x}, \tau) = -\mathbf{J}^{(1)} = -\Psi_{i,i}^{(1)} \quad (5.60)$$

which is equivalent to Zel'dovich's approximation (ZA), as expected. Going back now to the geodesic equation for particle's position, Equation (5.11), and taking its divergence we find:

$$\mathcal{J} \nabla_{\mathbf{x}} \left[ \frac{d^2 \mathbf{x}}{d\tau^2} + aH \frac{d\mathbf{x}}{d\tau} \right] = \frac{3}{2} a^2 H^2 \Omega_m(a) (\mathcal{J} - 1), \quad (5.61)$$

remembering that  $\nabla_{x_i} = \left( \delta_{ij}^{(K)} + \Psi_{i,j} \right) \nabla_{q_i}$ . Expanding the displacement field into a perturbative series:

$$\Psi = \Psi^{(1)} + \Psi^{(2)} + \Psi^{(3)} + \dots, \quad (5.62)$$

the jacobian can be similarly expanded, as it is merely a function of this field:

$$\mathcal{J} = \mathcal{J}^{(1)} + \mathcal{J}^{(2)} + \mathcal{J}^{(3)} + \dots, \quad (5.63)$$

and we can just plug these relations into the volume distortion relation, Equation (5.58), and get closed forms for each perturbative Jacobian in terms of the displacement field expansion:

$$\mathcal{J}^{(1)} = \mathcal{L}^{(1)} = \sum_i \Psi_{i,i}^{(1)}, \quad (5.64)$$

$$\mathcal{J}^{(2)} = \mathcal{L}^{(2)} + \mathcal{K}^{(2)} = \sum_i \Psi_{i,i}^{(2)} + \frac{1}{2} \sum_{i \neq j} \left[ \Psi_{i,i}^{(1)} \Psi_{j,j}^{(1)} - \Psi_{i,j}^{(1)} \Psi_{j,i}^{(1)} \right], \quad (5.65)$$

$$\mathcal{J}^{(3)} = \mathcal{L}^{(3)} + \mathcal{K}^{(2)} + \mathcal{M}^{(3)} = \sum_i \Psi_{i,i}^{(3)} + \frac{1}{2} \sum_{i \neq j} \left[ \Psi_{i,i}^{(2)} \Psi_{j,j}^{(1)} - \Psi_{i,j}^{(2)} \Psi_{j,i}^{(1)} + \det \Psi_{i,j}^{(1)} \right]. \quad (5.66)$$

From the Jacobian expansion we can find the corresponding orders of the density contrast up to second order:

$$\delta^{(1)}(\mathbf{x}, \tau) = - \sum_i \Psi_{i,i}^{(1)}(\mathbf{q}, \tau), \quad (5.67)$$

$$\delta^{(2)}(\mathbf{x}, \tau) = - \sum_i \Psi_{i,i}^{(2)}(\mathbf{q}, \tau) + \frac{1}{2} \sum_{i \neq j} \left[ \Psi_{i,i}^{(1)}(\mathbf{q}, \tau) \Psi_{j,j}^{(1)}(\mathbf{q}, \tau) - \Psi_{i,j}^{(1)}(\mathbf{q}, \tau) \Psi_{j,i}^{(1)}(\mathbf{q}, \tau) \right], \quad (5.68)$$

where the minus sign in front of the first term on the RHS of the second equation comes from the fact:

$$\det [\mathcal{I} + A] = 1 + \text{tr}(A) + \frac{1}{2} [\text{tr}^2(A) + \text{tr}(A^2)], \quad (5.69)$$

$$\det \left[ \frac{1}{\mathcal{I} + A} \right] = 1 - \text{tr}(A) + \frac{1}{2} [\text{tr}^2(A) + \text{tr}(A^2)], \quad (5.70)$$

where  $\mathcal{I}$  is the identity matrix. To find an expression for the power spectrum in LPT, we begin by integrating both sides of Equation (5.57), where we find:

$$1 + \delta(\mathbf{x}) = \int d^3q \delta_D(\mathbf{x} - \mathbf{q} - \Psi), \quad (5.71)$$

where I have omitted the time dependence to make the computation clearer. Taking the Fourier transform of Equation (5.71):

$$\delta_D(\mathbf{k}) + \delta(\mathbf{k}) = \int d^3q e^{i\mathbf{k} \cdot \mathbf{q}} \exp(i\mathbf{k} \cdot \Psi), \quad (5.72)$$

then we can find the power spectrum by simply computing  $(2\pi)^3 P_{\delta\delta} = \langle \delta(\mathbf{k}) \delta(\mathbf{k}') \rangle$ :

$$(2\pi)^3 \delta^{(3)}(k) + P(k) = \int d^3q \exp(-i\mathbf{q} \cdot \mathbf{k}) \langle \exp[-i\mathbf{k} \cdot \Delta\Psi] - 1 \rangle, \quad (5.73)$$

where  $\mathbf{q} = \mathbf{q}_1 - \mathbf{q}_2$  and  $\Delta\Psi = \Psi(\mathbf{q}_1) - \Psi(\mathbf{q}_2)$ . We still need, however, to find the appropriate solutions for the displacement field  $\Psi$ . This is done also perturbatively, and our starting point is Equation (5.61), that we can write it as:

$$\frac{1}{\delta_{ij}^{(K)} + \Psi_{i,j}} \nabla_q^j \frac{d^2\Psi_i(\mathbf{q}, T)}{dT^2} = -\nabla_x^2 \Phi(\mathbf{x}, T), \quad (5.74)$$

where  $T$  is a new time variable called super comoving time, defined as  $dT = d\tau/a$ . Approximating the denominator of this Equations as  $(\delta_{ij}^{(K)} + \Psi_{i,j})^{-1} \approx \delta_{ij}^{(K)} - \Psi_{i,j}$ , and expanding  $\Psi$  up to second order we rewrite the previous equation as:

$$\left( \frac{\partial}{\partial q_i} - \epsilon \frac{\partial \Psi^{(1)}(\mathbf{q}, T)}{\partial q^i} \frac{\partial}{\partial q^j} - \epsilon^2 \frac{\partial \Psi^{(2)}(\mathbf{q}, T)}{\partial q^i} \frac{\partial}{\partial q^j} \right) \left[ \epsilon \frac{d^2\Psi^{(1)}(\mathbf{q}, T)}{dT^2} + \epsilon^2 \frac{d^2\Psi^{(2)}(\mathbf{q}, T)}{dT^2} \right] = -\nabla_x^2 \Phi(\mathbf{x}, T) \quad (5.75)$$

where  $\epsilon$  is a small parameter used just to keep track of the order of the expansion. The first and second order equations of motion for the displacement field are then:

$$\frac{d^2\Psi_{i,i}(\mathbf{q}, T)}{dT^2} = \nabla_x^2 \Phi(\mathbf{x}, T) \quad (5.76)$$

and

$$\frac{d^2\Psi_{i,i}^{(2)}(\mathbf{q}, T)}{dT^2} - \Psi_{i,i}^{(1)}(\mathbf{q}, T) \frac{d^1\Psi_{i,i}^{(1)}(\mathbf{q}, T)}{dT^2} = \nabla_x^2 \Phi(\mathbf{x}, T). \quad (5.77)$$

Taking the Fourier transform with respect to  $\mathbf{q}$  in both sides of these equations leads us to:

$$\mathcal{F}_{\mathbf{q}} \left[ \frac{d^2\Psi_{i,i}^{(1)}}{dT^2} \right] (\mathbf{k}) = \mathcal{F}_{\mathbf{q}} [\nabla_x^2 \Phi(\mathbf{x}, T)] (\mathbf{k}), \quad (5.78)$$

$$\mathcal{F}_{\mathbf{q}} \left[ \frac{d^2\Psi_{i,i}^{(2)}}{dT^2} - \Psi_{i,i}^{(1)} \frac{d^1\Psi_{i,i}^{(1)}}{dT^2} \right] (\mathbf{k}) = \mathcal{F}_{\mathbf{q}} [\nabla_x^2 \Phi(\mathbf{x}, T)] (\mathbf{k}). \quad (5.79)$$

In the same way taking the Fourier transform of Equations (5.67) we have:

$$\tilde{\delta}^{(1)}(\mathbf{k}, T) = \mathcal{F}_{\mathbf{q}} \left[ \delta^{(1)}(\mathbf{x}, T) \right] = \mathcal{F}_{\mathbf{q}} \left[ \Psi_{i,i}^{(1)}(\mathbf{q}, T) \right] \quad (5.80)$$

$$\tilde{\delta}^{(2)}(\mathbf{k}, T) = \mathcal{F}_{\mathbf{q}} \left[ \delta^{(2)}(\mathbf{x}, T) \right] = \mathcal{F}_{\mathbf{q}} \left[ -\Psi_{i,i}^{(2)} + \frac{1}{2} \left( \Psi_{i,i}^{(1)} \Psi_{j,j}^{(1)} - \Psi_{i,j}^{(1)} \Psi_{j,i}^{(1)} \right) \right]. \quad (5.81)$$

Before moving on to solve Equations (5.78-5.79), note that the displacement field up to second order is an irrotational field, hence, can be written in terms of the gradient of a scalar field,  $\phi$  (not to be confused with the gravitational potential, which will always be referred as  $\Phi$ ):

$$\mathcal{F}_{\mathbf{q}} [\Psi_i(\mathbf{q}, T)] = ik_i \phi(\mathbf{k}, T). \quad (5.82)$$

From the Poisson Equation in Fourier space, we can relate the  $\Phi$  potential with the density contrast:

$$\mathcal{F}_{\mathbf{q}} [\nabla^2 \Phi(\mathbf{x}, T)](\mathbf{k}) = \kappa \tilde{\delta}(\mathbf{k}, T) = \kappa \left( \tilde{\delta}^{(1)} + \tilde{\delta}^{(2)} + \dots \right) \quad (5.83)$$

with  $\kappa = 4\pi G_N \rho a^4 = \frac{3}{2} \Omega_m(a) H_0^2 a$ . Then, if we insert this in Equation (5.78) we get:

$$\mathcal{F}_{\mathbf{q}} \left[ \frac{d^2 \Psi_{i,i}^{(1)}}{dT^2} \right](\mathbf{k}) = -\kappa \tilde{\delta}^{(1)} = \kappa \mathcal{F}_{\mathbf{q}} \left[ \Psi_{i,i}^{(1)} \right], \quad (5.84)$$

which after using Equation (5.82) becomes:

$$-k^2 \frac{d^2 \phi(\mathbf{k}, T)}{dT^2} = -k^2 \kappa \phi(\mathbf{k}, T) \quad (5.85)$$

In  $\Lambda$ CDM cosmology the growth of matter density perturbations is scale-independent at linear order, therefore, we can write:

$$\phi^{(1)}(\mathbf{k}, T) = D_1(T) \phi^{(1)}(\mathbf{k}, T_{\text{ini}}), \quad (5.86)$$

where  $D_1$  is the first order growth function, and  $\phi_{\text{ini}}^{(1)} = \delta^{(1)}(\mathbf{k}, T)/k^2$  is the initial state of the scalar field. Following these statements, we rewrite Equation (5.85) as:

$$\left[ \frac{d^2}{dT^2} - \kappa \right] D_1(T) = 0 \quad (5.87)$$

which can be solved analytically as long as we have the initial conditions  $D_1(T_{\text{ini}})$  and  $dD_1/dT|_{\text{ini}}$ . Deep inside matter domination era, the initial conditions are given by Einstein-de Sitter initial conditions:

$$D_1(T_{\text{ini}}) = 1, \quad \left( \frac{dD_1}{dT} \right)_{\text{ini}} = \left( \frac{1}{a} \frac{da}{dT} \right)_{\text{ini}}. \quad (5.88)$$

Once we have  $D_1$ , we then know how to express  $\Psi^{(1)}(\mathbf{k}, T)$ :

$$\Psi^{(1)}(\mathbf{k}, T) = ik_i \frac{D_1(T) \tilde{\delta}^{(1)}(\mathbf{k}, T_{\text{ini}})}{k^2}, \quad (5.89)$$

and the real space solution is found by taking the inverse Fourier transform:

$$\Psi^{(1)}(\mathbf{q}, T) = D_1(T) \int d^3k \exp(i\mathbf{k} \cdot \mathbf{q}) \frac{\tilde{\delta}^{(1)}(\mathbf{k}, T_{\text{ini}})}{k^2}. \quad (5.90)$$

For the second order solution we proceed in an analogous way:

$$\mathcal{F}_{\mathbf{q}} \left[ \frac{d^2 \Psi_{i,i}^{(2)}}{dT^2} - \Psi_{i,i}^{(1)} \frac{d^1 \Psi_{i,i}^{(1)}}{dT^2} \right] (\mathbf{k}) = \kappa \mathcal{F}_{\mathbf{q}} \left[ -\Psi_{i,i}^{(2)} + \frac{1}{2} \left( \Psi_{i,i}^{(1)} \Psi_{j,j}^{(1)} - \Psi_{i,j}^{(1)} \Psi_{j,i}^{(1)} \right) \right] (\mathbf{k}) \quad (5.91)$$

and substitute the solution of  $\Psi^{(1)}(\mathbf{k}, T)$ :

$$\mathcal{F}_{\mathbf{q}} \left[ \frac{d^2 \Psi_{i,i}^{(2)}}{dT^2} - \kappa \Psi_{j,i}^{(1)} \Psi_{i,j}^{(1)} \right] (\mathbf{k}) = \kappa \mathcal{F}_{\mathbf{q}} \left[ -\Psi_{i,i}^{(2)} + \frac{1}{2} \left( \Psi_{i,i}^{(1)} \Psi_{j,j}^{(1)} - \Psi_{i,j}^{(1)} \Psi_{j,i}^{(1)} \right) \right] (\mathbf{k}) \quad (5.92)$$

which rewritten becomes:

$$\left[ \frac{d^2}{dT^2} - \kappa \right] \mathcal{F}_{\mathbf{q}} \left[ \Psi_{i,i}^{(2)}(\mathbf{q}, T) \right] = -\frac{\kappa}{2} \mathcal{F}_{\mathbf{q}} \left[ \Psi_{i,i}^{(1)} \Psi_{j,j}^{(1)} - \Psi_{i,j}^{(1)} \Psi_{j,i}^{(1)} \right]. \quad (5.93)$$

The convolutions in these Equations are computed as follows:

$$\begin{aligned} \Psi_{l,m}^{(1)} \Psi_{m,l}^{(1)} &= D_1^2(T) \int \frac{d^3 k_1}{(2\pi)^3} \frac{d^3 k_2}{(2\pi)^3} i k_1^m e^{i \mathbf{k}_1 \cdot \mathbf{q}} \frac{i k_{1,l}}{k_1^2} i k_2^l e^{i \mathbf{k}_2 \cdot \mathbf{q}} \frac{i k_{2,m}}{k_2^2} \tilde{\delta}(\mathbf{k}_1, T) \tilde{\delta}(\mathbf{k}_2, T) \\ &= D_1^2(T) \int \frac{d^3 k_1}{(2\pi)^3} \frac{d^3 k_2}{(2\pi)^3} i^4 e^{(\mathbf{k}_1 + \mathbf{k}_2) \cdot \mathbf{q}} \frac{k_1^m k_{1,l} k_2^l k_{2,m}}{k_1^2 k_2^2} \tilde{\delta}(\mathbf{k}_1, T) \tilde{\delta}(\mathbf{k}_2, T) \\ &= D^{(1),2}(T) \int \frac{d^3 k_1}{(2\pi)^3} \frac{d^3 k_2}{(2\pi)^3} e^{(\mathbf{k}_1 + \mathbf{k}_2) \cdot \mathbf{q}} \frac{(\mathbf{k}_1 \cdot \mathbf{k}_2)^2}{k_1^2 k_2^2} \tilde{\delta}(\mathbf{k}_1, T_{\text{ini}}) \tilde{\delta}(\mathbf{k}_2, T_{\text{ini}}), \end{aligned} \quad (5.94)$$

where we now have the wave-numbers  $\mathbf{k}_1$  and  $\mathbf{k}_2$  appearing in the integrals due to the derivative in the displacement fields, and the other convolution is:

$$\Psi_{l,l}^{(1)} \Psi_{m,m}^{(1)} = D^{(1),2}(T) \int \frac{d^3 k_1}{(2\pi)^3} \frac{d^3 k_2}{(2\pi)^3} e^{(\mathbf{k}_1 + \mathbf{k}_2) \cdot \mathbf{q}} \tilde{\delta}(\mathbf{k}_1, T_{\text{ini}}) \tilde{\delta}(\mathbf{k}_2, T_{\text{ini}}). \quad (5.95)$$

Then we have:

$$\Psi_{l,m}^{(1)} \Psi_{m,l}^{(1)} - \Psi_{l,l}^{(1)} \Psi_{m,m}^{(1)} = \quad (5.96)$$

$$D_1^2(T) \int \frac{d^3 k_1}{(2\pi)^3} \frac{d^3 k_2}{(2\pi)^3} e^{(\mathbf{k}_1 + \mathbf{k}_2) \cdot \mathbf{q}} \left( 1 - \frac{(\mathbf{k}_1 \cdot \mathbf{k}_2)^2}{k_1^2 k_2^2} \right) \tilde{\delta}(\mathbf{k}_1, T_{\text{ini}}) \tilde{\delta}(\mathbf{k}_2, T_{\text{ini}}), \quad (5.97)$$

which when we take the Fourier transform:

$$\mathcal{F} \left[ \Psi_{l,m}^{(1)} \Psi_{m,l}^{(1)} - \Psi_{l,l}^{(1)} \Psi_{m,m}^{(1)} \right] = \quad (5.98)$$

$$D_1^2(T) \int \frac{d^3 k_1}{(2\pi)^3} \frac{d^3 k_2}{(2\pi)^3} \delta_D^{(3)}(\mathbf{k} - \mathbf{k}_{12}) \left( 1 - \frac{(\mathbf{k}_1 \cdot \mathbf{k}_2)^2}{k_1^2 k_2^2} \right) \tilde{\delta}(\mathbf{k}_1, T_{\text{ini}}) \tilde{\delta}(\mathbf{k}_2, T_{\text{ini}}), \quad (5.99)$$

with  $\mathbf{k}_{12} = \mathbf{k}_1 + \mathbf{k}_2$ . Since we have that:

$$\mathcal{F}_{\mathbf{q}} [\Psi_{i,i}(\mathbf{q}, T)] (\mathbf{k}) = -k^2 \phi(\mathbf{k}, T) \quad (5.100)$$

we can combine this equation with (5.98) and write:

$$-k^2 \left( \frac{d^2}{dT^2} - \kappa \right) \phi^{(2)}(\mathbf{k}, T) = -\frac{\kappa}{2} D_1^2(T) \int \frac{d^3 k_1}{(2\pi)^3} \frac{d^3 k_2}{(2\pi)^3} \delta_D^{(3)}(\mathbf{k} - \mathbf{k}_{12}) \quad (5.101)$$

$$\times \left( 1 - \frac{(\mathbf{k}_1 \cdot \mathbf{k}_2)^2}{k_1^2 k_2^2} \right) \tilde{\delta}(\mathbf{k}_1, T_{\text{ini}}) \tilde{\delta}(\mathbf{k}_2, T_{\text{ini}}). \quad (5.102)$$

Defining then:

$$\phi^{(2)}(\mathbf{k}, T) = \frac{D_2(T)}{2k^2} \int \frac{d^3k_1}{(2\pi)^3} \frac{d^3k_2}{(2\pi)^3} \delta_D^{(3)}(\mathbf{k} - \mathbf{k}_{12}) \tilde{\delta}(\mathbf{k}_1, T_{\text{ini}}) \tilde{\delta}(\mathbf{k}_2, T_{\text{ini}}), \quad (5.103)$$

(5.101) is recast as:

$$\left( \frac{d^2}{dT^2} - \kappa \right) D_2(T) = \kappa \left( 1 - \frac{(\mathbf{k}_1 \cdot \mathbf{k}_2)^2}{k_1^2 k_2^2} \right) D_1^2(T). \quad (5.104)$$

This equation can once again be solved provided we get appropriate initial conditions. In  $\Lambda$ CDM, during matter domination era, the physically relevant solutions for an EdS universe have  $D_2 = -\frac{3}{7}D_1^2$ , and we can then set:

$$D_{2,\text{ini}} = -\frac{3}{7}, \quad \left( \frac{dD_2}{dT} \right)_{\text{ini}} = -\frac{6}{7} \left( \frac{1}{a} \frac{da}{dT} \right)_{\text{ini}}. \quad (5.105)$$

The real-space second order displacement field is then written as:

$$\Psi^{(2)}(\mathbf{q}, T) = \frac{D_2(T)}{2} \int \frac{d^3k}{(2\pi)^3} e^{i\mathbf{k} \cdot \mathbf{q}} \frac{ik_i}{k^2} \quad (5.106)$$

$$\times \int \frac{d^3k_1}{(2\pi)^3} \frac{d^3k_2}{(2\pi)^3} \delta_D^{(3)}(\mathbf{k} - \mathbf{k}_{12}) \tilde{\delta}(\mathbf{k}_1, T_{\text{ini}}) \tilde{\delta}(\mathbf{k}_2, T_{\text{ini}}). \quad (5.107)$$

### 5.3. SPT in Modified Gravity

In this section I will go over the details of how to incorporate modified gravity effects in Standard Perturbation Theory. I will focus only on scalar tensor theories, which is the main topic of this thesis. The interplay between the scalar field and the tensor field at non-linear order is more intricate than at linear. At first order we had already seen that the growth of structure becomes scale-dependent, which spoils the separability between time and scale we have in LCDM. For this reason, we have to make a simplifying assumption before going into the details, which is to work under the quasi-static approximation. I will also work in the Newtonian gauge, i.e.:

$$ds^2 = -(1 + 2\Phi) + a^2(t) (1 - 2\Psi) \delta_{ij} dx^i dx^j, \quad (5.108)$$

where  $t$  is the cosmic time. I will also start by rewriting Equations (5.38) and (5.39) as:

$$a \frac{\partial \delta(\mathbf{k}, a)}{\partial a} + \theta(\mathbf{k}, a) = \int \frac{d^3k_1}{(2\pi)^3} \int \frac{d^3k_2}{(2\pi)^3} (2\pi)^3 \delta_D^{(3)}(\mathbf{k} - \mathbf{k}_1 - \mathbf{k}_2) \times \alpha(\mathbf{k}_1, \mathbf{k}_2) \delta(\mathbf{k}_1, a) \theta(\mathbf{k}_2, a), \quad (5.109)$$

$$a \frac{\partial \theta(\mathbf{k}, a)}{\partial a} + \left( 2 + \frac{aH'}{H} \right) \theta(\mathbf{k}, a) - \frac{k^2}{a^2 H^2} \Phi(\mathbf{k}, a) = - \int \frac{d^3k_1}{(2\pi)^3} \int \frac{d^3k_2}{(2\pi)^3} (2\pi)^3 \delta_D^{(3)}(\mathbf{k} - \mathbf{k}_1 - \mathbf{k}_2) \times \beta(\mathbf{k}_1, \mathbf{k}_2) \theta(\mathbf{k}_1, a) \theta(\mathbf{k}_2, a). \quad (5.110)$$

Where from now on I'll omit the time-dependence to simplify the notation, and will refer to a prime as a derivative with respect to the scale factor. Under the Quasi-static approximation,

where the time derivatives of the scalar field fluctuations are smaller than the Hubble rate, the time-time component of the equations of motion simplify considerably, and can be written as:

$$-\frac{k^2}{a^2 H^2} \Phi(\mathbf{k}) = \frac{3\Omega_m(a)}{2} G_{\text{eff}}(\mathbf{k}, a) \delta(\mathbf{k}, a) + S(\mathbf{k}), \quad (5.111)$$

up to third order in perturbation theory, where the modifications introduced by the scalar field are encoded in the Poisson equation. In this equation  $G_{\text{eff}}(\mathbf{k}, a)$  is a function that characterizes the relation between the scalar field and the Poisson equation, and  $S(\mathbf{k})$  is the source term that represents all the interaction vertices we have:

$$\begin{aligned} S(\mathbf{k}) &= \int \frac{d^3 \mathbf{k}_1 d^3 \mathbf{k}_2}{(2\pi)^3} \delta_D^{(3)}(\mathbf{k} - \mathbf{k}_{12}) \gamma_2(\mathbf{k}, \mathbf{k}_1, \mathbf{k}_2; a) \delta_0(\mathbf{k}_1) \delta_0(\mathbf{k}_2) \\ &+ \int \frac{d^3 \mathbf{k}_1 d^3 \mathbf{k}_2 d^3 \mathbf{k}_3}{(2\pi)^3} \delta_D^{(3)}(\mathbf{k} - \mathbf{k}_{123}) \gamma_3(\mathbf{k}, \mathbf{k}_1, \mathbf{k}_2, \mathbf{k}_3; a) \delta_0(\mathbf{k}_1) \delta_0(\mathbf{k}_2) \delta_0(\mathbf{k}_3). \end{aligned} \quad (5.112)$$

The  $\gamma_2$  and  $\gamma_3$  are symmetric under exchange of wave-number. While the effective Newton's constant  $G_{\text{eff}}(\mathbf{k}, a)$  is responsible for introducing the scale-dependence in the growth of structure at the linear level, at the non-linear level the theory will also include the information from the screening mechanism a certain theory is endowed with. At small scales and high density environments these mechanisms are able to restore GR, and at leading order in perturbation theory the terms  $\gamma_2$  and  $\gamma_3$  fully describe the description of screening in perturbation theory. A full description of these functions for different theories falls out of the scope of this thesis, but the reader can find their form in References [117, 119].

Proceeding in the same way as we did for LCDM, we can also find the  $n$ -th order solution of the density contrast and velocity divergence, by plugging Equations (5.45) and (5.46), in Equations (5.109)-(5.111):

$$\begin{aligned} \hat{T} \begin{bmatrix} F_n(\mathbf{k}_1, \dots, \mathbf{k}_n, \tau) \\ G_n(\mathbf{k}_1, \dots, \mathbf{k}_n, \tau) \end{bmatrix} &= \\ \sum_{j=1}^{n-1} \left[ -\frac{1}{2} \beta(\mathbf{k}_{1\dots j}, \mathbf{k}_{j+1\dots n}) G_j(\mathbf{k}_1, \dots, \mathbf{k}_j) G_{n-j}(k_{j+1}, \dots, k_n) - N_n(\mathbf{k}, \mathbf{k}_1, \dots, \mathbf{k}_n) \right] \end{aligned} \quad (5.113)$$

where

$$\hat{T} = \begin{bmatrix} a \frac{d}{da} & 1 \\ \frac{3}{2} \Omega_m(a) G_{\text{eff}}(\mathbf{k}, a) & a \frac{d}{da} + \left( 2 + \frac{aH'}{H} \right) \end{bmatrix} \quad (5.114)$$

and

$$N_2 = \gamma_2(\mathbf{k}, \mathbf{k}_1, \mathbf{k}_2) F_1(\mathbf{k}_1) F_2(\mathbf{k}_2) \quad (5.115)$$

$$\begin{aligned} N_3 &= \gamma_2(\mathbf{k}, \mathbf{k}_1, \mathbf{k}_{23}, \mathbf{k}_3) + \gamma_2(\mathbf{k}, \mathbf{k}_{12}, \mathbf{k}_3) F_2(\mathbf{k}_1, \mathbf{k}_2) F_1(\mathbf{k}_3) \\ &+ \gamma_3(\mathbf{k}, \mathbf{k}_1, \mathbf{k}_2, \mathbf{k}_3) F_1(\mathbf{k}_1) F_1(\mathbf{k}_2) F_1(\mathbf{k}_3). \end{aligned} \quad (5.116)$$

The corrections to the power spectrum then are:

$$P_{\delta\delta}^{22}(k) = 2 \int d^3 \mathbf{k}' F_2(\mathbf{k} - \mathbf{k}', \mathbf{k}') P_0(|\mathbf{k} - \mathbf{k}'|) P_0(k'), \quad (5.117)$$

$$P_{\delta\delta}^{13}(k) = 6 \int d^3 \mathbf{k}' F_3(\mathbf{k}, \mathbf{k}', -\mathbf{k}') P_0(k') F_1(k) P_0(k). \quad (5.118)$$

In order to solve these equations we need to have working expressions for the  $F_i$  and  $G_i$  kernels. The specific form of each depends on the model of gravity via the  $\gamma_i$  functions, however, we still need to specify their time-dependence. The explicit derivation of this dependence also falls out of the scope of this thesis, and the exact derivation of these solutions can be found in the review [113]. And a numerical algorithm that finds the solutions for these kernels for general modified gravity, assuming EdS initial conditions, is presented in [117, 119].

## 5.4. 2LPT in Modified Gravity

I will now discuss how we can introduce modified gravity at second order using Lagrangian Perturbation Theory. In order to do so, I will follow References [120, 121]. Once again I will use the super-comoving time  $dT = dt/a^2$ , and set  $\kappa = 4\pi G_N \rho a^4 = \frac{3}{2}\Omega_m H_0^2 a$ . I will start describing the modified gravity effects only via the function  $G_{\text{eff}}(k, T)$ , but later on I will describe how we can include other effects. Once again we start by taking the Fourier transform of the Poisson equation up to second order:

$$\begin{aligned} \mathcal{F}_{\mathbf{x}}[\nabla_{\mathbf{x}}^2 \Phi(\mathbf{x}, T)](\mathbf{k}, T) &= \kappa G_{\text{eff}}(k, T) \delta^{\text{E}}(\mathbf{k}, T) \\ + a^4 H^2 \int \frac{d^3 k_1 d^3 k_2}{(2\pi)^3} \delta^{(1)}(\mathbf{k}_1, T) \delta^{(1)}(\mathbf{k}_2, T) \gamma_2^{\text{E}}(\mathbf{k}, \mathbf{k}_1, \mathbf{k}_2, T), \end{aligned} \quad (5.119)$$

where  $\delta^{\text{E}}(\mathbf{k}, T) = \mathcal{F}_{\mathbf{x}}[\delta(\mathbf{x}, T)]$ . However, we know that LPT is written in terms of the Lagrangian coordinate  $\mathbf{q}$ , therefore we need the Fourier transform of the above equation with respect to the same quantity:

$$\begin{aligned} \mathcal{F}_{\mathbf{q}}[\nabla_{\mathbf{x}}^2 \Phi(\mathbf{x}, T)](\mathbf{k}, T) &= \kappa G_{\text{eff}}(k, T) \delta(\mathbf{k}, T) + a^4 H^2 \int \frac{d^3 k_1 d^3 k_2}{(2\pi)^3} \delta^{(1)}(\mathbf{k}_1, T) \delta^{(1)}(\mathbf{k}_2, T) \\ &\times \left[ \gamma_2^{\text{E}}(\mathbf{k}, \mathbf{k}_1, \mathbf{k}_2, T) + \frac{3}{2}\Omega_m(T) (G_{\text{eff}}(k, T) - G_{\text{eff}}(k_1, T)) \frac{\mathbf{k}_1 \cdot \mathbf{k}_2}{k_2^2} \right], \\ &= \kappa G_{\text{eff}}(k, T) \delta(\mathbf{k}, T) + a^4 H^2 \int \frac{d^3 k_1 d^3 k_2}{(2\pi)^3} \delta^{(1)}(\mathbf{k}_1, T) \delta^{(1)}(\mathbf{k}_2, T) \gamma_2(\mathbf{k}, \mathbf{k}_1, \mathbf{k}_2, T), \end{aligned} \quad (5.120)$$

with  $\gamma_2 = \gamma_2^{\text{E}} + \frac{3}{2}\Omega_m(T) [G_{\text{eff}}(k, T) - G_{\text{eff}}(k_1, T)] \frac{\mathbf{k}_1 \cdot \mathbf{k}_2}{k_2^2}$ . It is interesting to note that, if we have a scale-independent coupling between gravity and  $\Phi$ , i.e.  $G_{\text{eff}}(k, T) = G_{\text{eff}}(T)$ , then the second term in  $\gamma_2$  vanishes, like in DGP gravity. At first order, we can rewrite Equation (5.87) as:

$$\left( \frac{d^2}{dT^2} - \kappa G_{\text{eff}}(\mathbf{k}, T) \right) \phi^{(1)}(\mathbf{k}, T) = 0 \quad (5.121)$$

where I have already used the fact that we can write  $\Psi$  in terms of a gradient field  $\phi$ , as at first and second order  $\Psi$  is irrotational. Contrary to what we have in LCDM, in most modified gravity models, we cannot separate the scale and time evolution, however, we can still separate the time evolution for each  $k$  mode as  $\phi^{(1)}(\mathbf{k}, T) = D_1(k, T) \phi^{(1)}(\mathbf{k}, T_{\text{ini}})$  and arrive at

$$\frac{d^2 D_1}{dT^2} - \kappa G_{\text{eff}}(\mathbf{k}, T) D_1 = 0 \quad (5.122)$$

which can be solved using the previous EdS initial conditions as in the LCDM case:

$$D^{(1)}(T_{\text{ini}}) = 1, \quad \left( \frac{dD^{(1)}}{dT} \right)_{\text{ini}} = \left( \frac{1}{a} \frac{da}{dT} \right)_{\text{ini}}. \quad (5.123)$$

With  $\Psi^{(1)}(\mathbf{k}, T) = ik_i \phi^{(1)}(\mathbf{k}, T_{\text{ini}}) = ik_i D_1(\mathbf{k}, T) \delta^{(1)}(\mathbf{k}, T) / k^2$ . The first order displacement field in real space is then:

$$\Psi^{(1)}(\mathbf{q}, T) = \int \frac{d^3 k_1}{(2\pi)^3} e^{i\mathbf{q}\cdot\mathbf{k}} \frac{ik_i}{k^2} D_1(\mathbf{k}, T) \tilde{\delta}^{(1)}(\mathbf{k}, T_{\text{ini}}). \quad (5.124)$$

Moving now to the second order solution, we can expand  $\phi^{(2)}$  as:

$$\phi^{(2)}(\mathbf{k}, T) = -\frac{1}{2k^2} \int \frac{d^3 k_1 d^3 k_2}{(2\pi)^3} \delta_D^{(3)}(\mathbf{k} - \mathbf{k}_{12}) \delta^{(1)}(\mathbf{k}_1, T_{\text{ini}}) \delta^{(1)}(\mathbf{k}_2, T_{\text{ini}}) D_2(\mathbf{k}, \mathbf{k}_1, \mathbf{k}_2, T) \quad (5.125)$$

Written in this way, Equation (5.93) becomes:

$$\begin{aligned} \frac{d^2 D_2}{dT^2} - \kappa G_{\text{eff}}(\mathbf{k}, T) D_2 &= \kappa G_{\text{eff}}(\mathbf{k}, T) D_1(\mathbf{k}_1, T) D_1(\mathbf{k}_2, T) \\ &\times \left[ 1 - \left( \frac{2G_{\text{eff}}(\mathbf{k}_1, T) - G_{\text{eff}}(\mathbf{k}, T)}{G_{\text{eff}}(\mathbf{k}, T)} \right) \frac{(\mathbf{k}_1 \cdot \mathbf{k}_2)^2}{k_1^2 k_2^2} + \frac{2a^4 H^2}{\kappa G_{\text{eff}}(\mathbf{k}, T)} \gamma_2(\mathbf{k}, \mathbf{k}_1, \mathbf{k}_2, T) \right] \end{aligned} \quad (5.126)$$

with initial conditions given by:

$$D_{2,\text{ini}} = -\frac{3}{7} \left( 1 - \frac{(\mathbf{k}_1 \cdot \mathbf{k}_2)^2}{k_1^2 k_2^2} \right), \quad (5.127)$$

$$\left( \frac{dD_2}{dT} \right)_{\text{ini}} = -\frac{6}{7} \left( 1 - \frac{(\mathbf{k}_1 \cdot \mathbf{k}_2)^2}{k_1^2 k_2^2} \right) \left( \frac{1}{a} \frac{da}{dT} \right)_{\text{ini}}. \quad (5.128)$$

In most cases  $\gamma_2$  is a function of the absolute value of each wave-number and the dot product  $\mathbf{k}_1 \cdot \mathbf{k}_2$ , while the conservation of momentum enforced by the 3-dimensional Dirac delta forces that  $\mathbf{k}_2 = \mathbf{k} - \mathbf{k}_1$ , which makes solving Equation (5.126) a 3-dimensional problem for all configurations of  $k$ ,  $k_1$  and  $\cos \theta = \frac{\mathbf{k}_1 \cdot \mathbf{k}_2}{k_1 k_2}$ . The second order displacement field is then:

$$\begin{aligned} \Psi_i^{(2)}(\mathbf{q}, T) &= \frac{1}{2} \int \frac{d^3 k}{(2\pi)^3} e^{i\mathbf{k}\cdot\mathbf{q}} \frac{ik_i}{k^2} \int \frac{d^3 k_1 d^3 k_2}{(2\pi)^3} \delta_D^{(3)}(\mathbf{k} - \mathbf{k}_{12}) \\ &\times D_2(\mathbf{k}, \mathbf{k}_1, \mathbf{k}_2, T) \delta^{(1)}(\mathbf{k}_1, T) \delta^{(1)}(\mathbf{k}_2, T). \end{aligned} \quad (5.129)$$

An approximation for COLA (a quasi-N body code that will be described in Section 5.5): As we are interested in the displacement fields when using COLA, we can see that for each time-step taken in the simulation, we would need to solve the double integral for  $\mathbf{k}_1$  and  $\mathbf{k}_2$ . The problem is, however, that we will not be able to use the method of Fast Fourier Transform (FFT) to solve it numerically, as only the integral outside of Equation (5.129) can be performed using this method. Therefore, Reference [120], introduced an approximation that substitutes the dependence of  $D_2$  on  $\mathbf{k}_1$  and  $\mathbf{k}_2$ , setting it to only a function of  $\mathbf{k}$ . This is done as follows:

$$\begin{aligned} \phi^{(2)}(\mathbf{k}, T) &= -\frac{D_2(\mathbf{k}, T)}{2k^2} \int \frac{d^3 k_1 d^3 k_2}{(2\pi)^3} \delta_D^{(3)}(\mathbf{k} - \mathbf{k}_{12}) \\ &\times \left( 1 - \frac{(\mathbf{k}_1 \cdot \mathbf{k}_2)^2}{k_1^2 k_2^2} \right) \delta^{(1)}(\mathbf{k}_1, T) \delta^{(1)}(\mathbf{k}_2, T), \end{aligned} \quad (5.130)$$

so the displacement field becomes:

$$\begin{aligned} \Psi_i^{(2)}(\mathbf{q}, T) &= \frac{1}{2} \int \frac{d^3 k}{(2\pi)^3} e^{i\mathbf{k}\cdot\mathbf{q}} \frac{ik_i}{k^2} D_2(\mathbf{k}, T) \int \frac{d^3 k_1 d^3 k_2}{(2\pi)^3} \delta_D^{(3)}(\mathbf{k} - \mathbf{k}_{12}) \\ &\times \left( 1 - \frac{(\mathbf{k}_1 \cdot \mathbf{k}_2)^2}{k_1^2 k_2^2} \right) \delta^{(1)}(\mathbf{k}_1, T) \delta^{(1)}(\mathbf{k}_2, T), \end{aligned} \quad (5.131)$$

and the evolution equation for  $D_2$  is now:

$$\begin{aligned} \left[ \frac{d^2}{dT^2} - \kappa G_{\text{eff}}(k, T) \right] \left( 1 - \frac{(\mathbf{k}_1 \cdot \mathbf{k}_2)^2}{k_1^2 k_2^2} \right) D_2(\mathbf{k}, T) = \\ \left[ \kappa G_{\text{eff}}(k, T) \left( 1 - \frac{(\mathbf{k}_1 \cdot \mathbf{k}_2)^2}{k_1^2 k_2^2} \right) + 2a^4 H^2 \gamma_2^{\text{E}}(\mathbf{k}, \mathbf{k}_1, \mathbf{k}_2, T) \right] D_1(\mathbf{k}_1, T) D_1(\mathbf{k}_2, T). \end{aligned} \quad (5.132)$$

We can do one final approximation:

$$\frac{\gamma_2^{\text{E}}(\mathbf{k}, \mathbf{k}_1, \mathbf{k}_2, T)}{\left( 1 - \frac{(\mathbf{k}_1 \cdot \mathbf{k}_2)^2}{k_1^2 k_2^2} \right)} \approx \gamma_2^{\text{E}}(\mathbf{k}, \mathbf{k}/\sqrt{2}, \mathbf{k}/\sqrt{2}, T), \quad (5.133)$$

this choice of triangle configuration is such that it maximizes the weight of the possible choices in Equation (5.125), this last approximation then implies that the equation for the second order growth factor is simply:

$$\begin{aligned} \left[ \frac{d^2}{dT^2} - \kappa G_{\text{eff}}(k, T) \right] D_2(\mathbf{k}, T) = \\ \left[ \kappa G_{\text{eff}}(\mathbf{k}, T) + 2a^4 H^2 \gamma_2^{\text{E}}(\mathbf{k}, \mathbf{k}/\sqrt{2}, \mathbf{k}/\sqrt{2}, T) \right] D_1(\mathbf{k}_1, T) D_1(\mathbf{k}_2, T), \end{aligned} \quad (5.134)$$

which alongside with (5.131) is considerably faster to solve due to the use of FFT methods. In Figure 5.2, taken from [120], I show the validity of this approximation, at  $z = 0$ , when compared to the full solution of  $D_2$  for two models of  $f(R)$  gravity,  $F5 = |f_{R0}| = 10^{-5}$  and  $F6 = |f_{R0}| = 10^{-6}$ , which is characterized by the strength of the  $f(R)$  parameter,  $f_{R0}$  corresponding to the derivative of the  $f(R)$  function. We can see that for equilateral configurations ( $k = k_1 = k_2$ ) we have below percent deviations between the two solutions, while for Orthogonal ( $k = k_1 = k/\sqrt{2}$ ) and Squeezed ( $k = k_1, k_2 \approx 0$ ) we have deviations that exceed the percent threshold from  $k \geq 0.1 h/\text{Mpc}$ . While this can be seen as problematic, I will soon show that these approximations were developed in order to combine the 2LPT approach with a PM algorithm, which is also known as the COLA approach. Within this method, the LPT part of the code is only dominating the particle trajectories at large scales, while at quasi-linear to non-linear scales the PM part of the code dominates. Therefore, while we still make errors in  $D_2$ , this solution will not be affecting the output of our COLA simulations.

I will now discuss the implementation of the formalism discussed in the previous chapter, of relativistic effects. This implementation is inspired by the introduction of linear massive neutrinos in 2LPT, but it can be extend to more general linear density fields. The Poisson Equation with GR corrections in the N-Body gauge can be written as:

$$\begin{aligned} k^2 \Phi^{\text{GR}} &= 4\pi G_{\text{N}} a^2 \rho_{\text{m}} \left( \delta_{\text{m}}^{(1)} + \delta_{\text{m}}^{(2)} \right) \\ &= 4\pi G_{\text{N}} a^2 \left[ \rho_{\text{cb}} \delta_{\text{cb}}^{(1)} + \rho_{\text{GR}} \delta_{\text{GR}}^{(1)} + \rho_{\text{cb}} \delta_{\text{cb}}^{(2)} \right] \\ &= 4\pi G_{\text{N}} a^2 \rho_{\text{m}} \left[ f_{\text{cb}} \left( \delta_{\text{cb}}^{(1)} + \delta_{\text{cb}}^{(2)} \right) + f_{\text{GR}} \delta_{\text{GR}}^{(1)} \right]. \end{aligned} \quad (5.135)$$

where,

$$\delta_{\text{GR}} = \frac{\delta \rho_{\text{GR}}}{\rho_{\text{GR}}}, \quad \rho_{\text{GR}} = \rho_{\nu} + \rho_{\gamma} + \rho_{\text{ur}}, \quad f_{\text{cb}} = \frac{\rho_{\text{cb}}}{\rho_{\text{m}}}, \quad f_{\text{GR}} = \frac{\rho_{\text{GR}}}{\rho_{\text{m}}}, \quad (5.136)$$

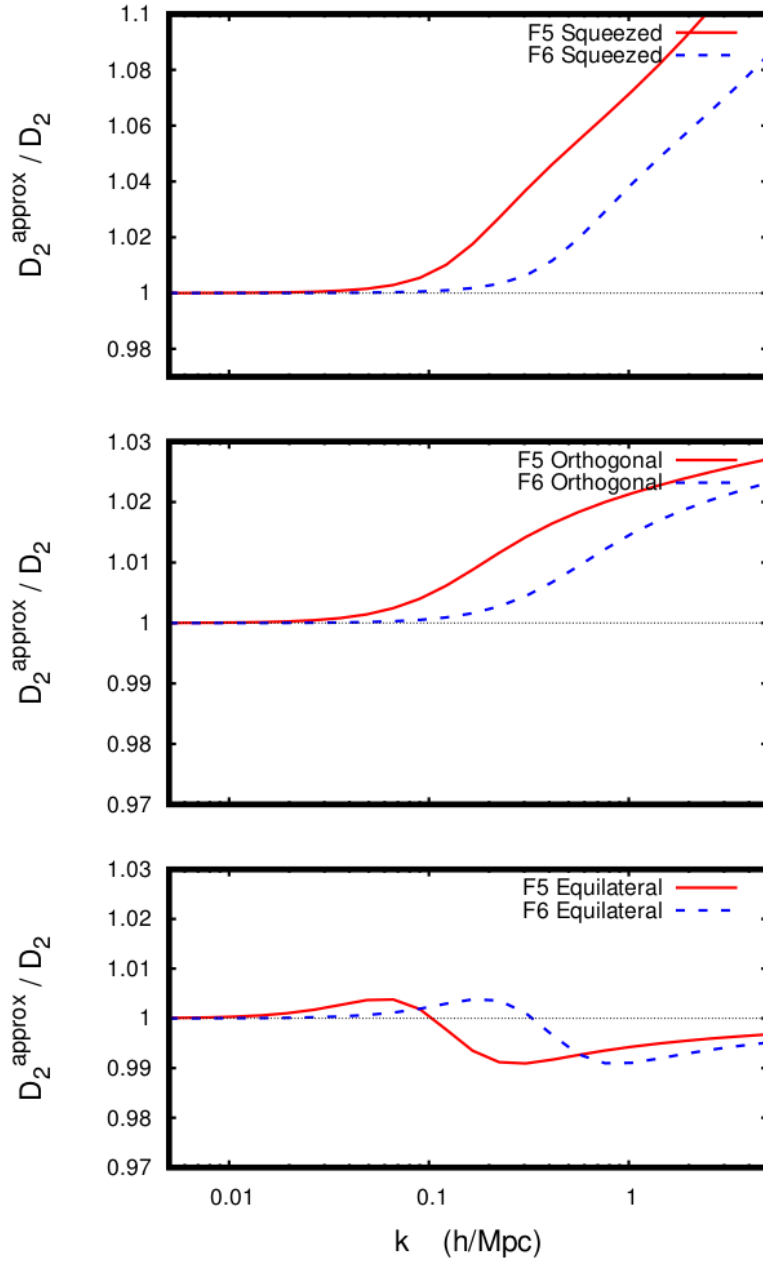


**Figure 5.2.** Ratio between the full solution for the second order growth factor  $D_2(k, k_1, k_2, \cos\theta, a = 1)$  and the approximate solution  $D_2^{\text{approx}}(k, a = 1) (1 - \cos\theta)^2$ , for three triangle configurations: equilateral  $k = k_1 = k_2$ , orthogonal:  $k_1 = k_2 = k/\sqrt{2}$  and squeezed:  $k = k_1$  and  $k_2 \approx 0$ . F5 and F6 in the plots refer to two different models of the  $f(R)$  “Hu-Sawicki” theory, with  $n = 1$  and  $|f(R_0)| = 10^{-5}$  ( $10^{-6}$ ) being the parameters of these theories. Figure taken from [120]

$\delta_{\text{cb}}$  is the density contrast of baryons and cold dark matter, and  $\rho_{\text{cb}}$ ,  $\rho_\nu$ ,  $\rho_\gamma$  and  $\rho_{\text{ur}}$  are the background energy density of baryons and cold dark matter, massive neutrinos, photons and massless neutrinos, respectively. All perturbative quantities are computed in the N-Body gauge, and the linear density field accounting for relativistic corrections is given by:

$$\delta\rho_{\text{GR}} = \delta\rho_\gamma^{\text{Nb}} + \delta\rho_{\text{ur}} + \delta\rho_\nu^{\text{Nb}} + \delta\rho_{\text{DE}}^{\text{Nb}} + \delta\rho_{\text{metric}}^{\text{Nb}}, \quad (5.137)$$

where the quantity  $\delta\rho_{\text{metric}}^{\text{Nb}}$  is given in Equation (4.31). Before moving to the modified gravity case, I'll discuss some details of how the scale-dependent growth of cosmologies with massive neutrinos is done at linear order. From the last line of (5.135), we can manipulate a bit more the terms as:

$$\begin{aligned}
 \rho_{\text{m}} \left( \delta_{\text{m}}^{(1)} + \delta_{\text{m}}^{(2)} \right) &= \rho_{\text{cb}} \delta_{\text{cb}}^{(1)} + \rho_{\text{GR}} \delta_{\text{GR}}^{(1)} + \rho_{\text{cb}} \delta_{\text{cb}}^{(2)} = \left( \frac{\rho_{\text{cb}}}{\rho_{\text{m}}} + \frac{\rho_{\text{GR}}}{\rho_{\text{m}}} \frac{\delta_{\text{GR}}}{\delta_{\text{cb}}} \right) \rho_{\text{m}} \delta_{\text{cb}}^{(1)} + \frac{\rho_{\text{cb}}}{\rho_{\text{m}}} \rho_{\text{m}} \delta_{\text{cb}}^{(2)} \\
 &= \left( f_{\text{cb}} + f_{\text{GR}} \frac{D_{\text{GR},1}(k, T)}{D_{\text{cb},1}(k, T)} \right) \rho_{\text{m}} \delta_{\text{cb}}^{(1)} + f_{\text{cb}} \rho_{\text{m}} \delta_{\text{cb}}^{(2)} \\
 &= \left( f_{\text{cb}} + f_{\text{GR}} \frac{T_{\text{GR}}(k, T)}{T_{\text{cb}}(k, T)} \right) \rho_{\text{m}} \delta_{\text{cb}}^{(1)} + f_{\text{cb}} \rho_{\text{m}} \delta_{\text{cb}}^{(2)} \\
 &= \rho_{\text{m}} \left( \mu_{\text{GR}}(k, T) \delta_{\text{cb}}^{(1)} + f_{\text{cb}} \rho_{\text{m}} \delta_{\text{cb}}^{(2)} \right), \tag{5.138}
 \end{aligned}$$

with

$$\mu_{\text{GR}}(k, T) = f_{\text{cb}} + f_{\text{GR}} \frac{T_{\text{GR}}(k, T)}{T_{\text{cb}}(k, T)} \tag{5.139}$$

where  $T_i(k, T)$  are the linear transfer functions computed using an Einstein-Boltzmann solver. It turns out that in order to make our lives easier, we can compute these in the N-Body gauge. We can see that the function  $\mu_{\text{GR}}$  has the same impact as the modified gravity function  $G_{\text{eff}}(k, T)$  as discussed in the previous paragraphs. Another fact is that, in the absence of modified gravity, the only relativistic species that will have an impact at small scales, and therefore introduce a scale-dependent growth even in  $\Lambda$ CDM cosmologies, are massive neutrinos, therefore, I will rename  $\mu_{\text{GR}}$  as  $\mu_{\nu}$ , in the absence of modified gravity. This is done in order to keep track with the historic development of massive neutrinos in 2LPT theory, and in N-Body simulations.

The Fourier transform of Equation (5.138) is then:

$$\mathcal{F}_{\mathbf{x}}[\nabla_{\mathbf{x}}^2 \Phi(\mathbf{x}, T)](\mathbf{k}) = \kappa \left( \mu_{\nu}(k, T) \delta_{\text{cb}}^{(1)} + f_{\text{cb}} \delta_{\text{cb}}^{(2)} \right), \tag{5.140}$$

and the Fourier transform with respect to  $\mathbf{q}$  is:

$$\begin{aligned}
 \mathcal{F}_{\mathbf{q}}[\nabla_{\mathbf{x}}^2 \Phi(\mathbf{x}, T)](\mathbf{k}) &= \kappa \mu_{\nu}(k, T) \delta_{\text{cb}}^{(1)}(k, T) + \kappa f_{\text{cb}} \delta_{\text{cb}}^{(2)}(k, T) \\
 &+ \kappa \int \frac{d^3 k_1 d^3 k_2}{(2\pi)^3} \delta_{\text{D}}^{(3)}(\mathbf{k} - \mathbf{k}_{12}) [G_{\text{eff}}(k, T) - G_{\text{eff}}(k_1, T)] \\
 &\quad \times \frac{\mathbf{k}_1 \cdot \mathbf{k}_2}{k_2^2} \delta_{\text{cb}}^{(1)}(k_1, T) \delta_{\text{cb}}^{(1)}(k_2, T), \tag{5.141}
 \end{aligned}$$

and the first order growth factor equation is then:

$$\left( \frac{d^2}{dT^2} - \kappa \mu_{\nu}(k, T) \right) D_{\text{cb},1} = 0. \tag{5.142}$$

In order to solve this equation we need to set proper initial conditions accounting for massive neutrinos, we can then proceed in two ways: we use a fitting formula given by [23] or we set them to EdS initial conditions again but compute  $\mu_{\nu}$  by taking the ratio of the massive neutrinos transfer function,  $T_{\nu}$ , with respect to the cold dark matter plus baryons one,  $T_{\text{cb}}$ , where both can be computed using an Einstein-Boltzmann solver. The difference between the two approaches is negligible, as shown in Figure 5.3, which makes the use of the latter approach easier as Boltzmann solvers are computationally fast.

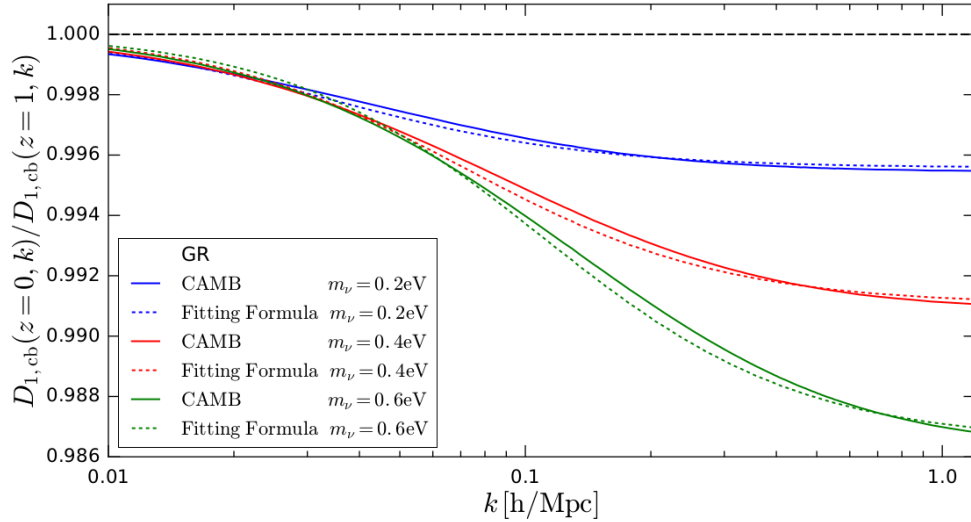


**Figure 5.3.** Ratio between the cold dark matter plus baryons first order growth factor,  $D_{1,cb}$ , computed at two redshifts,  $z = 0$  and  $z = 1$ , and for three different values of the sum of the masses of neutrinos: 0.2 eV, 0.4 eV and 0.6 eV. The solid lines are the calculated from the Einstein-Boltzmann solver CAMB, and the dotted calculated using the fitting formula of [122]. We can see that for smaller masses the two lines have a better agreement as the lower the mass of neutrinos, the more linear they are. Figure taken from [121].

To find the second order growth factor equation, we can substitute Equation (5.141) in Equation (5.93), already removing the first order terms, and arrive at:

$$\begin{aligned}
 k^2 \frac{d^2 \phi_{cb}^{(2)}}{dT^2} + \mathcal{F}_{\mathbf{q}} \left[ \Psi_{cb, j, i}^{(1)} \frac{d^2 \Psi_{i, j}^{(1)}}{dT^2} \right] &= \kappa f_{cb} \delta_{cb}(\mathbf{k}, T) \\
 &+ \kappa \int \frac{d^3 k_1 d^3 k_2}{(2\pi)^3} \delta_D(\mathbf{k} - \mathbf{k}_{12}) [\mu_\nu(k, T) - \mu_\nu(k_1, T)] \\
 &\times \frac{\mathbf{k}_1 \cdot \mathbf{k}_2}{k_2^2} \delta_{cb}^{(1)}(\mathbf{k}_1, T) \delta_{cb}^{(1)}(\mathbf{k}_2, T).
 \end{aligned} \tag{5.143}$$

We can use:

$$\delta_{cb}^{(2)} = -\Psi_{cb, i, i}^{(2)} + \frac{1}{2} \left[ \left( \Psi_{cb, i, i}^{(2)} \right)^2 + \left( \Psi_{cb, i, j}^{(2)} \right)^2 \right] \tag{5.144}$$

and rewrite (5.143) as:

$$\begin{aligned}
 k^2 \left( \frac{d^2}{dT^2} - \kappa f_{cb} \right) \phi_{cb}^{(2)}(\mathbf{k}, T) &= \frac{1}{2} \kappa f_{cb} \mathcal{F} \left[ \Psi_{cb, i, i}^{(1)} \Psi_{cb, j, j}^{(1)} + \Psi_{cb, i, j}^{(2)} \Psi_{cb, j, i}^{(2)} \right] \\
 -\mathcal{F}_{\mathbf{q}} \left[ \Psi_{cb, j, i}^{(1)} \frac{d^2 \Psi_{cb, i, j}^{(1)}}{dT^2} \right] &+ \kappa \int \frac{d^3 k_1 d^3 k_2}{(2\pi)^3} \delta_D(\mathbf{k} - \mathbf{k}_{12}) [\mu_\nu(k, T) - \mu_\nu(k_1, T)] \\
 &\times \frac{\mathbf{k}_1 \cdot \mathbf{k}_2}{k_2^2} \delta_{cb}^{(1)}(\mathbf{k}_1, T) \delta_{cb}^{(1)}(\mathbf{k}_2, T).
 \end{aligned} \tag{5.145}$$

If we write the second order gradient field expansion of the displacement field as in Equation

(5.125), we have:

$$\begin{aligned} \left( \frac{d^2}{dT^2} - \kappa f_{cb} \right) D_{2,cb}(\mathbf{k}, \mathbf{k}_1, \mathbf{k}_2, T) &= \kappa D_1(\mathbf{k}_1, T) D_1(\mathbf{k}_2, T) \\ &\times \left\{ [2\mu_\nu(k_1, T) - f_{cb}] \frac{(\mathbf{k}_1 \cdot \mathbf{k}_2)^2}{k_1^2 k_2^2} \right. \\ &\left. - f_{cb} + [\mu_\nu(k, T) - \mu_\nu(k_1, T)] \frac{\mathbf{k}_1 \cdot \mathbf{k}_2}{k_2^2} \right\} \end{aligned} \quad (5.146)$$

This equation is then the consistent implementation of massive neutrinos in 2LPT. However, in the same way as in the modified gravity case, the integral (5.125) cannot be solved directly using FFT, therefore, we can once more write an approximate version of that integral as in Equation (5.130) alongside with taking  $\mu_\nu(k, T) \rightarrow f_{cb}$  (this was first used in [123] for SPT calculations with massive neutrinos), and then the second order equation of motion of the growth factor is recast as:

$$\left( \frac{d^2}{dT^2} - \kappa f_{cb} \right) D_{cb,2}(k, T) = f_{cb} D_{cb,1}^2(k, T) \quad (5.147)$$

where if  $f_{cb} \rightarrow 1$  we recover the usual 2LPT equation for cosmologies without massive neutrinos. In a matter dominated Universe and at scales below the free streaming scale  $k_{fs}$  [124] given by:

$$k_{fs} = \sqrt{\frac{2}{3}} \frac{H(t)a(t)}{v_{th}(t)}, \quad \text{where } v_{th} \approx 150(1+z) \left[ \frac{1 \text{ eV}}{\sum_\nu m_\nu} \right] \text{ km/s} \quad (5.148)$$

with  $v_{th}$  being the thermal velocity of massive neutrinos, the initial conditions for  $D_{cb,2}$  are given by:

$$D_{2,cb} \sim - \frac{3f_{cb}}{3f_{cb} + 4(1 - p_{cb})^2} D_{1,cb} \quad (5.149)$$

with  $p_{cb}$  given by Equation (11) of [122]. Besides using the integral approximation, which has already compared with its full results in Figures 5.2, we also need to show how taking  $\mu_\nu(k, T) \rightarrow f_{cb}$  works out. In Figure 5.4, taken from [121] we can see that this approximation works at below 1% level from scales of 0.1  $h/\text{Mpc}$  for the lowest value of the neutrino mass, and it becomes worse as the mass increases. This is expected, as the larger the mass of the neutrinos, the worse will be our implementation of linear massive neutrinos. At the same time, we get errors of 1.5%, 3.0% and 4.5% for each value of the neutrino mass at large scales. While this points to us that the  $D_{2,cb}$  solution will be failing when compared to its full solution, at this scales the evolution of the CDM particles is known to be dominated by linear theory, i.e.  $D_{1,cb}$ , and each higher order term is suppressed the smaller the wave-numbers. How can we then investigate what is the impact of this trade-off of losing accuracy in  $D_{2,cb}$  but still getting  $D_{1,cb}$  correct? We need to investigate the matter power spectrum, and see what will be the observed impact! In the next section I'll combine the massive neutrinos approach with the modified gravity approach and show the comparison of the implementation of 2LPT in the COLA approach and check if this is consistent with simulated results.

## 5.5. COLA

In this section I will introduce the concepts behind the COLA [125, 126] approach to N-Body simulations. The COmoving Lagrangian Approach (COLA) is a quasi N-body method that is used

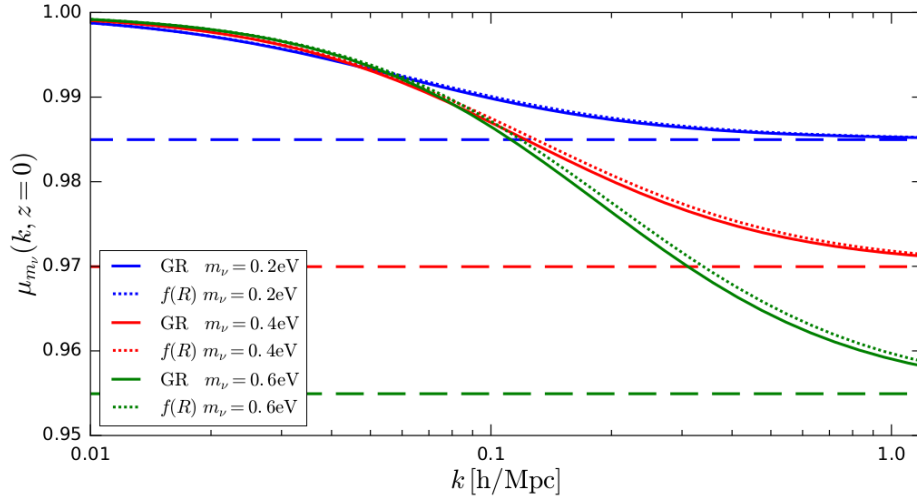


**Figure 5.4.** The value of  $\mu_\nu$  as a function of scale, computed using Equation (5.139) for two different gravity theories GR (solid lines) and  $f(R)$  “Hu-Sawicki” (dotted lines) and the same values of the mass of neutrinos as in Figure 5.3. The horizontal dashed lines are the limiting value  $f_{\text{cb}}$  at small scales, this approximation was used in Equation (5.146) in order to use Fast Fourier Transform algorithms to solve it. Figure taken from [121].

to generate fast realizations of the non-linear cold dark matter density field. This method relies on the use of cosmological Lagrangian Perturbation Theory (LPT) and a Particle-Mesh [127] (PM) N-Body algorithm. It takes advantage of the fact that at large scales, perturbation theory is an accurate description of the Universe while at large wave-numbers N-Body simulations correctly describe the particles trajectories. In this way, the evolution of the cold dark matter (CDM) particles is broken into two pieces: one that is valid at small wave-numbers, where the equations of motion can be solved analytically using second-order LPT, and one that is valid at large wave-numbers, which is able to introduce the fully non-linear behavior of matter by solving the Poisson equation on a PM grid using Fast Fourier Transforms.

As mentioned, the N-Body part of COLA is the implementation of a Particle-Mesh algorithm. To this end, I will briefly summarize the equations being solved by PM codes. As expected, we begin from the canonical equations for a dark matter particle’s position and momenta:

$$\begin{aligned} \frac{d\mathbf{x}}{da} &= \frac{\mathbf{p}}{a'a} = \frac{\mathbf{p}}{\dot{a}a^2}, \\ \frac{d\mathbf{p}}{da} &= -\frac{a'}{a}\nabla\Phi = -\frac{1}{\dot{a}}\nabla\Phi, \\ \nabla^2\Phi &= 4\pi G_N \frac{\rho_m}{a}\delta_m = \frac{3}{2}\frac{\Omega_{m,0}}{a}\delta_m. \end{aligned} \quad (5.150)$$

Equivalently, we can write these equations as:

$$\begin{aligned} \frac{d\mathbf{x}}{da} &= \mathcal{D}(a)\mathbf{p}, \\ \frac{d\mathbf{p}}{da} &= \mathcal{K}(a)\nabla\left[(\nabla^2)^{-1}\delta_m\right] \end{aligned} \quad (5.151)$$

where  $(\nabla^2)^{-1}$  is the inverse of the Laplacian operator,  $\mathcal{D}(a)$  is called the “Drift” pre-factor [128],  $\mathcal{K}(a)$  is the “Kick” pre-factor and I’ll further define a function  $f(a) = a/a' = \mathcal{H}^{-1}(a)$  as the

inverse of the conformal Hubble factor, in this way:

$$\mathcal{D}(a) = \frac{f(a)}{a^2}, \quad (5.152)$$

$$\mathcal{K}(a) = -\frac{3}{2} \frac{\Omega_{m,0} f(a)}{a}. \quad (5.153)$$

If one wants to implement the COLA method, however, we need to adapt the previous equations to the ones described in [125]. I start by recalling that in the Lagrangian description the particle's position is described by:

$$\mathbf{x}_{\text{LPT}}(a) = \mathbf{q} - D_1(a)\Psi_1 + D_2\Psi_2 \quad (5.154)$$

up to second order. We can also decompose the true dark matter position  $\mathbf{x}(a)$  as a 2LPT evolution plus a residual part, which will encode the full non-linear mode coupled (MC) evolution:

$$\mathbf{x}(a) = \mathbf{x}_{\text{LPT}}(a) + \mathbf{x}_{\text{MC}}(a), \quad (5.155)$$

which time derivative with respect to the scale factor gives us:

$$\frac{d\mathbf{x}}{da} = \frac{d\mathbf{x}_{\text{LPT}}}{da} + \frac{d\mathbf{x}_{\text{MC}}}{da}, \quad (5.156)$$

$$\frac{d\mathbf{x}_{\text{LPT}}}{da} = -\frac{dD_1}{da}\Psi_1 + \frac{dD_2}{da}\Psi_2 = \mathcal{D}(a)\mathbf{p}_{\text{LPT}}. \quad (5.157)$$

Equivalently we can define:

$$\frac{d\mathbf{x}_{\text{MC}}}{da} = \mathcal{D}(a)\mathbf{p}_{\text{MC}}. \quad (5.158)$$

The LPT momenta is defined as:

$$\frac{d\mathbf{p}_{\text{LPT}}}{da} = \frac{d}{da} \left( \frac{1}{\mathcal{D}(a)} \frac{d\mathbf{x}_{\text{LPT}}}{da} \right) = -\mathcal{K}(a)\mathcal{V}[\mathbf{x}_{\text{LPT}}](a), \quad (5.159)$$

where the operator  $\mathcal{V}[\cdot]$  is written as:

$$\mathcal{V}[\mathbf{X}](a) = -\frac{1}{\mathcal{K}(a)} \frac{d}{da} \left( \frac{1}{\mathcal{D}(a)} \frac{d\mathbf{X}}{da} \right). \quad (5.160)$$

With these notations and definitions the evolution of the full momenta is:

$$\frac{d\mathbf{p}(a)}{da} = \frac{d\mathbf{p}_{\text{LPT}}}{da} + \frac{d\mathbf{p}_{\text{MC}}}{da} = -\mathcal{K}(a)\mathcal{V}[\mathbf{x}_{\text{LPT}}](a) + \frac{d\mathbf{p}_{\text{MC}}}{da} = \mathcal{K}(a)\nabla \left[ (\nabla^2)^{-1} \delta_{\text{m}} \right]. \quad (5.161)$$

By comparing this equation with Equation (5.154), we find:

$$\mathcal{V}[\mathbf{x}_{\text{LPT}}](a) = -\mathcal{V}[D_1](a)\Psi_1 + \mathcal{V}[D_2](a)\Psi_2. \quad (5.162)$$

As mentioned before, the key point in the COLA approach is that we can compute the fictitious LPT force,  $\mathcal{V}[\mathbf{x}_{\text{LPT}}](a)$  acting on the particles analytically. The computation of  $\mathcal{V}[D_1](a)$  and  $\mathcal{V}[D_2](a)$  uses the differential equations for the first and second order growth factors in LPT and the second Friedmann equation. In summary, in the COLA framework the natural variables being solved are  $\mathbf{x}$  and  $\mathbf{p}_{\text{MC}}$ :

$$\frac{d\mathbf{x}}{da} = \mathcal{D}(a)\mathbf{p}_{\text{MC}} - \frac{dD_1}{da}(a)\Psi_1 + \frac{dD_2}{da}(a)\Psi_2, \quad (5.163)$$

$$\frac{d\mathbf{p}_{\text{MC}}}{da} = \mathcal{K}(a) \left[ \nabla \left( (\nabla^2)^{-1} \delta_{\text{m}} \right) - \mathcal{V}[D_1](a)\Psi_1 + \mathcal{V}[D_2](a)\Psi_2 \right]. \quad (5.164)$$

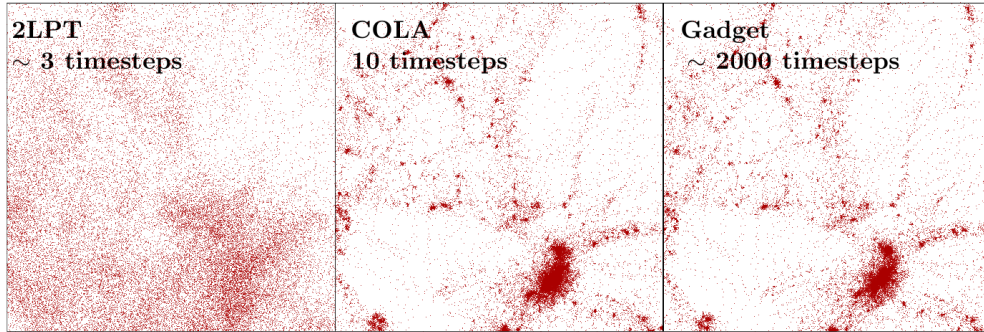


**Figure 5.5.** Snapshots at  $z = 0$  of three different methods, 2LPT, COLA and Gadget (full N-Body code). We can see that with the COLA method we are able to increase the resolution at small scales with only 10 time-steps, when compared to 2LPT. Figure taken from [125].

Figure 5.5 shows the comparison of three snapshots taken at  $z = 0$ . We can see that while 2LPT allows us to reach linear to quasi-linear scales, using the COLA method we are able to increase our resolution at small scales due to the Particle-Mesh N-Body algorithm.

When we generate the initial conditions using LPT, we have that  $\mathbf{p} = \mathbf{p}_{\text{LPT}}$ , therefore, initially,  $\mathbf{p}_{\text{MC}}$  vanishes. As we always have  $\mathbf{p}_{\text{LPT}}$  from solving the LPT equations of motion, at the end of the simulation we add  $\mathbf{p}_{\text{LPT}}$  to  $\mathbf{p}_{\text{MC}}$  to obtain the full momentum of particles. The greatest advantage of the COLA approach is precisely the fact that we can compute 2LPT corrections analytically, by simply integrating the equations of motion. This effectively reduces the total number of time-steps a simple N-Body simulation would require, while getting the correct behavior at large scales, where perturbations theory is known to be the accurate description of the Universe. When we move to smaller scales, the Particle-Mesh algorithm embedded in the COLA approach starts dominating the evolution of dark matter particles, and all the evolution is characterized by it.

In order to connect the physics of the early Universe with the late-time non-linear evolution of the Universe, we need to properly set the initial conditions. I will discuss two types of methods used in the literature to do so:

1) Backscaling:

Historically the most used approach of setting initial conditions, as well as the simplest. It begins by computing the linear matter power spectrum at a given redshift,  $z_{\text{target}}$ , using an Einstein-Boltzmann solver. After this, we rescale the matter distribution to the initial redshift of the simulation,  $z_{\text{ini}}$ , using the linear growth factor:

$$\delta_{\text{m}}(k, z_{\text{ini}}) = \frac{D_1(k, z_{\text{ini}})}{D_1(k, z_{\text{target}})} \delta^{\text{EB}}(k, z_{\text{target}}), \quad (5.165)$$

where  $\delta^{\text{EB}}$  is the linear relativistic matter density perturbation computed by the Einstein-Boltzmann solver, and  $\delta_{\text{m}}$  is the matter density perturbation backscaled using the linear growth factor  $D_1$  computed in an Einstein-de-Sitter Universe. The main advantage of this approach is that at the target redshift and its vicinity, the linear theory power spectrum computed in the simulation will match the one from the Einstein-Boltzmann solver. This is one way of introducing relativistic species, such as photons and neutrinos, in the simulation without having to modify the N-Body code. However, at redshifts far from  $z_{\text{target}}$  the linear prediction between simulation and the E-B solver will be different.

## 2) Forward approach:

In this approach the linear density fields relevant for the evolution of the late-time Universe are pre-computed using an Einstein-Boltzmann solver, and are fed to the N-Body code at each time-step of the simulation. As shown in [129] the output of any Newtonian simulation can always be interpreted in a relativistic framework by simply making coordinate transformations in the final particle's position and velocities. However, it is desirable to use a gauge in which the output can be easily interpreted in a relativistic way. One such gauge is the N-Body gauge presented in Section 4. In this gauge we can correctly understand the relativistic linear theory scales with it, while smoothly transitioning to the Newtonian description at small scales.

Schematically, in both approaches discussed above, we compute the two perturbation theory quantities that are important for us,  $\delta_m^{\text{EB}}$  and  $\theta_m^{\text{EB}}$ , in Fourier space from an Einstein-Boltzmann solver, and then Fourier transform them to real space, at a initial position  $\mathbf{q}$ . These two fields can be consistently mapped into Lagrangian quantities:

$$\mathbf{x}(\mathbf{q}, z_{\text{ini}}) = \mathbf{q} - \nabla \left[ (\nabla^2)^{-1} \delta_m^{\text{EB}}(\mathbf{q}, z_{\text{ini}}) \right], \quad \mathbf{v}(\mathbf{q}, z_{\text{ini}}) = \nabla \left[ (\nabla^2)^{-1} \theta_m^{\text{EB}}(\mathbf{q}, z_{\text{ini}}) \right], \quad (5.166)$$

this effectively corresponds to setting the initial conditions using the Zel'dovich approximation (ZA). After the important contributions from [114], it was noted that linear initial conditions (IC) suffered from transients - significant truncation errors between the linear IC's and the true non-linear evolution - and it was not able to fully capture higher-order moments of the distribution, such as the skewness and the kurtosis. Therefore, it is common nowadays to not set the IC's using the well-know ZA approach, Equation (5.80), but to set them using 2LPT theory, Equation (5.81). As we can see, the main difference between the two representations, ZA and 2LPT, is that as it was previously discussed, in first-order Lagrangian perturbation theory, the movement of dark matter particles contains no information coming from the acceleration, it is an inertial evolution. While at 2LPT we have information directly from the tidal tensor, seen in the bracket terms of Equation (5.81).

As it was already discussed, the COLA method is advantageous due to the reduced number of time-steps it takes to generate non-linear realisations of the density field. While one can always increase the number of time-steps, it is interesting to have about 40-50 time-steps for a high resolution simulations. Therefore, we can expect that COLA simulations will be dependent on how these time-steps are distributed in time, and at which redshift we have started our simulation. In Reference [130], the authors have done a detailed investigation of different COLA simulations with different values of  $z_{\text{ini}}$ , the total number of time-steps and their temporal distribution.

In Figure 5.6 I show the main plots of reference [130] regarding the variation of the previous simulation parameters and the accuracy of COLA simulations. Starting with the top left plot, we can directly conclude that by increasing the number of time-steps we will have a better agreement at small scales when compared to full N-Body simulations. This is understandable, as when we increase the number of time-steps the COLA method becomes a simple Particle-Mesh algorithm. The top right plot shows us the dependence of COLA with the initial redshift of the simulation, which shows that starting at higher redshifts will impact in the power resolution at small scales. This effect must be understood while having in mind that with the COLA method we are always considering fewer time-steps than when compared with a full N-Body simulation. By starting at increasingly higher redshifts will end up causing the code to waste a lot of time-steps at earlier times and reduce the resolution at late-times, where the bulk of the clustering of matter is happening. Nevertheless, starting at higher redshifts is always more desirable, as the

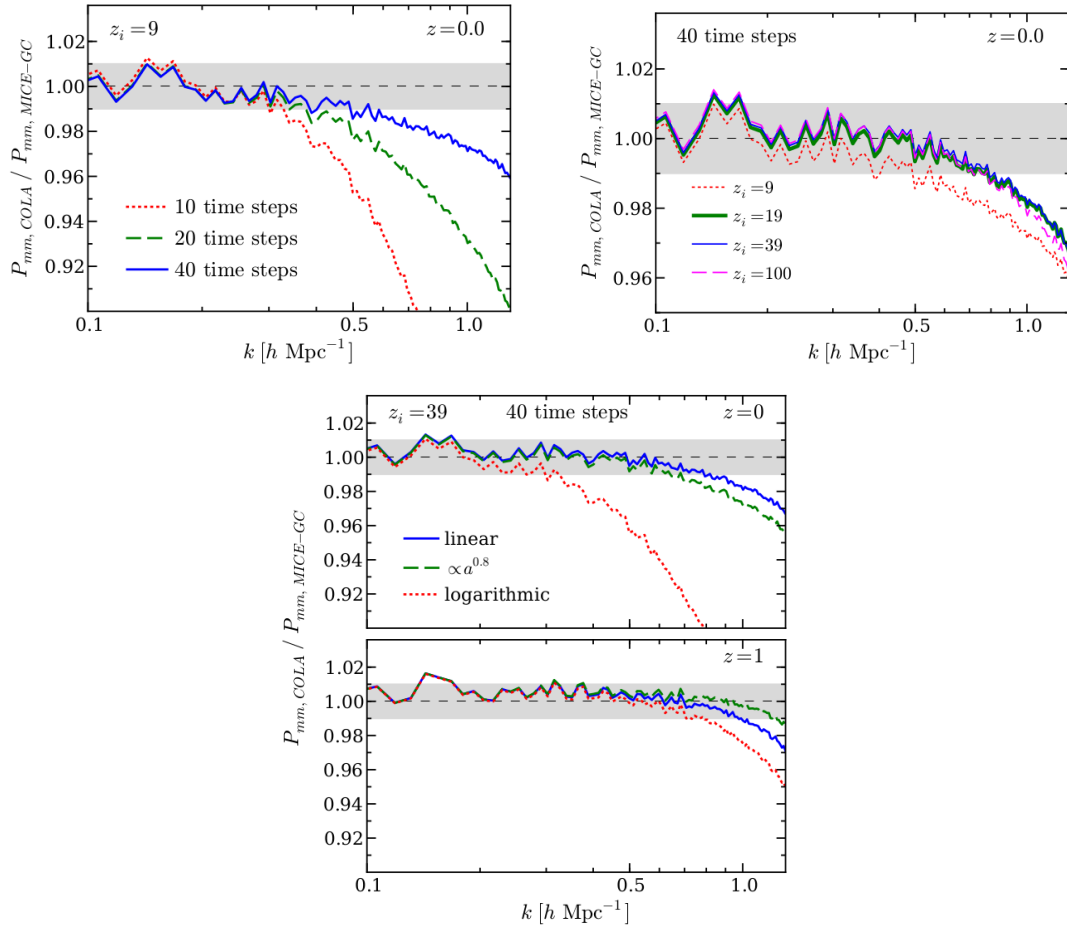


**Figure 5.6. Top left:** Ratio between the dark matter power spectrum computed using COLA simulations with different numbers of time-steps with respect to the same quantity computed with full N-Body simulations. **Top right:** Ratio between the dark matter power spectrum computed using COLA simulations with different initial redshifts with respect to the same quantity computed with full N-Body simulations. **Bottom:** Ratio between the dark matter power spectrum computed using COLA simulations with different spacing between time-steps with respect to the same quantity computed with full N-Body simulations. Figure taken from [130].

Universe is more linear, this is highlighted in the right bottom plot, where we can see the effect of starting at lower redshifts not capturing enough non-linearities. The bottom plot compares the temporal distribution of the time-steps in the simulation. It compares distributing 40 time-steps from  $z_{\text{ini}} = 39$  onto  $z = 0$  using different spacing: linear (solid blue),  $\propto a^{0.8}$  (dashed green) and logarithmic (dotted red). While the general conclusion points to us that by choosing either linear or  $\propto a^{0.8}$  have similar behaviors, a more important conclusion is to realize that we must have a sufficient number of time-steps from  $z = 1$  to  $z = 0$ , where we can see that using a logarithmic spacing fails considerably.

The implementation of modified gravity into COLA is done by introducing modified gravity in 2LPT, as seen in Section 5.4, and by modifying the Particle-Mesh part of the code. I start by

rewriting Equations (5.150) as:

$$\begin{aligned}\frac{d\mathbf{x}}{da} &= \frac{\mathbf{p}}{a'a} = \frac{\mathbf{p}}{\dot{a}a^2}, \\ \frac{d\mathbf{p}}{da} &= -\frac{a'}{a}\nabla\Phi = -\frac{1}{\dot{a}}\nabla\Phi, \\ \nabla^2\Phi &= 4\pi G_N \frac{\rho_m}{a}\delta_m + \frac{1}{2}\nabla^2\delta\phi,\end{aligned}\tag{5.167}$$

where  $\delta\phi$  is the scalar field perturbation. As we know, scalar-tensor theories introduces one extra degree of freedom, a scalar field, which has its own equation of motion. In the majority of modified gravity codes, the equation of motion for the scalar field perturbations is written by taking the QSA limit, and can be written in a condensed way as:

$$L[\delta\phi] = S[\delta\phi, \delta\rho_m],\tag{5.168}$$

where  $L$  is a spatial differential operator acting on the scalar field perturbations, and  $S$  is the source term, which is only a function of fluctuations of the scalar field and the matter density perturbations. The goal of these codes is to find a solution for  $\delta\phi$ , so we can substitute it in the Poisson Equation in (5.167). In this way, the geodesic equation that CDM particles follow will experience an extra force, introduced by the scalar field, as seen in the RHS of Equation (2.17). In order to solve Equation (5.168) we must use very complicated and time-consuming non-linear Gauss-Seidel relaxation methods. This ends up increasing the time these simulations take to finish. In the next section I will discuss a method to bypass this problem, by using the N-Body gauge approach combined with the QSA limit.

As I have previously mentioned, in order to shield the presence of this extra force in the motion of non-relativistic particles, modified theories of gravity are endowed with screening mechanisms, which help us restore GR in dense environments. Looking back at action (2.6), and rewriting it as:

$$S = \frac{1}{16\pi G_N} \int d^4x \sqrt{-g} \left( \phi R - \frac{\omega(\phi)}{\phi} \nabla_\mu \phi \nabla^\mu \phi + K \left[ (\nabla\phi)^2, \nabla^2\phi \right] - 2\Lambda(\phi) \right) + S_m[g_{\mu\nu},]\tag{5.169}$$

where  $K \left[ (\nabla\phi)^2, \nabla^2\phi \right]$  is a function of the first and second derivatives of the scalar field, screening mechanisms can be classified formally depending on which non-linear function appearing in this action [131, 132].

#### 1) *Chameleon Screening:*

In this mechanism we introduce a potential  $\Lambda(\phi)$ . The scalar field  $\phi$  will then assume a background value,  $\phi_0$ , and the potential introduces a mass term for the scalar field perturbation around this background value:

$$(3 + 2\omega_{\text{BD}}) \nabla^2\delta\phi + m(\phi_0)\delta\phi = -8\pi G_N \rho,\tag{5.170}$$

where I've used Jordan-Brans-Dicke theory as an example, thus  $\omega_{\text{BD}}$  appearing in the equation, and the mass term depends on the background value of the field. If we trace a parallel with Yukawa's theory for the description of the strong interactions of particle physics, we know that the field will not propagate beyond a certain wavelength, called Compton wavelength, inversely proportional to the mass term,  $\lambda_C = m^{-1}$ , as the solution for the scalar field perturbation decays as  $e^{-mr}$ , where  $r$  is the distance from the source.

As the mass depends on the background values of the scalar field, it is possible to realise a situation where the mass is large in dense environments like the Solar System, while it remains small in cosmological regimes. I will not go into the details of showing a specific form for the potential  $\Lambda(\phi)$  that allows us to modify gravity non-trivially, however, one can find in References [131, 132] examples of such choices.

2) *Dilaton and Symmetron Screening:*

In this screening mechanism the coupling between matter and scalar field is given in terms of the function  $\omega(\phi)$ , and its value is determined by the background value of the scalar field,  $\phi_0$ , thus depending as well on the background density. Therefore, it is also possible to choose a functional form for  $\omega(\phi)$  which is large for dense environments, satisfying conditions (2.7), and then transitions to values of  $\omega \sim \mathcal{O}(1)$  in cosmological scales.

3) *K-mouflage and Vainshtein screening:*

In both of these cases the screening is realised by using the non-linear kinetic term  $K \left[ (\nabla\phi)^2, \nabla^2\phi \right]$ . In the K-mouflage case we effectively suppress the coupling between matter and scalar field by using the first derivative of the scalar field, while for the Vainshtein case the second derivative.

To conclude the discussion regarding screening mechanisms, there is one other way of bypassing the stringent constraints coming from dense environments, such as the Solar System. These constraints come by observations made of baryonic objects, and, in this way, if we state that the scalar field couples only to dark matter we are able to evade all small scale and dense environments constraints we have in the literature. These models are known as interacting dark energy models in the Einstein frame where the scalar field is coupled only to matter, and with them we can modify gravity significantly in cosmological scales. By making this assumption, however, we break the Equivalence Principle, as now gravity will not be minimally coupled to matter. If we want to keep this principle, then we need to use the non-linearity of the scalar field driven by the non-linear matter density contrast to change the behaviour of the field from cosmology to the Solar System, using one of the models discussed above.

In this chapter I have summarized some of the methods available in the literature to describe the non-linear Universe. These were the tools I have learned and developed during my PhD. In the next section I will present some results of my publications using the formalism outlined in this section.

# Enabling power spectrum emulation in beyond- $\Lambda$ CDM cosmologies with COLA

*In this chapter I will discuss the non-linear matter power spectra in beyond- $\Lambda$ CDM cosmologies computed using the COLA approach. The results presented here are published in Reference [133], and they follow mainly the methodology described in Sections 5.2.2, 5.4 and 5.5.*

## 6.1. Introduction

One of the main efforts in Large Scale Structure (LSS) studies is to answer how initial small and Gaussian density perturbations in the very early Universe evolved to the highly non-Gaussian and non-linear matter distribution we see in our Universe today. In the next years we will have the first data release of the first Stage-IV LSS survey, DESI [134], as well as the launch of the Euclid satellite [135]. The bulk of the investigation in recent years is focused on the exploration of the matter two point correlation function in Fourier space, the matter power spectrum. In order to get fast predictions of this statistics, emulation techniques have gained much attraction in cosmology, and they are now seen as viable alternatives for extracting parameter constraints using the data from upcoming surveys.

Emulators are numerical interpolations that are trained using accurate N-body simulation outputs based on machine learning algorithms to quickly predict the matter power spectrum from linear to non-linear scales in the vast cosmological parameter space. Among the emulators already available in the literature, we will focus on two that have been considered as highly effective and validated, the Euclid Emulator 2<sup>1</sup> [136] (EE2) and Bacco<sup>2</sup> [137] in this paper, and use them to check the accuracy of predicting non-linear matter power spectra. Both have an accuracy of about 1% on small scales for  $\Lambda$ CDM cosmologies, and around 3% for dynamical dark energy and massive neutrinos cosmology in predicting the non-linear power spectrum.

The process of training these emulators heavily relies on the use of computationally expensive and time-consuming full N-body simulations. To overcome these limitations, there are several well established methods that allow us to quickly generate approximate non-linear realizations of the matter density field, such as, the COLA (COmoving Lagrangian Acceleration) approach [125, 126, 138], EZMOCKS [139], PATCHY [140], FastPM [141], GLAM [142], to name a few. Specifically, in our work, we will consider the first of these examples, the COLA approach. This method has been well-validated, and is known to give a good agreement on quasi non-linear scales in

<sup>1</sup><https://github.com/miknab/EuclidEmulator2>

<sup>2</sup><https://baccoemu.readthedocs.io/en/latest/>

$\Lambda$ CDM and beyond- $\Lambda$ CDM cosmologies when comparing its prediction for the matter power spectrum to the ones from full N-body simulations [130, 143, 120, 121, 144]. Additionally, a new avenue using the COLA method was presented in [145], where it was shown that the mapping from displacements in COLA simulations and those in full N-body simulations can be trained on simulations with a fixed value of the cosmological parameters, and this model can be used to correct the output of COLA simulations with different values of cosmological parameters including different masses of massive neutrinos with very high accuracy: the power spectrum and the cross-correlation coefficients are within 1% down to  $k = 1 h/\text{Mpc}$ .

This indicates that the inaccuracy in COLA's predictions is fairly cosmological parameter independent, and this can be corrected by a cosmological parameter independent model. Our work shows that COLA is capable of describing the non-linear response of the matter power spectrum to the change of cosmological parameters down to  $k = 1 h/\text{Mpc}$  with high accuracy. This is because the inaccuracy of COLA is largely cancelled by taking the ratio of power spectra in two different cosmologies. The accurate and fast computation of this response function is of great importance when building emulators, as it allows us to obtain quickly the expected non-linear prediction when parameters are varied with respect to a fixed pre-defined reference cosmology. Given the prediction of non-linear power spectra in a few sparsely sampled reference cosmologies by full N-body simulations, we can provide the prediction of the matter spectrum in a wide parameter space. This can be used to further extend the reach of the already accurate  $\Lambda$ CDM emulators to beyond- $\Lambda$ CDM cosmologies, for example, where running full N-body simulations are very expensive.

Within many different alternatives to the standard cosmology model, we will focus on studying the non-linear response function in scalar-tensor theories of gravity. These theories are possible explanations for the current accelerated expansion of our Universe. The simplest solution in General Relativity (GR) is the addition of the Cosmological Constant,  $\Lambda$ , to the Einstein's field equations. Modified gravity is an alternative to the addition of this constant, where the scalar field would naturally act as the driver of the late-time accelerated expansion. Therefore, creating new emulators, or extending current ones, to be able to quickly predict the small scale behavior of the matter power spectrum in these theories is of great importance for the upcoming LSS surveys. Examples of modified gravity emulators in the literature are [146, 147] where in both papers the emulators are built for one specific fully covariant model,  $f(R)$ .

In this chapter I will use the model-independent approach of the Effective Field Theory of Dark Energy [64, 65] (EFT of DE). Within this formalism, we can fully characterize the linear perturbation of Horndeski theories, using four time dependent functions. Under the quasi-static approximation [131], the modification to the matter power spectrum is characterised by a modified Newton constant called  $G_{\text{eff}}$ , which is a function of these four functions. In this work, to maintain the model-independent approach, we will assume small scale modifications are always characterised by this function in the modified Poisson equation. On large scales, we use the N-body gauge approach developed in [100, 101] to turn our simulations fully relativistic so that the linear power spectrum in COLA simulations agrees with that predicted by the Boltzmann code. The advantage of this approach is that relativistic corrections can be included in the same way as massive neutrinos and there is no additional cost in including EFT of DE in COLA simulations compared with simulations with massive neutrinos in  $\Lambda$ CDM models. I will avoid, for the moment, to discuss screening mechanisms, as these can be included separately, and are highly model dependent. However, I will revisit this issue at the end with some specific considerations.

## 6.2. Methodology

### 6.2.1. COLA

For the COLA part of this project, I used the COLA-FML implementation <sup>3</sup>. This is a C++ parallelized version of the COLA method, good to be used for greater resolution COLA simulations.

For these COLA simulations, the initial conditions were set using 2LPT, and I have used a “forward” approach to initiate our simulations, that is, I have introduced the N-body gauge formalism, described in Chapter 4, in the COLA-FML code. The linear density field encoding relativistic corrections, was computed using a modified version of the publicly available Einstein-Boltzmann solver `hi_class` [66, 67], and it was added at each time-step of the simulation. Therefore, instead of using the back-scaling method, where the linear matter power spectrum is given at  $z = 0$  and then back-scaled to the initial redshift,  $z_{\text{ini}}$ , of the simulation, we provide transfer functions as external data files from  $z_{\text{ini}}$  onto  $z = 0$ . I have used the same approach developed by [121] to introduce relativistic corrections, but have made the modifications to accommodate N-body gauge quantities.

In this work, I have considered simulations with GR as the gravity theory, and simulations with modified gravity. The Poisson equation the COLA code is solving for the GR simulations is given in Equation (5.135), while for the modified gravity ones:

$$k^2 \Phi^{\text{GR}} = 4\pi G_{\text{eff}} a^2 \rho_m \left[ f_{\text{cb}} \left( \delta_{\text{cb}}^{(1)} + \delta_{\text{cb}}^{(2)} \right) \right] + 4\pi G_{\text{N}} a^2 \rho_m f_{\text{GR}} \delta_{\text{GR, rel}}^{(1)}, \quad (6.1)$$

where the function  $G_{\text{eff}}$  is the function that describes the coupling between matter and gravity in modified theories of gravity, Equation (5.119), and  $\delta_{\text{GR, rel}}$  is given in Equation (4.39). The geodesic equation of dark matter particles being solved is then:

$$\ddot{\mathbf{x}} + 2H\dot{\mathbf{x}} = -\nabla\Phi^{\text{GR}}, \quad (6.2)$$

where for GR simulations  $\Phi^{\text{GR}}$  is given by Equation (5.135), and for modified gravity ones  $\Phi^{\text{GR}}$  is given in Equation (6.1). The COLA simulations have all the same specifications, shown in

Parameter	Value
Volume ( $\text{Mpc}^3/h^3$ )	$1024^3$
Number of particles	$1024^3$
Number of PM grids	$2048^3$
Initial redshift	19

**Table 6.1.** COLA simulation specifications.

Table 6.1. Other specifications of COLA simulations used in this chapter are show in Appendix B.

### 6.2.2. Emulators

In sight of Stage-IV LSS surveys, the efforts have been made towards producing fast and accurate theoretical predictions of summary statistics by means of emulators. Emulation methods interpolate the results of cosmological simulations in a broad range of models and cosmological parameters using machine learning techniques [148, 149]. Among the various emulators produced

<sup>3</sup><https://github.com/HAWinther/FML>

so far, the Bacco emulator and EE2 are setting the standards in terms of the accuracy and parameters space coverage. The Bacco emulator takes advantage of Principal Components Analysis

Parameter	Min.	Max.
$h$	0.6	0.8
$\Omega_b$	0.04	0.06
$\Omega_{\text{cdm+b}}$	0.23	0.40
$n_s$	0.92	1.01
$\sigma_8$	0.73	0.9
$\sum_\nu m_\nu$	0.0 eV	0.4 eV
$w_0$	-1.15	-0.85
$w_a$	-0.3	0.3

**Table 6.2.** Bacco training set cosmological parameter space.

(PCA) to reduce the dimensionality of the interpolation problem and applies Gaussian Process Regression to emulate each of the dimensions selected in the PCA. It has been trained on a set of 16000 power spectra spanning the parameter space schematised in Table 6.2. These power spectra have been obtained using the Cosmology Rescaling algorithm [150], on a small suite of only 6  $\Lambda$ CDM simulations obtained with L-Gadget3 [151, 152]. The Cosmology Rescaling algorithm enables a much faster production of the training set at the expenses of a modest loss of accuracy. It has been proven to be 1% accurate in  $\Lambda$ CDM and 3% accurate for dynamical dark energy ( $w_0 - w_a$ ) and massive neutrinos implementations. The emulator intrinsic accuracy is  $\sim 2\%$  up to scales of 5  $h/\text{Mpc}$ , so the overall accuracy is  $\sim 2\%$  in  $\Lambda$ CDM and  $\sim 3\%$  in the DE and massive neutrino cases. Similarly to the Bacco emulator, EE2 performs dimensionality reduction using PCA, but, then relies on a Polynomial Chaos Expansion to emulate the resulting components. The power spectra are measured at 100 time-steps between  $z = 10$  and  $z = 0$  in a suite of 108 pair-fixed simulations [153] performed with PKDGRAV3 [154]. The cosmological parameters space spanned of EE2 is illustrated in Table 6.3.

While both emulators share some similarities in their emulation techniques, the treatment of massive neutrinos in their respective simulations is different. In the PKDGRAV3 simulations, dark energy and massive neutrinos are introduced in the same way as we have implemented in our COLA code. That is, they are introduced inside the general relativistic source term,  $\delta\rho_{\text{GR}}^{\text{Nb}}$ , as a linear density field on a Particle-Mesh (PM) grid. For the L-Gadget3 simulations of the Bacco project, they have used a cosmology rescaling algorithm [155] to mimic the effects of massive neutrinos. This procedure is found to be 1% accurate up to scales of 2  $h/\text{Mpc}$  [155], and 3% accurate up to scales of 5  $h/\text{Mpc}$  [137]. However, in [156], L-Gadget3 simulations with massive neutrinos were performed using a hybrid approach, where they split massive neutrinos into “fast” and “slow” components. This allows one to combine the linear treatment of neutrinos on a PM grid, with the more accurate description of massive neutrinos as low-mass collisionless particles with large thermal velocities following CDM trajectories, which is able to incorporate in the simulations back-reaction effects of neutrinos that reduce the suppression introduced by them [124]. This hybrid approach, however, agrees at below the 0.1% level in the matter power spectrum with the PM method. The only major difference between these different implementations can be seen in the massive neutrinos power spectrum. Therefore, for the purposes of this work, all three methods used here, EE2, Bacco and the COLA implementation are well in agreement with each other with respect to massive neutrinos.

The non-linear boost factors for the training and test sets are computed by taking the ratio of the simulations power spectra with the linear power spectra from CLASS [21]. The EE2 provides  $\sim 1\%$  accuracy up to  $k = 10 h/\text{Mpc}$  in the ellipsoid centered on the reference cosmology and extending to the edges of the interpolation range.

Parameter	Min.	Max.	Center
$h$	0.61	0.73	0.67
$\Omega_b$	0.04	0.06	0.05
$\Omega_m$	0.24	0.40	0.32
$n_s$	0.92	1.0	0.96
$A_s$	$1.7 \times 10^{-9}$	$2.5 \times 10^{-9}$	$2.1 \times 10^{-9}$
$\sum_\nu m_\nu$	0.0 eV	0.15 eV	0.075 eV
$w_0$	-1.3	-0.7	-1.0
$w_a$	-0.7	0.7	0.0

**Table 6.3.** EE2 parameters.

In this chapter all EE2 non-linear matter power spectra shown, were computed from the linear matter power spectrum in the N-body gauge using our own version of the Einstein-Boltzmann solver hiclass, and then multiplied by the boost factor coming from EE2. As EE2 has been trained using relativistic simulations with N-body gauge linear transfer functions, our choice is therefore equivalent to theirs, and for this reason in the Figures shown below the agreement at large scales between COLA and EE2 is well below 0.1% where linear theory is valid. For the Bacco non-linear power spectra, however, I have used their own non-linear matter power spectrum prediction, that is, the linear matter power spectrum is computed inside the emulator, and the non-linear power spectra is just the Bacco boost factor multiplied by their linear prediction. This introduces a slight deviation between COLA and EE2 with Bacco at linear scales. These disagreements are expected since Bacco is not trained with relativistic simulations, nor uses the N-body gauge to compute its linear spectra.

### 6.2.3. Boost and response function

The focus of this work is to study the impact of the non-linear prescriptions by comparing different combinations of the cosmological parameters with different models of modified gravity theory and GR. Since COLA is an approximate fast method, it is not capable of predicting the non-linear power spectrum at large wave-numbers accurately. However, as I will show, COLA is capable of describing the response of the matter power spectrum with respect to the change of cosmological parameters up to  $k \sim 1 h/\text{Mpc}$  as long as the change of the matter power spectrum is not too large. Note that COLA's accuracy depends on a number of settings, such as the number of time steps and the number of grids for the PM part, and it is always a trade-off between accuracy and speed. In Appendix B, I detail the specifications of COLA used for the simulations used in this chapter. I emphasize that all the comparisons and results using our COLA simulations shown in this work can be further improved by changing these specifications at the cost of speed.

Therefore, I will compare the ratio between the linear and non-linear matter power spectrum in different cosmologies with respect to a pre-defined reference cosmology, which in our case will be  $\Lambda$ CDM with the cosmological parameters shown in Table 6.4. I define the linear and non-linear

Parameter	Value
$h$	0.67
$\Omega_b$	0.049
$\Omega_m$	0.319
$n_s$	0.96
$A_s$	$2.1 \times 10^{-9}$
$\sum m_\nu$	0.058 eV

**Table 6.4.** Reference parameters.

response functions as

$$R_{\text{lin}}(k, z) = \frac{P_{\text{lin}}^{\text{case}}(k, z)}{P_{\text{lin}}^{\text{ref}}(k, z)}, \quad R_{\text{non}}(k, z) = \frac{P_{\text{non}}^{\text{case}}(k, z)}{P_{\text{non}}^{\text{ref}}(k, z)} \quad (6.3)$$

respectively, where the superscript “case” refers to a given case cosmology being investigated, and the superscript “ref” always refers to predictions of GR with parameters from Table 6.4. I will also define the non-linear boost as the function that maps the linear matter power spectrum to the non-linear one

$$P_{\text{non}}^{\text{case/ref}}(k, z) = B^{\text{case/ref}}(k, z) \times P_{\text{lin}}^{\text{case/ref}}(k, z), \quad (6.4)$$

and then I can get the non-linear boost in a different cosmology from the reference boost and the ratio of the response functions:

$$B^{\text{case}}(k, z) = B^{\text{ref}}(k, z) \times \frac{R_{\text{non}}^{\text{case}}(k, z)}{R_{\text{lin}}^{\text{case}}(k, z)}. \quad (6.5)$$

In the following sections, I will check the validity of using COLA to compute  $R_{\text{non}}^{\text{case}}(k, z)/R_{\text{lin}}^{\text{case}}(k, z)$  against emulators in  $\Lambda$ CDM and then compute them in modified gravity models.

## 6.3. LCDM Analyses

### 6.3.1. Variation of cosmology parameters

In this section I compare COLA simulations with massless neutrinos with EE2 in terms of the response function defined by Equation (6.3), by varying cosmological parameters one at a time. Throughout this work I fixed the dark energy equation of state to that of a cosmological constant, i.e.,  $w_0 = -1$  and  $w_a = 0$ , as well as the Hubble constant and baryon energy density to their reference values,  $h = 0.67$  and  $\Omega_b = 0.049$ . In this section, the reference cosmology is defined by Table 6.4 but with  $\sum_\nu m_\nu = 0$ .

After making these choices we are left with only three cosmological parameters,  $\Omega_m$ ,  $n_s$  and  $A_s$ , which when varied independently alongside the fixed choices of parameters, impact differently the matter power spectrum. That is, increasing (reducing) the value of the amplitude of the primordial scalar perturbations,  $A_s$ , leads to a re-scaling of the matter power spectrum amplitude up (down), while the variation of the spectral index,  $n_s$ , enhances or suppresses power at small scales. Augmenting the total amount of matter in the Universe, while keeping the baryon densities fixed, leads to increasing the value of the dark matter density. This imprints the matter power spectrum by first changing the scale of equality between matter and radiation era,  $k_{\text{eq}}$ , and by

tilting the spectrum at small scales, i.e., if we have a bigger  $\Omega_{\text{cdm}}$  we will have steeper gravitational potentials, leading to more matter clustering at small scales, while a smaller value for  $\Omega_{\text{cdm}}$  gives you the opposite. To get a better perspective of these features, Figure 6.1 shows the linear

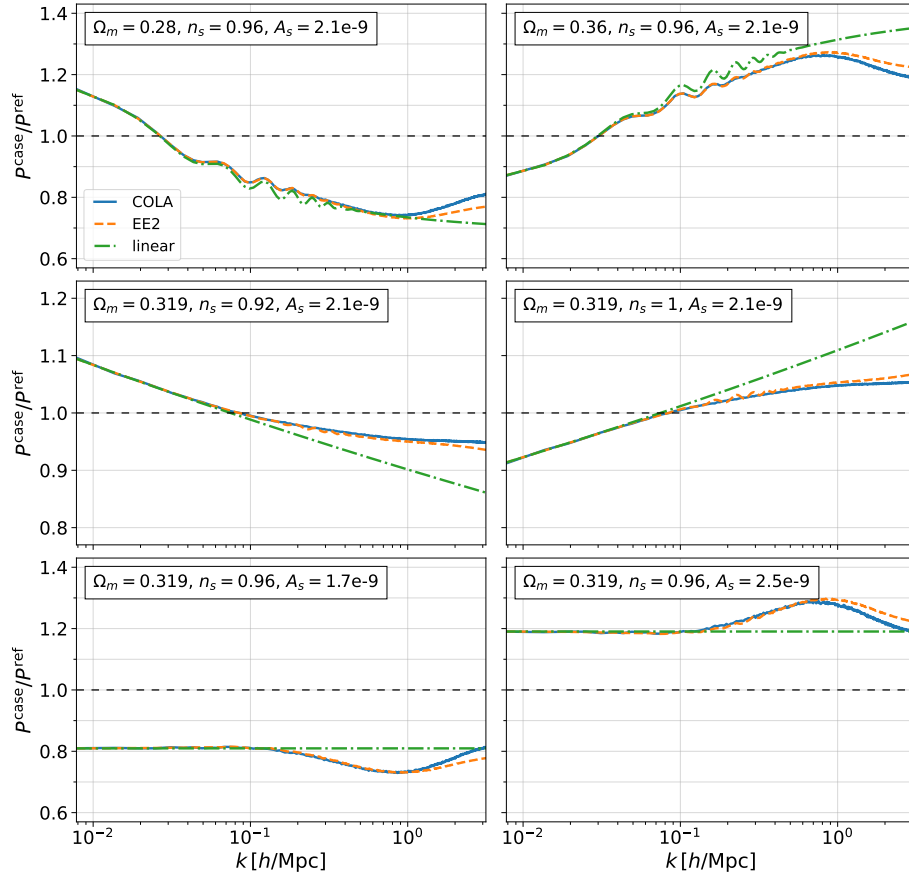


**Figure 6.1.** Non-linear and linear response functions for each variation of the cosmological parameters with respect to the reference cosmology. Blue solid lines are computed from COLA simulations, orange dashed lines are obtained from EE2, and dash-dotted green lines are the linear predictions computed using `hi_class`.

response and non-linear response from COLA simulations and EE2 for massless neutrinos at  $z = 0$ . At large scales (small  $k$  values), all curves agree with each other, while at higher  $k$  values we see non-linear corrections in the solid blue and dashed orange curves.

In our COLA simulations, cosmological parameters were varied in the range shown in Table 6.5. However, in this section, I present the results and comparisons only for the cases which I will refer as “large” variations, that is, the minimum and maximum values shown in the same Table.

Parameter	Min.	Max.
$\Omega_{\text{m}}$	0.28	0.36
$n_{\text{s}}$	0.92	1.0
$A_{\text{s}}$	$1.7 \times 10^{-9}$	$2.5 \times 10^{-9}$

**Table 6.5.** “Large” variation of parameters.

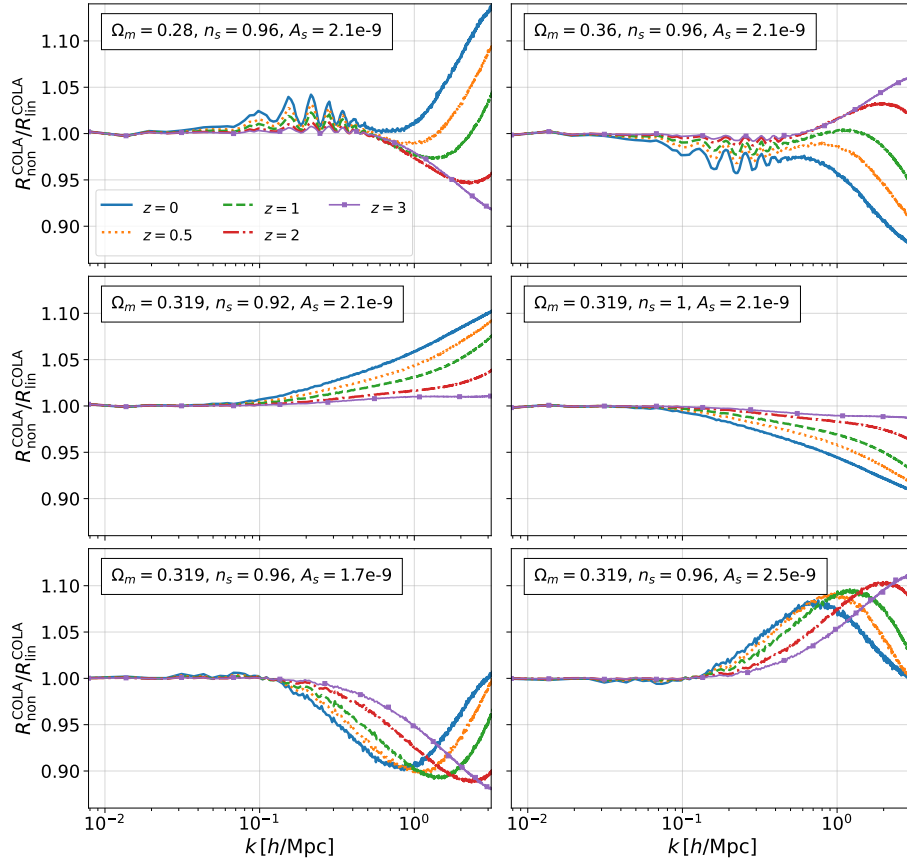


**Figure 6.2.** Ratio between the non-linear and linear response functions computed from COLA simulations. I show this quantity for five different redshifts:  $z = 0$  (solid blue),  $z = 0.5$  (dotted orange),  $z = 1$  (dashed green),  $z = 2$  (dash-dotted red) and  $z = 3$  (solid-squared purple). I use the same convention in all other figures when I show the results at these five redshifts.

The difference between linear and non-linear predictions for  $P^{\text{case}}/P^{\text{ref}}$  in Figure 6.1 is characterised by  $R_{\text{non}}/R_{\text{lin}}$ , which needs to be computed by simulations. Figure 6.2 show the predictions for this function by COLA at different redshifts. In our COLA implementation, the linear prediction from COLA and the one from `hi_class` have a 0.1% agreement with each other. For the change of  $\Omega_m$ , we see oscillations on quasi non-linear scales, which describe the smoothing of BAO oscillations in  $P^{\text{case}}/P^{\text{ref}}$  by non-linearity. For the change of  $n_s$  and  $A_s$ , the non-linearity gives a scale-dependent enhancement or suppression at large  $k$ .

To investigate how well COLA fares with EE2 in predicting  $R_{\text{non}}/R_{\text{lin}}$ , in Figure 6.3 we plot the ratio between the non-linear response from COLA with respect to that of EE2 for the same massless neutrinos case. We can see that we get 2% agreements up to  $k \sim 1 h/\text{Mpc}$  when varying  $\Omega_m$ . When we vary  $n_s$  we get 1% agreements, and for  $A_s$  we obtain 2% agreements at higher redshifts, while at  $z \leq 1$ , they become 1% up to  $k \sim 1 h/\text{Mpc}$ . In Appendix B, I show a comparison between EE2 and Bacco. Note that Bacco does not cover the largest  $\Omega_m$  and  $A_s$  used in this analysis. At  $k < 1 h/\text{Mpc}$ , the agreement between EE2 and Bacco is comparable to that between EE2 and COLA although the agreement is much better at  $k > 1 h/\text{Mpc}$  as expected.

In the above studies, I consider the cases where the matter power spectrum changes up to 30% compared with the reference cosmology as shown in Figure 6.1. The future surveys have the ability to constrain the power spectrum at 1% level. In Appendix C I show the results for small

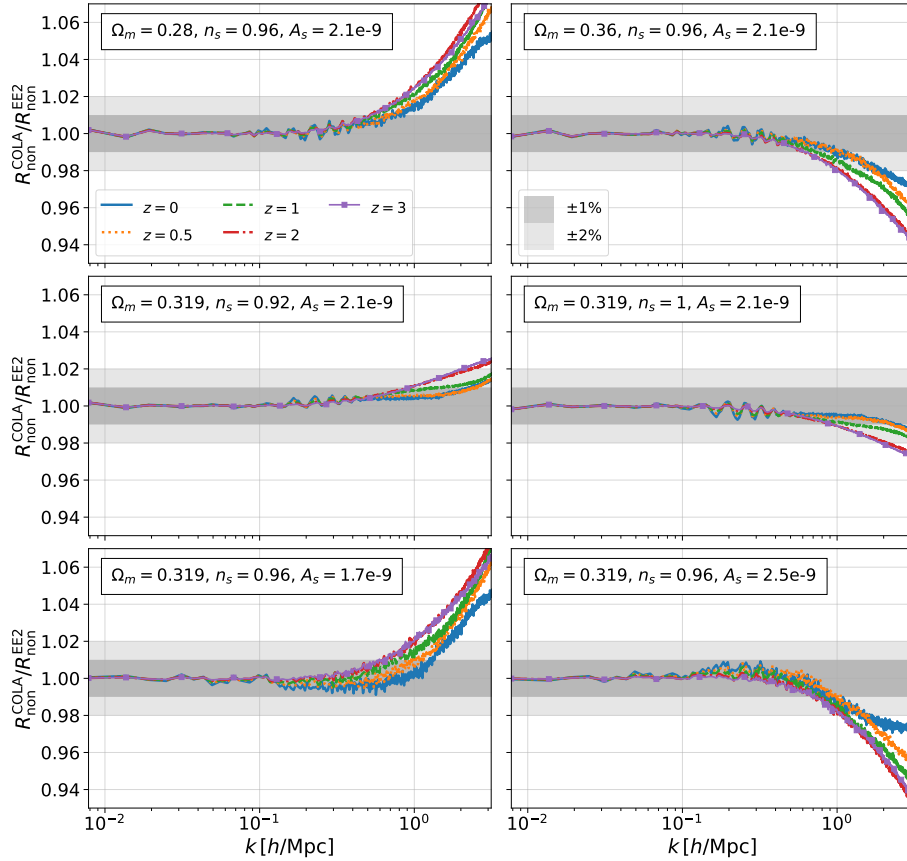


**Figure 6.3.** Ratio between the non-linear response function computed using COLA and the EE2 for the massless neutrinos case.

variations of the cosmological parameters, where there are 1% variations in the matter power spectrum. In this case, COLA is able to reproduce the same results for  $R_{\text{non}}/R_{\text{lin}}$  as EE2 and Bacco with excellent precision ( $< 0.1\%$ ) up to  $k \sim 1 h/\text{Mpc}$ .

This shows that COLA can predict the boost factor defined in Equation (6.5) up to  $k \sim 1 h/\text{Mpc}$  as long as the deviations of the matter power spectrum from the reference cosmology are not too large. This means that COLA can be used to emulate the matter power spectrum with given  $B^{\text{ref}}(k, z)$  in a few chosen reference cosmologies where we require full N-body simulations to obtain the non-linear boost.

### 6.3.2. Inclusion of massive neutrinos

The observation of the flavour oscillations of neutrinos confirmed that the sum of neutrino masses is not zero. While its exact value is not yet known, massive neutrinos play an important role in cosmology. The matter power spectrum is affected by the variation of the sum of neutrino masses in two different ways. Firstly massive neutrinos introduce relativistic corrections at small  $k$  values, where the bigger the value of their mass, the larger the deviation from a simulation where these species are not correctly introduced [111]. The other imprint massive neutrinos leave in the power spectrum is the suppression of the growth of structure at small scales, which makes the growth scale-dependent. At a specific scale, called the free-streaming scale, neutrinos travel freely out of the gravitational potentials generated by cold dark matter. At the linear level, the

suppression present in the dark matter power spectrum is found to be proportional to the ratio between the neutrinos and total matter energy densities [157],  $f_\nu = \Omega_\nu/\Omega_m$ , therefore, the larger the mass the greater the suppression. Since the two effects have their intensities related to the sum of the masses of neutrinos, this highlights the importance that neutrinos have for the next generation LSS surveys.

As both emulators used in this work have been trained assuming three degenerate massive neutrinos, I ran COLA simulations accordingly for two different values of the sum of the masses, 0.058 eV and 0.15 eV, and I also compare both of these cases with the massless case.

With the output of our simulations we then computed the quantity

$$R_{\text{non}}^{\text{ratio,COLA}} = \frac{P_{\text{non}}^{m_{\nu i}}}{P_{\text{non}}^{m_{\nu j}}}, \quad (6.6)$$

which is the non-linear response function between two different neutrino masses, where  $i, j$  refers to one of the three masses considered:  $\sum_\nu m_\nu = 0.0$  eV, 0.058 eV and 0.15 eV. As I am interested in the comparison of COLA and emulators, I evaluated the same quantity for EE2 and Bacco as well. The result is plotted in Figure 6.4, which shows the ratio of the non-linear response function (6.6) for each method. The curves shown in Figure 6.4 show us how the non-linear suppression between different prescriptions of the matter power spectrum are in agreement with each other. From Figure 6.4, at  $z = 1$  we can see that COLA and EE2 have a below 0.1% agreement with each other in almost the full range of scales, i.e., from small scales to beyond  $1 h/\text{Mpc}$ . While at  $z = 0$  the agreement slightly degrades at  $k > 1 h/\text{Mpc}$  due to the fact that EE2 is more accurate than COLA simulations at smaller scales. We find a similar agreement between Bacco and EE2 at  $k < 1 h/\text{Mpc}$ . Therefore, modulo deviations smaller than 0.5% up until  $k = 1 h/\text{Mpc}$ , the three methods are in excellent agreement, and the implementation of massive neutrinos in COLA does not introduce any biases when compared to the well validated emulators.

## 6.4. Modified Gravity

In this section I will study how modified gravity affects the growth of structure. I will use the model-independent formalism of the EFT of DE to introduce non-linear corrections sourced by the scalar field. That is, I ran COLA simulations following Equation (6.1), where the  $G_{\text{eff}}$  function is given by

$$G_{\text{eff}} = 1 + \frac{c_{\text{sN}}^2 (2 - 2M_*^2 + 2\alpha_{\text{T}}) + (\alpha_{\text{B}} + 2\alpha_{\text{M}} - 2\alpha_{\text{T}} + \alpha_{\text{B}}\alpha_{\text{T}})^2}{2c_{\text{sN}}^2 M_*^2}, \quad (6.7)$$

and  $\alpha_i$ ,  $M_*^2$  and  $c_{\text{sN}}^2$  functions are given in 2.4. The common approach of modified gravity N-body codes compute  $G_{\text{eff}}$  by solving the scalar field fluctuation equation under the Quasi-static approximation (QSA), and then substitute the solution into the Poisson equation. In this approach, however, we are able to bypass this by splitting the dark energy perturbations into two parts: one that is purely relativistic (dynamical) and another that is sourced by matter density perturbations (QSA). In this way we are able to model the scale-dependence of the growth function present in modified gravity theories at large scales by  $\delta_{\text{GR, rel}}$  (Equation 4.39), while allowing non-linearities in matter perturbations using  $G_{\text{eff}}$ .

Note that there is no additional cost to include  $\delta_{\text{GR, rel}}$  (Equation 4.39) in our simulations compared with simulations with massive neutrinos. We just need to use  $\delta_{\text{GR, rel}}$  including both massive neutrinos and modified gravity effects.

Although not discussed in this work, there is one last step that is necessary to complete the description of modified gravity simulations, i.e. the introduction of screening mechanisms. In the

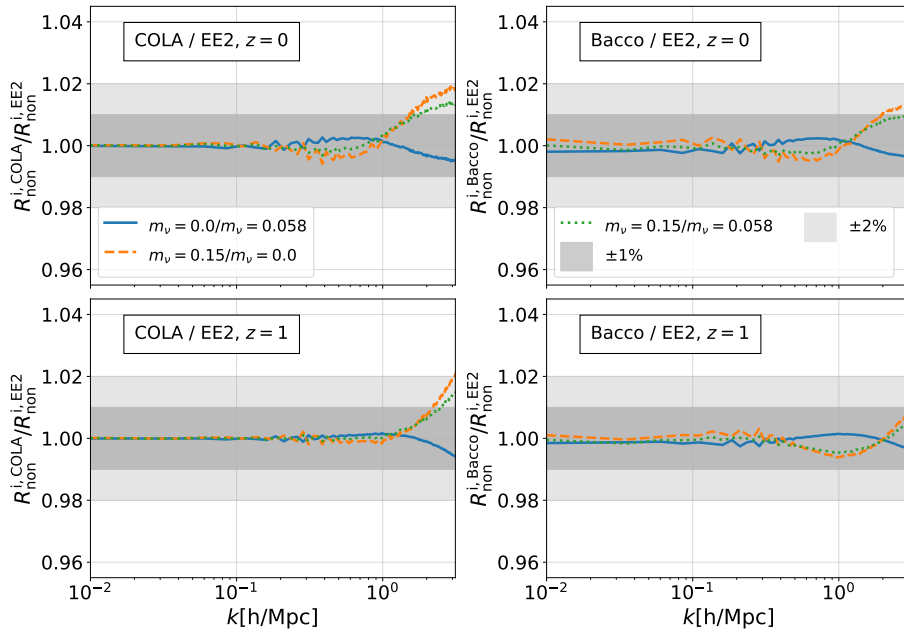


**Figure 6.4.** Ratio of non-linear response function, Equation (6.6), between COLA and EE2 (left column plots) and between Bacco and EE2 (right column plots) for two redshifts,  $z = 0$  (top row plots) and  $z = 1$  (bottom row plots). Solid blue lines compare the ratio  $\sum_{\nu} m_{\nu} = 0.0 \text{ eV} / \sum_{\nu} m_{\nu} = 0.058 \text{ eV}$ , orange dashed lines compare the ratio  $\sum_{\nu} m_{\nu} = 0.15 \text{ eV} / \sum_{\nu} m_{\nu} = 0.058 \text{ eV}$ , and dotted green lines compare the ratio  $\sum_{\nu} m_{\nu} = 0.15 \text{ eV} / \sum_{\nu} m_{\nu} = 0.058 \text{ eV}$ .

FML implementation of COLA<sup>4</sup>, screening mechanisms can be included either using screening approximations or solving the exact scalar field equation using a multi-grid solver. However, screening mechanisms are model-dependent, and, therefore, we need to first choose a modified gravity theory, and then investigate which screening mechanism will be realised in this theory. This spoils the model-independent approach I want to discuss in this work. For this reason, I chose not to model the shielding of the fifth-force at small scales. However, this has been well studied in the literature [158], and can be easily introduced in our formalism.

Continuing our model-independent approach, we need to select a parametrization for the time-dependent  $\alpha_i$  functions [61]. For the sake of generality and familiarity with previous works, I will use the following parametrization:

$$\alpha_i = c_i \times a, \quad i = \text{M, B, K, T}, \quad (6.8)$$

where the  $c_i$ 's are constants and  $a$  is the scale factor. I will fix the kineticity function,  $\alpha_K = 10 \times a$ , and I will focus on only two sets of Horndeski theories [159], one where we have  $\alpha_B \neq 0$  and  $\alpha_M = \alpha_T = 0$ , i.e., only-brading case, and the Jordan-Brans-Dicke [51] like case,  $\alpha_B = -\alpha_M \neq 0$  and  $\alpha_T = 0$ . Additionally, following the EFT of DE approach, besides fixing the  $\alpha_i$  functions, we are still left to choose one more function that fully characterizes the evolution of dark energy models in a model-independent framework, the background evolution history,  $H(a)$ . For simplicity, and due to the multiple constraints one can get on the expansion of our Universe, I choose to fix it to an  $\Lambda$ CDM evolution with the energy fractional densities given by Table 6.4 or Table 6.5. I emphasize that these functions have been chosen for illustrations of our approach and any other functions can be used in the simulations.

<sup>4</sup><https://github.com/HAWinther/FML>

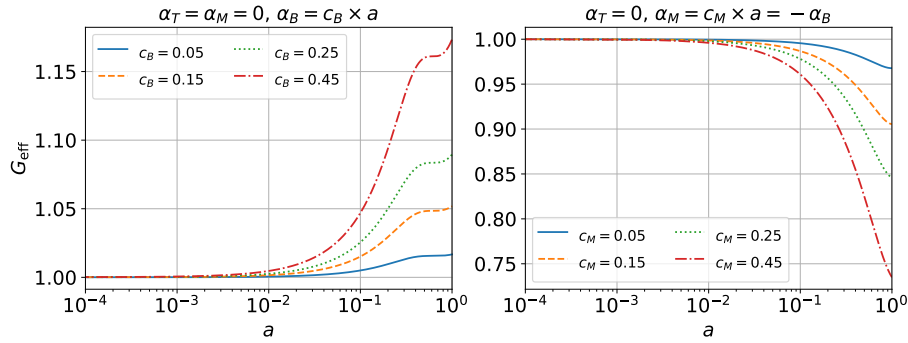


**Figure 6.5.** **Left:** Evolution of the  $G_{\text{eff}}$  function in the “only-braiding” gravity model i.e.  $\alpha_B = c_B \times a$  and  $\alpha_T = \alpha_M = 0$ , for  $c_B = 0.05$  (solid blue), 0.15 (dashed orange), 0.25 (dotted green) and 0.45 (dash-dotted red). **Right:** Evolution of the  $G_{\text{eff}}$  function in the “JBD-like” gravity model, i.e.  $\alpha_B = -\alpha_M = c_M \times a$  and  $\alpha_T = 0$ , for  $c_M = 0.05$  (solid blue), 0.15 (dashed orange), 0.25 (dotted green) and 0.45 (dash-dotted red). In both cases  $\alpha_K = 10 \times a$ .

I show in Figure 6.5 the evolution of  $G_{\text{eff}}$  for the two models for different values of the proportionality constants. As shown in [100, 101], the kineticity function affects the matter power spectrum only at sufficiently large scales,  $k \sim 10^{-3} h/\text{Mpc}$ , and due to the size of our simulations, shown in Table 6.1, the specific value and functional form for  $\alpha_K$  is not relevant for the exposition of our results, which is the reason to have kept it fixed. As discussed in Section 6.2, our COLA simulations incorporate the relativistic effects of photons, neutrinos and dark energy using the N-body gauge approach, following the same approach used by EE2. In all COLA simulations in this modified gravity section I fix the sum of neutrinos masses to 0.058 eV.

### 6.4.1. Fixed cosmology

To investigate the interplay between modified gravity (MG) and the cosmological parameters I will first compare the linear and non-linear response,  $R_{\text{lin}}^{\text{MG}}$  and  $R_{\text{non}}^{\text{MG}}$ , for the modified gravity cases mentioned above, while keeping the cosmological parameters fixed to their reference values shown in Table 6.4.

From Figures 6.6 and 6.7 we can see that non-linear effects are stronger for larger values of the constant of proportionality, in accordance with the plots shown in Figure 6.5. More interestingly, from the top left plot of Figure 6.6, the lowest value of  $c_B$ , we see almost no non-linear corrections in the response function up to  $k \sim 1 h/\text{Mpc}$ . In the “only-braiding” gravity model, non-linearity introduces an enhancement, while in the “JBD-like” model, non-linearity gives an additional suppression at large  $k$ . At small  $k$ , linear and COLA predictions are in excellent agreement due to the correct implementation of the relativistic effects in COLA simulations described in Section 6.2.

The impact of non-linear corrections in the matter power spectrum for each model discussed is shown in Figures 6.8 and 6.9. I plot the ratio between the matter power spectrum in modified gravity with respect to the one computed using GR with the same cosmological parameters. If we use the quasi-static approximation and linear approximations, we see a constant off-set caused by  $G_{\text{eff}}$ .

The deviation from the constant offset at small  $k$  arises from relativistic corrections that are computed by the Boltzmann code. We see that at small  $k$  values, the non-linear (solid lines) and linear curves (dashed lines) have the same behavior, as expected, since in the COLA

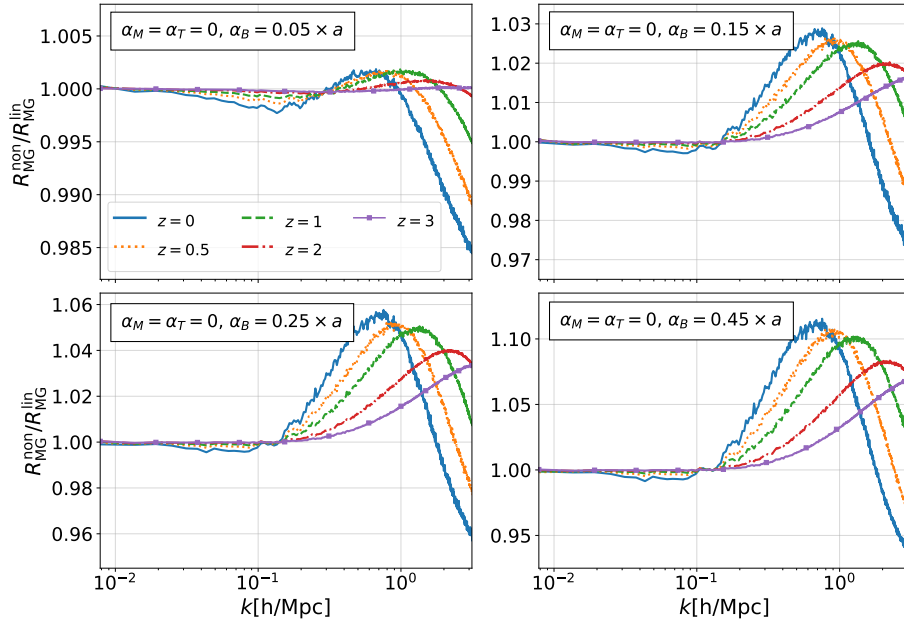


**Figure 6.6.** Ratio between non-linear and linear response functions in modified gravity (MG) “only-braiding” models with different proportionality constants  $c_B$ .

implementation we have consistently introduced relativistic corrections.

At large wave-numbers, the deviations from the constant off-set arise from non-linear effects, which are more prominent at smaller redshifts and for larger values of the modified gravity parameters,  $c_B$  (only-braiding) and  $c_M$  (JBD) as expected as non-linearity is stronger. We see that non-linearity gives an additional enhancement at large  $k$  in the “only-braiding” case while it gives an additional suppression in the “JBD” model. As shown in the previous section, COLA should be able to capture these non-linear corrections accurately up to  $k \sim 1 h/\text{Mpc}$ .

### 6.4.2. Varying cosmology

I now move to the next discussion where I will vary the cosmological parameters  $A_s$ ,  $n_s$  and  $\Omega_m$  as shown in Table 6.5. Our main goal in this section is to investigate the dependence of modified gravity effects on these parameters. Since the effect of the Horndeski scalar field seen in Figures 6.6 and 6.7 is very similar in different models modulo the difference between enhancing/suppressing the growth, I chose to select only one case of modified gravity, i.e. the only-braiding case with  $c_B = 0.45$ . This value is of particular interest as the non-linear response with respect to the linear one is roughly 10% at  $z = 0$ , and I will refer to this value as “cB10”. Note that the effect on the matter power spectrum is around 30% on linear scales at  $z = 0$ .

In the left hand side of Figure 6.10, I plot  $B^{\text{case}}/B^{\text{ref}}$  in the reference cosmology and the model with “cB10”. The superscript “case” refers to one of the 6 cases of “large” values in Table 6.5. The right hand side of the plot shows the ratio:

$$\mathcal{R}_{\text{cB10,GR}} = \frac{B_{\text{cB10}}^{\text{case}}}{B_{\text{cB10}}^{\text{ref}}} \times \left( \frac{B_{\text{GR}}^{\text{case}}}{B_{\text{GR}}^{\text{ref}}} \right)^{-1} \quad (6.9)$$

We can see that all cases where the variation of the cosmological parameters decreased their values from the reference ones, the ratio  $B^{\text{case}}/B^{\text{ref}}$  increase in the “cB10” model compared with

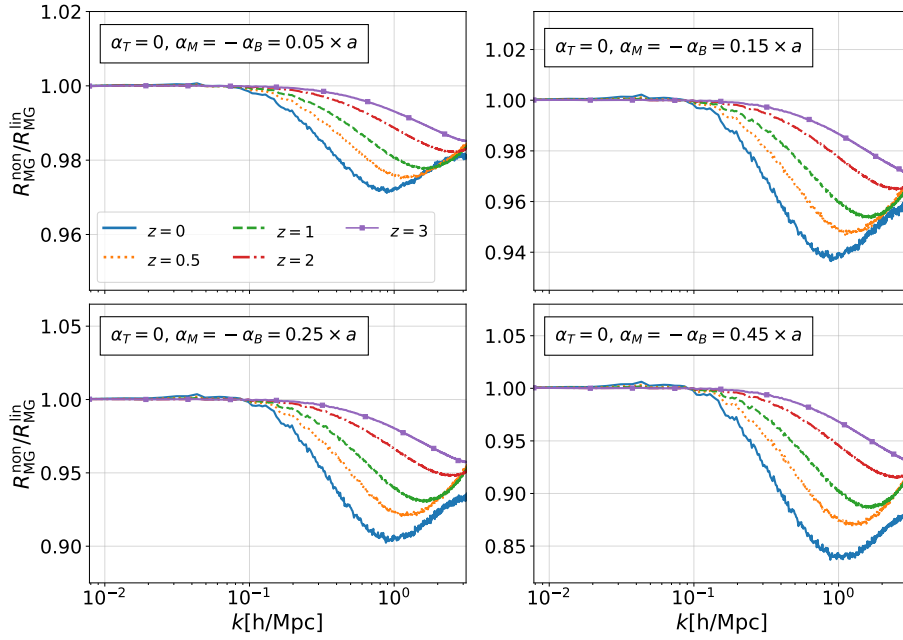


**Figure 6.7.** Ratio between non-linear and linear response functions in modified gravity “JBD-like” models with different proportionality constants  $c_M$ .

the reference cosmology in GR. Note that in these cases, the effect of changing these cosmological parameters is to decrease the amplitude of the power spectrum on small scales while the effect of the modified gravity considered here is to enhance the amplitude. The increase in the ratio  $B^{\text{case}}/B^{\text{ref}}$  is more prominent in the cases of the parameters  $\Omega_m$  and  $A_s$ , as these two are related to changes in the overall amplitude of the power spectrum, while it is milder in the case of the spectral index reaching at most an increase of 2%. When the cosmological parameters increase, we see an opposite effect. Overall, compared with  $B^{\text{case}}/B^{\text{ref}}$  in the reference cosmology, the effect of modified gravity is fairly weak at  $k < 1 h/\text{Mpc}$  except for  $\Omega_m$ .

The ratio  $\mathcal{R}_{\text{cB10,GR}}$  can be rewritten as

$$\mathcal{R}_{\text{cB10,GR}} = \frac{R_{\text{non,cB10}}^{\text{case}}}{R_{\text{lin,cB10}}^{\text{case}}} \times \left( \frac{R_{\text{non,cB10}}^{\text{ref}}}{R_{\text{lin,cB10}}^{\text{ref}}} \right)^{-1} \quad (6.10)$$

where

$$R_{\text{non,cB10}}^{\text{case}} = \frac{P_{\text{non,cB10}}^{\text{case}}}{P_{\text{non,GR}}^{\text{ref}}}, \quad R_{\text{non,cB10}}^{\text{ref}} = \frac{P_{\text{non,cB10}}^{\text{ref}}}{P_{\text{non,GR}}^{\text{ref}}}, \quad (6.11)$$

$$R_{\text{lin,cB10}}^{\text{case}} = \frac{P_{\text{lin,cB10}}^{\text{case}}}{P_{\text{lin,GR}}^{\text{ref}}}, \quad R_{\text{lin,cB10}}^{\text{ref}} = \frac{P_{\text{lin,cB10}}^{\text{ref}}}{P_{\text{lin,GR}}^{\text{ref}}} \quad (6.12)$$

which is accordance with our previous definitions in Equations (6.3), where the reference non-linear and linear matter power spectra are always computed with cosmological parameters in Table 6.4 and GR as the gravity theory. Thus  $\mathcal{R}_{\text{cB10,GR}}$  can be interpreted in two ways: how modified gravity changes the cosmological parameter dependence of the boost factor as discussed above, and how cosmological parameters affect the response of the matter power spectrum to modified gravity parameters. As we have seen, the cosmological parameter dependence of  $\mathcal{R}_{\text{cB10,GR}}$

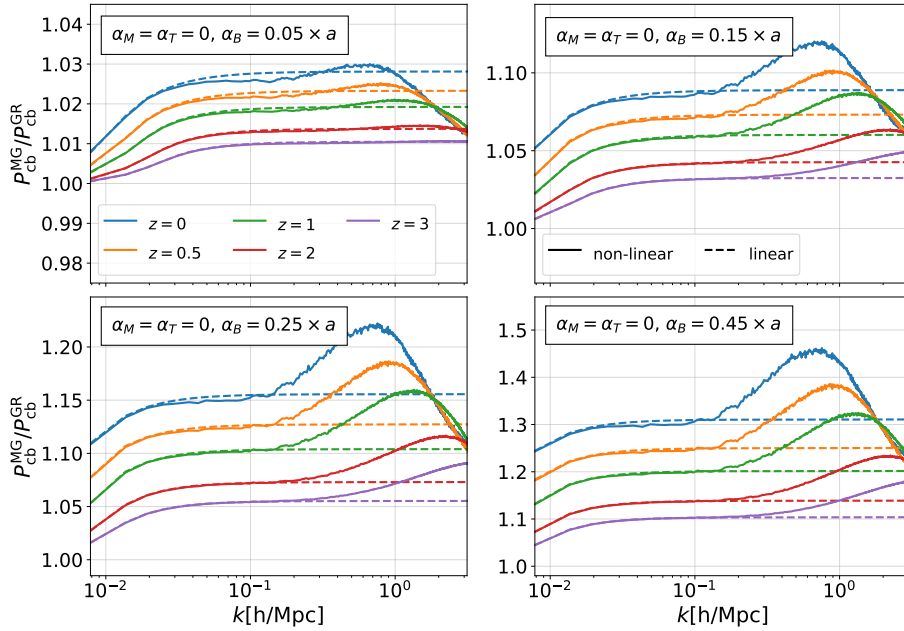


**Figure 6.8.** Ratio between modified gravity and GR power spectra in the “only-braiding” model. The solid lines refer to the non-linear prediction, while the dashed ones to the linear one.

is fairly weak at  $k < 1 h/\text{Mpc}$  except for  $\Omega_m$ . This property is useful when creating emulators for the response functions for modified gravity parameters. This is consistent with what was found in  $f(R)$  gravity in [160].

It is worth stressing how general our results are in view to the large freedom we have to choose the parametrization for the  $\alpha_i$  functions. For late-time dark energy models, the choice of parametrization is such that, as the Universe evolves, the impact of dark energy on the matter power spectrum also increases. In this work, I have chosen to the  $\alpha_i$  functions proportional to the scale factor, in order to highlight the new features introduced by the scalar field. Indeed, making the  $\alpha_i$  functions linearly proportional to the scale factor allows them to impact at an earlier period of time than the case where we have  $\alpha_i \propto \Omega_{\text{DE}}$ , another common choice in the literature. The latter parametrization forces the scalar field density perturbations to be relevant only at redshifts during dark energy domination era,  $z \lesssim 0.7$ . However, the same analysis and conclusions of this thesis are still be valid.

## 6.5. Closing remarks

In this work, I have validated COLA simulations with two existing emulators in the literature, the EE2 and the Bacco emulator. In order to do so, I have made use of the non-linear response function, defined in Equation (6.3), where the reference cosmology is given in Table 6.4. In each case we varied the cosmology by changing one of the following cosmological parameters: the total matter energy density, spectral index and amplitude of the primordial fluctuations, within the range detailed in Table 6.5. All COLA simulations followed the same specifications presented in Table 6.1 and Appendix C. The performance of COLA can be improved further at the cost of computational time and complexity.

In Section 6.3.1 I have analysed how the ratio between the non-linear and linear response

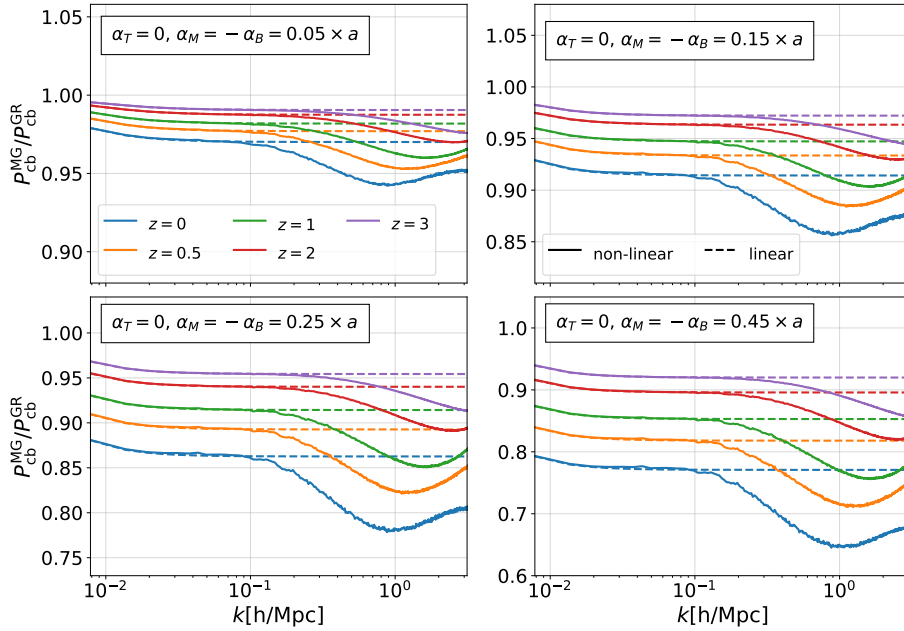


**Figure 6.9.** Ratio between modified gravity and GR power spectra in the “JBD-like” model. The solid lines refer to the non-linear prediction, while the dashed ones to the linear.

functions, computed using COLA, is affected by varying the cosmological parameters to large deviation values, i.e. the boundaries of the ranges shown in Table 6.5 as displayed in Figure 6.2. To investigate the agreement between COLA and EE2, in Figure 6.3 I showed the ratio between the non-linear response function computed using each method, and we can conclude that both predictions agree at the 2% level up until  $k = 1 h/\text{Mpc}$ . For small variations of the cosmological parameters (0.5% variations), the agreement is even better, being well below the 0.1% level as shown in Appendix C, which also includes the validation with the Bacco emulator.

To test the implementation of massive neutrinos in COLA, in Section 6.3.2, I computed the non-linear suppression computed by each non-linear prescription, i.e. Equation (6.6), at  $z = 0$  and  $z = 1$ . I used three different values of the sum of the neutrino masses, 0.0 eV, 0.058 eV and 0.15 eV, in our COLA simulations. In Figure 6.4, I plotted the ratio of the non-linear suppression between the different cases of neutrino masses evaluated by each method, COLA, EE2 and Bacco. I found that all three were in agreement at below 0.5% level at both redshifts down to  $k = 1 h/\text{Mpc}$ , showing that the treatment of massive neutrinos in COLA does not introduce any biases, and the non-linear response function computed using COLA simulations can be used to extend existing emulators in the literature, as well as to train new ones.

In Section 6.4 I introduced the implementation of scalar-tensor theories of gravity in COLA via the model-independent approach of the EFT of DE. In order to do so, all non-linearities arising from the scalar field fluctuations are encoded in the  $G_{\text{eff}}$  function, Equation (6.7), which functional form is found by assuming that non-linear corrections of modified gravity are sourced only by matter density perturbations (QSA limit). At the same time, I also implemented relativistic corrections from the scalar field perturbations via the N-body gauge approach developed in [100, 101].

In Figures 6.6 and 6.7 I showed how non-linearities affect the response function in two different models, the only-braiding model and the JBD-like one. The main effect corresponds to a rescaling of the amplitude of the matter power spectrum by either enhancing the power at small scales

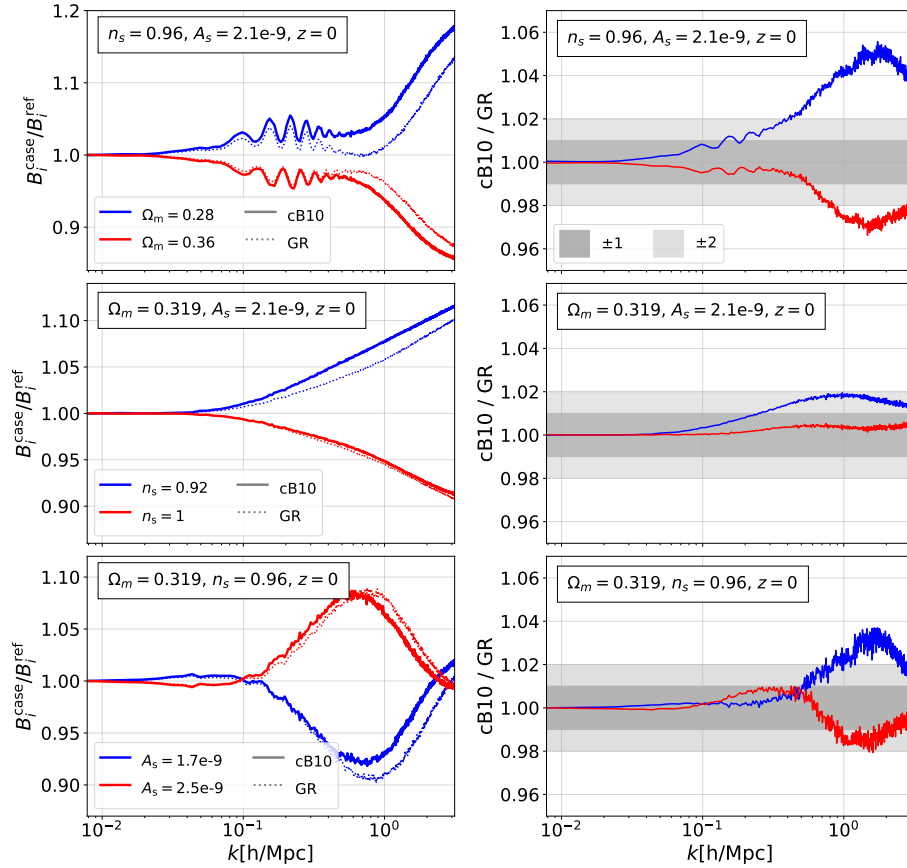


**Figure 6.10.** In the left panel, I show the ratio between the boost factor in each “large” cosmological parameter variation case and that in the reference cosmology. The solid lines show this quantity in the modified gravity “only-braiding” case (cB10) while dotted ones show this in GR. In the right panel, I show the ratio of this ratio between modified gravity and GR. Top, middle and bottom row plots show variations with respect  $\Omega_m$ , the spectral index  $n_s$  and the amplitude of the primordial perturbations  $A_s$ , respectively.

in the only-braiding case, or suppressing the growth of structure at these scales in the JBD-like model as shown in Figures 6.8 and 6.9. These figures showed also that our COLA simulations included dynamical effects of relativistic species including the scalar field on large scales as well as non-linear clustering of dark energy driven by non-linear matter perturbations on smaller scales.

Based on this analysis, in Section 6.4.2, I have then chosen a specific case of the only-braiding gravity, “cB10”, to investigate how modified gravity impacts the variation of cosmological parameters. This was done by running new COLA simulations for large variation values of  $\Omega_m$ ,  $A_s$  and  $n_s$ , but with the gravity theory being described by “cB10”. As showed in Figure 6.10, our results showed that the dependence of the response function with respect to the change of the modified gravity parameter on  $A_s$  and  $n_s$  is fairly weak up to  $k = 1$  h/Mpc. For  $\Omega_m$ , we saw a stronger dependence, which was also found in reference [160].

With the results of our investigations, we can state that COLA simulations can be used to extend emulators already available in the literature, as well as to train new ones, via the use of the response functions computed from these simulations. This method is able to push the regime of validity of COLA down to  $k = 1$  h/Mpc with accuracy below 1% if the deviations from the reference cosmology are small enough. For beyond- $\Lambda$ CDM cosmologies this is particularly

important, as running COLA simulations are much faster than full N-body ones. Also, since the dependence on cosmological parameters is fairly mild in the response function with respect to modified gravity parameters, we can use cosmology-independent methods to include new theories of gravity into emulators, which is a very desirable feature for the upcoming LSS surveys.

---

# Conclusions and Future Avenues

## 7.1. Conclusion

Modified theories of gravity continue to attract a lot of attention in the community, as they offer a natural explanation for the late-time acceleration of the Universe. However, we have reached a turning point on the investigation of these models. As we prepare for the first data release of the upcoming stage-IV LSS surveys, such as DESI, there is an unprecedented need to increase the performance and accuracy of the theoretical tools developed in beyond- $\Lambda$ CDM models.

This thesis focused on the study of effects of modified gravity in the Large Scale Structure of our Universe. We have seen that at linear order we are able to perform tests either in a model-dependent or a model-independent way, by parameterizing the equations of motion for the growth of structure and light propagation in the Universe. When we move to the non-linear Universe, much of the model independent formalism is lost, as we need to introduce screening mechanisms, which depend on which modified theory of gravity we are working with. Nevertheless, in Chapter 6, I presented a way to extend the model independent framework of the Effective Field Theory of Dark Energy into COLA simulations. This was done by combining the N-Body gauge approach to introduce relativistic effects into Newtonian simulations, with the Quasi-static approximation, which allows us to capture all the effects introduced by the scalar field fluctuations that are sourced by matter perturbations. In this way, we can absorb the QSA part of the dark energy perturbations into an effective Newton's constant,  $G_{\text{eff}}$ , while still introducing relativistic (dynamical) perturbations of the scalar field at linear order with the N-Body gauge. The results shown in Chapter 6 are in line with other results in the literature that compare full N-Body simulations of modified gravity theories, such as [160].

In view of stage-IV LSS surveys that will soon release their much awaited data, this implementation of beyond- $\Lambda$ CDM models in the COLA method is a very desirable feature, as it allows us to generate fast approximate realizations of the non-linear matter density field models, which when ran using full N-Body codes are very costly.

The results I have presented in this thesis are shown in the bibliography section, and they refer to references [73, 100, 101, 133]. In the following section, I will discuss some possible continuations of the works I have done in my PhD, with also some motivations as to why I deem them important.

## 7.2. Future

### 7.2.1. Relativistic simulations

Future LSS surveys will deliver data from larger scales of the Universe. To robustly interpret the data, we will need to measure the correlation function at these bigger distances, where we must take into account relativistic projection effects that come from the perturbation of our past light-cone due to the clustering of matter. Besides this effect, the position of galaxies is measured in terms of angles and redshifts, and we need to model the proper motion of galaxies as well as lensing effects that affect these measurements. This has already been well-studied and incorporated within linear theory, however, at lower redshifts and smaller scales the matter density perturbations become non-linear, and linear theory stops being valid, we then need to compute the relativistic corrections of galaxy positions using of relativistic simulations. In order to calculate with increasing accuracy the relativistic corrections to galaxy positions in our Universe, the introduction of relativistic effects into N-Body codes was developed [161]. With the output of relativistic simulations we can generate relativistic mock galaxy catalogs, that are important for the estimation of covariance matrices, which help increase the robustness of cosmological parameters inference, and are useful to model signals including non-linearity on small scales as well. I am interested in performing these analysis with the relativistic simulations I have developed in my PhD. Combined with this, I can also perform ray-tracing techniques to investigate different effects that will be central for future LSS surveys, such as lensing magnification [162] and the ISW effect [161, 163].

### 7.2.2. Emulators in Horndeski Gravity

There have been many advances in modified gravity non-linear modelling. These range from fast approximate methods such as COLA, fitting formulae for the small scale matter power spectrum, to semi-analytical methods, such as higher-order perturbation theory and halo model predictions. A recently proposed way is to use emulation as a path to quickly sample the parameter space of modified gravity models [146, 147, 160]. So far these emulators have focused on archetypal theories of which we already have complete N-Body simulations. Therefore, I am interested in using emulation methods already developed in the literature in combination with relativistic Horndeski simulations.

### 7.2.3. Extracting Modified Gravity from LSS data

Many modified gravity models exhibit environmental-dependent behaviors, such as accentuated deviations from GR in under-dense regions. Due to the presence of screening mechanisms in modified theories of gravity, it has been often proposed in the literature to consider density transformations [164] that up-weights the regions with lower density, and therefore unscreened, as a way to enhance modified gravity features [165, 166, 167]. One of these is the “marked” density transformation [168] that up-weight low densities.

I am interested in using these transformations to test still viable Horndeski models, as most of the studies so far have relied on studying very specific theories that have already been constrained by multiple tests. In order to test modified gravity in highlighted unscreened regions, we must rely as well on modified gravity simulations. Therefore, I will use the implementation presented in Section 6, to test Horndeski’s gravity with density estimators. As these are enhancing the signal in low-density regions, this reduces the need to add non-linear corrections, reducing the computational complexity in N-Body simulations.

## hiclass specifications N-body gauge

In this appendix I will show some consistency checks I have performed to see if the implementation of the N-Body gauge in hiclass is consistent. To this end, I plot the ratio between the solution of the second order differential equation for the matter density contrast in the N-Body gauge, Equation (4.29), computed inside hiclass, with respect to the gauge transformed quantity, Equation (4.32). In order to perform these tests I have used the precision parameters given in Table A.1.

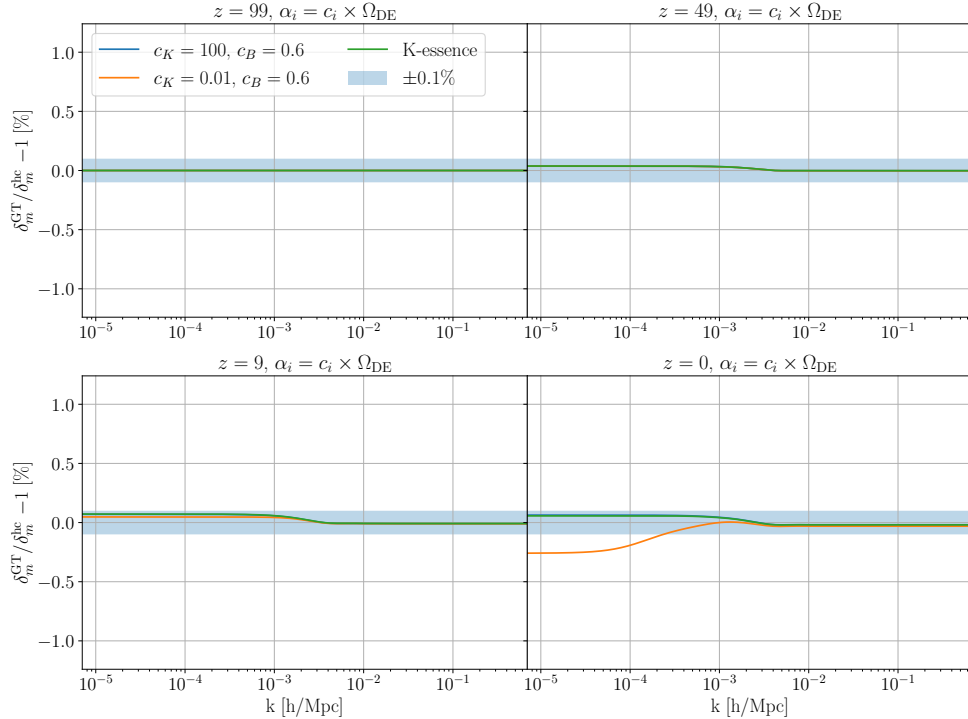


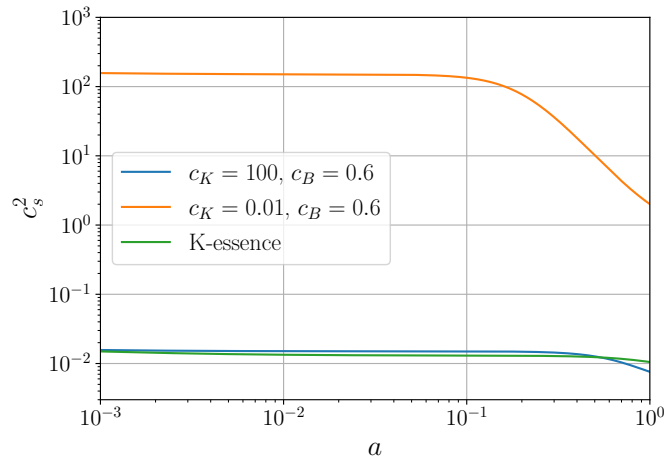
**Figure A.1.** ratio between the solution of the second order differential equation for the matter density contrast in the N-Body gauge, Equation (4.29), computed inside hiclass, with respect to the gauge transformed quantity, Equation (4.32), for three different modified gravity theories and for four redshifts. The k-essence model shown here is the same one shown discussed in Figure 4.6.

The precision parameters in Table A.1 that have in their names the “approximation” refer to the usual CLASS approximation schemes, described in [21]. For these runs I have turned off these approximation schemes, as for late times we get a better accuracy by integrating the Boltzmann hierarchy in its generality, instead of resorting to these approximation schemes,

Parameter	Assigned value
radiation_streaming_approximation	3
evolver	0
ur_fluid_approximation	2
k_per_decade_for_pk	40
k_per_decade_for_bao	80
P_k_max_h/Mpc	1.0
back_integration_stepsize	1.0e-4
ncdm_fluid_approximation	3

**Table A.1.** Precision parameters.

which were developed to increase speed and accuracy for the computation of the  $C_\ell$ 's in the CMB. The `evolver` flag sets the numerical integrator for the Einstein-Boltzmann equations to the usual fourth-order Runge Kutta integrator. I have also decided to decrease the stepsize for the integration steps taken in the background module of the code by changing the parameter `back_integration_stepsize` to  $1e-4$ . This was done after checking that the default setting was not accurate enough. The other precision parameters in the Table were modified just to increase the number of  $k$  modes per decade and to set the maximum value of the matter power spectrum. In Figure A.1, I show the ratio between the two matter density contrasts computed


**Figure A.2.** Evolution of the sound speed of the scalar field fluctuations for the three gravity models shown in Figure A.1.

using hiclass.  $\delta_m^{\text{GT}}$  is the quantity calculated using the usual gauge transformation rule shown in Equation (4.32). While  $\delta_m^{\text{hc}}$  is the full solution of Equation (4.29) computed inside hiclass from the initial redshift  $z_{\text{ini}} = 99$ . We can see that for the four redshifts shown, we have a below 0.1% agreement between the two quantities, which is more than satisfactory for all the purposes we have discussed in this thesis, except for one case at  $z = 0$  and a modified theory of gravity with  $\alpha_B = 0.6 \times \Omega_{\text{DE}}$  and  $\alpha_K = 0.01 \times \Omega_{\text{DE}}$ . This is not an unexpected result, nor it represents that our implementation is failing.

As discussed in the main text the kineticity function is inversely proportional to the sound speed in which the scalar field perturbations propagate, therefore, the smaller  $\alpha_K$  bigger  $c_s^2$ . For

all physically relevant theories, a sound speed greater than one, which represents the speed of light, are not physically sound, and require some further investigations as a quantum level this field would be breaking causality. To get a better perspective of the orders of magnitude of the sound speed between the three cases shown in Figure A.1, I plot in Figure A.2. We can see in the plot that while the only-braiding modified theory of gravity with a smaller value for the kineticity function and for the k-essence model, we have sound speeds of the order of  $\mathcal{O}(10^{-2})$ , while for the only-brading theory with  $\alpha_K = 0.01 \times \Omega_{\text{DE}}$  we have  $c_s^2 \sim \mathcal{O}(10^2)$ , roughly four order of magnitude of difference. Therefore, our implementation shows an excellent agreement for all physically relevant cases, and care should be taken when considering different cases of modified gravity theories in the N-Body gauge using our implementation.

## COLA specifications

COLA is a quasi N-body code, that is, it is an approximate method that allows us to reduce the number of time-steps that usual full N-body simulations require getting faster realizations of the non-linear density field. Therefore, if we want to get more accurate descriptions of clustering on small scales, we can just increase the number of time-steps in our COLA simulations to make it closer to full N-body codes. However, there is an obvious setback to this, as we increase time-steps we increase the time our simulations take to finish. Also, the initial redshift of these

Redshift	Number of time-steps
19 $\rightarrow$ 3	12
3 $\rightarrow$ 2	5
2 $\rightarrow$ 1	8
1 $\rightarrow$ 0.5	9
0.5 $\rightarrow$ 0	17

**Table B.1.** Number of time-steps intervals.

simulations impacts the large  $k$  behavior as well, since the higher the redshift we choose, the more time-steps between  $z_{\text{ini}}$  to smaller redshifts we will need. Another parameter COLA is sensitive to, is the number of cell grids in its PM algorithm. As COLA solves the Poisson equation using inverse and normal FFTs, by increasing the number of cells we will be making our mesh finer and increasing the force resolution.

These specifications used in this work follow closely the discussion presented in [130] where detailed analyses were performed to find the best specifications for COLA simulations. All our simulations use the box size of  $1024 h/\text{Mpc}$  with  $N_p^3 = 1024^3$  particles. In Table 6.1 I chose to use 50 time-steps for our COLA simulations starting at  $z_{\text{ini}} = 19$ , with the time-steps subdivided as shown in Table B.1.

These time steps are linearly distributed in the scale factor. As we can see from this table that the COLA method generally uses a very sparse time-stepping at higher redshifts, which can be a problem if we have a very low force resolution. In order to not have a loss of power at small scales in our simulations, I then chose to use a force mesh grid number of  $N_{\text{mesh}}^3 = (2N_p)^3 = 2048^3$  as it was shown that increasing this to  $(3N_p)^3$  has  $\sim 1\%$  effects on the matter power spectrum at  $k < 1 h/\text{Mpc}$ . In Figure B.1 I show the ratio between the absolute non-linear power spectrum measured from our COLA simulation using the reference values of Table 6.4, and the EE2 non-linear matter power spectrum. I use the paired-fixed simulations to reduce the cosmic variance. We see that the ratio between the two is highly oscillatory when we go to large  $k$  values, due to the residual sample variance effects of our COLA simulation. The time steps are chosen to reproduce

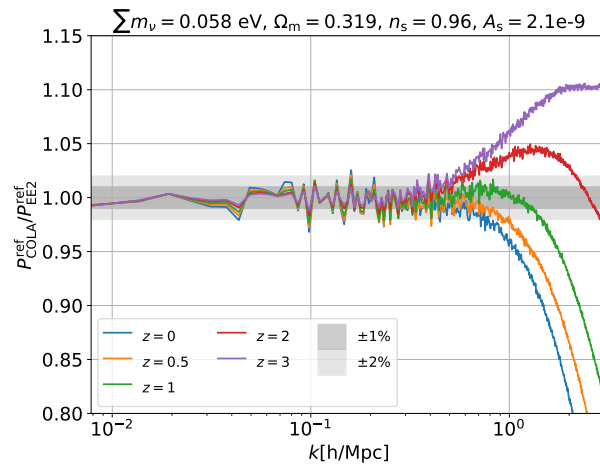


**Figure B.1.** Ratio between the absolute non-linear dark matter power spectrum computed using COLA and EE2 for the reference cosmology.

the matter spectrum better at  $z \leq 1$ . At  $z \leq 3$ , the non-linear power spectrum from COLA agrees with EE2 at 1% level at  $k \leq 0.5 \text{ h/Mpc}$ . As shown in this paper, COLA gives a better accuracy up to higher  $k$  in predicting reactions of the matter power spectrum to the change of cosmological parameters as well as massive neutrino mass. Also since the reaction is defined as a ratio of the power spectrum, using the same initial seed, we can suppress the sample variance and obtain much smoother predictions. To compute the reaction, I used fixed amplitude simulations and the same initial seed for all the simulations. I emphasize that all the comparisons and results using our COLA simulations shown in this work can be even further improved by increasing the temporal resolution of our simulations, i.e., increasing the total number of time-steps, the force resolution, i.e., increasing the the number of cell grids in our PM algorithm, and the particle number. Finally, in the main text, I only showed comparisons between COLA and EE2 for the prediction of the reaction. Here, for completeness, I show a comparison between EE2 and Bacco in Figure B.2. As noted in the main text, Bacco do not cover the largest values of  $\Omega_m$  and  $A_s$  used in our analysis. In the plot, I used  $\Omega_m = 0.355$  and  $A_s = 2.45 \times 10^{-9}$  instead. We get below 2% agreements in all cases.

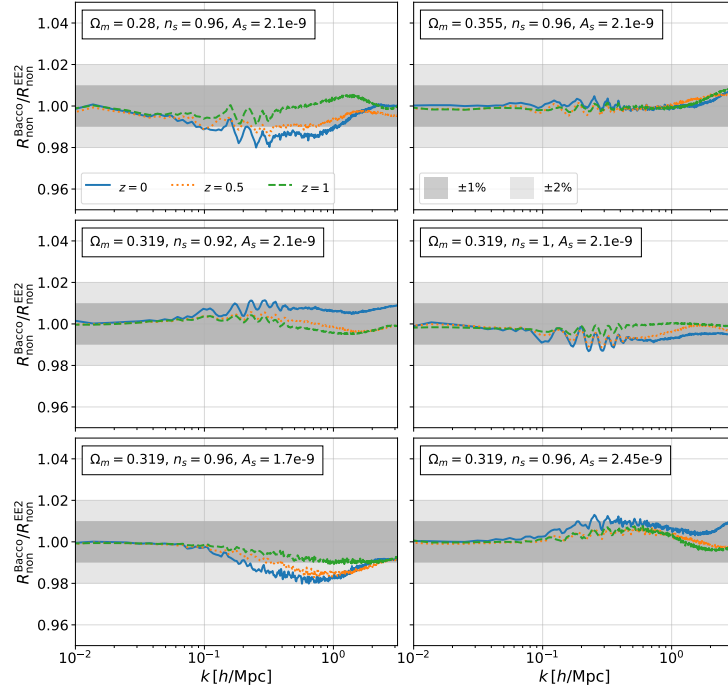


**Figure B.2.** Ratio between the non-linear response function computed using Bacco and the EE2 for the massless neutrinos case.

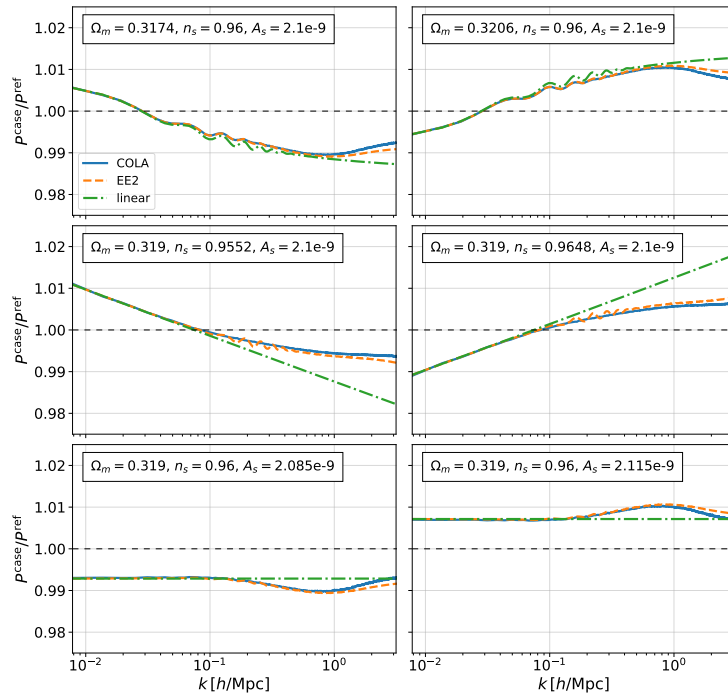


**Figure B.3.** Non-linear and linear response functions computed using COLA, EE2 and hi\_class, for small variations of the cosmological parameters.

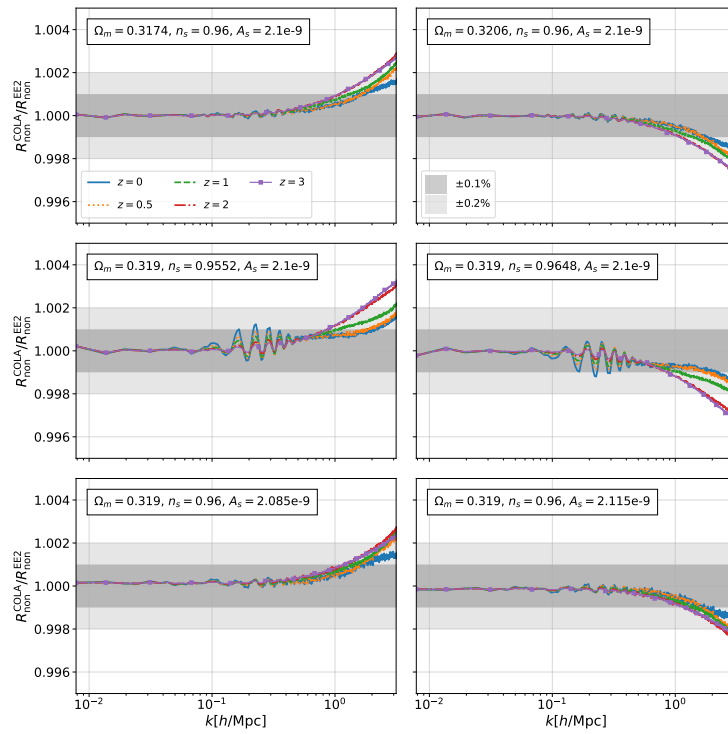


**Figure B.4.** The same ratio as in Figure 6.3, but for small variations of the cosmological parameters.

## Small variations of cosmological parameters

In this Section, I show the results for small variations of cosmological parameters between COLA and EE2. Our choice of small variations represent increasing and decreasing 0.5% of the reference value of  $\Omega_m$ ,  $A_s$  and  $n_s$ . This small change in the parameters has smaller effects on the linear and non-linear response functions, as opposed to the large variation cases considered in Figure 6.1. Their impact on the matter power spectrum is shown in Figure B.3. It is important to check that COLA can reproduce the response function with much better accuracy in the case.

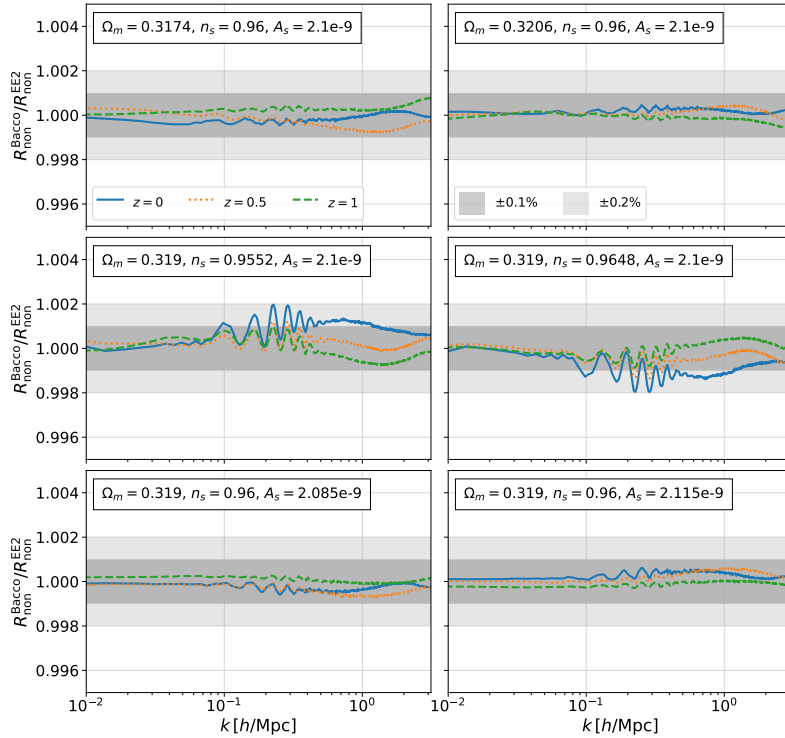


**Figure C.1.** The same ratio as in Figure B.2, but for small variations of the cosmological parameters.

In Figures B.4 and C.1 I show the impact on the ratio of the non-linear response of this change for COLA and EE2, and for Bacco and EE2, respectively. We see that in all cases COLA agrees with these emulators well within the 0.1% threshold for up until  $k = 1 h/\text{Mpc}$ .

# Bibliography

- [1] A. Einstein. *The Field Equations of Gravitation*. Sitzungsber. Preuss. Akad. Wiss. Berlin (Math. Phys. ) **1915** 844 (1915). Cited on page [1](#).
- [2] B. F. Schutz. *A FIRST COURSE IN GENERAL RELATIVITY*. Cambridge Univ. Pr. Cambridge, UK 1985. Cited on page [2](#).
- [3] A. Einstein. *Cosmological Considerations in the General Theory of Relativity*. Sitzungsber. Preuss. Akad. Wiss. Berlin (Math. Phys. ) **1917** 142 (1917). Cited on page [3](#).
- [4] A. Friedman. *On the Curvature of space*. *Z. Phys.* **10** 377 (1922). Cited on page [4](#).
- [5] G. Lemaître. *Un Univers homogène de masse constante et de rayon croissant rendant compte de la vitesse radiale des nébuleuses extra-galactiques*. Annales de la Société Scientifique de Bruxelles **47** 49 (1927). Cited on page [4](#).
- [6] S. Perlmutter et al. *Measurements of  $\Omega$  and  $\Lambda$  from 42 high redshift supernovae*. *Astrophys. J.* **517** 565 (1999). [arXiv:astro-ph/9812133](#). Cited on pages [4](#), [24](#), and [25](#).
- [7] A. G. Riess et al. *Observational evidence from supernovae for an accelerating universe and a cosmological constant*. *Astron. J.* **116** 1009 (1998). [arXiv:astro-ph/9805201](#). Cited on pages [4](#) and [24](#).
- [8] D. Brout et al. *The Pantheon+ Analysis: Cosmological Constraints*. 2022). [arXiv:2202.04077](#). Cited on page [6](#).
- [9] M. J. Reid, J. A. Braatz, J. J. Condon, L. J. Greenhill, C. Henkel, and K. Y. Lo. *The Megamaser Cosmology Project: I. VLBI observations of UGC 3789*. *Astrophys. J.* **695** 287 (2009). [arXiv:0811.4345](#). Cited on page [6](#).
- [10] K. C. Wong et al. *H0LiCOW – XIII. A 2.4 per cent measurement of H0 from lensed quasars: 5.3 $\sigma$  tension between early- and late-Universe probes*. *Mon. Not. Roy. Astron. Soc.* **498** 1420 (2020). [arXiv:1907.04869](#). Cited on page [6](#).
- [11] W. L. Freedman et al. *The Carnegie-Chicago Hubble Program. VIII. An Independent Determination of the Hubble Constant Based on the Tip of the Red Giant Branch*. 2019). [arXiv:1907.05922](#). Cited on page [6](#).
- [12] L. Verde, T. Treu, and A. G. Riess. *Tensions between the Early and the Late Universe*. *Nature Astron.* **3** 891 (2019). [arXiv:1907.10625](#). Cited on page [6](#).
- [13] N. Aghanim et al. *Planck 2018 results. VI. Cosmological parameters*. *Astron. Astrophys.* **641** A6 (2020). [Erratum: *Astron. Astrophys.* 652, C4 (2021)]. [arXiv:1807.06209](#). Cited on pages [6](#) and [22](#).

- [14] T. M. C. Abbott et al. *Dark Energy Survey Year 1 Results: A Precise  $H_0$  Estimate from DES Y1, BAO, and D/H Data*. *Mon. Not. Roy. Astron. Soc.* **480** 3879 (2018). [arXiv:1711.00403](#). Cited on page 6.
- [15] W. Hu. *Covariant linear perturbation formalism*. ICTP Lect. Notes Ser. **14** 145 (2003). [arXiv:astro-ph/0402060](#). Cited on page 7.
- [16] H. Kodama and M. Sasaki. *Cosmological Perturbation Theory*. *Prog. Theor. Phys. Suppl.* **78** 1 (1984). Cited on page 7.
- [17] J. M. Bardeen. *Gauge Invariant Cosmological Perturbations*. *Phys. Rev. D* **22** 1882 (1980). Cited on page 7.
- [18] V. F. Mukhanov, H. A. Feldman, and R. H. Brandenberger. *Theory of cosmological perturbations. Part 1. Classical perturbations. Part 2. Quantum theory of perturbations. Part 3. Extensions*. *Phys. Rept.* **215** 203 (1992). Cited on page 7.
- [19] C. Fidler, T. Tram, C. Rampf, R. Crittenden, K. Koyama, and D. Wands. *Relativistic initial conditions for N-body simulations*. *JCAP* **06** 043 (2017). [arXiv:1702.03221](#). Cited on pages 8 and 60.
- [20] C.-P. Ma and E. Bertschinger. *Cosmological perturbation theory in the synchronous and conformal Newtonian gauges*. *Astrophys. J.* **455** 7 (1995). [arXiv:astro-ph/9506072](#). Cited on pages 14, 18, 19, 21, and 60.
- [21] D. Blas, J. Lesgourgues, and T. Tram. *The Cosmic Linear Anisotropy Solving System (CLASS) II: Approximation schemes*. *JCAP* **07** 034 (2011). [arXiv:1104.2933](#). Cited on pages 16, 18, 19, 106, and 122.
- [22] A. Lewis, A. Challinor, and A. Lasenby. *Efficient computation of CMB anisotropies in closed FRW models*. *Astrophys. J.* **538** 473 (2000). [arXiv:astro-ph/9911177](#). Cited on page 18.
- [23] D. J. Eisenstein and W. Hu. *Baryonic features in the matter transfer function*. *Astrophys. J.* **496** 605 (1998). [arXiv:astro-ph/9709112](#). Cited on pages 18 and 92.
- [24] P. J. E. Peebles and J. T. Yu. *Primeval adiabatic perturbation in an expanding universe*. *Astrophys. J.* **162** 815 (1970). Cited on pages 21 and 75.
- [25] C. Pitrou. *The tight-coupling approximation for baryon acoustic oscillations*. *Phys. Lett. B* **698** 1 (2011). [arXiv:1012.0546](#). Cited on page 21.
- [26] S. Dodelson and F. Schmidt. *Modern Cosmology*. Elsevier Science 2020. URL: <https://books.google.com.br/books?id=GGjfywEACAAJ>. Cited on pages 21, 76, and 81.
- [27] J. A. Peacock. *Cosmological Physics*. 1999. Cited on page 21.
- [28] I. A. Strukov, A. A. Brukhanov, D. P. Skulachev, and M. V. Sazhin. *Anisotropy of the microwave background radiation*. *Soviet Astronomy Letters* **18** 153 (1992). Cited on page 22.
- [29] G. F. Smoot et al. *Structure in the COBE differential microwave radiometer first year maps*. *Astrophys. J. Lett.* **396** L1 (1992). Cited on page 22.

- [30] P. de Bernardis et al. *A Flat universe from high resolution maps of the cosmic microwave background radiation*. *Nature* **404** 955 (2000). [arXiv:astro-ph/0004404](#). Cited on page 22.
- [31] A. Balbi et al. *Constraints on cosmological parameters from MAXIMA-1*. *Astrophys. J. Lett.* **545** L1 (2000). [Erratum: *Astrophys.J.Lett.* 558, L145–L146 (2001), Erratum: *Astrophys.J.* 558, L145–L146 (2001)]. [arXiv:astro-ph/0005124](#). Cited on page 22.
- [32] D. N. Spergel et al. *First year Wilkinson Microwave Anisotropy Probe (WMAP) observations: Determination of cosmological parameters*. *Astrophys. J. Suppl.* **148** 175 (2003). [arXiv:astro-ph/0302209](#). Cited on page 22.
- [33] M. M. Phillips. *The absolute magnitudes of Type IA supernovae*. *Astrophys. J. Lett.* **413** L105 (1993). Cited on page 24.
- [34] M. Hamuy, M. M. Phillips, R. A. Schommer, N. B. Suntzeff, J. Maza, and R. Aviles. *The Absolute luminosities of the Calan/Tololo type IA supernovae*. *Astron. J.* **112** 2391 (1996). [arXiv:astro-ph/9609059](#). Cited on page 25.
- [35] M. Vogelsberger, F. Marinacci, P. Torrey, and E. Puchwein. *Cosmological Simulations of Galaxy Formation*. *Nature Rev. Phys.* **2** 42 (2020). [arXiv:1909.07976](#). Cited on page 25.
- [36] D. J. Eisenstein et al. *Detection of the Baryon Acoustic Peak in the Large-Scale Correlation Function of SDSS Luminous Red Galaxies*. *Astrophys. J.* **633** 560 (2005). [arXiv:astro-ph/0501171](#). Cited on page 25.
- [37] L. Amendola and S. Tsujikawa. *Dark Energy: Theory and Observations*. Cambridge University Press 2015. Cited on page 26.
- [38] S. Alam et al. *The clustering of galaxies in the completed SDSS-III Baryon Oscillation Spectroscopic Survey: cosmological analysis of the DR12 galaxy sample*. *Mon. Not. Roy. Astron. Soc.* **470** 2617 (2017). [arXiv:1607.03155](#). Cited on pages 26 and 48.
- [39] M. Ata et al. *The clustering of the SDSS-IV extended Baryon Oscillation Spectroscopic Survey DR14 quasar sample: first measurement of baryon acoustic oscillations between redshift 0.8 and 2.2*. *Mon. Not. Roy. Astron. Soc.* **473** 4773 (2018). [arXiv:1705.06373](#). Cited on page 26.
- [40] N. Kaiser. *Clustering in real space and in redshift space*. *Mon. Not. Roy. Astron. Soc.* **227** 1 (1987). Cited on page 26.
- [41] W. J. Percival. *Large Scale Structure Observations*. In *186th Course of International School of Physics 'Enrico Fermi': New Horizons for Observational Cosmology* volume 186 pages 101–135 2014. [arXiv:1312.5490](#). Cited on page 27.
- [42] T. Okumura et al. *The Subaru FMOS galaxy redshift survey (FastSound). IV. New constraint on gravity theory from redshift space distortions at  $z \sim 1.4$* . *Publ. Astron. Soc. Jap.* **68** 38 (2016). [arXiv:1511.08083](#). Cited on page 28.
- [43] F. W. Dyson, A. S. Eddington, and C. Davidson. *A Determination of the Deflection of Light by the Sun's Gravitational Field, from Observations Made at the Total Eclipse of May 29, 1919*. *Philosophical Transactions of the Royal Society of London Series A* **220** 291 (1920). Cited on page 28.

- [44] T. M. C. Abbott et al. *Dark Energy Survey Year 3 results: Cosmological constraints from galaxy clustering and weak lensing*. *Phys. Rev. D* **105** 023520 (2022). [arXiv:2105.13549](#). Cited on page [28](#).
- [45] D. Lovelock. *The Einstein tensor and its generalizations*. *J. Math. Phys.* **12** 498 (1971). Cited on page [30](#).
- [46] D. Lovelock. *The four-dimensionality of space and the einstein tensor*. *J. Math. Phys.* **13** 874 (1972). Cited on page [30](#).
- [47] P. Rastall. *Generalization of the einstein theory*. *Phys. Rev. D* **6** 3357 (1972). Cited on page [31](#).
- [48] M. Visser. *Rastall gravity is equivalent to Einstein gravity*. *Phys. Lett. B* **782** 83 (2018). [arXiv:1711.11500](#). Cited on page [31](#).
- [49] J. C. Fabris, O. F. Piattella, D. C. Rodrigues, D. C. Rodrigues, and E. C. O. Santos. *A note on non-vanishing divergence of the stress-energy tensor in theories of gravity*. (2020). [arXiv:2011.10503](#). Cited on page [31](#).
- [50] M. Maggiore and M. Mancarella. *Nonlocal gravity and dark energy*. *Phys. Rev. D* **90** 023005 (2014). [arXiv:1402.0448](#). Cited on page [31](#).
- [51] C. Brans and R. H. Dicke. *Mach's principle and a relativistic theory of gravitation*. *Phys. Rev.* **124** 925 (1961). Cited on pages [31](#) and [112](#).
- [52] V. Faraoni and S. Capozziello. *Beyond Einstein Gravity: A Survey of Gravitational Theories for Cosmology and Astrophysics*. Springer Dordrecht 2011. Cited on pages [31](#) and [32](#).
- [53] G. Brando, J. C. Fabris, F. T. Falciano, and O. Galkina. *Stiff matter solution in Brans–Dicke theory and the general relativity limit*. *Int. J. Mod. Phys. D* **28** 1950156 (2019). [arXiv:1810.07860](#). Cited on page [32](#).
- [54] R. Blumenhagen and E. Plauschinn. *Introduction to conformal field theory: with applications to String theory* volume 779. 2009. Cited on page [32](#).
- [55] C. Deffayet, G. Esposito-Farese, and A. Vikman. *Covariant Galileon*. *Phys. Rev. D* **79** 084003 (2009). [arXiv:0901.1314](#). Cited on page [33](#).
- [56] T. Kobayashi, M. Yamaguchi, and J. Yokoyama. *Generalized G-inflation: Inflation with the most general second-order field equations*. *Prog. Theor. Phys.* **126** 511 (2011). [arXiv:1105.5723](#). Cited on page [33](#).
- [57] E. J. Copeland, A. R. Liddle, and D. Wands. *Exponential potentials and cosmological scaling solutions*. *Phys. Rev. D* **57** 4686 (1998). [arXiv:gr-qc/9711068](#). Cited on page [34](#).
- [58] P. J. Steinhardt, L.-M. Wang, and I. Zlatev. *Cosmological tracking solutions*. *Phys. Rev. D* **59** 123504 (1999). [arXiv:astro-ph/9812313](#). Cited on page [34](#).
- [59] L. Amendola, R. Gannouji, D. Polarski, and S. Tsujikawa. *Conditions for the cosmological viability of  $f(R)$  dark energy models*. *Phys. Rev. D* **75** 083504 (2007). [arXiv:gr-qc/0612180](#). Cited on page [35](#).

- [60] L. Amendola, D. Polarski, and S. Tsujikawa. *Are  $f(R)$  dark energy models cosmologically viable ?* *Phys. Rev. Lett.* **98** 131302 (2007). [arXiv:astro-ph/0603703](#). Cited on page 35.
- [61] E. Bellini and I. Sawicki. *Maximal freedom at minimum cost: linear large-scale structure in general modifications of gravity.* *JCAP* **07** 050 (2014). [arXiv:1404.3713](#). Cited on pages 37 and 112.
- [62] C. de Rham and S. Melville. *Gravitational Rainbows: LIGO and Dark Energy at its Cutoff.* *Phys. Rev. Lett.* **121** 221101 (2018). [arXiv:1806.09417](#). Cited on page 37.
- [63] R. Gsponer and J. Noller. *Tachyonic stability priors for dark energy.* *Phys. Rev. D* **105** 064002 (2022). [arXiv:2107.01044](#). Cited on page 39.
- [64] G. Gubitosi, F. Piazza, and F. Vernizzi. *The Effective Field Theory of Dark Energy.* *JCAP* **02** 032 (2013). [arXiv:1210.0201](#). Cited on pages 39 and 103.
- [65] J. Gleyzes, D. Langlois, and F. Vernizzi. *A unifying description of dark energy.* *Int. J. Mod. Phys. D* **23** 1443010 (2015). [arXiv:1411.3712](#). Cited on pages 39 and 103.
- [66] M. Zumalacárregui, E. Bellini, I. Sawicki, J. Lesgourgues, and P. G. Ferreira. *hi\_class: Horndeski in the Cosmic Linear Anisotropy Solving System.* *JCAP* **08** 019 (2017). [arXiv:1605.06102](#). Cited on pages 40 and 104.
- [67] E. Bellini, I. Sawicki, and M. Zumalacárregui. *hi\_class: Background Evolution, Initial Conditions and Approximation Schemes.* *JCAP* **02** 008 (2020). [arXiv:1909.01828](#). Cited on pages 40 and 104.
- [68] M. Doran, M. J. Lilley, J. Schwindt, and C. Wetterich. *Quintessence and the separation of CMB peaks.* *Astrophys. J.* **559** 501 (2001). [arXiv:astro-ph/0012139](#). Cited on pages 40 and 52.
- [69] R. Bean, S. H. Hansen, and A. Melchiorri. *Early universe constraints on a primordial scaling field.* *Phys. Rev. D* **64** 103508 (2001). [arXiv:astro-ph/0104162](#). Cited on page 40.
- [70] M. Bartelmann, M. Doran, and C. Wetterich. *Non-linear structure formation in cosmologies with early dark energy.* *Astron. Astrophys.* **454** 27 (2006). [arXiv:astro-ph/0507257](#). Cited on page 40.
- [71] M. Doran and G. Robbers. *Early dark energy cosmologies.* *JCAP* **06** 026 (2006). [arXiv:astro-ph/0601544](#). Cited on page 40.
- [72] M. Zumalacárregui. *Gravity in the Era of Equality: Towards solutions to the Hubble problem without fine-tuned initial conditions.* *Phys. Rev. D* **102** 023523 (2020). [arXiv:2003.06396](#). Cited on page 40.
- [73] G. Brando, F. T. Falciano, E. V. Linder, and H. E. S. Velten. *Modified gravity away from a  $\Lambda$ CDM background.* *JCAP* **11** 018 (2019). [arXiv:1904.12903](#). Cited on pages 43, 46, 48, 49, and 120.
- [74] I. Sawicki and E. Bellini. *Limits of quasistatic approximation in modified-gravity cosmologies.* *Phys. Rev. D* **92** 084061 (2015). [arXiv:1503.06831](#). Cited on page 43.

- [75] F. Pace, R. Battye, E. Bellini, L. Lombriser, F. Vernizzi, and B. Bolliet. *Comparison of different approaches to the quasi-static approximation in Horndeski models*. *JCAP* **06** 017 (2021). [arXiv:2011.05713](#). Cited on page 43.
- [76] J. Noller, L. Santoni, E. Trincerini, and L. G. Trombetta. *Scalar-tensor cosmologies without screening*. *JCAP* **01** 045 (2021). [arXiv:2008.08649](#). Cited on page 43.
- [77] Y.-S. Song, W. Hu, and I. Sawicki. *The Large Scale Structure of  $f(R)$  Gravity*. *Phys. Rev. D* **75** 044004 (2007). [arXiv:astro-ph/0610532](#). Cited on page 45.
- [78] G.-B. Zhao, L. Pogosian, A. Silvestri, and J. Zylberberg. *Searching for modified growth patterns with tomographic surveys*. *Phys. Rev. D* **79** 083513 (2009). [arXiv:0809.3791](#). Cited on page 45.
- [79] E. Bertschinger and P. Zukin. *Distinguishing Modified Gravity from Dark Energy*. *Phys. Rev. D* **78** 024015 (2008). [arXiv:0801.2431](#). Cited on page 45.
- [80] L. Amendola, D. Bettoni, A. M. Pinho, and S. Casas. *Measuring gravity at cosmological scales*. *Universe* **6** 20 (2020). [arXiv:1902.06978](#). Cited on page 45.
- [81] L. Amendola, M. Kunz, M. Motta, I. D. Saltas, and I. Sawicki. *Observables and unobservables in dark energy cosmologies*. *Phys. Rev. D* **87** 023501 (2013). [arXiv:1210.0439](#). Cited on page 46.
- [82] M. Motta, I. Sawicki, I. D. Saltas, L. Amendola, and M. Kunz. *Probing Dark Energy through Scale Dependence*. *Phys. Rev. D* **88** 124035 (2013). [arXiv:1305.0008](#). Cited on page 46.
- [83] C. Deffayet, O. Pujolas, I. Sawicki, and A. Vikman. *Imperfect Dark Energy from Kinetic Gravity Braiding*. *JCAP* **10** 026 (2010). [arXiv:1008.0048](#). Cited on page 46.
- [84] M. Kunz, S. Nesseris, and I. Sawicki. *Using dark energy to suppress power at small scales*. *Phys. Rev. D* **92** 063006 (2015). [arXiv:1507.01486](#). Cited on page 46.
- [85] E. V. Linder. *No Slip Gravity*. *JCAP* **03** 005 (2018). [arXiv:1801.01503](#). Cited on pages 46 and 48.
- [86] E. V. Linder. *Challenges in connecting modified gravity theory and observations*. *Phys. Rev. D* **95** 023518 (2017). [arXiv:1607.03113](#). Cited on page 47.
- [87] F. Beutler, C. Blake, M. Colless, D. H. Jones, L. Staveley-Smith, G. B. Poole, L. Campbell, Q. Parker, W. Saunders, and F. Watson. *The 6dF Galaxy Survey:  $z \approx 0$  measurement of the growth rate and  $\sigma_8$* . *Mon. Not. Roy. Astron. Soc.* **423** 3430 (2012). [arXiv:1204.4725](#). Cited on page 48.
- [88] C. Blake et al. *Galaxy And Mass Assembly (GAMA): improved cosmic growth measurements using multiple tracers of large-scale structure*. *Mon. Not. Roy. Astron. Soc.* **436** 3089 (2013). [arXiv:1309.5556](#). Cited on page 48.
- [89] C. Blake et al. *The WiggleZ Dark Energy Survey: Joint measurements of the expansion and growth history at  $z < 1$* . *Mon. Not. Roy. Astron. Soc.* **425** 405 (2012). [arXiv:1204.3674](#). Cited on page 48.

- [90] S. de la Torre et al. *The VIMOS Public Extragalactic Redshift Survey (VIPERS). Galaxy clustering and redshift-space distortions at  $z=0.8$  in the first data release.* *Astron. Astrophys.* **557** A54 (2013). [arXiv:1303.2622](#). Cited on page 48.
- [91] E. V. Linder. *The Mirage of  $w=-1$ .* 2007). [arXiv:0708.0024](#). Cited on page 48.
- [92] J. Renk, M. Zumalacárregui, and F. Montanari. *Gravity at the horizon: on relativistic effects, CMB-LSS correlations and ultra-large scales in Horndeski's theory.* *JCAP* **07** 040 (2016). [arXiv:1604.03487](#). Cited on page 48.
- [93] J. Renk, M. Zumalacárregui, F. Montanari, and A. Barreira. *Galileon gravity in light of ISW, CMB, BAO and  $H_0$  data.* *JCAP* **10** 020 (2017). [arXiv:1707.02263](#). Cited on pages 48 and 49.
- [94] J. Noller and A. Nicola. *Cosmological parameter constraints for Horndeski scalar-tensor gravity.* *Phys. Rev. D* **99** 103502 (2019). [arXiv:1811.12928](#). Cited on page 48.
- [95] S. Ho, C. Hirata, N. Padmanabhan, U. Seljak, and N. Bahcall. *Correlation of CMB with large-scale structure: I. ISW Tomography and Cosmological Implications.* *Phys. Rev. D* **78** 043519 (2008). [arXiv:0801.0642](#). Cited on pages 50 and 51.
- [96] J. J. Condon, W. D. Cotton, E. W. Greisen, Q. F. Yin, R. A. Perley, G. B. Taylor, and J. J. Broderick. *The NRAO VLA Sky Survey.* **115** 1693 (1998). Cited on page 50.
- [97] M. Brush, E. V. Linder, and M. Zumalacárregui. *No Slip CMB.* *JCAP* **01** 029 (2019). [arXiv:1810.12337](#). Cited on page 50.
- [98] R. G. Crittenden and N. Turok. *Looking for Lambda with the Rees-Sciama effect.* *Phys. Rev. Lett.* **76** 575 (1996). [arXiv:astro-ph/9510072](#). Cited on page 52.
- [99] J. Samsing, E. V. Linder, and T. L. Smith. *Model Independent Early Expansion History and Dark Energy.* *Phys. Rev. D* **86** 123504 (2012). [arXiv:1208.4845](#). Cited on page 53.
- [100] G. Brando, K. Koyama, and D. Wands. *Relativistic Corrections to the Growth of Structure in Modified Gravity.* *JCAP* **01** 013 (2021). [arXiv:2006.11019](#). Cited on pages 55, 103, 113, 117, and 120.
- [101] G. Brando, K. Koyama, D. Wands, M. Zumalacárregui, I. Sawicki, and E. Bellini. *Fully relativistic predictions in Horndeski gravity from standard Newtonian  $N$ -body simulations.* *JCAP* **09** 024 (2021). [arXiv:2105.04491](#). Cited on pages 55, 103, 113, 117, and 120.
- [102] J. M. Bardeen, J. R. Bond, N. Kaiser, and A. S. Szalay. *The Statistics of Peaks of Gaussian Random Fields.* *Astrophys. J.* **304** 15 (1986). Cited on page 57.
- [103] N. Aghanim et al. *Planck 2018 results. I. Overview and the cosmological legacy of Planck.* *Astron. Astrophys.* **641** A1 (2020). [arXiv:1807.06205](#). Cited on pages 58 and 59.
- [104] C. Bonvin and R. Durrer. *What galaxy surveys really measure.* *Phys. Rev. D* **84** 063505 (2011). [arXiv:1105.5280](#). Cited on page 58.
- [105] M. Bruni, R. Crittenden, K. Koyama, R. Maartens, C. Pitrou, and D. Wands. *Disentangling non-Gaussianity, bias and GR effects in the galaxy distribution.* *Phys. Rev. D* **85** 041301 (2012). [arXiv:1106.3999](#). Cited on page 58.

- [106] U. Seljak. *Extracting primordial non-gaussianity without cosmic variance*. *Phys. Rev. Lett.* **102** 021302 (2009). [arXiv:0807.1770](#). Cited on page 58.
- [107] C. Fidler, C. Rampf, T. Tram, R. Crittenden, K. Koyama, and D. Wands. *General relativistic corrections to  $N$ -body simulations and the Zel'dovich approximation*. *Phys. Rev. D* **92** 123517 (2015). [arXiv:1505.04756](#). Cited on pages 59 and 60.
- [108] C. Fidler, T. Tram, C. Rampf, R. Crittenden, K. Koyama, and D. Wands. *Relativistic Interpretation of Newtonian Simulations for Cosmic Structure Formation*. *JCAP* **09** 031 (2016). [arXiv:1606.05588](#). Cited on page 60.
- [109] C. Fidler, T. Tram, C. Rampf, R. Crittenden, K. Koyama, and D. Wands. *General relativistic weak-field limit and Newtonian  $N$ -body simulations*. *JCAP* **12** 022 (2017). [arXiv:1708.07769](#). Cited on page 60.
- [110] J. Adamek and C. Fidler. *The large-scale general-relativistic correction for Newtonian mocks*. *JCAP* **09** 026 (2019). [arXiv:1905.11721](#). Cited on page 60.
- [111] T. Tram, J. Brandbyge, J. Dakin, and S. Hannestad. *Fully relativistic treatment of light neutrinos in  $N$ -body simulations*. *JCAP* **03** 022 (2019). [arXiv:1811.00904](#). Cited on pages 61 and 110.
- [112] Y. B. Zeldovich. *Gravitational instability: An Approximate theory for large density perturbations*. *Astron. Astrophys.* **5** 84 (1970). Cited on page 75.
- [113] F. Bernardeau, S. Colombi, E. Gaztanaga, and R. Scoccimarro. *Large scale structure of the universe and cosmological perturbation theory*. *Phys. Rept.* **367** 1 (2002). [arXiv:astro-ph/0112551](#). Cited on pages 75, 76, and 88.
- [114] M. Crocce, S. Pueblas, and R. Scoccimarro. *Transients from Initial Conditions in Cosmological Simulations*. *Mon. Not. Roy. Astron. Soc.* **373** 369 (2006). [arXiv:astro-ph/0606505](#). Cited on pages 75 and 98.
- [115] S. Matarrese, L. Verde, and A. F. Heavens. *Large scale bias in the universe: Bispectrum method*. *Mon. Not. Roy. Astron. Soc.* **290** 651 (1997). [arXiv:astro-ph/9706059](#). Cited on page 75.
- [116] F. R. Bouchet, S. Colombi, E. Hivon, and R. Juszkiewicz. *Perturbative Lagrangian approach to gravitational instability*. *Astron. Astrophys.* **296** 575 (1995). [arXiv:astro-ph/9406013](#). Cited on page 75.
- [117] A. Taruya. *Constructing perturbation theory kernels for large-scale structure in generalized cosmologies*. *Phys. Rev. D* **94** 023504 (2016). [arXiv:1606.02168](#). Cited on pages 76, 87, and 88.
- [118] C. Barrera-Hinojosa, B. Li, M. Bruni, and J.-h. He. *Vector modes in  $\Lambda$ CDM: the gravito-magnetic potential in dark matter haloes from relativistic  $N$ -body simulations*. *Mon. Not. Roy. Astron. Soc.* **501** 5697 (2021). [arXiv:2010.08257](#). Cited on page 78.
- [119] B. Bose and K. Koyama. *A Perturbative Approach to the Redshift Space Power Spectrum: Beyond the Standard Model*. *JCAP* **08** 032 (2016). [arXiv:1606.02520](#). Cited on pages 87 and 88.

- [120] H. A. Winther, K. Koyama, M. Manera, B. S. Wright, and G.-B. Zhao. *COLA with scale-dependent growth: applications to screened modified gravity models*. *JCAP* **08** 006 (2017). [arXiv:1703.00879](#). Cited on pages [88](#), [89](#), [90](#), [91](#), and [103](#).
- [121] B. S. Wright, H. A. Winther, and K. Koyama. *COLA with massive neutrinos*. *JCAP* **10** 054 (2017). [arXiv:1705.08165](#). Cited on pages [88](#), [93](#), [94](#), [95](#), [103](#), and [104](#).
- [122] D. J. Eisenstein and W. Hu. *Power spectra for cold dark matter and its variants*. *Astrophys. J.* **511** 5 (1997). [arXiv:astro-ph/9710252](#). Cited on pages [93](#) and [94](#).
- [123] S. Saito, M. Takada, and A. Taruya. *Impact of massive neutrinos on nonlinear matter power spectrum*. *Phys. Rev. Lett.* **100** 191301 (2008). [arXiv:0801.0607](#). Cited on page [94](#).
- [124] S. Bird, M. Viel, and M. G. Haehnelt. *Massive Neutrinos and the Non-linear Matter Power Spectrum*. *Mon. Not. Roy. Astron. Soc.* **420** 2551 (2012). [arXiv:1109.4416](#). Cited on pages [94](#) and [105](#).
- [125] S. Tassev, M. Zaldarriaga, and D. Eisenstein. *Solving Large Scale Structure in Ten Easy Steps with COLA*. *JCAP* **06** 036 (2013). [arXiv:1301.0322](#). Cited on pages [94](#), [96](#), [97](#), and [102](#).
- [126] S. Tassev, D. J. Eisenstein, B. D. Wandelt, and M. Zaldarriaga. *sCOLA: The N-body COLA Method Extended to the Spatial Domain*. 2015). [arXiv:1502.07751](#). Cited on pages [94](#) and [102](#).
- [127] R. W. Hockney and J. W. Eastwood. *Computer simulation using particles*. 1988. Cited on page [95](#).
- [128] T. R. Quinn, N. Katz, J. Stadel, and G. Lake. *Time stepping N body simulations*. 1997). [arXiv:astro-ph/9710043](#). Cited on page [95](#).
- [129] N. E. Chisari and M. Zaldarriaga. *Connection between Newtonian simulations and general relativity*. *Phys. Rev. D* **83** 123505 (2011). [Erratum: *Phys.Rev.D* 84, 089901 (2011)]. [arXiv:1101.3555](#). Cited on page [98](#).
- [130] A. Izard, M. Crocce, and P. Fosalba. *ICE-COLA: Towards fast and accurate synthetic galaxy catalogues optimizing a quasi N-body method*. *Mon. Not. Roy. Astron. Soc.* **459** 2327 (2016). [arXiv:1509.04685](#). Cited on pages [98](#), [99](#), [103](#), and [125](#).
- [131] K. Koyama. *Cosmological Tests of Modified Gravity*. *Rept. Prog. Phys.* **79** 046902 (2016). [arXiv:1504.04623](#). Cited on pages [100](#), [101](#), and [103](#).
- [132] T. Clifton, P. G. Ferreira, A. Padilla, and C. Skordis. *Modified Gravity and Cosmology*. *Phys. Rept.* **513** 1 (2012). [arXiv:1106.2476](#). Cited on pages [100](#) and [101](#).
- [133] G. Brando, B. Fiorini, K. Koyama, and H. A. Winther. *Enabling matter power spectrum emulation in beyond- $\Lambda$ CDM cosmologies with COLA*. 2022). [arXiv:2203.11120](#). Cited on pages [102](#) and [120](#).
- [134] A. Aghamousa et al. *The DESI Experiment Part I: Science, Targeting, and Survey Design*. 2016). [arXiv:1611.00036](#). Cited on page [102](#).
- [135] R. Laureijs et al. *Euclid Definition Study Report*. 2011). [arXiv:1110.3193](#). Cited on page [102](#).

- [136] M. Knabenhans et al. *Euclid preparation: IX. EuclidEmulator2 – power spectrum emulation with massive neutrinos and self-consistent dark energy perturbations*. *Mon. Not. Roy. Astron. Soc.* **505** 2840 (2021). [arXiv:2010.11288](#). Cited on page 102.
- [137] R. E. Angulo, M. Zennaro, S. Contreras, G. Aricò, M. Pellejero-Ibañez, and J. Stücker. *The BACCO simulation project: exploiting the full power of large-scale structure for cosmology*. *Mon. Not. Roy. Astron. Soc.* **507** 5869 (2021). [arXiv:2004.06245](#). Cited on pages 102 and 105.
- [138] C. Howlett, M. Manera, and W. J. Percival. *L-PICOLA: A parallel code for fast dark matter simulation*. *Astron. Comput.* **12** 109 (2015). [arXiv:1506.03737](#). Cited on page 102.
- [139] C.-H. Chuang, F.-S. Kitaura, F. Prada, C. Zhao, and G. Yepes. *EZmocks: extending the Zel’dovich approximation to generate mock galaxy catalogues with accurate clustering statistics*. *Mon. Not. Roy. Astron. Soc.* **446** 2621 (2015). [arXiv:1409.1124](#). Cited on page 102.
- [140] F.-S. Kitaura, G. Yepes, and F. Prada. *Modelling Baryon Acoustic Oscillations with Perturbation Theory and Stochastic Halo Biasing*. *Mon. Not. Roy. Astron. Soc.* **439** 21 (2014). [arXiv:1307.3285](#). Cited on page 102.
- [141] Y. Feng, M.-Y. Chu, U. Seljak, and P. McDonald. *FastPM: a new scheme for fast simulations of dark matter and haloes*. *Mon. Not. Roy. Astron. Soc.* **463** 2273 (2016). [arXiv:1603.00476](#). Cited on page 102.
- [142] A. Klypin and F. Prada. *Dark matter statistics for large galaxy catalogues: power spectra and covariance matrices*. *Mon. Not. Roy. Astron. Soc.* **478** 4602 (2018). [arXiv:1701.05690](#). Cited on page 102.
- [143] G. Valogiannis and R. Bean. *Efficient simulations of large scale structure in modified gravity cosmologies with comoving Lagrangian acceleration*. *Phys. Rev. D* **95** 103515 (2017). [arXiv:1612.06469](#). Cited on page 103.
- [144] B. Fiorini, K. Koyama, A. Iazard, H. A. Winther, B. S. Wright, and B. Li. *Fast generation of mock galaxy catalogues in modified gravity models with COLA*. *JCAP* **09** 021 (2021). [arXiv:2106.05197](#). Cited on page 103.
- [145] N. Kaushal, F. Villaescusa-Navarro, E. Giusarma, Y. Li, C. Hawry, and M. Reyes. *NECOLA: Towards a Universal Field-level Cosmological Emulator*. 2021). [arXiv:2111.02441](#). Cited on page 103.
- [146] N. Ramachandra, G. Valogiannis, M. Ishak, and K. Heitmann. *Matter Power Spectrum Emulator for  $f(R)$  Modified Gravity Cosmologies*. *Phys. Rev. D* **103** 123525 (2021). [arXiv:2010.00596](#). Cited on pages 103 and 121.
- [147] C. Arnold, B. Li, B. Giblin, J. Harnois-Déraps, and Y.-C. Cai. *FORGE – the  $f(R)$  gravity cosmic emulator project I: Introduction and matter power spectrum emulator*. 2021). [arXiv:2109.04984](#). Cited on pages 103 and 121.
- [148] S. Agarwal, F. B. Abdalla, H. A. Feldman, O. Lahav, and S. A. Thomas. *PkANN - I. Non-linear matter power spectrum interpolation through artificial neural networks*. *Mon. Not. Roy. Astron. Soc.* **424** 1409 (2012). [arXiv:1203.1695](#). Cited on page 104.

- [149] S. Habib, K. Heitmann, D. Higdon, C. Nakhleh, and B. Williams. *Cosmic Calibration: Constraints from the Matter Power Spectrum and the Cosmic Microwave Background*. *Phys. Rev. D* **76** 083503 (2007). [arXiv:astro-ph/0702348](#). Cited on page 104.
- [150] R. E. Angulo and S. D. M. White. *One simulation to fit them all - changing the background parameters of a cosmological N-body simulation*. *Mon. Not. Roy. Astron. Soc.* **405** 143 (2010). [arXiv:0912.4277](#). Cited on page 105.
- [151] V. Springel. *The Cosmological simulation code GADGET-2*. *Mon. Not. Roy. Astron. Soc.* **364** 1105 (2005). [arXiv:astro-ph/0505010](#). Cited on page 105.
- [152] R. E. Angulo, V. Springel, S. D. M. White, A. Jenkins, C. M. Baugh, and C. S. Frenk. *Scaling relations for galaxy clusters in the Millennium-XXL simulation*. *Mon. Not. Roy. Astron. Soc.* **426** 2046 (2012). [arXiv:1203.3216](#). Cited on page 105.
- [153] R. E. Angulo and A. Pontzen. *Cosmological N-body simulations with suppressed variance*. *Mon. Not. Roy. Astron. Soc.* **462** L1 (2016). [arXiv:1603.05253](#). Cited on page 105.
- [154] D. Potter, J. Stadel, and R. Teyssier. *PKDGRAV3: Beyond Trillion Particle Cosmological Simulations for the Next Era of Galaxy Surveys*. 2016). [arXiv:1609.08621](#). Cited on page 105.
- [155] M. Zennaro, R. E. Angulo, G. Aricò, S. Contreras, and M. Pellejero-Ibáñez. *How to add massive neutrinos to your  $\Lambda$ CDM simulation - extending cosmology rescaling algorithms*. *Mon. Not. Roy. Astron. Soc.* **489** 5938 (2019). [arXiv:1905.08696](#). Cited on page 105.
- [156] S. Bird, Y. Ali-Haïmoud, Y. Feng, and J. Liu. *An Efficient and Accurate Hybrid Method for Simulating Non-Linear Neutrino Structure*. *Mon. Not. Roy. Astron. Soc.* **481** 1486 (2018). [arXiv:1803.09854](#). Cited on page 105.
- [157] R. Takahashi, M. Sato, T. Nishimichi, A. Taruya, and M. Oguri. *Revising the Halofit Model for the Nonlinear Matter Power Spectrum*. *Astrophys. J.* **761** 152 (2012). [arXiv:1208.2701](#). Cited on page 111.
- [158] H. A. Winther et al. *Modified Gravity N-body Code Comparison Project*. *Mon. Not. Roy. Astron. Soc.* **454** 4208 (2015). [arXiv:1506.06384](#). Cited on page 112.
- [159] G. W. Horndeski. *Second-order scalar-tensor field equations in a four-dimensional space*. *Int. J. Theor. Phys.* **10** 363 (1974). Cited on page 112.
- [160] H. Winther, S. Casas, M. Baldi, K. Koyama, B. Li, L. Lombriser, and G.-B. Zhao. *Emulators for the nonlinear matter power spectrum beyond  $\Lambda$ CDM*. *Phys. Rev. D* **100** 123540 (2019). [arXiv:1903.08798](#). Cited on pages 116, 118, 120, and 121.
- [161] M. Borzyszkowski, D. Bertacca, and C. Porciani. *LIGER: mock relativistic light-cones from Newtonian simulations*. *Mon. Not. Roy. Astron. Soc.* **471** 3899 (2017). [arXiv:1703.03407](#). Cited on page 121.
- [162] F. Lepori et al. *Euclid preparation: XIX. Impact of magnification on photometric galaxy clustering*. 2021). [arXiv:2110.05435](#). Cited on page 121.
- [163] F. Hassani, J. Adamek, and M. Kunz. *Clustering dark energy imprints on cosmological observables of the gravitational field*. *Mon. Not. Roy. Astron. Soc.* **500** 4514 (2020). [arXiv:2007.04968](#). Cited on page 121.

- [164] R. K. Sheth, A. J. Connolly, and R. Skibba. *Marked correlations in galaxy formation models*. 2005). [arXiv:astro-ph/0511773](#). Cited on page [121](#).
- [165] G. Valogiannis and R. Bean. *Beyond  $\delta$ : Tailoring marked statistics to reveal modified gravity*. *Phys. Rev. D* **97** 023535 (2018). [arXiv:1708.05652](#). Cited on page [121](#).
- [166] C. Hernández-Aguayo, C. M. Baugh, and B. Li. *Marked clustering statistics in  $f(R)$  gravity cosmologies*. *Mon. Not. Roy. Astron. Soc.* **479** 4824 (2018). [arXiv:1801.08880](#). Cited on page [121](#).
- [167] K. Hinterbichler and J. Khoury. *Symmetron Fields: Screening Long-Range Forces Through Local Symmetry Restoration*. *Phys. Rev. Lett.* **104** 231301 (2010). [arXiv:1001.4525](#). Cited on page [121](#).
- [168] S. Alam et al. *Towards testing the theory of gravity with DESI: summary statistics, model predictions and future simulation requirements*. *JCAP* **11** 050 (2021). [arXiv:2011.05771](#). Cited on page [121](#).